Effect of Microstructure on Hydrogen Permeation in X70 Steel

by

Lu Sun

A thesis submitted in partial fulfillment of the requirements for the degree of

Doctor of Philosophy
in
Materials Engineering

Department of Chemical and Materials Engineering
University of Alberta

Abstract

The susceptibility of pipeline steel to hydrogen induced degradation is closely related to the interaction between hydrogen and some microstructural features of the steel such as precipitates, inclusions, phase type and grain size. These microstructural features can act as hydrogen traps (irreversible or reversible) and delay hydrogen diffusion process. Thermomechanical controlled processing (TMCP), by which advanced pipeline steels are manufactured, have great influence on the formation and distribution of these microstructural features and hence the trapping ability of the pipeline steels.

In the present study, two groups of X70 pipeline steel with different microstructures were obtained by different TMCP. The microstructure of each steel was characterized using optical microscopy (OM), scanning electron microscopy (SEM), transmission electron microscopy (TEM) and electron back scattering diffraction (EBSD). Meanwhile, the effective diffusion coefficient (D_{eff}) and hydrogen trap density (N_t) were calculated by t-lag method and curve-fitting method based on the hydrogen permeation curves obtained by Devanathan-Stachurski (DS) electrochemical hydrogen permeation test. Furthermore, a trap efficiency model was established to evaluate the trapping ability of the phases presented in X70 steel; and a hydrogen diffusion numerical simulation model was developed to determine the diffusivity, trap density and binding energy based on experimental hydrogen permeation data.

It is shown that nano-sized NbC precipitates are irreversible hydrogen traps that can decrease the amount of diffusible hydrogen. Also, it is found that a great amount of these fine precipitates was generated during coiling process, the count density of which increased with

decreased cooling rate after runout table. Conversely, large (~ 100 nm) TiN precipitates (including complex NbC/TiN precipitates), were not effective hydrogen traps under the test condition.

Non-metallic inclusions (NMIs), mostly CaS and Al_2O_3, were found acting as strong irreversible hydrogen traps. Finer NMIs trap hydrogen more efficiently due to their larger specific surface area. And it is shown that an increase in overall rolling deformation resulted in a finer NMI size distribution.

In addition, pocket/block boundaries of lath low bainite are high angle grain boundaries (HAGBs) that act as irreversible traps. The fraction of these HAGBs is greatly affected by prior austenite grain (PAG) size and can be controlled by rough rolling process.

A trapping efficiency model was established to correlate the characterization results to the hydrogen permeation test results. According to the modelling result, the reversible trapping efficiency of the phases in X70 steel rank in the order of M/A > bainite > ferrite.

At last, a numerical simulation model was established and gives D_{eff} values that are very close to those calculated by time-lag method. According to the model, the average binding energy of irreversible traps in 3E-Coiled is higher at surface region than near centerline region.

Preface

This thesis is an original work by Lu Sun. No part of this thesis has been previously published.

Acknowledgements

I would like to express my deep appreciation to Dr. Hani Henein, who offered me great encouragement and generous help and who believes in me even more than I do myself. I would also like to thank Dr. Weixing Chen for his guidance and welcome advice, which is the key to my success in experimental work. I also thank Dr. Ivey for his important suggestions and comments on the characterization part of work. Special thanks go to Dr. J. Barry Wiskel, who is a patient and passionate teacher as well as a great friend to me, and who is always there for me whenever I need help.

I would also like to thank Dr. Jonas Vallonton for his great help and training for my lab work. Many thanks go to my colleagues in steel group for their valuable challenging questions and inspiring discussions. Financial assistance from Canmet and EVRAZ is greatly acknowledged.

I would like to take this opportunity to express my gratitude to my family: my husband, my mother, and my parents-in-law. Thank you so much for your great support and unconditional love. I would never achieve this without any of you. And finally, I would like to thank my dearest daughters, Siqi and Shannon. Your smiles are the sunshine in my life, giving me warmth and hope, even in winter and darkness; your love is the most powerful engine in the world, driving me to realize all my dreams, even the craziest ones. I love you to the moon and back.

I would like to give my deepest gratitude to God for his accompany, every day and night, every minute and second. No matter failure or success, pain or joy, He listens to me; He guides me; and He is with me.

Table of Contents

List of Tables

List of Figures

Nomenclature

ADF image	Annular dark field image
AF	Acicular ferrite
AIDE	Adsorption-induced dislocation emission
APT	Atom probe tomography
BC map	Band contrast map
BF	Bainitic ferrite
BF image	Bright field image
CCT diagram	Continuous cooling transformation
CE	Counter electrode
CP	Cathodic protection
CT	Coiling temperature
DP	Degraded pearlite
DS cell	Devanathane-Stachurski cell
EBSD	Electron backscatter diffraction
EDS	Electron dispersive spectroscopy
EDTA	Ethylenediaminetetraacetic acid
EIS	Electrochemical impedance spectroscopy
FESEM	Field emission scanning electron microscope
GB	Granular bainite
HAC	Hydrogen assisted cracking
HAGB	High angle grain boundary
HE	Hydrogen embrittlement
HEE	Hydrogen environmental embrittlement
HEDE	Hydrogen enhanced decohesion
HELP	Hydrogen enhanced localized plasticity
HER	Hydrogen evolution reaction
HIBC	Hydrogen induced blister crack
HIC	Hydrogen induced cracking
HMT	Hydrogen microprint technique

HPT	Hydrogen permeation test
HR-TEM	High resolution-Transmission electron microscopy
HSC	Hydrogen stress cracking
HSLA steel	High-strength low-alloy steel
IF	Irregular ferrite
IHE	Internal hydrogen embrittlement
IPF	Inverse pole figure
IQ value	Image quality value
KAM	Kernel average misorientation
LAGB	Low angle grain boundary
LB	Lower bainite
M/A	Martensite/austenite
MLIL	Mean lineal intercept length, μm
MSE	Mean square error
NMIs	Non-metallic inclusions
NNpHSCC	Near-neutral pH SCC
OLAC	Online accelerate cooling
OM	Optical microscopy
P	Pearlite
PAG	Prior austenite grain
PF	Polygonal ferrite
PMMA	Polymethyl methacrylate
RA	Retained austenite
RE	Reference electrode
RSE	Relative standard error
SAED	Selected area electron diffraction
SANS	Small-angle neutron scattering
SCC	Stress corrosion cracking
SEM	Scanning electron microscopy
SOHIC	Stress-oriented hydrogen induced cracking
SSC	Sulfide stress cracking
STD	Standard deviation

TDS	Thermal desorption spectrometry
TEM	Transmission electron microscopy
TMCP	Thermomechanical controlled processing
UB	Upper bainite
bcc	Body-Centered Cubic
bct	Body-Centered Tetragonal
fcc	Face-Centered Cubic
A	Exposed area of the specimen, cm^{-2}
$\bar{A}$	Vector of trap efficiency factor
A_0	Reaction rate constant, $mol \cdot s^{-1}$
A_{c1}	Lower critical temperature, at which austenite starts to transform from ferrite, °C
A_{c1f}	Pearlite dissolution finish temperature, at which pearlite begin to transform into austenite, °C
A_{c3}	Upper critical temperature, at which austenite is completely transformed from ferrite, °C
A_{ir}	Constant in semi-empirical equation (5-1), $mol \cdot cm^{-3}$
A_p	Measured sectional area of a precipitate, μm^2
A_{r3}	Austenite to ferrite transformation temperature, °C
C_0	Critical carbon concentration, $mol \cdot cm^{-3}$
D	Diameter of nano-sized NbC precipitates, nm
D_0	Precipitate diameter at the maximum of the size distribution of nano-sized NbC precipitates, nm
$D_{0,1}$	D_0 of peak 1 of the nano-sized NbC precipitate size distribution, nm
$D_{0,2}$	D_0 of peak 2 of the nano-sized NbC precipitate size distribution, nm
D_{av}	Average diameter of precipitates, μm
D_{eff}	Effective diffusion coefficient, $cm^2 \cdot s^{-1}$
D_L, D_l	Diffusion coefficient of hydrogen in ferrite lattice, $cm^2 \cdot s^{-1}$
D_m	Mean value of the diameter of the nano-sized NbC precipitates, nm
D_w	Diffusion coefficient of H due to reversible traps during 2nd round of HPT, $cm^2 \cdot s^{-1}$
E_a	Activation energy for hydrogen escape from the trapping site, $kJ \cdot mol^{-1}$
E_d	Diffusion activation energy, $kJ \cdot mol^{-1}$
E_{des}	Desorption barrier, eV

E_i	Binding energy for irreversible traps in hydrogen permeation model, kJ·mol^{-1}
ΔE_x, E_b	Binding energy, kJ·mol^{-1}
ΔE_{TLi}	Trapping energy corresponding to temperature T_{pi} in TDS test
F	Faraday constant, 96 485.3321 s·A· mol^{-1}
I	Oxidation current, A
I_{ss}	Steady-state oxidation current, A
I_t	Oxidation current at time t, A
J	Hydrogen flux, mol·cm^{-2}·s^{-1}
J_{ss}	Steady-state hydrogen flux, mol·cm^{-2}·s^{-1}
K	Equilibrium constant between hydrogen in trap and hydrogen in lattice site
K_r	Equilibrium constant between hydrogen in reversible trap and hydrogen in lattice site
L	Thickness of the sample, mm
N	Trap density, mol·cm^{-3}
N_0	Total number of precipitates in the size distribution of nano-sized NbC precipitates
$N_{c,cl}$	Irreversible trap density in 3F-Coiled-Centerline sample, mol·cm^{-3}
N_L	Density of normal lattice sites, 7.52×10^{28} m^{-3}
N_p	Number of precipitates per unit area, count·cm^{-3}
N^s_t, N^q_t, N^c_t	Trap density of surface, quarter distance and centerline sample, mol·cm^{-3}
N_t, $N_{t,total}$	Total trap density, mol·cm^{-3}
$N_{t,ir}/N_i$	Irreversible trap density, mol·cm^{-3}
$N_{t,r}/N_r$	Reversible trap density, mol·cm^{-3}
$N_{wq,cl}$	Irreversible trap density in 3F-Water quenched-Centerline sample, mol·cm^{-3}
$N'_{wq,cl}$	Updated irreversible trap density in 3F-Water quenched-Centerline sample, mol·cm^{-3}
$N'_{wq,s}$	Updated irreversible trap density in 3F-Water quenched-Surface sample, mol·cm^{-3}
Q	Activation energy for transformation, kJ·mol^{-1}
R	Gas constant, 8.13 J·K^{-1}mol^{-1}
S	Measured SEM image area, μm^2
T	Temperature, °C
T_c	Temperature at the desorption peak, °C

T_e	Ending temperature of transformation, °C
T_{nf}	Recrystallization temperature, °C
T_{pi}	Peak temperature in TDS, K
T_s	Starting temperature of transformation, °C
X	Hydrogen amount that escaped from a trap site
X_γ	Global volume fraction of austenite
a_f, a_b, a_a, a_m	Trapping efficiency factor of ferrite, bainite, M/A and martensite, $mol \cdot cm^{-3}$
a_L	Activity of hydrogen on the lattice site, $kJ \cdot mol^{-1}$
a_x	Activity of hydrogen on the trapping site, $kJ \cdot mol^{-1}$
b	Constant of equation (6-3), $mol \cdot cm^{-3}$
b_0	Constant of equation (6-5), $mol \cdot cm^{-3}$
b_{ir}	Constant in semi-empirical equation (5-1)
c_0	Subsurface concentration of hydrogen atoms at the charging side of the sample, $mol \cdot cm^{-3}$
c_{app}	Apparent concentration of hydrogen on entrance surface, $mol \cdot cm^{-3}$
$c_{app,i}$	Apparent concentration of hydrogen of ith transient, $mol \cdot cm^{-3}$
$c_{in,cl}$	NMIs density in 3F-Water quenched-Centerline sample, $mol \cdot cm^{-3}$
$c_{in,s}$	NMIs density in 3F-Water quenched-Surface sample, $mol \cdot cm^{-3}$
c_l	Lattice hydrogen concentration, $mol \cdot cm^{-3}$
c_L, c	Hydrogen concentration at exit side surface of the sample, $mol \cdot cm^{-3}$
c_s	Hydrogen concentration at location x = s, $mol \cdot cm^{-3}$
c_T	Total hydrogen concentration, $mol \cdot cm^{-3}$
c_x	Hydrogen concentration in traps, $mol \cdot cm^{-3}$
c_∞	Hydrogen concentration at entrance side at steady state, $mol \cdot cm^{-3}$
d	Lattice distance, nm
f	Fraction of transformed phase, %
$f_m, f_{M/A}, and\ f_{RA}$	Volume fraction of martensite, M/A and RA, respectively
i_0	Constant current applied on entrance side of the sample, A
i_∞	Steady-state current at exit side of the sample, A
i_L	Oxidation current at the exit side of the sample, A
j_0	Constant hydrogen flux at entrance side of the sample, $mol \cdot cm^{-2} \cdot s^{-1}$
$k\ and\ p$	Trapping and detrapping constants

k_B	Boltzmann constant, 1.380649×10^{-23} m^2 ·kg· s^{-2} ·K^{-1}
m	constant in hydrogen permeation equations under constant flux/constant concentration conditions
n'	Number of slices divided in hydrogen permeation model
n, τ_0	Avrami parameters
n_e	Number of elements in a finite element model
n_p	Total number of measured precipitates
n_{roll}	Number of rough rolling passes
$n_{wq,cl}$	Trap density due to micro-cracks in 3F-Water quenched-Surface sample, mol·cm^{-3}
$n_{wq,s}$	Trap density due to micro-cracks in 3F-Water quenched-Centerline sample, mol·cm^{-3}
p	Reaction order of the desorption process in TDS test
q	Elementary charge, 1.602×10^{-19} C
t	Time, s
t_b	Breakthrough time, s
t_{lag}	Elapsed time, s
v_0	Attempt frequency, s^{-1}
x	Spatial coordinate
x_a	Area fraction of M/A, %
x_b	Area fraction of bainite, %
x_f	Area fraction of ferrite, %
x_j^i	Area fraction of phase j at location i, %
x_m	Area fraction of martensite, %
Θ	Coverage of adsorbates in the unit of monolayer
Φ_α, Φ_γ	Permeation coefficients of the martensite and austenite phases, respectively
Ψ	Vector of reversible trap density in different phases
χ	Matrix of phase faction at various locations
α	A fitting parameter related to the width of the distribution β via equation (4-3)
α-Fe	Ferrite
β	Width of the size distribution of the nano-sized NbC precipitates
γ-Fe	Austenite
θ	Fraction of reversible traps that are occupied by hydrogen atoms

θ_L	Fraction of occupied sites in normal lattice
τ'	Normalized hydrogen permeation time
τ	Characteristic time in Avrami equation
σ	The standard deviation of the nano-sized NbC precipitate size distribution, nm
φ	Heating rate in TDS test, $K \cdot s^{-1}$

1 Introduction

Pipeline steels are widely used in transportation of oil and natural gas for long distance and play a crucial role in supporting our increasing energy demand. However, hydrogen generated from corrosion and/or cathodic protection process can cause mechanical properties degradation of pipeline steels leading to severe hydrogen embrittlement (HE)[1]. Initiation and propagation of cracks assisted by hydrogen often give rise to catastrophic consequences such as explosions or leaking, economic loss, environmental pollution or even casualties. The hydrogen assisted cracking (HAC) process can be classified into many types such as stress corrosion cracking (SCC) and stress-oriented hydrogen induced cracking (SOHIC) in which external stress plays a role, and hydrogen induced cracking (HIC) which is generally used for hydrogen degradation without consideration of external stress. These forms of hydrogen induced degradation is one the main threats to the integrity of pipeline steel. Therefore, thermomechanical controlled process (TMCP) designed for manufacturing of pipeline steels with low hydrogen susceptibility is a promising way to solve the issue.

To date, a great amount of work has been done to reveal the effect of hydrogen on the integrity of pipeline steel. However, few of them focused on the effect of manufacturing process on the formation or distribution of hydrogen traps. In the present investigation, the influence of different steps of TMCP on various kinds of microstructural features that are effective hydrogen traps were studied, which gives us insights about how to produce pipeline steels with high HIC resistance. Furthermore, in contrary to the qualitatively comparison of trapping ability between phases in pipeline steel by many other researchers, the trapping efficiency model proposed in the present study quantitatively evaluated the trapping efficiency of phases including M/A, ferrite and bainite and hence gave more accurate estimation to the trapping ability of these phases. In addition, most of the models that are commonly used to analyze hydrogen permeation curves are established based on theories for reversible traps. But in the present study, a numerical simulation model is proposed to simulate the trapping effect of reversible traps and irreversible traps separately based on hydrogen permeation curves obtained during 2nd and 1st round of charging, respectively. In this way, the trap density and binding energy of irreversible traps can be calculated more reasonably.

There are several types of hydrogen permeation/characterization tests including: hydrogen microprint technique (HMT)[2, 3], thermal desorption spectrometry (TDS)[4-6], Devanathane-Stachurski (DS) cell hydrogen permeation test [7-9], Electrochemical impedance spectroscopy (EIS)[7, 10], atom probe tomography (APT)[11], etc. For this work, DS cell hydrogen permeation testing technique is used to quantify the permeation curve, diffusion coefficient and trap density in an X70 steel.

To better understand the mechanism of the HIC process, many theories have been proposed, among which the most discussed are two seemly opposite ones: hydrogen enhanced decohesion (HEDE) and hydrogen enhanced localized plasticity (HELP). However, no widely accepted theory exists so far and many details of hydrogen effects on mechanical properties remains unknown[12, 13]. Despite an unclear fundamental mechanism, using some advanced techniques, some progress has been made in understanding the interaction between hydrogen and microstructure when hydrogen atoms enter in the base metal. Hydrogen diffusion and entrapment in microstructural defect sites, such as inclusions, interfaces, grain boundaries, precipitates etc., are considered responsible factors for HIC of steels and determines the failure mechanism[12, 14]. These defects can be classified as reversible and irreversible traps according to their trapping ability and play different roles in HIC susceptibility of the steel.

Over the past several decades, numerous mathematical models for investigating the phenomenon of hydrogen trapping in metals through parameters like hydrogen trap binding energy (E_b) and density of the trapping sites (N_T) have been proposed. McNabb and Foster [15]proposed a trapping-detrapping model based on the assumption that a dynamic equilibrium is maintained between trapped hydrogen and lattice hydrogen. Oriani [16] made more specific treatment based on the local equilibrium hypothesis and concluded that the effective diffusivity is a function of trap density and of the magnitude of the trap depth with some practical equations. Based on their work, many new mathematical models are proposed by other researchers trying to determine the density of hydrogen trap sites[17-19] or simulate the hydrogen diffusion process[20-22]. In this work, a model supported by experimental data will be established to reveal the effect of different microstructures on the hydrogen permeation process.

Microstructural features, such as precipitates, secondary-phases, grain size, can be significantly affected by steel processing. Advanced pipeline steels are low carbon microalloyed

steels produced by thermomechanical controlled processing (TMCP) method, which consists of several important stages including casting, rough rolling, finish rolling, accelerated cooling, and coiling. All these stages will affect the types of traps and the amount of each type of trap involved as well as the distribution of these traps. In this work eleven (11) micro-alloyed steel plates will be examined. Each has been processed differently and has a different microstructure.

The research aims of this work are as follows:

1) Quantify the microstructure including precipitates, phases and grain morphologies of the four (4) plates of Group I and seven (7) plates of Group II using TEM, EBSD, OM and SEM. These groups of plates are X70 pipeline steels with the same chemistry composition but produced under different TMCP. Group I steels have been through rough rolling, finish rolling, and accelerated cooling followed by coiling, air cooling or water quench; whereas Group II steels were only subjected to various passes of rough rolling, and all were water quenched without finish rolling process.

2) Conduct DS electrochemical hydrogen permeation test on the four (4) plates of group I and seven (7) plates of group II and calculate the hydrogen diffusivity and trap density via hydrogen permeation curves.

3) Develop a model correlating microstructure characteristics and trap density (including reversible and irreversible traps) in microalloyed steels.

4) Establish a hydrogen diffusion model to simulate the diffusion process with trapping effect and make evaluations about parameters such as diffusivity, trap density and binding energy by comparing with experimental data.

5) Develop a CCT diagram of the steel with the same composition using Gleeble data under different cooling rate (Appendix D).

A literature review of hydrogen induced cracking process and trapping theory is presented in Chapter 2, followed by a background study of different hydrogen permeation testing techniques with a specific focus on double-cell electrochemical hydrogen permeation test (HPT) including

data analysis methods based on HPT results. An introduction about TMCP is also presented as well as a review about hydrogen trapping ability of different microstructures in pipeline steels and the role these microstructures have in the HIC process. At the end of Chapter 2, previous work in the field of hydrogen trapping modelling is reviewed.

Chapter 3 is mainly about materials and experimental methods. The composition, TMCP parameters, sampling location and orientation of two groups of steels investigated are presented separately. Following the material part is a detailed description of experimental techniques used in the study including hydrogen permeation test, sample preparation methods for TEM, EBSD, SEM and OM. Data analysis methods for hydrogen permeation test and characterization test results are also involved.

In Chapter 4, characterization and hydrogen permeation results of group I samples are shown and discussed. Using EBSD, volume fractions of phases are obtained by calculation based on band contrast map, and misorientation distribution and grain size are also evaluated; size distribution and area fraction as well as the lattice parameter of nano-sized NbC precipitates are obtained by TEM; microstructure and inclusions are revealed by OM and SEM with EDS results showing the composition of inclusions. Hydrogen permeation curves obtained using double-cell electrochemical hydrogen permeation test are shown and analyzed using two methods: time lag method and curve fitting method.

In Chapter 5, characterization and hydrogen permeation results of group II samples are shown and discussed. EBSD results including misorientation distribution histogram and grain boundaries distribution map are presented; morphology and size distribution of TiN and NbC precipitates are revealed and measured by TEM under STEM mode with composition obtained using EDS and lattice diffraction patterns of these precipitates are obtained using selected area electron diffraction (SAED) mode of TEM; the hydrogen permeation results of group II samples are shown and analyzed in the same way as presented in Chapter 4.

Based on characterization and hydrogen permeation results shown in Chapter 4 and Chapter 5, a trapping efficiency model and two hydrogen permeation simulation models are presented in Chapter 6. The trapping efficiency model is used to quantitatively estimate the reversible trapping ability of phases in the steel, and the simulation models give information

including diffusivity, trap density and binding energy by simulating the hydrogen permeation process and comparing simulation data with experimental data.

In Chapter 7, the results presented in chapters are discussed and analyzed from a processing perspective, including the effect of rough rolling deformation on TiN-NbC precipitation and PAG/HAGB, the effect of rolling process on non-metallic inclusions, the effect of coiling process on nano-size NbC precipitates, and the effect of TMCP on M/A constituents.

Finally, the findings are summarised, and conclusions are drawn based on these findings in Chapter 8. In the end, the areas that need further work both experimentally and theoretically are identified, and possible future work to build up-on the work done in the thesis and to further enhance the models is outlined in Chapter 9.

2 Literature Review

Since 1875, when Johnson[23] first discovered the detrimental effect of H cause to steel, great efforts have been made to better understand the underlying mechanism behind the phenomenon and to lower the potential risk it brings to industries. However, no agreement has been attained yet on the mechanism of hydrogen induced cracking (HIC) and millions of dollars are lost each year due to the HIC of pipeline steel[13, 24-26].

This thesis focuses on the effect of various microstructural features caused to hydrogen diffusion behavior in X70 pipeline steel and investigates the beneficial microstructure for higher HIC resistance of the steel. In this section, some background information of the present study is provided, including thermomechanical controlled process (TMCP) which is a commonly used manufacturing technique in pipeline steel industry, some commonly seen HIC phenomenon and most cited HIC mechanisms, introduction of hydrogen permeation techniques widely used in research, experimental results about interactions between microstructures and hydrogen.

2.1 *Thermomechanical controlled process of steels*

Thermo-mechanically controlled processing (TMCP) is a combination of advanced steel manufacturing techniques involving controlled rolling, controlled cooling and optimization of microalloying (e.g., niobium addition). Since 1956, when the first industrial-scale manufacturing process with online quenching on hot-rolled plates, a prototype of modern TMCP, was introduced in Japan[27], TMCP has been extensively developed and widely adopted by steel manufacturing companies across the world, especially in pipeline industry. The controlled rolling and controlled cooling techniques make it possible to produce steel plates with high strength and high toughness, due to grain size refinement and accurate controlled austenite to ferrite transformation. One the other hand, minimization in alloy addition enables great improvement of weldability as well as reduction of cost.[27, 28]

Fig.2.1 shows a typical TMCP for pipeline steel and Fig.2.2 shows the microstructure of steels in corresponding process. Low-temperature reheating (1200°C or less) is favorable to start the following controlled rolling process at a low temperature where the prior austenite grain size is carefully controlled [29]. As shown in Fig.2.2, rough rolling is conducted in the recrystallization temperature range (about 900°C~1100°C). During this stage, austenite grains are refined by

recrystallization and most of the crystallographic discontinuities such as ledges and deformation bands that introduced by the rolling disappear due to recrystallization. The finish rolling process is conducted at a temperature between T_{nf} and A_{r3} (800°C~950°C). As shown in Fig.2.2, since no recrystallization can occur at this temperature, the austenite grains are elongated into pancake shape and more crystallographic discontinuities are introduced into grains.[28] Actually, one of the main differences between conventional hot-rolling and controlled-rolling lies in that, α grains nucleate exclusively on ɣ grain boundaries in the former, whereas in the latter, nucleation also occurs at deformation bands inside grains. Low-temperature finish rolling is considered as an effective technique to refine the recrystallized ɣ grains and hence improves the notch toughness and yield strength of the steel[29]. After rolling, the plate will be sent to the runout table for accelerate cooling, i.e., online accelerate cooling (OLAC). During this stage, the retaining deformation ledges and bands act as heterogeneous nucleation sites for the austenite to ferrite transformations and contribute to grain refinement[27]. The cooling strategies governs the final microstructure and define the mechanical properties of the steels. For most high-strength low-alloy pipeline steel, the initial cooling temperature and cooling rate are selected to obtain fine and uniform acicular ferrite or upper bainite.
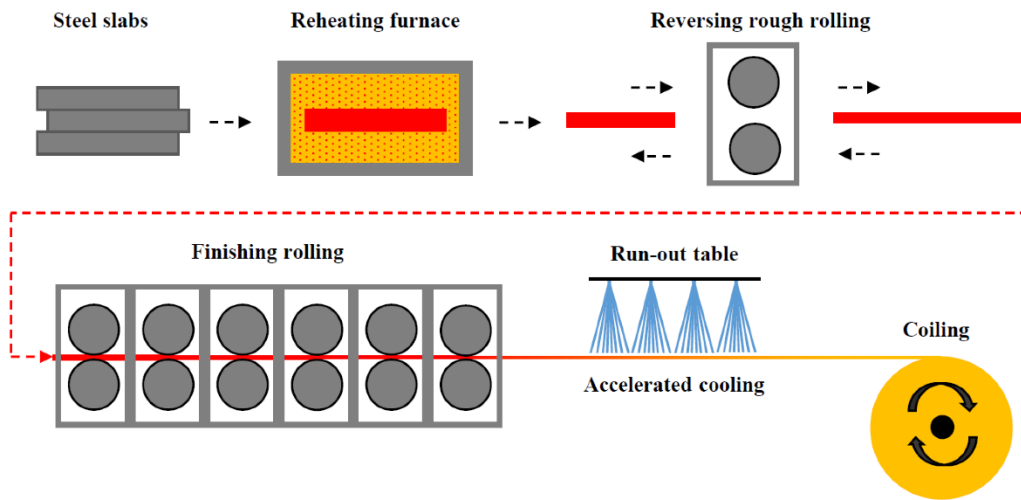
Fig. 2.1 Schematic representation of a typical TMCP for pipeline steel. [30]
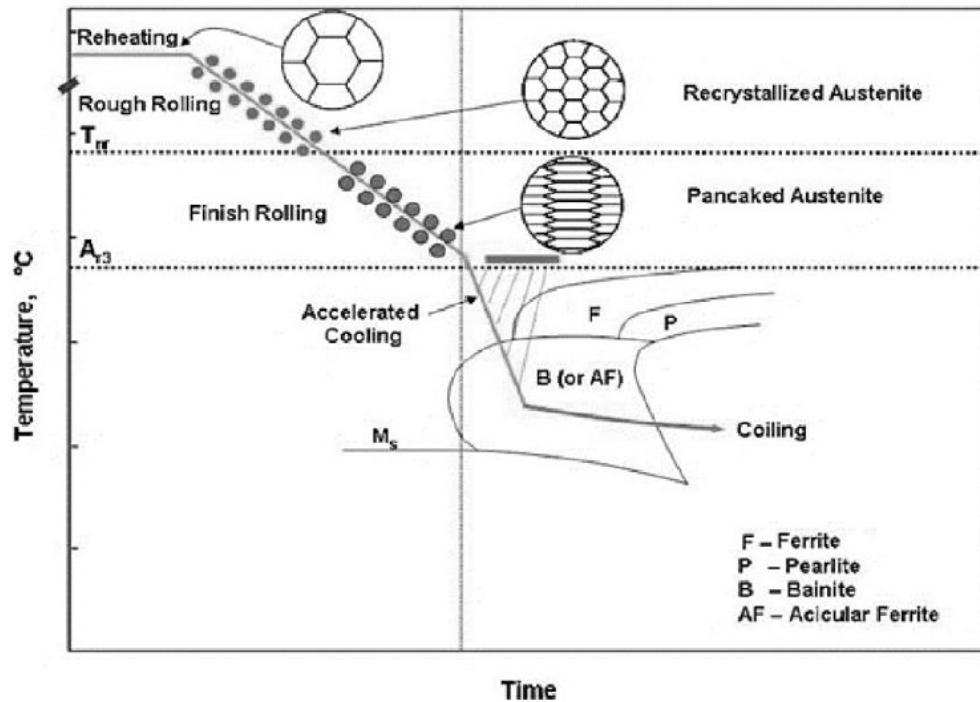
Fig. 2.2 Schematic diagram of a TMCP schedule, superimposed on a CCT diagram, indicating the phase transformations during processing.[31]

Apart from low temperature rolling and accelerate cooling, addition of microalloying elements also plays an important role in TMCP techniques. The strengthening effect of these alloying additives derives from the fundamental behaviors of these microalloying elements, such as solubility, precipitation of carbide or nitride and retardation of austenitic recrystallization[29]. Trace of niobium can considerably improve toughness and strength of the plate in three ways: 1) grain size refinement during rolling process through Nb solute drag (retard the onset of recrystallization) and pinning effect of Nb(CN) precipitates (impede the coarsening of grains); 2) lowering the austenite to ferrite transformation temperature (A_{r3}); 3) precipitation strengthening due to niobium carbides and nitrides[32]. Niobium precipitation at each TMCP stage and its effect on ferrite grain refinement and precipitation strengthening are illustrated in Fig. 2.3. Giant NbC precipitates (~300 nm) can restrain austenite grain coarsening by pinning effect during slab reheating; large NbC (~50 nm) generated during finish rolling process prevent austenite recrystallization; fine NbC (~10 nm) formed during cooling process improve yield strength of the steel via precipitation hardening effect. The size of Nb(CN) precipitates decreases with the

temperature. Nano-sized (~10 nm) niobium precipitates, which affect the hydrogen diffusion process [33, 34] and are of interest in this study, are formed during laminar cooling process and subsequent coiling process, where the temperature is about 600°C and below.

After finish rolling, the pipeline steel plates are subjected to the coiling processing, where the plates are coiled up at certain temperature in the range of bainite transformation temperature and slowly cooled down. During this process, carbon in bainite diffused into untransformed austenite (partitioning process of carbon), leading to the increase of carbon content in austenite. Large amount of austenite transformed into martensite due to the high concentration of carbon, which combined with remained austenite (RA) in form of M/A constituents[35]. Therefore, the coiling temperature (CT) plays a crucial role in microstructure control. For example, it is reported that as CT decreases, the average size of M/A islands decreases[36]. In addition, CT also has significant effect on precipitation of microalloying elements, such as Nb, V and Ti. It is claimed that precipitation of these carbides/nitrides/carbonitrides can be accelerated by high CT, which at the same time may lead to coarsening of precipitates and hence decreasing in strength [37].
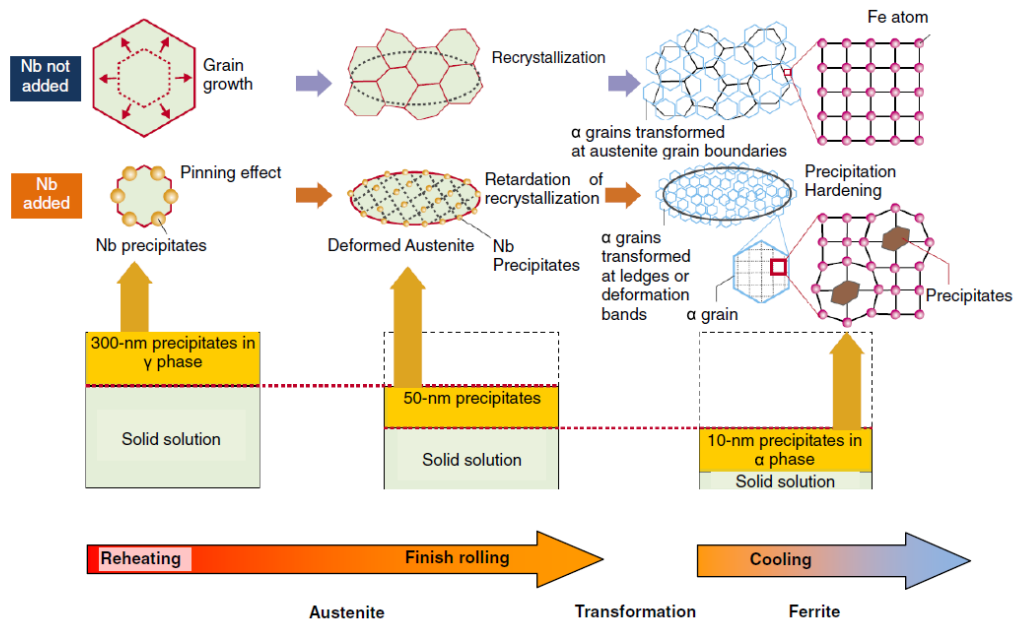
Fig. 2.3 Effect of niobium precipitations on grain refinement at each stage of TMCP. [27]

2.2 Hydrogen related degradation of steel

2.2.1 Category

Hydrogen has high mobility in metals due to its small atomic radius and can cause mechanical property degradation of materials in various ways (as shown in Fig. 2.4). Some forms of damage are associated with tensile stress, such as stress assisted diffusion and sulfide stress cracking; whereas some can occur without stress, for example, hydrogen induced cracking, blistering and stepwise cracking. However, the mechanisms of these types of hydrogen induced degradation are not completely understood yet.
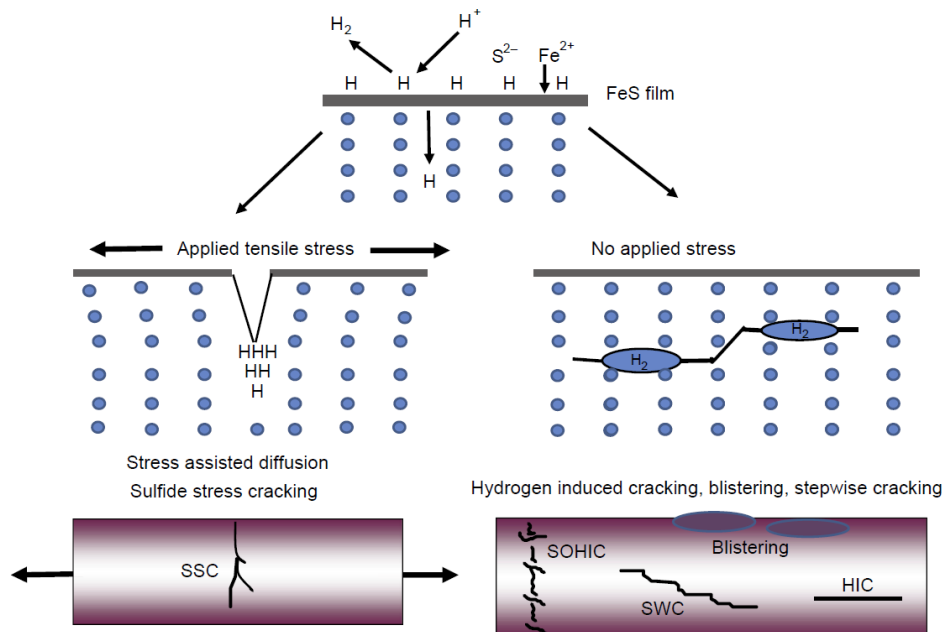
Fig. 2.4 Various forms of hydrogen damage in materials. [39]

For clarification, as different terminologies are used in the literature, some common forms of hydrogen degradation are described as follows.

Hydrogen embrittlement (HE): HE means the phenomena of reduction in ductility and toughness of a metal when hydrogen is absorbed[38]. However, it has also been used to mention the effect of hydrogen on materials in general[39]. Depending on the source of hydrogen, HE can

be divided into two types: internal hydrogen embrittlement (IHE) and hydrogen environmental embrittlement (HEE)[40].

Hydrogen-induced cracking (HIC): Hydrogen atoms absorbed in steels can recombine into gaseous molecules in voids and lead to internal cracks without external stress. HIC is one of the most challenging problems in oil and gas industry, causing severe equipment failure, environmental pollution and economic losses[41]. The HIC susceptibility of a steel is closely related to its microstructure, and hence can be controlled by the composition and manufacturing process. It has been reported that Non-metallic Inclusions (NMIs) such as Al and Ca oxides, elongated MnS and TiN can help initiation of HIC by providing hydrogen traps, i.e., micro-voids around inclusion surface[42-44], as shown in Fig. 2.5. Moreover, HIC initiation at local M/A constituents concentrated region has also been observed[45]. On the other hand, some recent research found that nano-sized NbC precipitates can increase HE susceptibility of martensitic steel by pinning hydrogen-dislocation Cottrell atmospheres during HE failure and capturing hydrogen from the atmospheres [46]. Some research also shows nano-sized NbC precipitates improve HIC resistance by providing large amount of highly dispersed irreversible traps and prevent grain growth to increase the number of grain boundaries which act as reversible traps[47]. However, coarse (Nb, Ti, V)(C,N) particles that formed in liquid steel during solidification might act as crack initiation sites, and hence decrease the HIC resistance of the steel[48]. In addition, HIC resistance of a phase/structure is associated with multiple factors. Huang claimed that microstructures with better hydrogen trapping abilities have higher HIC susceptibility since more hydrogen is trapped[49]. It is also concluded that HIC tends to initiate and propagate in less ductile microstructures. For example, segregated bainitic or martensitic structures are detrimental[50], whereas a refined homogeneous quenched and tempered bainite/martensite microstructure exhibited improved HIC resistance[51]. In this sense, Park claimed that acicular ferrite (AF) is the most desired microstructure for pipeline steel because it prevents the local agglomeration of hard M/A constituents although AF shows higher reversible trapping efficiency than bainite[45].
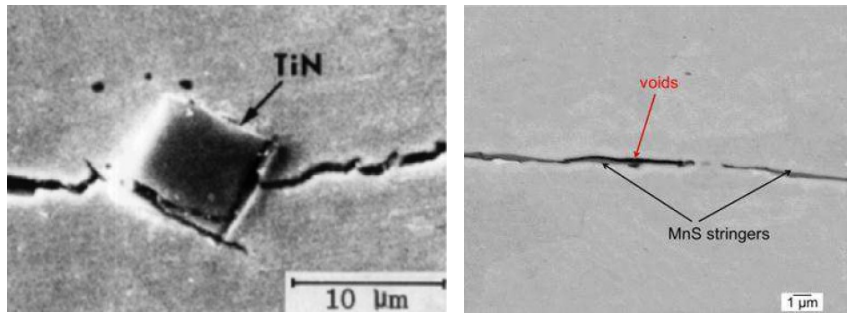
Fig. 2.5 HIC cracks initiated at TiN a)[52] and along MnS stringers b)[53]

Hydrogen-assisted cracking (HAC): is generally used to mention a wide range of hydrogen related degradation of metals, including HSC, SCC and HIC[1, 54].

Hydrogen blistering: When molecular hydrogen and atomic hydrogen accumulated in steel, the pressure can be high enough to cause blisters and eventually failure of the structure[41].

Hydrogen stress cracking (HSC): HSC, also called sulfide stress cracking (SSC), occurs in the presence of hydrogen sulfide under external stress[41]. There are two types of SSC, Type I (or stress-oriented hydrogen induced cracking, SOHIC), which is formed by alignment of hydrogen induced blister crack (HIBC) and Type II, which is a critical HE caused cracking[1].

Stress corrosion cracking (SCC): SCC is defined as sub-critical cracking of materials under sustained loads (residual or applied) in most liquid and some gaseous environments. Two forms of SCC have been mainly observed in pipeline steel: high pH SCC and near-neutral SCC. The former usually occurs in the presence of a concentrated carbonate/bicarbonate environment at a pH greater than 9, resulting in an intergranular cracking; whereas the latter is always associated with electrolyte characterized with anaerobic diluted solutions with pH in the range of 6-7.5 and has a transgranular, quasi-cleavage crack morphology with very little branching[55, 56]. Although in earlier studies, hydrogen was usually ruled out as a cause of near-neutral pH SCC (NNpHSCC), recent studies show that generation and ingress of hydrogen at crack tip plays an important role in NNpHSCC. It is widely accepted that solute hydrogen ahead of crack tips either weakens interatomic bonds and facilitates decohesion or enhances dislocation activity and promotes crack growth[40] and the crack propagation is actually driven by a corrosion-fatigue mechanism[56]. It has been reported that nano-sized NbC precipitates can significantly hinder SCC of HSLA steel by providing large amount of hydrogen traps to reduce the amount of diffusible hydrogen[57].

In addition to the hydrogen-related degradation mentioned above, hydrogen can also accelerate the fatigue crack growth via enabling successive crack growth without crack tip blunting, as shown in Fig.2.6. In sum, hydrogen can cause great degradation in mechanical properties of pipeline steels and significant threat to the integrity of pipelines.
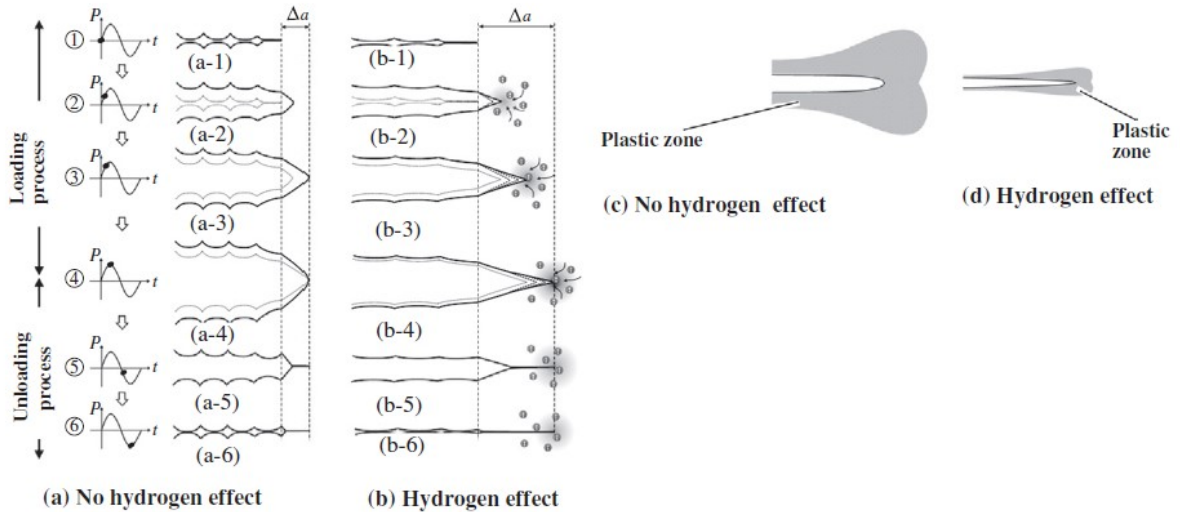
Fig. 2.6 Mechanism of fatigue crack growth acceleration by hydrogen concentration at crack tip at low test frequency[38].

2.2.2 Mechanism of HE

Although the actual mechanism of HE is still not fully understood, many hypotheses have been proposed. Some of these theories are widely accepted and used to explain pipeline steel failure associated with HE, such as hydrogen enhanced decohesion mechanism (HEDE), hydrogen enhanced local plasticity model (HELP), adsorption-induced dislocation emission (AIDE) and hydride formation. However, it should be noted that the hydrogen induced degradation of the properties of steel is a complex process with many of the proposed mechanisms involved rather than a process controlled by a single mechanism.[58]

1)   Hydrogen enhanced decohesion mechanism (HEDE):

This mechanism is one of the two most used HE models and the simplest one. It was introduced in 1959 by Troiano who claimed that interatomic bond strength between the atoms has reduced since hydrogen 1s electron comes in 3d cell of iron atom[59]. When hydrogen atoms diffuse inside a material, the cohesive strength of lattice plane or interface boundaries is weakened due to the segregation of hydrogen, leading to initiation/propagation of cracks under a stress lower than the designed value. An important assumption for this mechanism is that sufficiently high concentration of hydrogen is accumulated at the sharp crack tip region due to the hydrostatic stress field[60]. This mechanism is characterized with smooth fracture surface (intergranular fracture) and limited plasticity and supported by various experimental data and theoretical calculations.[61, 62] As shown in Fig. 2.7, it has been observed that cracks can initiated at notch tip (different radius) in hydrogenated specimens under static loading. However, the weakening effect of hydrogen on interatomic interactions in the metal has not been proved experimentally[63].
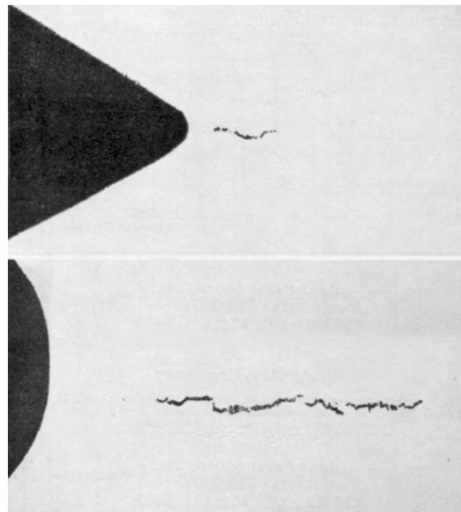
Fig. 2.7 Cracks observed at notch tip (different radius) in hydrogenated specimens under static loading. Longitudinal section at ×100.[64]

2)   Hydrogen enhanced local plasticity mechanism (HELP):

This mechanism is another widely accepted HE model which is firstly proposed in 1972. It is established on the observation that hydrogen increases the dislocation mobility under conditions of constant stress[65]. This effect is greatest at the crack tip where local hydrogen concentration is increased by slip process or the loading stress. Under specific temperature and

strain-rate range, local ductile fracture occurs as the material in front of the crack is softened by hydrogen[66]. This softening behavior promotes dislocation motion via enhancement of screw dislocation mobility, enhancement of dislocation injection at surfaces, and the promotion of shear instabilities.[58] And the damage process is actually a localized plastic-type fracture instead of an embrittlement, which is supported by some high-resolution studies. As shown in Fig. 2.8, although the a pipeline steel shows typical "flat" hydrogen induced fracture surface (Fig.2.8a), curvature and fine features are observed under higher resolution (Fig.2.8b) and microstructure immediately beneath the fracture surface consists of a high density of dislocations[67]. The HELP mechanism is illustrated in Fig. 2.9. High hydrostatic stress and presence of hydrogen at the tip of crack leads to growth and coalescence of voids, which speed up the crack propagation and material failure.
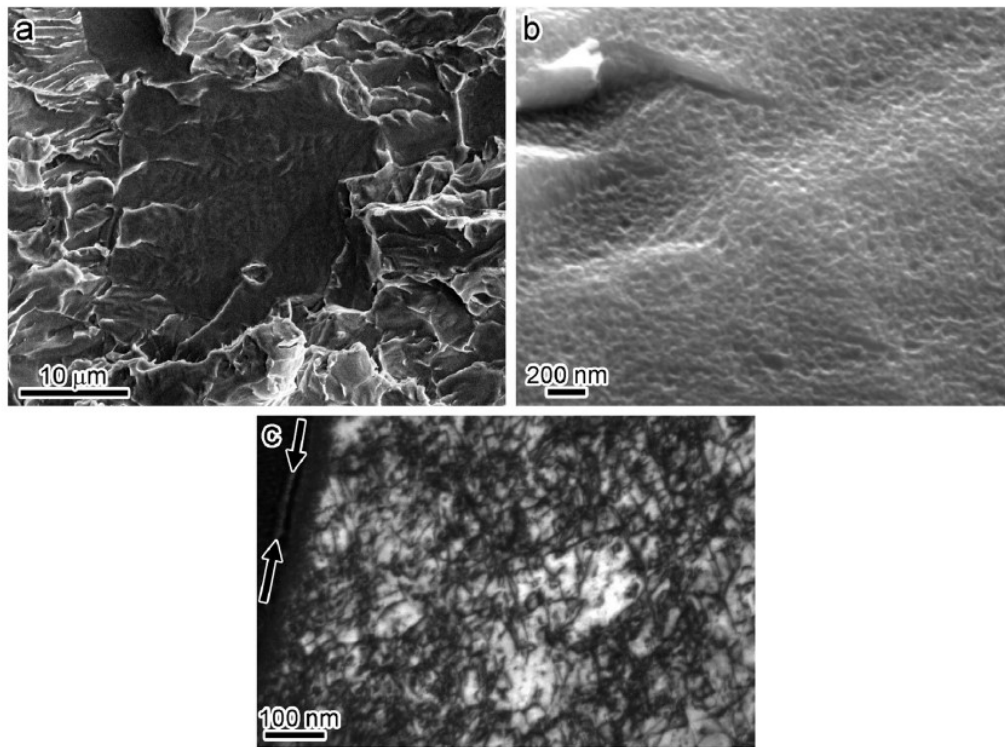
Fig. 2.8 Hydrogen-induced fracture features in ferritic pipeline steel. Compact tension specimens underwent fracture toughness testing in a high-pressure hydrogen gas environment. a) SEM image of the fracture surface, b) Higher magnification SEM image (titled at 70°), c) TEM image of microstructure beneath the fracture surface[67].
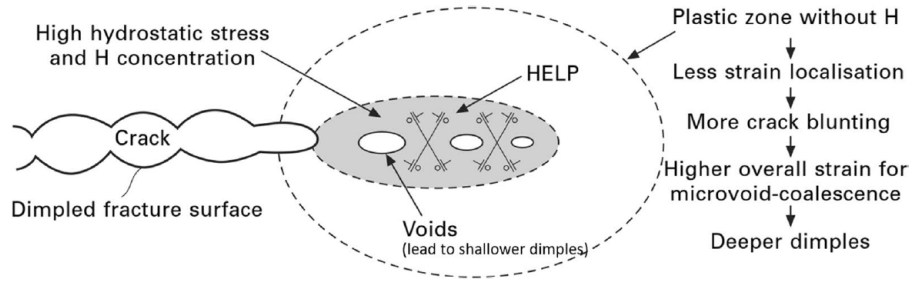
Fig. 2.9 Schematic diagram showing the failure mechanism induced by the HELP model.[40]

3)   Adsorption-induced dislocation emission (AIDE):

This mechanism is based on the sufficient evidence that H atoms are easily absorbed at free surfaces and subsurface sites[68]. The surface-absorbed H near crack tip not only weaken the interatomic bond or cohesive strength of the material (HEDE mechanism) but also facilitates dislocation injection from the crack tip and hence the crack propagation by slip and formation of micro voids (HELP mechanism), as shown in Fig.2.10. Therefore, AIDE mechanism combined HEDE and HELP and attribute the nucleation and growth of cracks to decohesion and dislocation emission at the crack tip[25, 69].
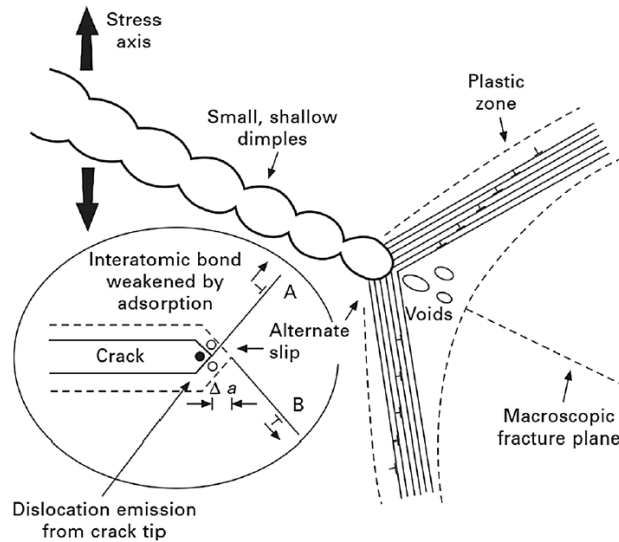
Fig. 2.10 Schematic diagram showing the failure mechanism induced by the AIDE model.[40]

2.2.3 Environment for HE of pipeline steels

Protective coating and cathodic protection (CP) are the two main methods used to maintain pipeline integrity[70]. When disbandment of the coating occurs, as CP cannot reach to the crevice bottom to provide effective protection, corrosive gases, water and/chemical species may enter the disbanded crevice area and form an electrochemical environment for corrosion with the following equations involved [1, 71].

$$\text{Anodic reaction: } Fe \rightarrow Fe^{2+} + 2e^{-} \qquad \text{(Iron dissolution)} \qquad\qquad (2\text{-}1)$$

$$\text{Cathodic reaction: } 2H^{+} + 2e^{-} \rightarrow H_2 \qquad \text{(Hydrogen reduction)} \qquad\qquad (2\text{-}2)$$

$$O_2 + 2H_2O + 4e^{-} \rightarrow 4OH^{-} \qquad \text{(Oxygen reduction in neutral and alkalis media)} \ (2\text{-}3)$$

$$O_2 + 4H^{+} + 4e^{-} \rightarrow 2H_2O \qquad \text{(Oxygen reduction in acidic media)} \qquad\qquad (2\text{-}4)$$

$$\text{Overall corrosion reaction: } Fe + 2H^{+} \rightarrow Fe^{2+} + H_2 \qquad\qquad\qquad (2\text{-}5)$$
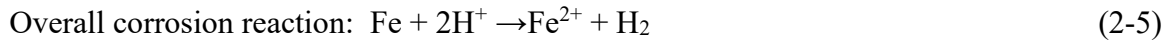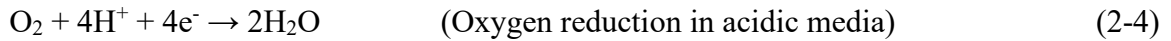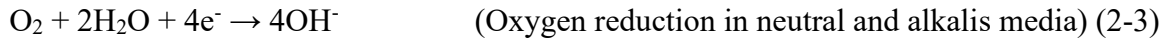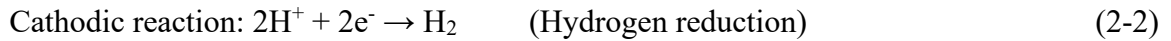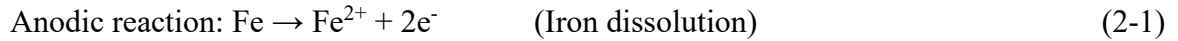
Atomic hydrogen generated by corrosion will either recombine into hydrogen molecules or migrated into the pipeline steel surface. Hydrogen sulfide (H_2S), as a so-called "poison", can significantly increase the hydrogen uptake by prohibiting the recombination of hydrogen atoms and hence lead to severe hydrogen induced damage.

Besides, cathodic protection can lead to generation of hydrogen when the applied potential is more negative than the potential of steels in surrounding environment (such as soil solution), which is also called "over protection". Hydrogen evolved on the surface of steel will diffuse in and cause HE to the material.[72]

In addition, absorption of molecular hydrogen from the atmosphere near the pipeline and introduction of hydrogen via production and fabrication processes, such as welding, electroplating and heat treatment, are also possible ways for hydrogen ingress. Furthermore, to fight against energy crisis and global warming, green or renewable hydrogen is widely considered as the most promising option to substitute conventional fossil fuel[73]. And existing natural gas pipeline system can be repurposed for transport of hydrogen gas and is being tested in many countries[74, 75]. This application proposes a great challenge to pipelines integrity and security.

2.3 Hydrogen permeation test techniques

To better understand the mechanism of hydrogen-induced degradation of pipeline steel, techniques that can precisely measure interaction between hydrogen and the steel microstructure are needed. In this section, four types of most used techniques are introduced with the pros and cons listed.

2.3.1 Devanathan-Stachurski (DS) method

DS method, also called "double-cell" method, is an electrochemical testing method proposed by Devanathan and Stachurski in 1962[8]. It is widely used in investigations about hydrogen permeation process and hydrogen trapping effect because of its simple procedure, economic facility, and flexibility towards variation of experimental conditions, such as electrolyte, temperature[76], charging method, stress condition, etc.[7, 77-79].

2.3.1.1 Experimental setup

This technique involves using a double-cell apparatus with a membrane sandwiched between the cells, as shown in Fig. 2.11. (CE and RE represent counter electrode and reference electrode). One cell (cathodic cell) is applied with constant current/voltage by a gavanolstat/potentialstat to provide hydrogen charging to the entrance side of the sample under constant hydrogen flux/concentration condition. After penetrating through the thickness of the sample, atomic hydrogen is oxidized into hydrogen ions at the exit side of the sample via the potentialstat applied on the anodic cell. The oxidation current, which corresponds to the hydrogen flux, is a direct measure of the instantaneous hydrogen permeation rate through the sample and recorded by a computer connected to the potentiastat on the anodic cell[9]. With proper design, this technique can also be used to study hydrogen diffusion behavior under various temperature or stress conditions.
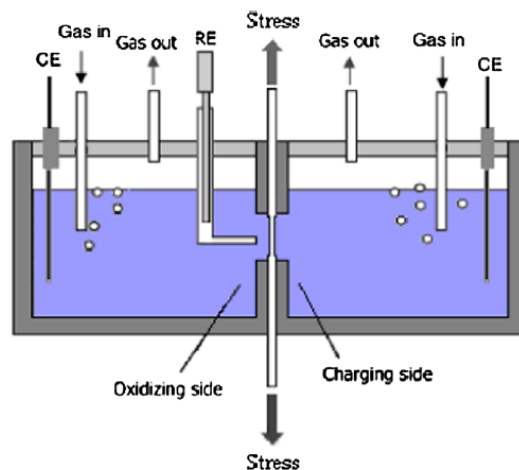
Fig. 2.11 Schematic diagram of electrochemical cell for hydrogen permeation test.[80]

As an oxidation current passes through the exit side of the sample during the hydrogen permeation test, a thin layer of palladium (or nickel) is deposited on this side of the sample to reduce the possibility of passivation and avoid damage. Besides, oxidation occurs more efficiently on a palladium surface, which prohibits the recombination of atomic hydrogen at the exit surface and hence makes sure that the recorded oxidation curve is accurate and meaningful[81]. This deposit should be easy to produce, adheres well, free from pores or cracks, and resistant to 0.1 M NaOH, which is the electrolyte in oxide cell[82]. Different methods of applying a layer of palladium on the samples are adopted, including ion sputtering, electroplating[83, 84], plating, etc.

On the other side, soaking in NaOH solution leads to formation of a barrier layer at the interface between electrolyte and the sample, which hinders the entry of hydrogen into the bulk of the sample[84, 85]. Therefore, various kinds of promoters are chosen to promote the entry process based on the testing environment and safety concern, such as arsenic oxide, hydrogen sulfide, iodide ions[86], phosphorus[87], calcium hydroxide [88], etc. It is reported that in the presence of EDTA (ethylenediaminotetraacetic acid), a strongly complexing agent that can effectively dissolve iron oxide, the passive film on the sample can be completely removed and hence significantly enhance the entry of hydrogen into the steel[84, 89, 90]. In the present study, EDTA is selected as the promoter of hydrogen permeation test for its safety and efficacy.

It is worth mentioning that the hydrogen entry rate in alkaline solutions is significantly lower than that in acid solutions, due to the different mechanisms of hydrogen evolution reaction (HER) and different surface states[91, 92].

ISO 17081[93] and ASTM G148-97[94] are the two most used standards for hydrogen permeation test. Some requirements about the testing system and procedure are explicitly indicated to guarantee the test results reproducible and comparable. For example, according to these standards, the ratio of radius to thickness of the sample should be no smaller than 10:1 to enable analysis of the permeation transient based on one-dimensional diffusion. Smooth surface (at least 600 grit surface finish), galvanostatic charging, coating on the exit surface of the sample are also suggested[94].

One of the advantages of DS method is that researchers can try different testing procedures and establish their own models to explain the data recorded and to study the hydrogen permeation process. Akiyama used various cathodic hydrogen charging conditions and claimed that a hydrogen charging current density equal to or greater than $2A/m^2$ is recommended to avoid the influence of diffusion-limited oxygen reduction reaction [79]; McKibben studied hydrogen diffusion and trapping behavior in metal using a potentiostatic double-step method[95]; Zakroczymski proposed a technique using build-up and decay of hydrogen permeation transient to study the entry, transport and trapping of hydrogen in iron[77].

2.3.1.2 Data analysis

The most important parameters that can be obtained from hydrogen permeation curve are effective diffusion coefficient (D_{eff}), trap density (N_t) and binding energy (E_b). Many calculation methods have been proposed and some of the most used are introduced briefly herein.

1) Calculation of D_{eff}

Effective diffusion coefficient (D_{eff}) is commonly used to characterize the trapping ability of the steel. To obtain D_{eff}, the first step is to transfer the current (I) into flux (J) by equation (2-6):

$$J = \frac{I/A}{F} \tag{2-6}$$

Wherein A is the exposed area of the specimen, F is Faraday constant.

The obtained I(t) curve can be plotted in the form of normalized flux ($J(t)/J_{ss}$) against the logarithm of normalized time τ' ($\tau' = D_{eff}t/L^2$). The steady-state permeation current (J_{ss}) gives

information on the subsurface concentration of hydrogen atoms at the charging surface (c_0) as follows:

$$J_{ss} = \frac{I_{ss}/A}{F} = \frac{D_l c_0}{L} \tag{2-7}$$

Wherein L is the thickness of the specimen.

There are a couple of ways to compute the value of D_{eff}, which can be classified as point methods, slope methods and curve-fitting methods as follows:

a.   Point methods: The effective diffusion coefficient (D_{eff}) can be calculated based on the elapsed time (t_{lag}) at $J(t)/J_{ss}=0.63$ and the breakthrough time (t_b) as shown in equations (2-8) and (2-9). The derivation of equations (2-8) and (2-9) can be found in reference [9, 96].

$$D_{eff} = \frac{L^2}{6t_{lag}} \tag{2-8}$$

$$D_{eff} = \frac{L^2}{15.3t_b} \tag{2-9}$$

Wherein t_b is found by extrapolating the linear portion of the initial hydrogen permeation current transient to $I_t = 0$, and the time of t_{lag} corresponds to the point on the permeation curve at which $I_t = 0.63I_{ss}$.

Time-to-breakthrough (t_b) method and Time-lag method (t_{lag}) are the most widely used methods to calculated D_{eff}, and are recommended in standards ASTM G148-97 [94]and ISO 17081[97].

b.   Slope methods

i. Fourier method[98]: The equation of the hydrogen permeation transient is given by

$$\frac{I_t}{I_{ss}} = 1 - 2\exp\left(\frac{\pi^2 D_{eff} t}{L}\right) \tag{2-10}$$

The hydrogen diffusion coefficient is derived from the slope of the plot of $\ln(1-I_t/I_{ss})$ against the time, t.

ii. Laplace method[98]: This method makes use of the first term of the summation series [9]

$$\frac{I_t}{I_{ss}} = \frac{2}{(\pi\tau')^{1/2}} \sum_{n=0}^{\infty} exp\left[-\frac{(2n+1)^2}{4\tau'}\right] \qquad (2\text{-}11)$$

to give

$$\frac{I_t}{I_{ss}} = \frac{2}{\sqrt{\pi}} \frac{L}{\sqrt{D_{eff}t}} exp\left(-\frac{L^2}{4D_{eff}\tau'}\right) \qquad (2\text{-}12)$$

Rearranging equation (2-12) gives

$$\ln(I_t t^{1/2}) = const. - \frac{L^2}{4D_{eff}t} \qquad (2\text{-}13)$$

Thus, D$_{eff}$ can be easily obtained from the slope of the plot of $\ln(I_t t^{1/2})$ vs t^{-1}.

Because the Fourier and Laplace methods use a number of points on the permeation curve it might be expected that these would give a better measure of the average diffusion coefficient. An example of a typical plot using the Laplace method is shown in Fig. 2.12.
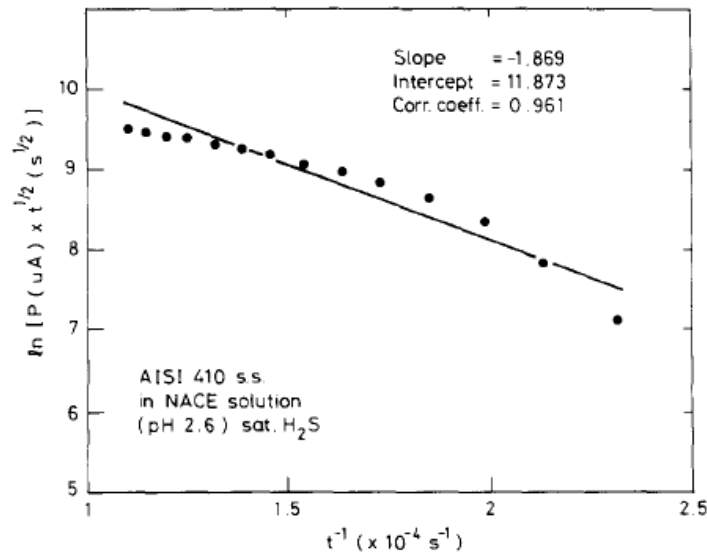
Fig. 2.12 Graphical method of calculation of the effective diffusion coefficient using the first term of the Laplace equation[98].

c.   Curve fitting methods[99]: By fitting equations (2-12) and (2-13) to the obtained data, the effective diffusion coefficient (D$_{eff}$) can be attained for the tested sample. As an example, Fig. 2.13 shows the fitted curves for the as-received sample. The fitted curves give a value of 1.21×10^{-6} cm^2/s for Laplace method and a value of 1.25×10^{-6} cm^2/s for Fourier method.
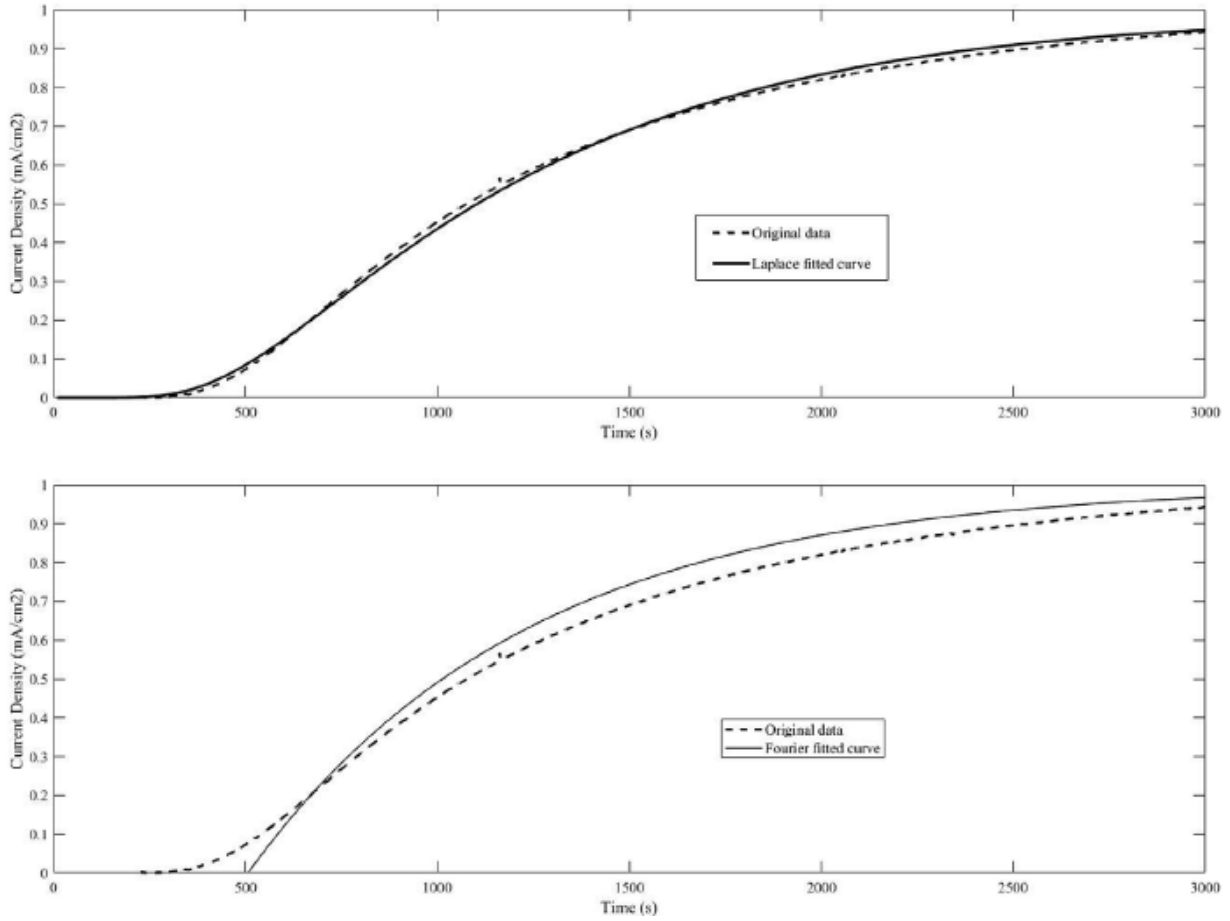
Fig. 2.13 Laplace and Fourier fitted curves[99].

iii. Calculation of trap density and binding energy.

McNabb and Foster [100] proposed a trapping-detrapping model based on the assumption that a dynamic equilibrium is maintained between trapped hydrogen and lattice hydrogen. The theory has been widely accepted. Oriani [16] made more specific treatment based on the local equilibrium hypothesis and concluded that the effective diffusivity is a function of trap density and of the magnitude of the trap depth with some practical equations.

According to Kumnick and Johnson[18] the overall trap density can be calculated using the following equation:

$$N = \frac{c_0}{3}\left(\frac{D_l}{D_{eff}} - 1\right) \tag{2-14}$$

23

where N is the number of trapping sites per unit volume and D_l is the lattice diffusion coefficient (D_l=1.28×10^{-4} cm^2/s). (Assumption: heavily occupied)

Haq [19] and Dong[17] used equation (2-15) to calculate trap density based on Oriani's [16] work (in domain of low coverage).

$$N_t = N_L(D_L/D_{eff} - 1)e^{-\Delta E_X/RT} \tag{2-15}$$

(wherein N_L is the density of normal lattice sites and is taken as 7.52×10^{28} m^{-3}; ΔE_x is the binding energy of traps and is taken as 0.3 eV; N_t is the trap density; D_L and D_{eff} are diffusivity in lattice and effective diffusivity, respectively).

According to Oriani [16], in the domain of low coverage ($\theta_x \approx 0$),

$$\boldsymbol{D_{eff}} = D_L(1 + KN_x/N_L)^{-1} \tag{2-16}$$

$$K = \exp(-\Delta E_x/RT) \tag{2-17}$$

Wherein K is the equilibrium constant between hydrogen in trap and hydrogen in lattice site.

2.3.2 Thermal desorption spectrometry (TDS)

TDS is a technique that firstly developed in surface science area and used to study hydrogen diffusion and trapping behavior since 1980s[101]. By continuously heating up a sample that has been charged with hydrogen following a predefined temperature profile. During this process the amount of desorbed hydrogen gas is recorded, and finally a plot of the flow of gas as a function of temperature is obtained as a TDS spectrum (Fig.2.14). The desorption rate is described in an Arrhenius expression called the Polanyi-Wigner equation as follows:

$$-\frac{d\Theta}{dT} = \frac{\Theta^p v_0}{\beta}\exp\left(-\frac{E_{des}}{k_B T}\right) \tag{2-18}$$

Where Θ is the coverage of adsorbates in the unit of monolayer (ML), p is the reaction order of the desorption process, v_0 is the attempt frequency, E_{des} is the desorption barrier, k_B is the Boltzmann constant, and T is the sample temperature. p has information on the adsorption and desorption mechanism, and E_{des} and v_0 determine the desorption rate of each molecule.[4]
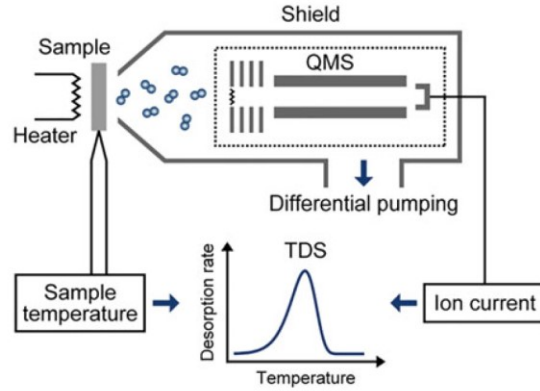
Fig. 2.14 Schematic setup of the TDS measurement.[4]

Data analysis for TDS is a difficult task since multiple processes are involved, including surface processes, bulk processes and different thermodynamic phases, and the effectiveness of dada analysis strongly depends on using the appropriate model[1]. Among all the popular models, Mc-Nabb-Foster model is the most used to determine the activation energy for a chemical reaction, wherein the following equation is applied[102].

$$\frac{dX}{dt} = A_0(1-X)\exp\left(-\frac{E_a}{RT_c}\right) \tag{2-19}$$

Wherein X is the hydrogen amount that escaped from a trap site, A_0 is the reaction rate constant, T_c is the temperature at the desorption peak.

Thermal desorption profiles make it possible to identify temperatures corresponding to each peak T_{pi} as presented in Fig. 2.15. The difference in peak temperature suggests a difference in binding forces between hydrogen and the trapping sites, and the trapping energy can be calculated by equation (2-20)[103].

$$\frac{\partial ln\left(\frac{\varphi}{T_{pi}^2}\right)}{\partial\left(\frac{1}{T_{pi}}\right)} = -\frac{\Delta E_{TL_i}}{R} \tag{2-20}$$

with φ the heating rate (Ks⁻¹), T_{pi} the peak temperature (K) and R the gas constant (8.13 J K⁻¹mol⁻¹)
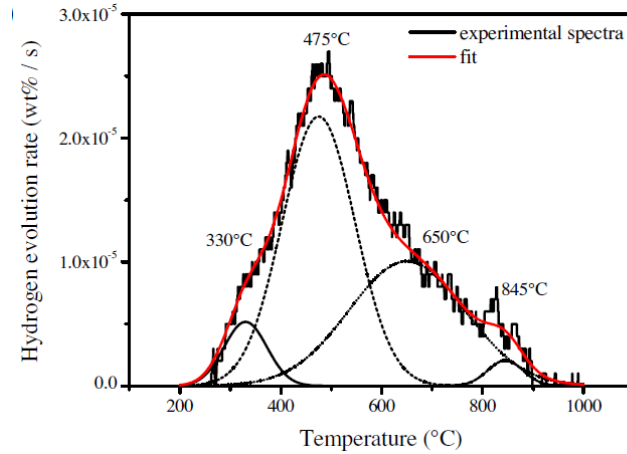
Fig. 2.15 The Gaussian simulation of the experimental spectra. [103]

Nowadays, this powerful experimental technique plays an important role in the research about hydrogen trapping. It was used to study the interaction between hydrogen and different microstructural constituents and revealed that the amount of trapped hydrogen considerably increased with the carbon content in lab cast Fe-C alloys[104]; Depover studied the interaction between a steel microstructure and hydrogen using TDS technology and drew several important conclusions about the effect of various microstructural feature in a steel on HE resistance[105].

2.3.3 *Hydrogen microprint (silver decoration) technique (HMT)*

HMT, also called silver decoration, was developed by Ovejero-Garcia in 1980s[3]. The simplicity and precision of this technique makes it a powerful tool in the study of hydrogen embrittlement of metals and alloys. As shown in Fig. 2.16-17, this technique involves four steps, including emulsion coating, hydrogen permeation, fixing and SEM observation. A monogranular, densely packed layer of AgBr is applied on the surface of the polished sample. During the "fixing" process, the silver ions (Ag^+) in silver bromide (AgBr) are reduced by the hydrogen flux as indicated by equations (2-21) and (2-22). Then a fixing solution comprising of 1.4 mol/l sodium nitrate ($NaNO_2$) and 0.6 mol/l of sodium thiosulfate ($Na_2S_2O_3$) is used to wash off unreduced crystals of AgBr, leaving only reduced Ag^0 on the steel surface[1-3].

$$AgBr + 1/2H_2 = Ag^0 + H^+ + Br^- \qquad (2-21)$$

$$Ag^+ + H^0 \rightarrow Ag^0 + H^+ \qquad (2-22)$$
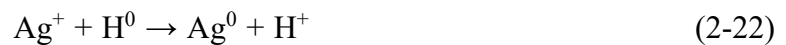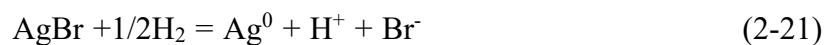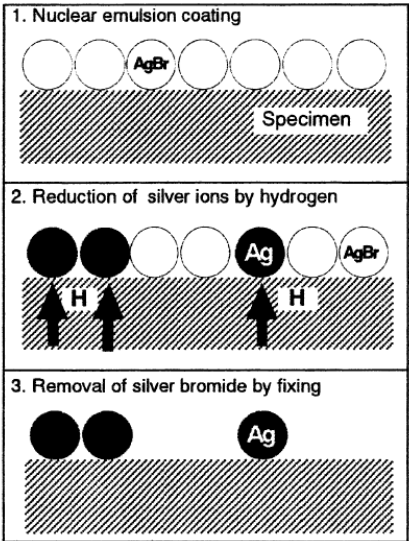
Fig. 2.16 Principle of hydrogen microprint technique.[106]
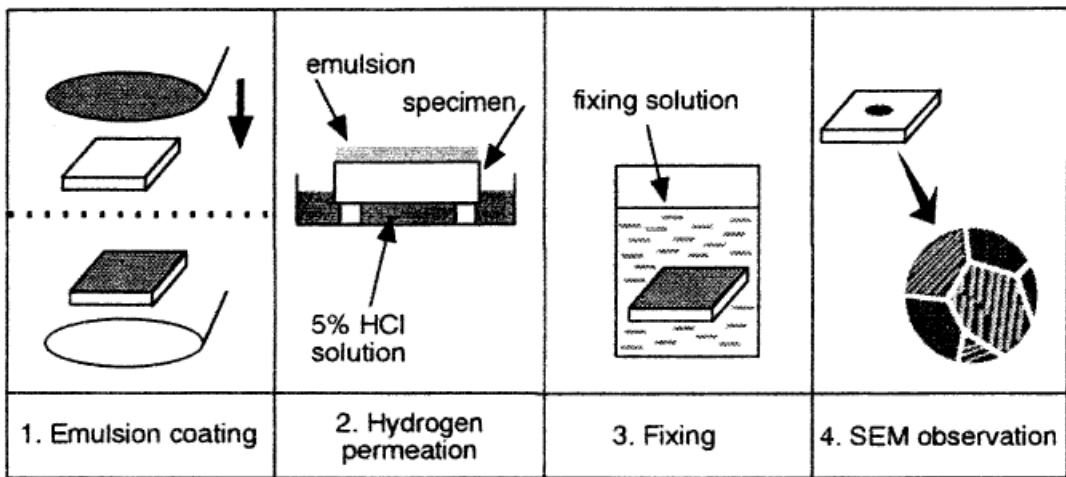
Fig. 2.17 Experimental procedure of hydrogen microprint technique.[106]

One of the advantages of HMT is that it can be used to visualize the hydrogen diffusion. For example, Thomas successfully revealed the hydrogen trapping sites in various microstructure by the agglomeration of Ag particles (Fig. 2.18) [107]. Besides, some other applications have also been proposed, such as visualization of hydrogen emission under stress gradient[108] and visualization of hydrogen distribution around a notch[106]. However, HMT only gives qualitative results in terms of trapping sites or diffusion path and can hardly be used for quantitative purpose.

a)

b)

c)

d)
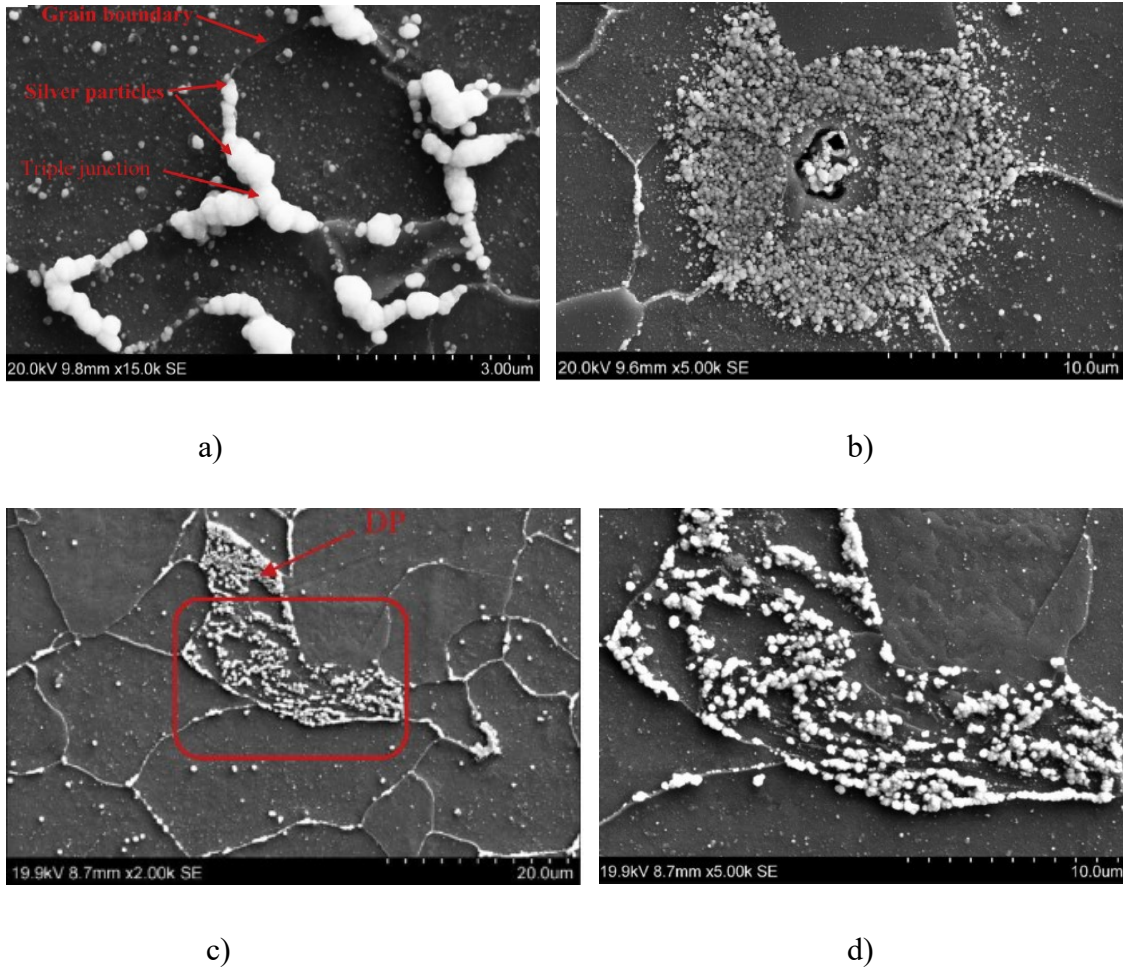
Fig. 2.18 SEM images after HMT showing hydrogen trapping sites in grainboudary a), around inclusions b), and boundaries of cementite lath in degraded pearlite (DP) c,d).[107]

2.3.4 Other techniques

In addition to the testing methods mentioned above, some other techniques are also available for studies about hydrogen diffusion and hydrogen trapping behavior in steels, including electrochemical impedance spectroscopy (EIS)[55], small-angle neutron scattering (SANS)[109], atom probe tomography (APT)[110], etc. These techniques provide complimentary perspectives in observation of hydrogen permeation process. EIS is a very powerful tool in electrochemical study, and is claimed to have potential in evaluating steel susceptibility of corrosion cracking due to the sensitivity of some impedance equivalent circuit parameters to hydrogen content in steel[111]. SANS is considered as an appropriate technique for detecting hydrogen segregation in

nanoscale precipitates. It is reported that by comparing measured SANS profiles of samples with and without hydrogen charging, trapped hydrogen was detected even though the total concentration of hydrogen is only in the range of a few tens of atomic ppm[109]. A recent study demonstrates an approach to directly observe trapping of hydrogen within the core of fine carbides with quantitative composition profiles using APT[110].

2.4 *Interaction between microstructure and hydrogen*

2.4.1 *Hydrogen traps*

Hydrogen is the smallest and lightest of solute elements, which enables it to diffuse in metals over large distance at ambient temperature. It has extraordinarily high mobility and high solubility especially in iron and other body-centered cubic (bcc) metals[112]. However, it is observed that both the solubility and diffusivity of hydrogen in iron and steel shows departure from theoretical calculations at lower temperature[58]. Therefore, hypothesis about trapping effect of imperfections in steels was proposed to explain this divergence between theoretical and experimental results[113].

In 1949, Darken and Smith firstly suggested that the diffusivity of dissolved hydrogen is hindered by defects in the lattice of a cold-worked steel and proposed a theory based on the assumption of local equilibrium between hydrogen in lattice sites and in trap sites[16]. It is believed that atomic or microstructural imperfections, such as vacancies, solute atoms, dislocations, grain boundaries, interface of second phase, and voids, can trap hydrogen and cause decrease in diffusivity and increase in solubility[14]. Hydrogen diffusion is a concentration-driven process, during which hydrogen atoms hop between interstitial lattice sites. However, the rate of hydrogen hopping is hindered if the hydrogen atoms are captured by hydrogen traps[114]. Hydrogen trapped in voids or cracks can recombined together and form molecules. Thus, voids and cracks are classified as non-saturable traps. As more hydrogen atoms are captured, the pressure inside voids or cracks could increase and might give rise to acceleration of void coalescence via HELP mechanism[115].

On the other hand, for saturable traps, according to local equilibrium theory, hydrogen diffused in steel will occupy a trapping site and an equilibrium will be established when the chemical potential of hydrogen in lattice and trap sites equals external chemical potential. Trapped hydrogen atoms can only escape from the traps if an energy substantially larger than the lattice migration energy is acquired. As a result, the mean residence time of these hydrogen atoms is significantly longer in trapping sites than in lattice sites leading to the apparent diffusivity (or effective diffusivity) of hydrogen in iron/steel larger than theoretic diffusivity in iron lattice by orders of magnitude[14].

As illustrated in Fig. 2.19, the activation energy for a hydrogen atom to jump from a trap site to a lattice site E_a, equals to the activation energy needed to jump between adjacent lattice site E_d (diffusion activation energy), plus the trap binding energy E_b: $E_a = E_d + E_b$. Based on the trap binding energy, hydrogen traps are commonly classified as reversible ($|E_b| \leq 60$ kJ/mol) and irreversible traps ($|E_b| \geq 60$ kJ/mol). (Other threshold values are also used in literatures, for example, 77kJ/mol[116]). Reversible traps can release hydrogen when the hydrogen chemical potential in adjacent lattice is lower or exchange hydrogen with stronger traps, and hence act as a source, whereas the binding energy of irreversible traps are so high that it is extremely hard for hydrogen atoms to get rid of. Therefore, irreversible traps were also called "sinks" in earlier literatures[117]. It should be noted that the energy calculated from hydrogen permeation test (DS technique) is binding energy (E_b), whereas the energy obtained via hydrogen thermal desorption (HTD) analysis is the activation energy for hydrogen escape from the trapping site (E_a). However, the diffusion activation energy (E_d) is often ignored as it is relatively small (~7kJ/mol)[118].

Generally, dislocations, low angle grain boundaries (LAGBs) and voids are considered as reversible traps[114]; fine precipitates[46, 119, 120], inclusions[43, 121], interfaces, high angle grain boundaries (HAGBs) are classified as irreversible traps. Hydrogen atoms captured by reversible traps are still diffusible since they can easily jump out as a result of thermal energy fluctuation. Contrarily, it is hard to escape from irreversible traps due to the large activation energy. Table 2-1 shows the binding energy ($|E_b|$) of various types of traps published in literatures.
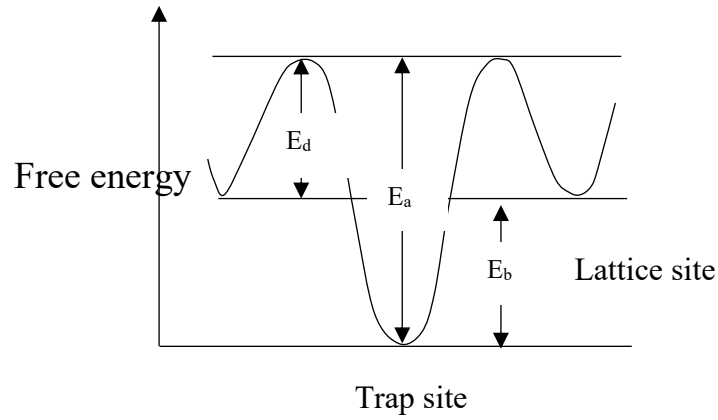
Fig. 2.19 Schematic view of energy relations during hydrogen trapping.

Table 2-1 Binding energy of different types of traps reported.

Microstructural features	Trapping site	Binding energy reported in literatures (kJ/mol)
HAGBs	Prior austenite grain boundary	47.4[122],48[123],61.3~62.2[124]
	Packet boundary	
	Block boundary	
LAGBs	Lath boundary	9.6[125],15~35[123]
Dislocation	Cores of screw dislocation	19.2[125],18[123]
Voids	Micro-void	27.6[125],48.3[126]
Cementite particle	Incoherent interface	72[123], 10.9[127]
Inclusions	MnS surface	72.3[126]
Nanosized (Ti, Mo)C precipitates	Broad interface between platelet and matrix	28.1[120]

It is suggested that reversible traps are harmful and have significant effect on HE, whereas irreversible traps are beneficial to HE resistance of steel because they can decrease the amount of diffusive hydrogen[58]. And it is generally accepted that irreversible traps play a dominant role in crack initiation, whereas reversible traps facilitate crack propagation by releasing H to crack tip.

However, some recent studies show that the effect of some irreversible traps, for example, non-metallic inclusions, depends on their characters such as shape, chemical composition, and distribution [128-130]. This will be discussed in detail in the following sections.

2.4.2 Effect of phases

Generally, a pipeline steel is comprised of various types of phases/structures, including polygonal ferrite (PF), acicular ferrite (AF), granular bainite (GB), upper bainite (UB), lower bainite (LB), martensite (M), pearlite (P), degraded pearlite (DP), retained austenite (RA), M/A constituents, etc. Since the HE phenomenon has been discovered, great efforts have been made to study the susceptibility of each type of phase/structure so as to provide important information for appropriate phase/structure selection in terms of HIC resistance.

Among these common phases/structures in pipeline steels, AF demonstrates the best HIC resistance and is claimed to be the most desirable microstructure of high strength pipeline steel that can provide excellent high SSC resistance[45, 131]. It has been reported that cracks preferentially initiated and propagated along the grain boundary of PF rather than AF under hydrogen charging environment[132].

On the contrary, martensite is very prone to HIC cracking. This is because the lath interface in martensite is efficient trapping site that can trap large amount of hydrogen with high binding energy (~50kJ/mol), and hence martensite possesses the very low hydrogen apparent diffusivity and highest hydrogen solubility, therefore large amount of trapping hydrogen can have interaction with the microstructure and cause HIC [133-136]. Meanwhile, high density of dislocations and high degree of lattice strain contribute to the high density of reversible trapping of martensite, and act as hydrogen source to promote the crack propagation[136]. It is also claimed that the susceptibility of martensite is due to its high hardness (400 Vickers), since it is widely accepted that hardness is closely related to HIC susceptibility[137]. However, the trapping ability and HIC susceptibility of martensite decreases after it is tempered, which might be related to the decrease in dislocation density during tempering[133].

Turk found that RA has larger solubility and lower diffusivity than martensite and ferrite, and even the presence of a small amount of it can have a significant impact on the diffusion rate [138, 139]. But Chan argued that as compared with RA, the interface between RA and martensite/bainite plates plays a more important role in hydrogen trapping (as shown in Fig.2.20)[140]. A technique about introducing a layer of nano-film austenite between the martensite laths to reduce HE susceptibility was proposed by Wang[141].

M : martensite
A : retained austenite
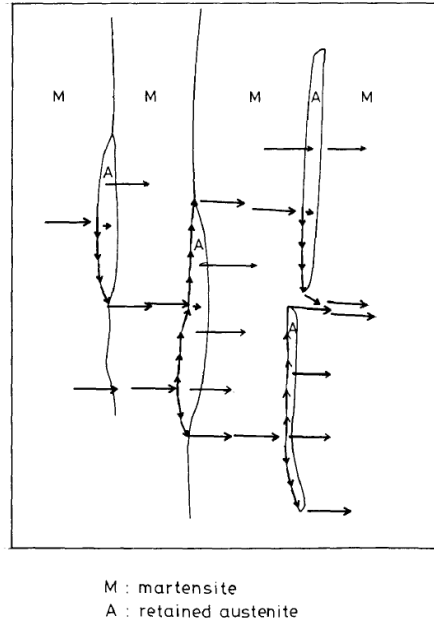
Fig. 2.20 Schematic diagram showing the hydrogen diffusion as retarded by the fine film of retained austenite between the martensitic plates.[140]

According to Chatzidouros[142], bainitic structure is susceptible to HIC due to M/A constituents and stringers along ferrite. The interfaces of a large amount of inter-lath cementite within the bainitic structure are inhibitor for hydrogen diffusion[45, 134]. Arafin claimed that similar to martensite, bainitic lath can trap hydrogen and hence lath bainite is more vulnerable than ferrite/GB microstructure to HE [143].

M/A constituent is of great importance in high-strength pipeline steel microstructure regarding mechanical properties. During TMCP, the rapid cooling after deformation suppresses carbon diffusion and enables the formation of residual austenite and high-carbon martensite, i.e., M/A constituents, which exist in form of layers over boundaries between laths, or "island" if the

bainite matrix is granular. Both the morphology and size distribution of M/A has great effect on properties [144]. M/A constituents are efficient hydrogen traps mainly due to the interface between martensite and austenite[139]. HMT results show that M/A and martensite filling in the space between the basket-weave acicular ferrite are the main irreversible trapping sites for weld metal, which significantly increases the hydrogen apparent solubility[145]. Experimental results showed that M/A constituents are easily embrittled by hydrogen and locally agglomerated M/A constituents can lead to crack initiation site when exposed to hydrogen[45]. It is observed that irregular M/A constituents distributed along the grain boundaries parallel to the rolling direction cause the reduction of HIC propagation resistance[146].

The cementite lamellae within a pearlitic colony can retard the hydrogen diffusion across the pearlite effectively. As shown in Fig. 2.21, hydrogen diffusivity in banded ferrite/pearlite structure is highly anisotropic, which is higher along the longitudinal direction but lower along the transverse and through-surface directions as compared with a random structure [133]. Hydrogen damage mechanism for ferrite/pearlite is associated with diffusion pathways along ferrite bands and accumulation of hydrogen on ferrite/pearlite interfaces as well as different hardness for adjacent ferrite/pearlite bands[142]. It is observed that HIC initiated primarily at the interface of ferritic/pearlitic bands, where most hydrogen atoms are trapped[44].
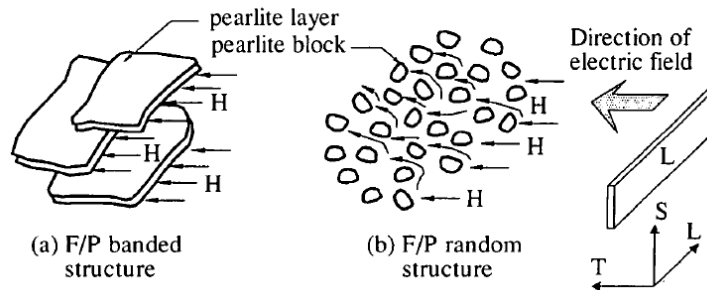
Fig. 2.21 Schematic diagram indicating the path of hydrogen penetration in both ferrite/pearlite structures.[147]

Experimental results from different research groups give a conclusion with consistency, that the HIC resistance of these phases commonly seen in pipeline steel follow the sequence of AF > ferrite > bainite> pearlite>martensite [131, 133, 143]. However, all these works just qualitatively

compare the trapping ability and HIC resistance among the phases based on experimental data. In the present work, a model is established to quantitatively evaluate the trapping efficiency of each type of phase.

2.4.3   Effect of precipitates

Microalloying elements such as Nb, Ti, V are commonly added to improve the properties of pipeline steel with TMCP. These elements can retard austenite recrystallization and hence lead to finer grain size due to more nuclei for the austenite/ferrite transformation. Also, as the temperature goes down, they can precipitate in form of carbides/carbonitrides and enhance the mechanical properties via pinning effect on dislocations[148, 149].

In addition, it is found that these precipitates have potential to reduce HE susceptibility of steels. Depover observed that micro-alloyed high strength steel with Nb and Ti precipitates showed almost no sign of hydrogen embrittlement in SSRT after charging as compared with the results of test in air [150]. Nagao reported that nanosized (Ti, Mo)C precipitates cause the fracture mode changing from along lath boundaries to a mixed mode of microvoid coalescence and along lath boundary. And this improvement in HIC resistance is attributed to the trapping ability of these precipitates[151]. Zhang's study shows that nano-size NbC (~10 nm) decreases HE susceptibility in three different ways: alleviation of hydrogen accumulation by NbC itself as well as the additional grain boundaries due to NbC (trapping effect); retardation of HELP by pinning effect; reducing $\sum 3$ boundary fraction [46]. Li found that increasing V addition leads to decreased diffusivity of the steel and decreased HIC, and suggested that VC precipitates (< 60 nm) are irreversible trapping sites that can reduce the possibility of H diffusing to harmful defects, such as large oxide inclusions and elongated MnS inclusions, which might cause crack initiation more easily[152].

Although the trapping ability of these precipitates has been proved by many researchers in different ways[109, 153], there is still controversy about the mechanism. Some believed that it is closely related to the coherency of the precipitates, and consequently, only small precipitates are strong irreversible traps, and coarsening of these precipitates will result in loss of the trapping ability[33, 105, 120, 154, 155]. Cui explained that the misfit of fine NbC precipitates (3~10nm) and the matrix (X80 steel) is close to coherent interface and introduces a higher strain field than

semi-coherent and incoherent interfaces, which makes the precipitates more effective irreversible traps for hydrogen[33]. However, Escobar claimed that, as it is shown by TDS results, the trapping capability of TiC and detrapping activation energy increases as the size increases[156]. Malard reported that the measurement of interaction between H and VC precipitates via SANS is consistent with the homogeneous trapping of H within the precipitates rather than at the interface[157]. To solve this problem, Wei applied TDS to samples with TiC precipitates after electrochemical charging at room temperature and gas charging at elevated temperature, and found that as TiC grows, the precipitate loses it coherency with the matrix and cannot trap hydrogen by cathodic charging at room temperature due to the increased trapping activation energy; however, the incoherent precipitates are able to trap hydrogen by octahedral carbon vacancies by gas charging at higher temperature[155]. Wallaert used a similar method on NbC and NbN and obtained consistent results that small NbC and NbN can trap hydrogen by electrochemical charging with a smaller detrapping activation energy (39-48kJ/mol and 23-24 kJ/mol, respectively); whereas incoherent NbC and NbN can only trap hydrogen during gaseous charging and the desorption activation energy is much higher (63-68 kJ/mol and 100-143 kJ/mol, respectively)[119].

The trapping ability of NbC, VC and TiC is compared and ranked in order of NbC > TiC >> VC. This is because these particles demonstrate a surface area dependence of trapping capacity, and the deep trapping site is probably the core of misfit dislocations. Since NbC has higher and VC has lower lattice mismatch than TiC, they are predicted to trap more and less hydrogen than TiC, respectively, as shown in Fig.2.22-23 [34]. The detrapping activation energy of NbC, VC and TiC precipitates are listed in Table 2-2.
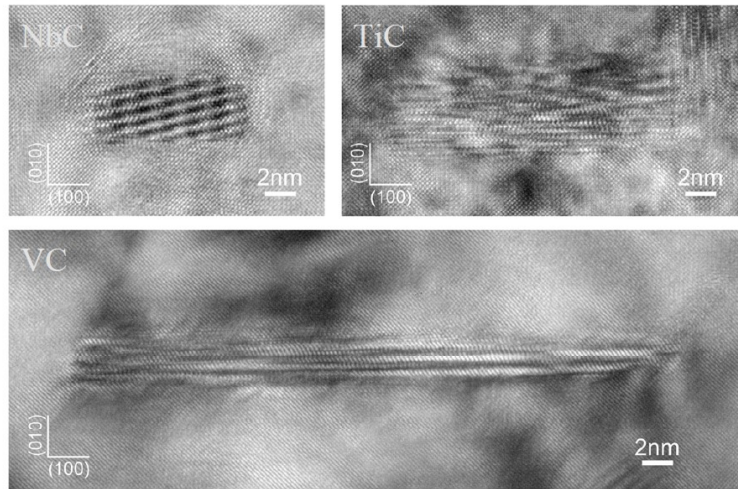
Fig. 2.22 High resolution TEM micrographs of NbC, TiC and VC precipitates.[34]
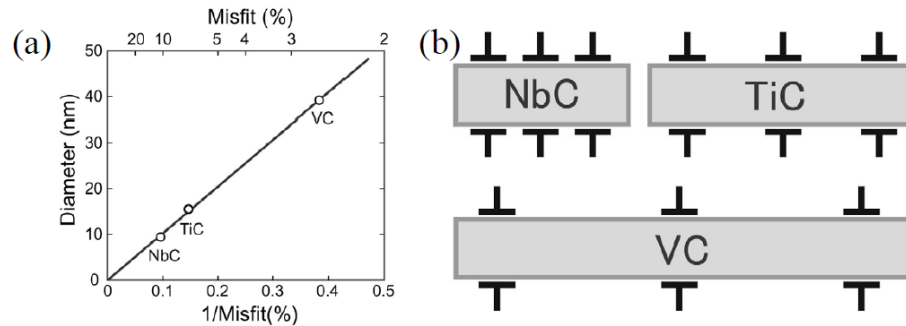
Fig. 2.23 Size and morphology of disk-like NbC, TiC and VC precipitates. a) Relationship between diameter and lattice misfit, b) illustration of misfit dislocations on the broad faces of the precipitates.[34]

Table 2-2 Detrapping activation energy of Nb, Ti and V carbides/nitrides precipitates (kJ/mol).

	Coherent/semi-coherent	Incoherent
NbC	39~48[119]	63~68[119]
NbN	23~24[119]	100~143[119]
TiC	55.8[155]	86.9[120], 68~137[155]
VC	33~35 [158]	/

It is worth noticing that although presence of fine microallyed carbonitride/carbide particles can improve HIC resistance of steels, coarse Ti(C,N) and TiN precipitates were reported to be HIC initiation sites and are harmful in terms of HE susceptibility[52].

2.4.4 Effect of inclusions

Some recent studies show that non-metallic inclusions might cause crack initiation depending on the chemical composition and shape as well as distribution of the inclusions[128], as shown in Fig.2.24. For pipeline steels, hard oxide/sulfide of Ca, Al, Si, elongated MnS and large cuboidal TiN/Ti(C,N) are the most commonly seen detrimental inclusions. Kim reported that clusters of oxides of Al and Ca are the main site for crack initiation during HIC, especially those with size over 20 µm in maximum length[159]. Comparing these types of inclusions, many researchers argue that oxide inclusions are more sensitive to HIC than MnS and nitrides and hence need greater concern. Dong observed that more cracks were initiated from inclusions such as calcium oxides (or Ca-oxysulfides) rather than nitrides and explained that this is possibly because the oxides inclusions can attract more hydrogen [132]. Xue found that HIC only initiated at inclusions enriching in Si and Al oxides rather than other types of inclusions such as Al-Mg-Ca-O and MnS, which is attributed to the hard and brittle nature of Si and Al oxides[121]. Similar results were also obtained by Jin [43]. However, Rahman claimed that spinal non-metallic inclusions (such as MnS) have a much more important influence on HIC than globular inclusions (such as CaO-Al$_2$O$_3$) and rectangular inclusions (such as TiN), since a small number of long spinal NMIs can significantly promote HIC by interlinking of micro-cracks [160].

a)   b)
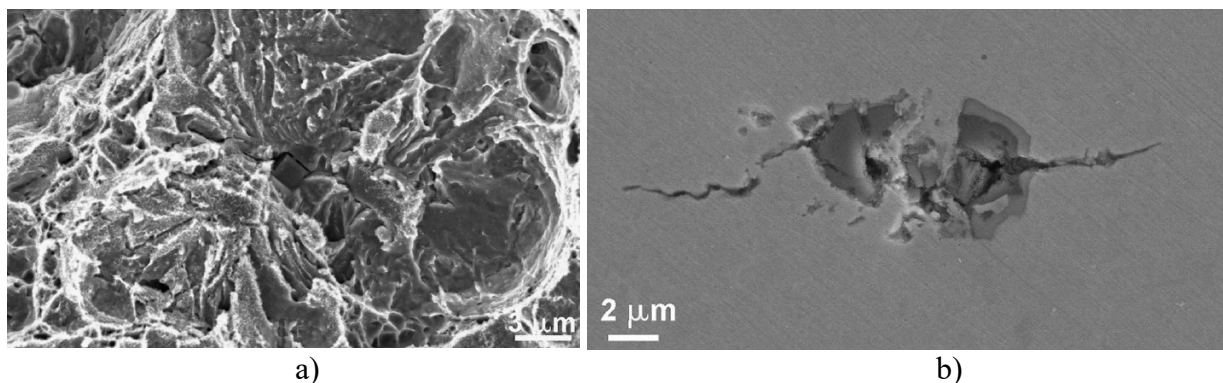
Fig. 2.24 Micrographs of fracture surface a) and the side surface b) after constant load test with continuous hydrogen charging of a high strength carbon steel. [161]

Regarding to the mechanism of inclusions initiated HIC, it is generally believed that the micro-voids at the interface between the inclusions and matrix are irreversible hydrogen traps and can draw hydrogen away from other regions. The trapped hydrogen atoms can combine into hydrogen molecules and cause internal pressure and stress field at the trapping site, which will eventually lead to decohesion between inclusions and matrix[159]. This theory agrees well the Luu's HMT results, which revealed that the inclusion-matrix interface is the main trapping site[162]. Todoshchenko confirmed the role of interface by the proportional relationship between the amount of trapped hydrogen and the NMI surface fraction[161].

In order to improve HIC resistance of the steel, it is suggested that the morphology and size of these inclusions should be controlled properly[128, 160]. For example, the size of MnS and oxide inclusions should be smaller than 2.5 µm and 0.4 µm, respectively[128]. It has been reported that when MnS is compound with other inclusions into sphere or the size of MnS inclusion is controlled into submicron scale, the HIC resistance could be improved[128, 163].

2.4.5 *Effect of grain boundary (LAGBs and HAGBs)*

Grain boundaries can also trap hydrogen and have important effect on HE susceptibility. The trapping capability of grain boundaries is a function of the grain boundary angle[164]. As shown in Table 2-1, prior austenite grain boundaries (PAGs), block boundaries and packet boundaries of martensite/bainite are high angle grain boundaries (HAGBs) with a binding energy ranging from 40 to 60 kJ/mol. Therefore, HAGBs is generally considered as irreversible traps [165]. PAGs are random boundaries, whereas packet and block boundaries have specific orientation with respect to the prior austenite matrix (variant). These boundaries can prohibit the dislocation movement, which gives rise to dislocation pileups [166, 167]. Lath boundaries, on the other hand, are low angle grain boundaries (LAGBs), which are composted of tilt and twist boundaries corresponding to edge and screw dislocations[168]. It is reported that hydrogen deposit at HAGBs can cause debonding of the grain boundaries by impinging dislocation pile-ups, leading to decohesion at PAGs (intergranular failure) (Fig. 2.25a) or block boundaries ("quasi-cleavage" transgranular failure) (Fig. 2.25b) [169].
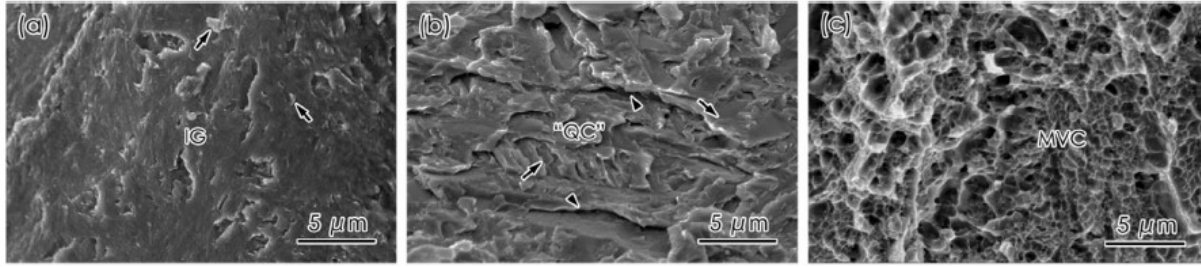
Fig. 2.25 SEM images of fracture surfaces of ruptured four-point bend specimens. "flat" intergranular feature a) and "quasi-cleavage" feature b) of the hydrogen-charged steel A500 exposed to hydrogen gas; c) ductile microvoid coalescence feature of the uncharged steel B550. Arrows indicate the fine tear ridges in a) and fine serrated markings and secondary cracks in b) [169].

2.5   Summary

As described in this chapter, the existence of nascent hydrogen in pipeline steel can lead to different forms of property degradation of the steel depending on the environment it is exposed to and cause unexpected structure failures. Some advanced techniques, such as electrochemical permeation test, thermal desorption spectrometry (TDS), hydrogen microprint technique, etc., have been widely used to study the mechanisms of HE, and many theories were proposed, among which HEDE, HELP and AIDE mechanisms are the most widely accepted. It is found that some microstructural features, including dislocations, grain boundaries, fine precipitates and non-metallic inclusions have interactions with hydrogen atoms and act as traps which can delay the permeation process. This interaction significantly influences the susceptibility of steel to HE and varies according to the type of microstructure feature. However, due to the co-existence of different microstructural features, it is difficult to reveal the effect of each type of these traps or quantitively evaluate the trapping ability of each phase. And few of studies focused on either the effect of TMCP parameters on different traps or how to control hydrogen trapping by adjusting TMCP parameters.

Although the mechanism of hydrogen-induced degradation of pipeline steel has been widely investigated in the past several decades, there are still some knowledge gaps in understanding the mechanism of the phenomena and producing high HE resistant pipeline steels. Firstly, most studies focused on the trapping capability of specific microstructures or the influence

of some microstructures on HE susceptibility of the steel, whereas the relationship between TMCP and various types of traps are seldomly covered. Furthermore, the trapping ability of phases in pipeline steels are commonly compared qualitatively by researchers without any quantitative standard or reference. This makes it is hard to estimate the trapping efficiency and HIC resistance of a complicate microstructure. In addition, most hydrogen diffusion models only focus on reversible traps or assume that all traps in the steel are reversible, which can hardly give accurate calculations on irreversible traps.

In the present work, via double-cell electrochemical hydrogen permeation tests and characterization techniques such as OM, SEM, EDX, TEM and EBSD, various types of hydrogen traps in X70 pipeline steels were well studied. All investigated steels have the same chemical composition but have been through different TMCP process and hence have different microstructures. Therefore, the trapping effects of various microstructural features were revealed by comparison of testing results of these samples, as well as the effect of TMCP on the formation or distribution of some microstructures. Besides, samples from centerline region and non-centerline regions (near surface and near ¼ distance) were adopted giving insights about traps variation through thickness. Furthermore, based on EBSD band contrast maps and hydrogen permeation test results, a trapping efficiency model was developed to quantitatively evaluate the trapping ability of the phases presented in X70 steel, including ferrite, bainite, martensite and M/A constituents. Finally, a simulation model of hydrogen permeation process was developed to calculate characterization parameters associated with hydrogen traps, such as effective diffusion coefficient, trap density and binding energy.

In sum, the present investigation shed lights on the influence of TMCP on microstructural features in X70 pipeline steel that are hydrogen traps, studied the trapping ability and distribution of various hydrogen traps, and provided a trapping efficiency model to quantitatively evaluated the trapping capability of phases and a numerical simulation model that can be used to calculate irreversible trap density and binding energy.

3 Materials and Experimental Methodology

This chapter contains description of the micro-alloyed steels analyzed, and microstructure analysis and hydrogen permeation test. The first section presents the steel plates studied, including chemistry, TMCP parameters, sample locations and sectioning of the samples. The second section is about techniques and analysis methods for OM, SEM, EBSD and TEM, which is followed by a detailed description of DS hydrogen permeation test in the third section, including sample preparation, electroplating process, experiment set-up, experiment process and data analysis of hydrogen permeation test.

3.1 Steel composition and processing

Two (2) groups of plates (Group I and Group II) are studied in the present work, which consist of four (4) and seven (7) plates, respectively. Group I was equivalent to industrial process; Group II was laboratory plates without finish rolling. All these plates have the same composition as shown in Table 3-1.

Table 3-1 Chemical composition of steels studied.

	C	Mn+ Mo+Cr	Nb+V+Ti	Ni	N
wt.%	0.03~0.04	1.7~1.8	0.09~0.10	0.4~0.5	<80ppm

The four plates in Group I were subjected to oven cooling (to simulate coiling process), air cooling and water quenching, respectively, after accelerate cooling to 565°C by runout table as shown in Fig.3.1a. The purpose of the different processing is to obtain samples with different microstructure combination and various precipitate morphology. TMCP processing of Group II plates is shown in Fig.3.1b. Different rough rolling and cooling process were used to study the precipitation process during rough rolling as well as the effect of various precipitate morphologies and microstructures on hydrogen permeation process.
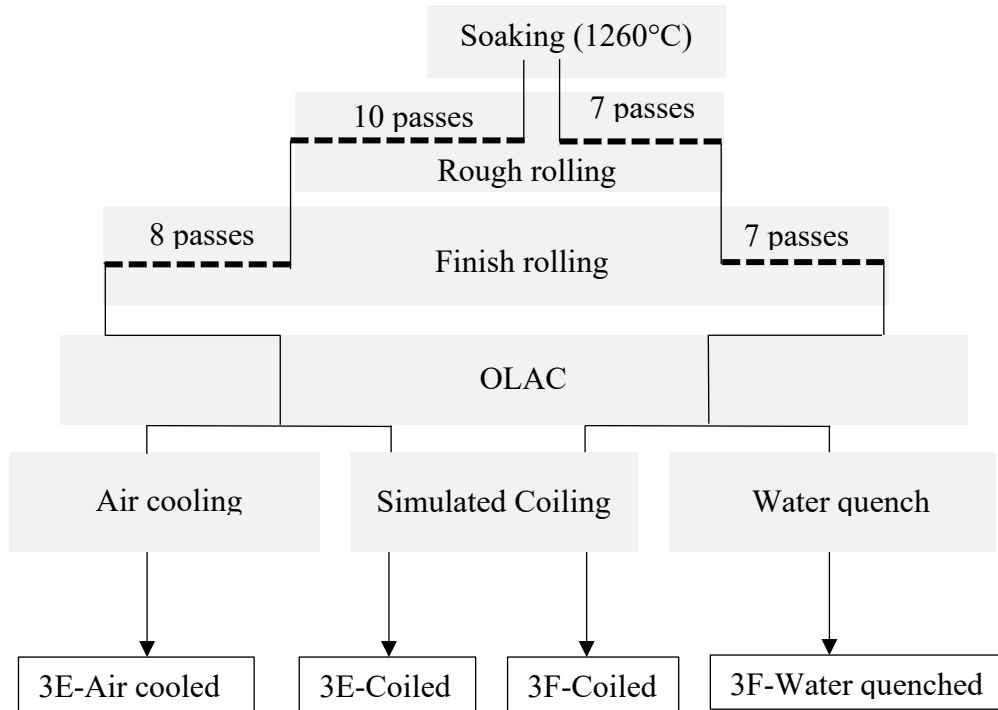
a)
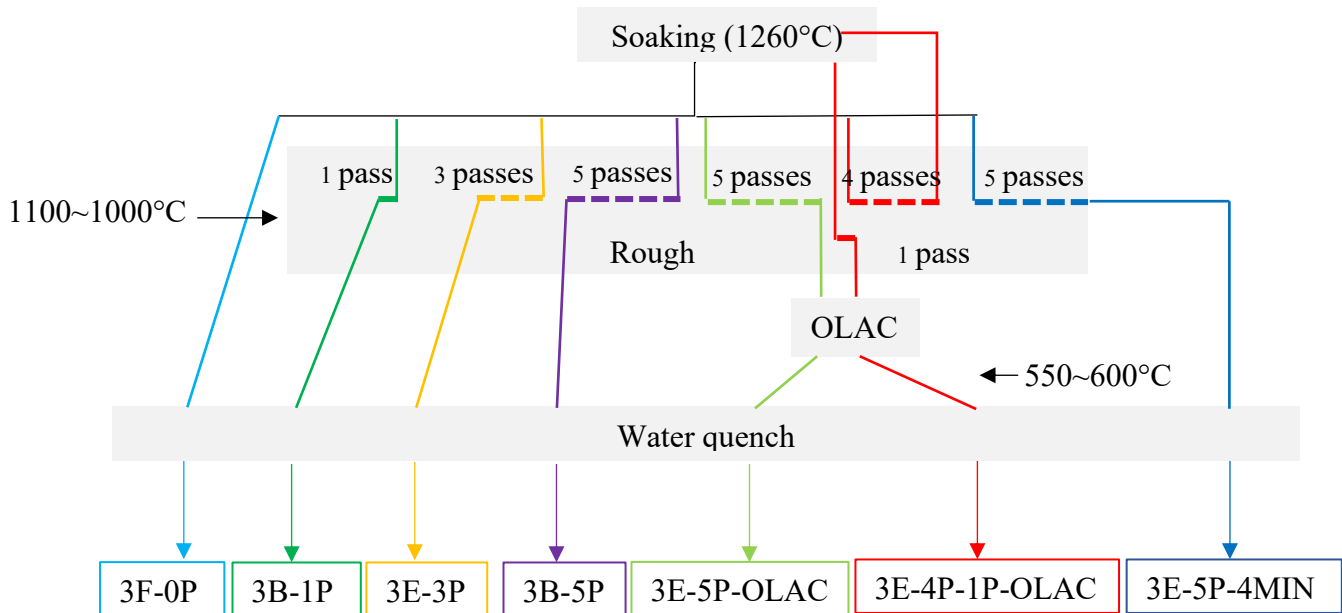
b)

Fig. 3.1 TMCP conditions of samples in Group I (a) and Group II (b).

Fig.3.2 shows the locations of samples for both microstructure characterization tests and hydrogen permeation test in corresponding plates. In Group I, 3E skelp is thicker (19 mm) than 3F skelp (15 mm) which enables sampling from three locations: surface, ¼ distance and centerline; two locations (surface and centerline) were sampled for 3F. For all Group II plates, only samples cut from surface region were studied. All surface samples are 1mm below the surface of the plates.

a)

b)

c)
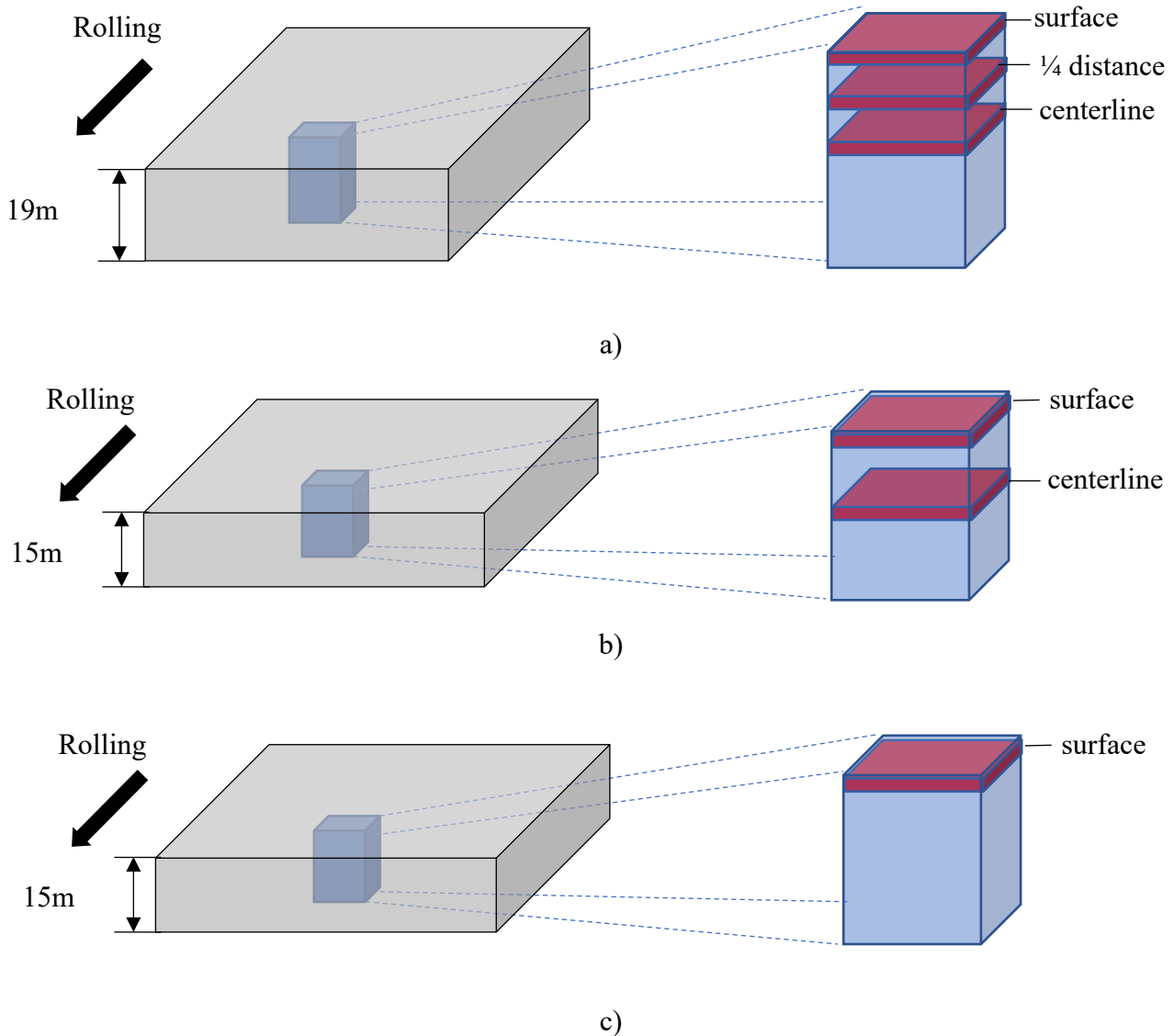
Fig. 3.2 Schematic representation of location of samples for characterization test and hydrogen permeation test. a) 3E-Coiled/3E-Air cooled; b)3F-Coiled/3F-Water quenched; c) Group II

3.2 Experimental parameters and analysis methods for characterization tests

In this section, etchants used for OM images and experimental parameters chosen for TEM and EBSD tests are listed. Also, a phase quantification technique based on EBSD band contrast maps is explained with an example. Detailed description about the sample preparation methods and procedures for all characterization tests can be found in Appendix A.

3.2.1 OM & SEM & EDX analysis

Four etchants were chosen for different purposes as shown in Table 3.2. Samples for OM and SEM/EDX analysis were polished to 0.05 µm before etching. Samples for inclusions and large TiN precipitates study are prepared in a similar way without etching.

Table 3-2 Composition and effects of etchant used in present study.

Etchant	Composition	Purpose
Nital(2%)	2 mL nitric acid +98 mL ethanol	Reveal ferrite grain boundaries and cementite
PAG etchant	2g picric acid + 1g sodium dodecylbenzene sulfonate + 100 ml H_2O	Develop prior austenitic grain boundaries in martensite and bainite structures.
Lepera	1g $Na_2S_2O_5$ + 100 mL distilled H_2O+ 4% Picral (4g dry picric acid + 100 mL ethanol)	Reveal M/A phase

Zeiss Sigma Field Emission Scanning Electron Microscope (FESEM) with EDS was used for microstructure, large TiN precipitates, and inclusions characterization via in-lens secondary electron detector at 20kV under high current mode. To study morphology of M/A phase, Oxford SEM was used with secondary electron detector at 30kV.

3.2.2 TEM analysis

In this work, JEOL JEM-ARM200CF S/STEM was used to study the morphology, composition, lattice parameters, size distribution and density of precipitates in plates. For all plates, surface samples were used for TEM analysis. In addition, for 3E-Coiled, precipitates near

¼ distance and centerline region were also studied. Carbon replica extraction technique was adopted for TEM sample preparation. The process of sample preparation is described in detail in Appendix A-1.

TEM mode was used to characterize the morphology of large precipitates (> 20 nm) (Fig.3.3). Annular dark field (ADF) imaging (Fig.3.5a) and bright field (BF) imaging (Fig.3.5b) under STEM mode were used for observation of fine precipitates (< 20 nm).
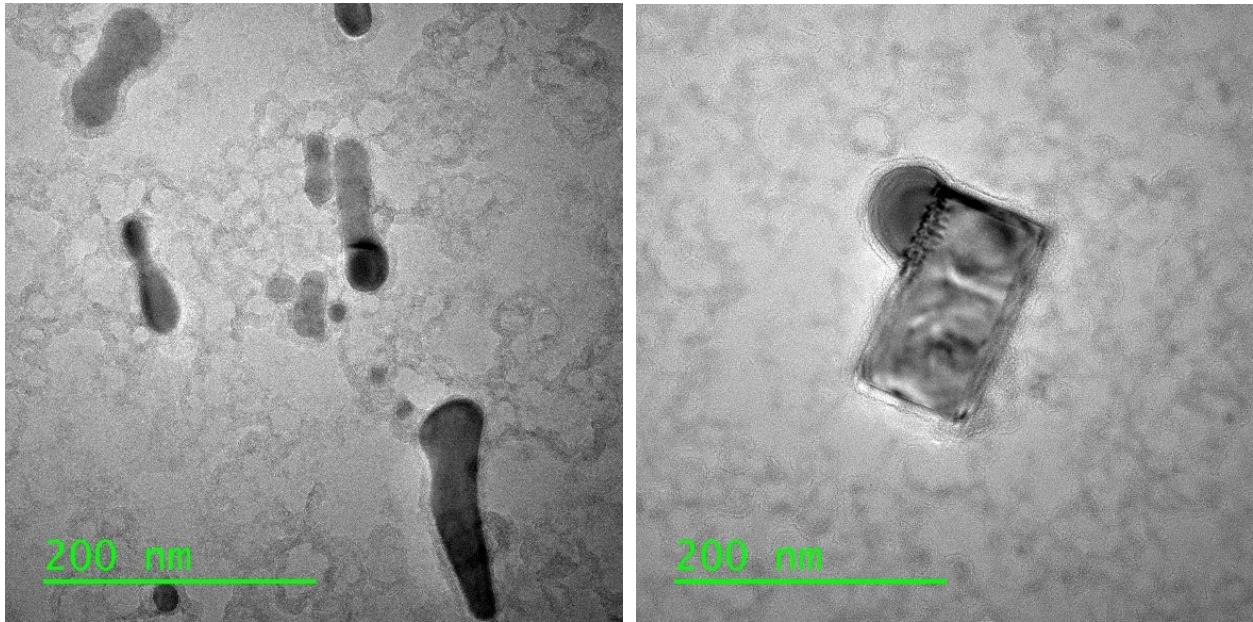
Fig. 3.3 Morphology of large precipitates under TEM mode.

Two different methods were used to statistically analyze the size distribution of precipitates. For large precipitates, the contrast in ADF image is good enough for application of software Gatan which can automatically select and measure each precipitate on the image as it is shown in Fig.3.4 and Table 3-3. However, for fine precipitates, software ImageJ was applied to manually measure the area (A_p) covered by each precipitate on ADF images as it is shown in Fig.3.5a. Then the average diameter (D_{av}) is calculated using equation $D_{av} = 2\sqrt{\frac{A_p}{\pi}}$. ADF images were also used for the calculation of area density of fine precipitates, i.e., number of precipitates per unit area (N_p), which is obtained by equation $N_p = \frac{1}{15}\sum_{i=1}^{15}\frac{n_p}{S}$. Herein, for each sample, the sum of precipitates (n_p) on each of 15 ADF images (1M×) were divided by the aera covered in the

image (S). The area density of large precipitates is measured and calculated similarly based on SEM images at magnification of 30,000×.

a)   b)
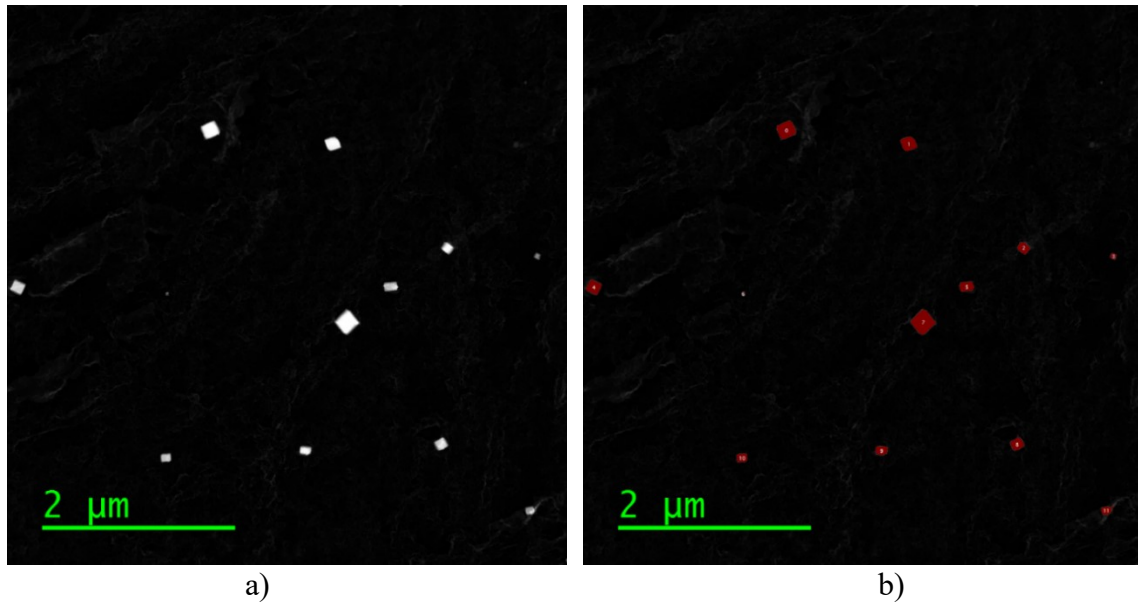
Fig. 3.4 ADF image of large TiN precipitates before a) and b) after processed by Gatan software.

Table 3-3 Measured data of the precipitates in Fig.3.4.

No.	Area (pixel^2)	Perimeter (pixel)	CircDiameter (pixel)	CenterX (pixel)	CenterY (pixel)
0	805	115.1544	33.14915	371.7807	228.5547
1	562	95.84064	27.6585	595.621	253.8274
2	323	72.66904	20.81895	805.5062	444.4412
3	82	38.97056	10.38953	969.6829	459.3781
4	491	91.49749	26.30364	19.76273	516.1476
5	387	84.87006	23.95741	701.7093	514.854
6	18	16.82843	4.716244	293	527.5
7	1202	143.8234	42.02465	621.6863	579.9867
8	395	79.84063	23.03812	793.862	803.0241
9	300	68.97057	19.99601	545.68	814.5333
10	259	64.72792	18.78601	290.6815	827.8861
11	233	79.94113	20.82668	957.4742	924.1696
12	4	10	2.544434	1023.5	1015

Area: 57.934 nm^2

a)   b)
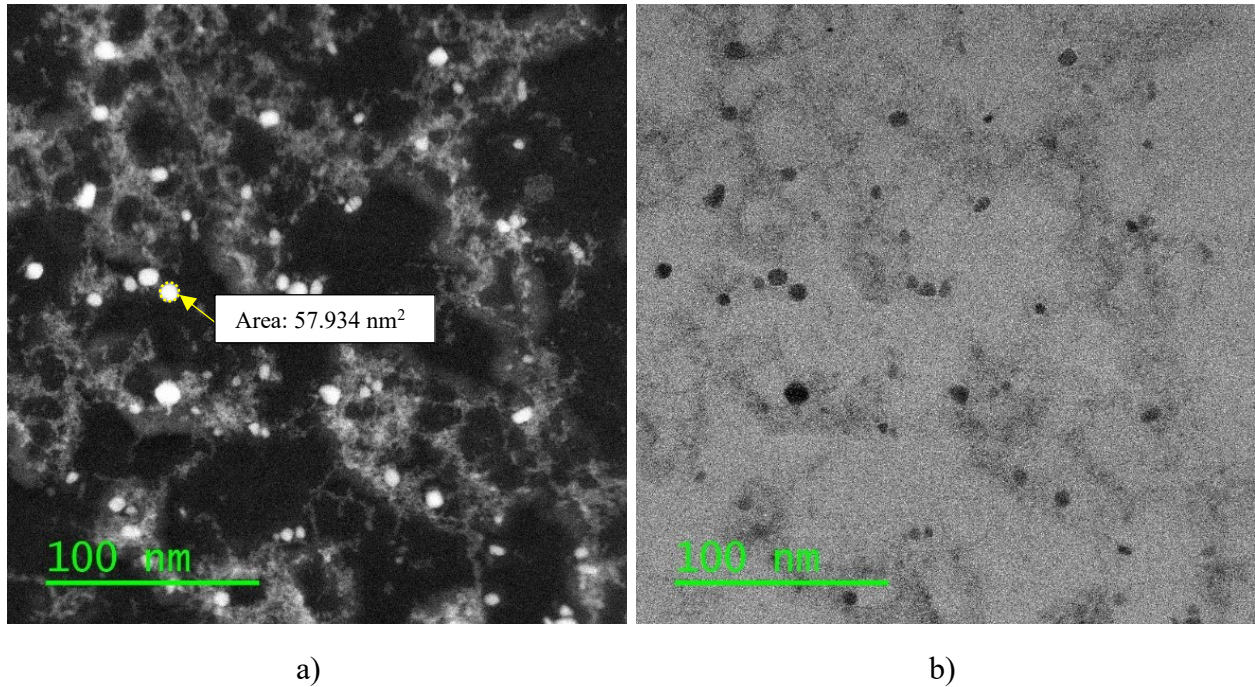
Fig. 3.5 ADF image (a) and BF image (b) of fine NbC precipitates in 3F-Coiled.

The chemical composition of precipitates was determined by EDS microanalysis. To distinguish combined TiN and NbC precipitates, EDS mapping images were obtained with distribution of Ti, N and Nb as it is shown in Fig.3.6. To identify the crystal structure and confirm the composition of precipitates, the space between specific group of planes of the precipitates were measured using selected area electron diffraction (SAED) (Fig.3.7) and HR-TEM (Fig.3.8) techniques for large precipitates (> 20 nm) and fine precipitates (< 20 nm), respectively. Then the measured values were compared with the lattice parameters of common precipitates in pipeline steel (provided on website of Material Project) to determine the crystal structure of the precipitates.
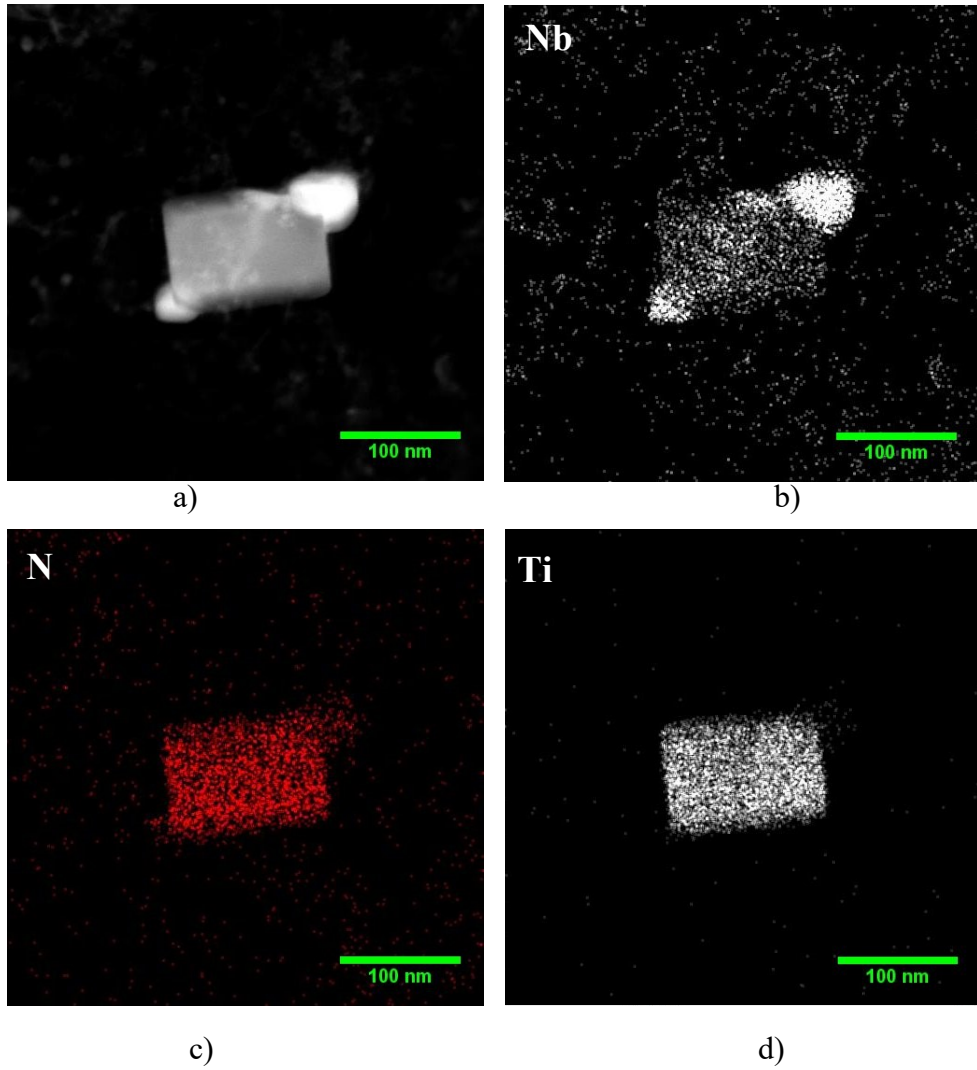
Fig. 3.6 Compositional elemental mapping of a (Nb, Ti) (C, N) precipitate.
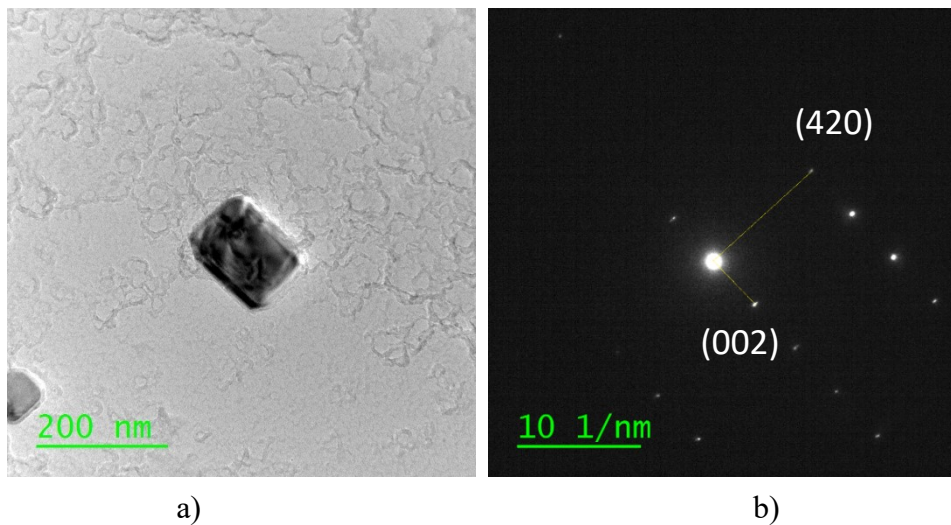
Fig. 3.7 The SAED pattern b) of a TiN precipitate shown in a).
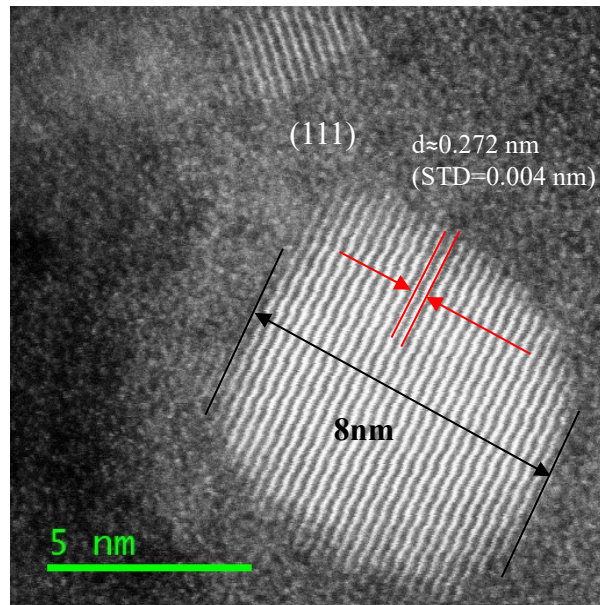
Fig. 3.8 HR-TEM image of a NbC precipitate.

3.2.3 EBSD analysis

EBSD provided a wide range of information about the microstructure of the steel, including types and distribution of phases, dislocations densities, grain size, misorientation distributions. In the present investigation, all samples cut from locations mentioned in section 3.1 have been studied by EBSD.

The first step of EBSD sample preparation was the same as OM/SEM sample preparation with non-crystalizing colloidal silica polishing suspension as the final polishing. Then the samples were rinsed in a beaker filled with ethanol and washed in an ultrasonic machine for 10 min. After dried by pressured air flow, the samples were ready for use.

Step size and scanning area are two important parameters for EBSD imaging as they can affect the accuracy of the data collected and the time needed for each image. Three (3) combinations of step size and scanning area were used for different purposes as shown in Table 3-4.

Table 3-4 Parameters used for collecting EBSD data

No.	Step size (μm)	Scanning area (μm^2)	Purpose	Chapter of results
1	0.5	120 ×150	Grain size measurement	4.1.4
2	0.1	40 × 30	Phase identification and quantification	4.1.2
3	0.2	500 × 400	Phase quantification	Appendix D

To quantitively evaluate the fractions of these phases, a EBSD technique developed by Jinghui Wu[170] was adopted. This technique is based on the image quality map (or band contrast map) which is a metric describing the quality of a diffraction pattern. The image quality (IQ) value is proportional to the sharpness of the Kikuchi Pattern. Crystalline defects such as dislocation and sub-grain boundaries can distort the lattice and hence give rise to a distorted Kikuchi Pattern and results in a lower IQ value. In this way, ferrites formed at lower temperature, e.g., acicular and bainitic, can be distinguished from polygonal ferrite that formed at higher temperature by contrast due to the difference of their dislocation density (as seen in Fig.3.9a).

The distribution curve of IQ in Fig. 3.9c can be fitted by three normal distribution curves using deconvolution calculation in Origin® software. These normal distribution curves represent ferrite with high quality, bainite with medium quality and M/A with low quality diffraction patterns. The thresholds between these phases are determined by the cross points of the curves. These thresholds separate the IQ distribution curve into 3 regions. All points are assorted to ferrite (>threshold 2), bainite (threshold 1~threshold 2) and M/A (< threshold 1) based on the range that the IQ index fall in and colored accordingly (Fig.3.9b). Then the volume fraction of these phases can be obtained through the ratio of the area of the phase to total area. The Python code used for calculation of phase volume fraction and colored phase mapping can be found in Appendix A-2.
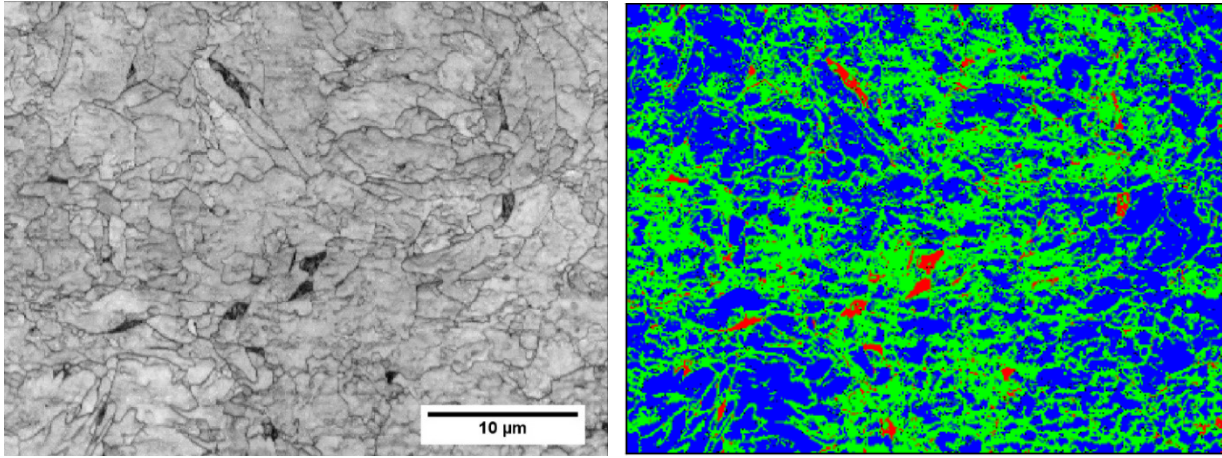
a)   b)
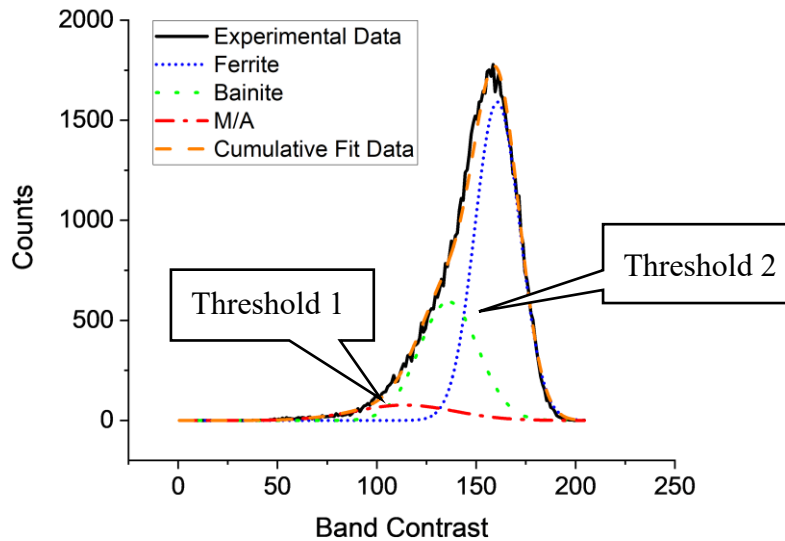
c)

Fig. 3.9 Phase fraction evaluation by EBSD IQ map. a) Band contrast map; b) phases labeled by color: blue: ferrite; green: bainite; red: M/A; c) Band contrast distribution curve.

3.2.4   Devanathane-Stachurski (DS) hydrogen permeation test

DS hydrogen permeation test (or so-called double-cell hydrogen permeation test) is a widely adopted test in hydrogen embrittlement study due to its simple configuration and reliable results. One of the most important advantages of this method is the unlimited options of experiment

environment and parameters for researchers according to their study interests. In this section, the electrochemical hydrogen permeation test used in the present study is present with detail, including sample preparation with electroplating process described in a separate section, experimental set-up as well as the test process and data analysis. The testing method in the present study is established based on ASTM G148-97[94] and ISO 17081:2004[93].

3.2.4.1 Sample preparation

The orientation and dimensions of hydrogen permeation test samples is shown in Fig.3.10. The testing surface of the sample is parallel to the rolling direction so that the hydrogen flux direction in test will be the same as it is in field for pipeline. A thickness of 1.2 mm is chosen (thickness recommended in ASTM G148-97 and ISO 17081:2004 is > 1.0 mm) to ensure a diffusion-controlled process and minimize the effect of surface reaction process. Due to the large size, the sample needed to be ground on the polisher up to 4000 grit by hand to ensure a mirror surface. After washed by flowing water and quickly dried by compressed air flow, it was washed in an ultrasonic machine with acetone for 20 min and then with ethanol for another 20 min. Polished samples were subjected to Pd electroplating and hydrogen permeation test subsequently within 2 hours to minimize the effect of oxidation of the fresh sample surface (charging side) on hydrogen entry during the hydrogen permeation test.
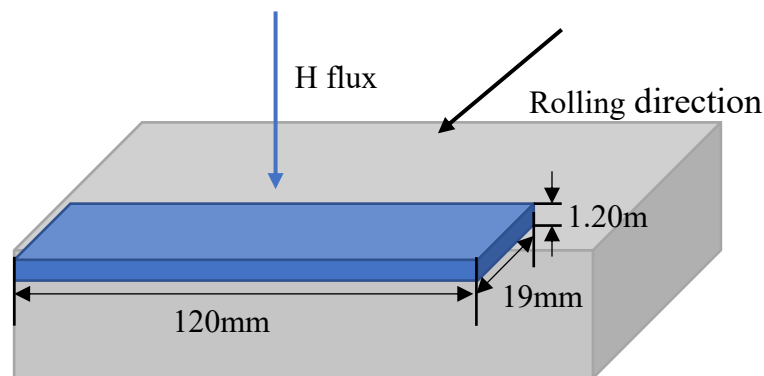
Fig. 3.10 Orientation and dimensions of the sample for hydrogen permeation test.

3.2.4.2 Electroplating process

To ensure a stable oxidation curve, a thin Pd layer (~2 μm) should be added to the exit side (oxidation side) to protect the sample surface from oxidization during test so as to reduce the possibility of passivation[171]. Furthermore, oxidation reaction of H occurs more easily on a

palladium surface than on an iron surface, which can significantly suppress the competing non-electrochemical hydrogen atom recombination reaction. Hence, the measured current reflects the real evolution of the hydrogen flux and is correctly exploited[172]. Electroplating is an easy and economical way that has been widely used for Pd coating as compared with other methods like sputtering. However, the electroplating current should be selected carefully since hydrogen atoms might be introduced into the material and influence the subsequent permeation measurements. It is reported that a plating current density higher than 20 mA/cm^2 can cause damage to the surface deposit due to the build-up of hydrogen ions, and 5 mA/cm^2 is recommended to maximize current efficiency[81].

To maintain a stable surface condition during hydrogen permeation test, the deposit must be easily reproducible, uniform, well adherent, free from pores and cracks, and resistant to 0.1M NaOH[82]. It is shown that deposits generally display some porosity at thickness < 1.3 μm and a palladium coating of about 2 μm will not materially affect the hydrogen permeation kinetics. Therefore, a thickness of Pd coating in range of 1.5-2 μm is recommended[81].

In this study, a plating current density of 4.2 mA/cm^2 was chosen and a smooth and uniform surface was obtained (as shown in Fig.3.11). The thickness of the Pd coating is about 1.4~1.5 μm (as shown in Fig. 3.12 and Table 3-5). The Pd electroplating set-up, condition and process can be found in Appendix A-3.

a)   b)
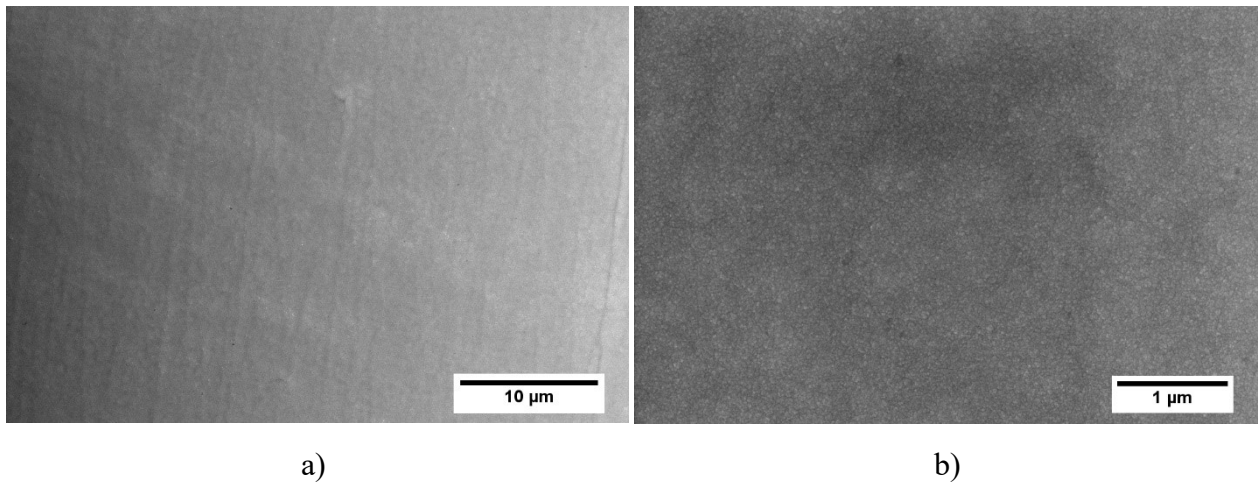
Fig. 3.11 Surface of Pd layer by SEM.
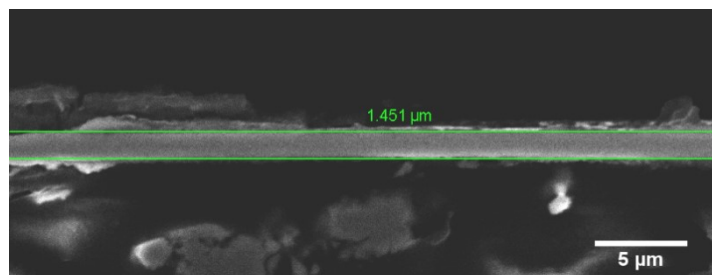
Fig. 3.12 The thickness of Pd layer measured by SEM.

Table 3-5 Thickness of Pd electroplating layer.

	Thickness of Pd layer (µm)
1	1.451
2	1.414
3	1.451
4	1.451
5	1.489
mean	1.451
STD	0.026

3.2.4.3 Experimental set-up

Two-compartmental cell is composed of a charging cell (cathodic cell) and an oxidation cell (anodic cell) constructed from polymethyl methacrylate (PMMA), as shown in Fig.3.13. The cells are separated by the sample clamped in a sample holder. The sample surface on each side is exposed to the solution in the cell of that side through three holes (total exposed area: 1.9 mm^2) in the sample holder. The test conditions are listed in Table 3-6.

In the charging cell, the production of H was carried out by cathodic polarization in 0.1 M NaOH at a constant current provided by a galvanostat according to the reactions $2H_2O + 2e^- \rightarrow H_2 + 2OH^-$ and $H_2{\rightarrow}2H$. A complexing agent ethylenediaminetetraacetic acid (EDTA) (0.01 M) is used as the promoter to remove the formation of an unreducible porous layer on the charging

surface of the sample during cathodic polarisation[91]. The addition of EDTA not only enhanced hydrogen entry into the tested sample but also improved the reproducibility of the test results[7, 91]. In the oxidation (anodic) cell, a constant potential (+300 mV SCE) was provided by a potentiostat to ionize any hydrogen arriving at the surface after diffusing through the metal by the reaction $H_{ads} \rightarrow H^+ + e^-$. N_2 gas is bubbled into both cells continuously during the test.
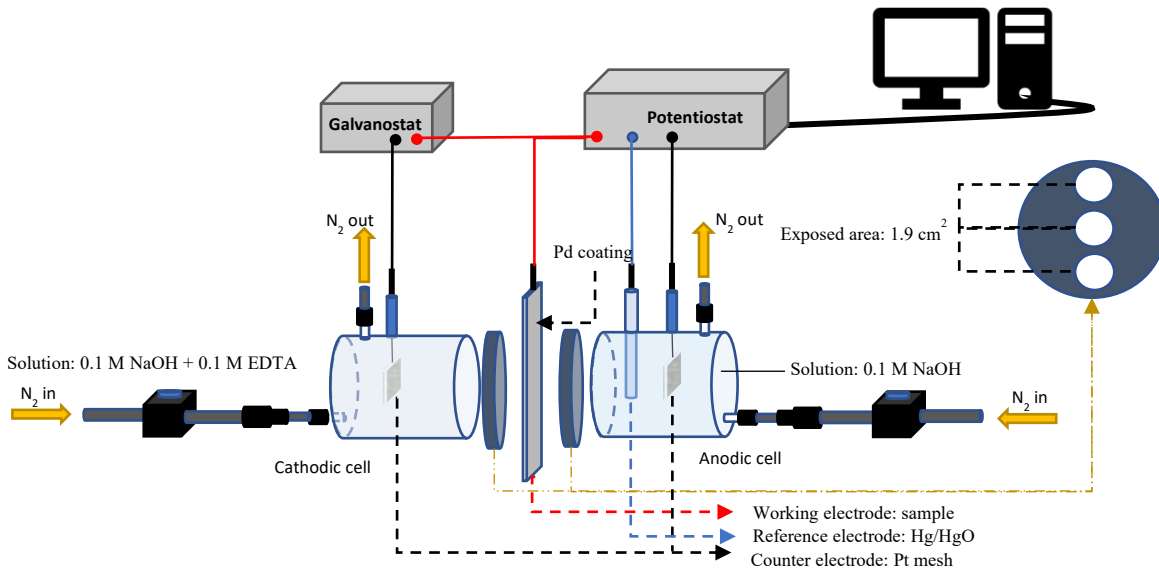
Fig. 3.13 Experimental setup of hydrogen permeation test.

Table 3-6 Test conditions of DS double-cell hydrogen permeation test

Conditions	Charging cell	Oxidation cell
Electrolyte solution	0.1 M NaOH+0.01 M EDTA	0.1 M NaOH
Anode	platinum mesh electrode	Sample (working electrode)
Cathode	sample	platinum mesh electrode (counter)
Reference electrode	/	6mm Hg/HgO reference electrode
Constant current	19 mA	/
Constant potential	/	+300 mV SCE

3.2.5   Experimental procedure

The testing process is summarized in Fig.3.14. To minimize the intervention of background noise, the potential of oxidation cell was set to the control value (+300 mV SCE) (polarization) at least 24 hours before charging to passivate the sample until the oxidation current is as low and stable as possible. The start time of charging was recorded for calculation of lag-time (t_{lag}), and the test was stopped when the oxidation current reached to a steady-state. To distinguish the effect of reversible and irreversible trapping on hydrogen transport, repetitive permeation transients were performed on the same sample. During the first permeation transient, both irreversible and reversible trapping sites are filled. Then, the hydrogen charging is interrupted, and hydrogen in lattice and in reversible traps is discharged from the sample whereas hydrogen in irreversible traps remains trapped. Therefore, the second permeation transient is only affected by reversible traps, and a shorter second permeation transient proves the existence of irreversible traps. Detailed experimental procedure refers to Appendix A-4.

3.2.6   Data analysis of hydrogen permeation test results

The measured oxidation curve in double-cell hydrogen permeation test gives wealthy information about the hydrogen traps in matrix. In the present study, time-lag method and curve-fitting method are adopted to calculate D_{eff} (effective diffusion coefficient) based on the oxidation curve obtained from hydrogen permeation test. Among many published models, Dong's model is selected for estimation of N_t in this work. The derivation of equations in this section is shown in Appendix A-5.

Data pre-processing was conducted prior to further analysis, including cutting off the data collected during passivation stage, smoothing data with Savitzky–Golay filter (window length=101, polyorder=2), and substruction of background current from the measured oxidation curve. An introduction of Savitzky–Golay filter refers to Appendix A-6. The data before and after pre-processing are shown in Fig.3.16a) and b), respectively.
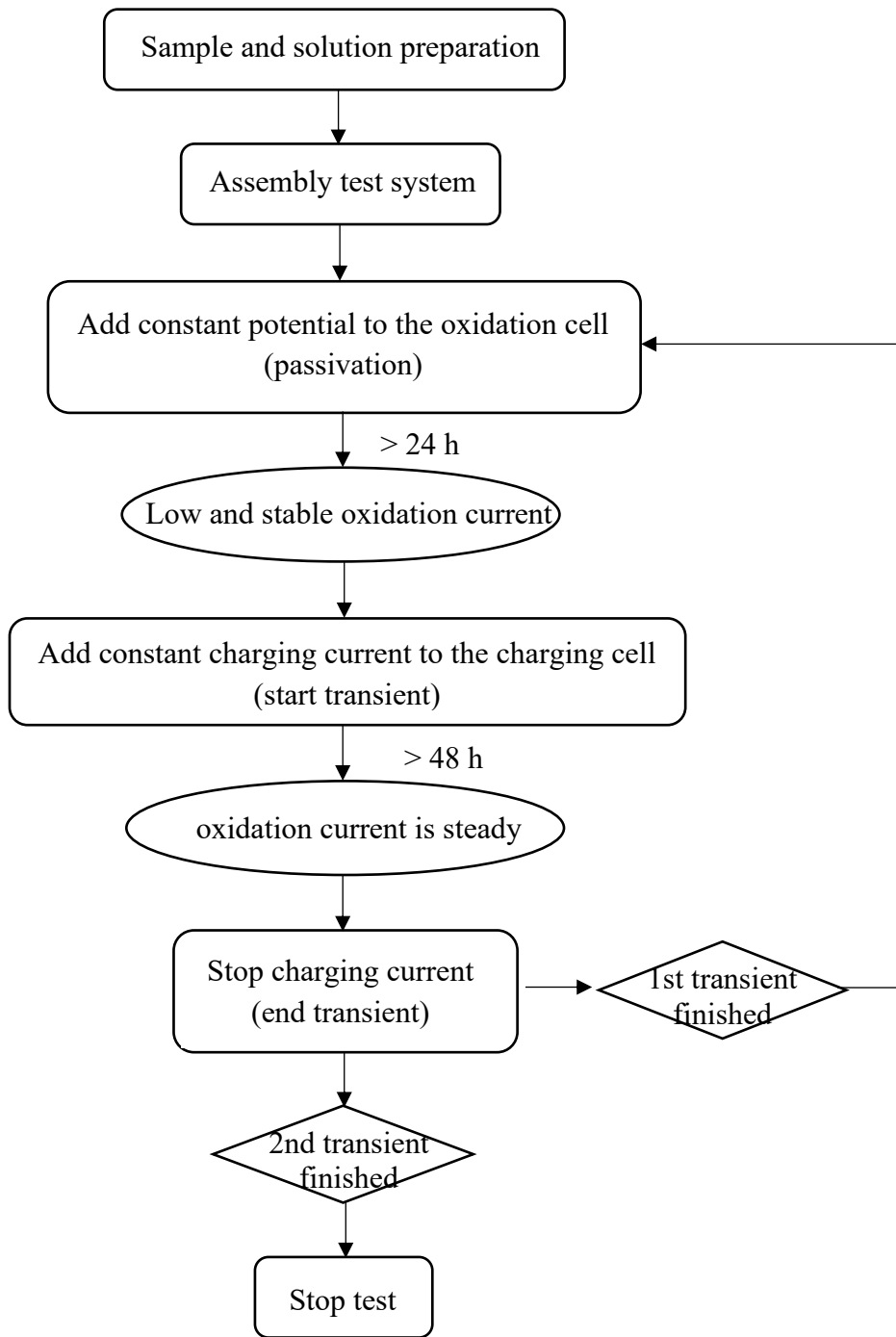
Fig. 3.14 Flow chart of the process of hydrogen permeation test.

3.2.6.1 Estimation of D$_{eff}$ using time-lag method

In time-lag method, t_{lag} is defined as the time in which the metallic matrix begins to be saturated by hydrogen[173]. Following the time integral of current ($\int i_L dt$), i.e., the total quantity of hydrogen emerging from the detection side, the slope of the curve becomes constant when a stationary linear concentration gradient has been established in the sample as shown in Fig. 3.15a. The intercept on the t-axis of the extrapolation of the straight line gives the so-called time lag, t_{lag} (Fig. 3.15b)[7] . As a commonly used empirical method, the t value of oxidation curve at J(t)/J$_{ss}$=0.63 is used as an estimate of t_{lag} ,wherein J(t) is the flux of hydrogen at exit side, and J$_{ss}$ is J at steady state. J$_{ss}$ can be converted from I$_{ss}$ (steady-state current) by equation (3-1). Fig.3.16c is an example of finding t_{lag} using normalized oxidation curve.

$$J_{ss} = \left(-D_{eff}\frac{\partial c}{\partial x}\right)_{x=L} = \frac{I_{ss}/A}{F} \tag{3-1}$$

Wherein F is faraday's constant (9.6485×10^4 coulombs/mol), A is the exposed area of sample in the oxidation cell.
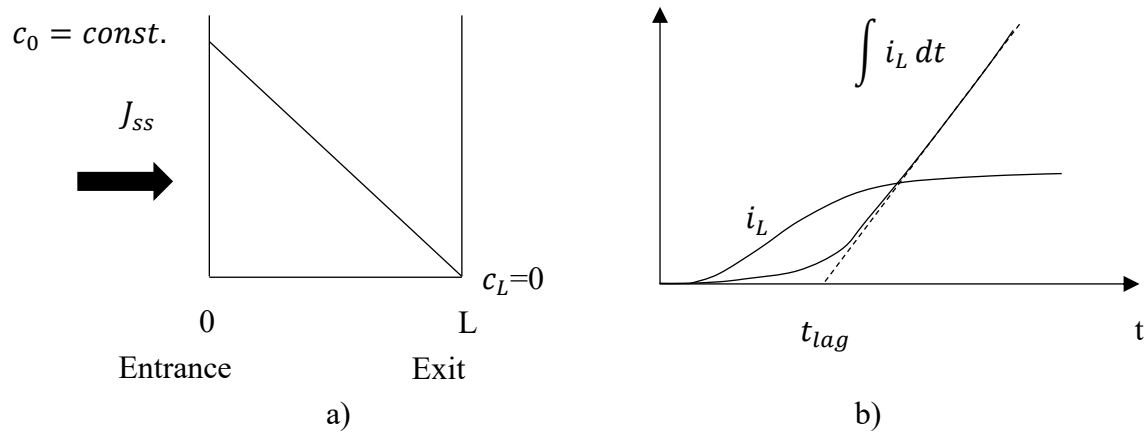
Fig. 3.15 Definition of t_{lag}. c_0 and c_L are hydrogen concentration at entrance side and exit side, respectively; and i_L is the oxidation current at the exit side.
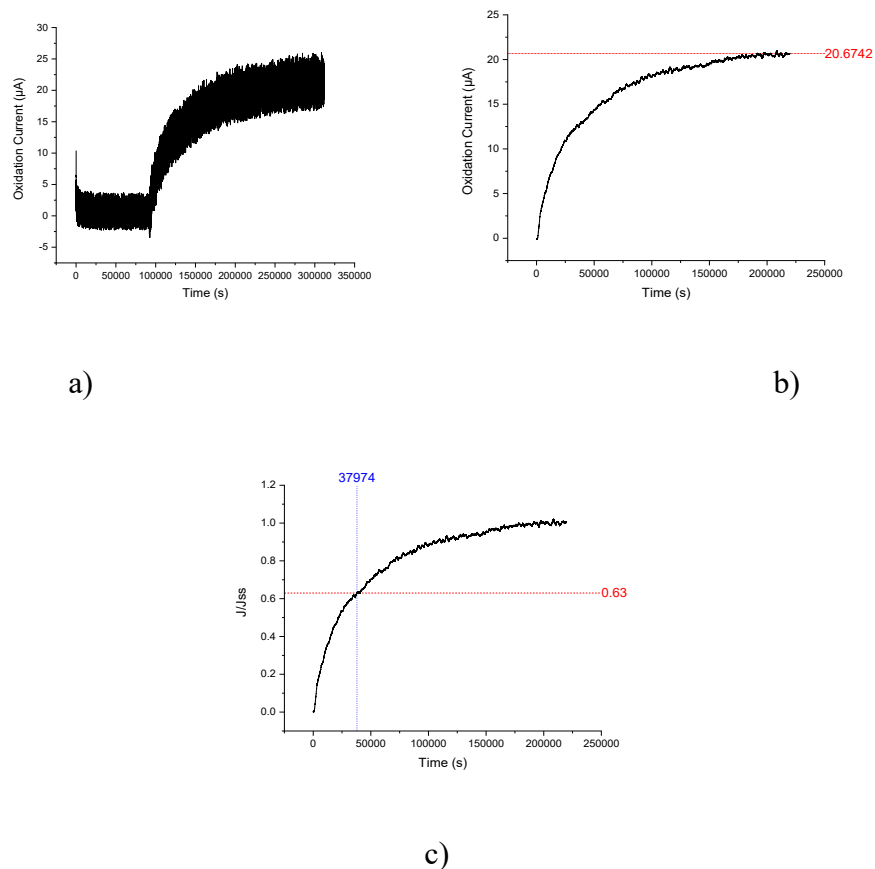
Fig. 3.16 Data preprocessing and determination of t_{lag}. a) original data; b) preprocessed data; c) determine t_{lag}.

In most publications the diffusivity of hydrogen is estimated using equations derived based on the assumption of constant concentration at entrance side even if a potentiostat is used for charging. And it is also the only recommended calculating method in ASTM G148-97 and ISO 17081:2004[93, 94]. However, it is more appropriate for the double-potentiostatic method to consider the concentration of hydrogen on the surface of the sample to be constant as the boundary conditions, while the condition for the galvanostatic-potentiostatic method should be constant flow [7, 173]. This conclusion is also confirmed by the curve-fitting results which will be shown in the following section. Therefore, in this study, equation (3-2) for constant flux condition is used for calculation of D_{eff} instead of equation (3-3), which should be applied to constant concentration condition.

$$t_{lag} = \frac{1}{2} \frac{L^2}{D_{eff}} \tag{3-2}$$

$$t_{lag} = \frac{1}{6}\frac{L^2}{D_{eff}} \tag{3-3}$$

3.2.6.2 Estimation of D$_{eff}$ using curve-fitting method

In present investigation, curve-fitting method is also used for the estimation of diffusion coefficient. And both equation (3-4) (constant flux) and equation (3-5) (constant concentration)[7] are applied for comparation, wherein m=3000 is adopted for good accuracy. (m≥3 is recommended in ASTM G148-97[94]). D$_{eff}$ is determined by nonlinear least square minimization of equations (3-4) and (3-5) with an initial value of 0.000001. Fig.3.17 shows the fitting data under constant flux and constant concentration condition on linear scale and logarithmic scale.

$$i_L(t) = i_0 \left(1 - \frac{4}{\pi}\sum_0^\infty \frac{(-1)^m}{2m+1} exp\left(-\frac{(2m+1)^2\pi^2 D_{eff}t}{4L^2}\right)\right) \tag{3-4}$$

$$i_L(t) = i_\infty \left(1 + 2\sum_1^\infty (-1)^m exp\left(-\frac{D_{eff}m^2\pi^2 t}{L^2}\right)\right) \tag{3-5}$$

Wherein i_L is the oxidation current at exit side, i_0 is the constant current applied on entrance side, i_∞ is the steady-state current at exit side.
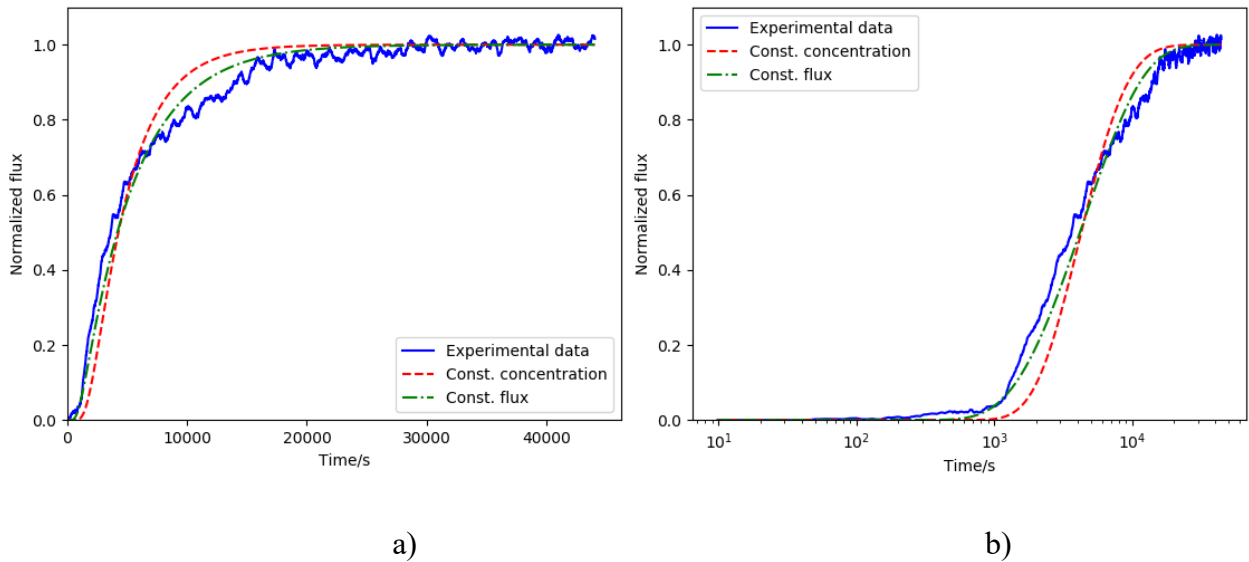
Fig. 3.17 An example of curve-fitting with linear scale a) and logarithmic scale b).

3.2.6.3 Estimation of N_t using Dong's model

McNabb and Foster [100]proposed a trapping-detrapping model based on the assumption that a dynamic equilibrium is maintained between trapped hydrogen and lattice hydrogen. Oriani [16] made more specific treatment onto the local equilibrium hypothesis and concluded that the effective diffusivity is a function of trap density and of the magnitude of the trap depth with some practical equations. Therefore, equations (3-6) and (3-7) were proposed in the scenario that the hydrogen coverage is low:

$$D_{eff} = D_L(1 + KN_t/N_L)^{-1} \tag{3-6}$$

$$K = exp(-\Delta E_b/RT) \tag{3-7}$$

Wherein D_{eff} is the effective diffusion coefficient; N_t is the trap density; D_L and N_L are the diffusivity in lattice and density of normal lattice sites; ΔE_b is the binding energy of the trap; R and T are gas constant and temperature (in Kelvin).

Based on Oriani's work, Dong [17] used equation (3-8) to calculate trap density, and assumed that the binding energy ($|\Delta E_b|$) equals to 0.3 eV.

$$N_t = N_L \left(\frac{D_L}{D_{eff}} - 1\right)^{-\Delta E_b/RT} \tag{3-8}$$

wherein N_L is taken as 7.52×10^{28} m^{-3}; D_L is taken as 1.28×10^4 cm$^2 \cdot$s^{-1}.

Apparent hydrogen solubility (c_{app}) is the lattice concentration at the entrance surface of the sample, which can be defined by equation (3-9) if the surface hydrogen is in thermodynamic equilibrium with subsurface hydrogen.

$$c_{app} = \frac{J_{ss}L}{D_{eff}} \tag{3-9}$$

$$J_{ss} = \frac{I_{ss}}{FA} \tag{3-10}$$

Wherein J_{ss} is the hydrogen flux at steady status; L is the thickness of the sample; I_{ss} is the oxidization current at steady statues; F is Faraday constant, which is taken as 96,485 C/mol; A is the exposed area of the sample, which is 1.9 cm^2.

As it is explained in section 3.3.5, both reversible and irreversible traps are active during the first transient, whereas only reversible traps affect the permeation curve during the second transient. Equations (3-11), (3-12) and (3-13) are used to calculate the density of reversible ($N_{t,r}$)and irreversible traps ($N_{t,ir}$).

$$\text{First transient: } N_{t,1} = N_{t,ir} + N_{t,r} = \frac{C_{app,1}}{3}\left(\frac{D_l}{D_{eff,1}} - 1\right) \tag{3-11}$$

$$\text{Second transient: } N_{t,2} = N_{t,r} = \frac{C_{app,2}}{3}\left(\frac{D_l}{D_{eff,2}} - 1\right) \tag{3-12}$$

$$N_{t,ir} = N_{t,1} - N_{t,2} \tag{3-13}$$

4   Microstructure and hydrogen trapping ability of Group I steels

In this section, the study is focused on Group I steels to reveal the interactions between various microstructural features, such as different phase types, precipitates, inclusions and hydrogen atoms during the hydrogen permeation process, as well as the effect of TMCP process on these features. Group I consist of four (4) X70 pipeline steel plates: 3E-Coiled, 3E-Air cooled, 3F-Coiled and 3F-Water quenched, which have been through different TMCP processes. The microstructure of these plates was studied via OM, SEM/EDX and quantitively evaluated based on EBSD band contrast (BC) maps and OM images. The chemistry of inclusions was analyzed by EDX, and the density of inclusions in different locations through thickness of the plates was evaluated via OM. TEM was used to study the precipitates in terms of morphology, density, size distribution, chemistry, and lattice structure. Double-cell hydrogen permeation test was conducted on samples from various locations through thickness, which gives information such as hydrogen diffusivity, trap density and hydrogen solubility.

4.1   *Microstructure analysis*

In this section, the microstructure of group I plates at surface, ¼ distance and the centerline are characterized qualitatively by SEM and OM in terms of phase types and morphology of M/A constituents. To quantitatively evaluate the volume fractions of each phase, EBSD BC maps and OM images are used for calculation. The EBSD technique also provides information on the structure of M/A constituents and grain size distribution.

4.1.1   *Qualitative observation of microstructure via OM and SEM*

Fig. 4.1 shows the microstructures of group I plates near the surface of the skelp (OM images of group I samples at ¼ distance and centerline are presented in Appendix B-1). 3E-Coiled and 3F-Coiled mainly consist of granular bainite (GB), irregular ferrite (IF), and martensite-austenite (M/A) constituent distributed on both grain interior and grain boundary (Fig.4.1a, c). In 3E-Air cooled (Fig.4.1b), GB, acicular ferrite (AF), granular M/A islands and irregular ferrite (IF)

are observed. 3F-Water quenched, which has been cooled at higher cooling rate, consists of AF, GB, and large M/A blocks between AF laths (Fig.4.1d).
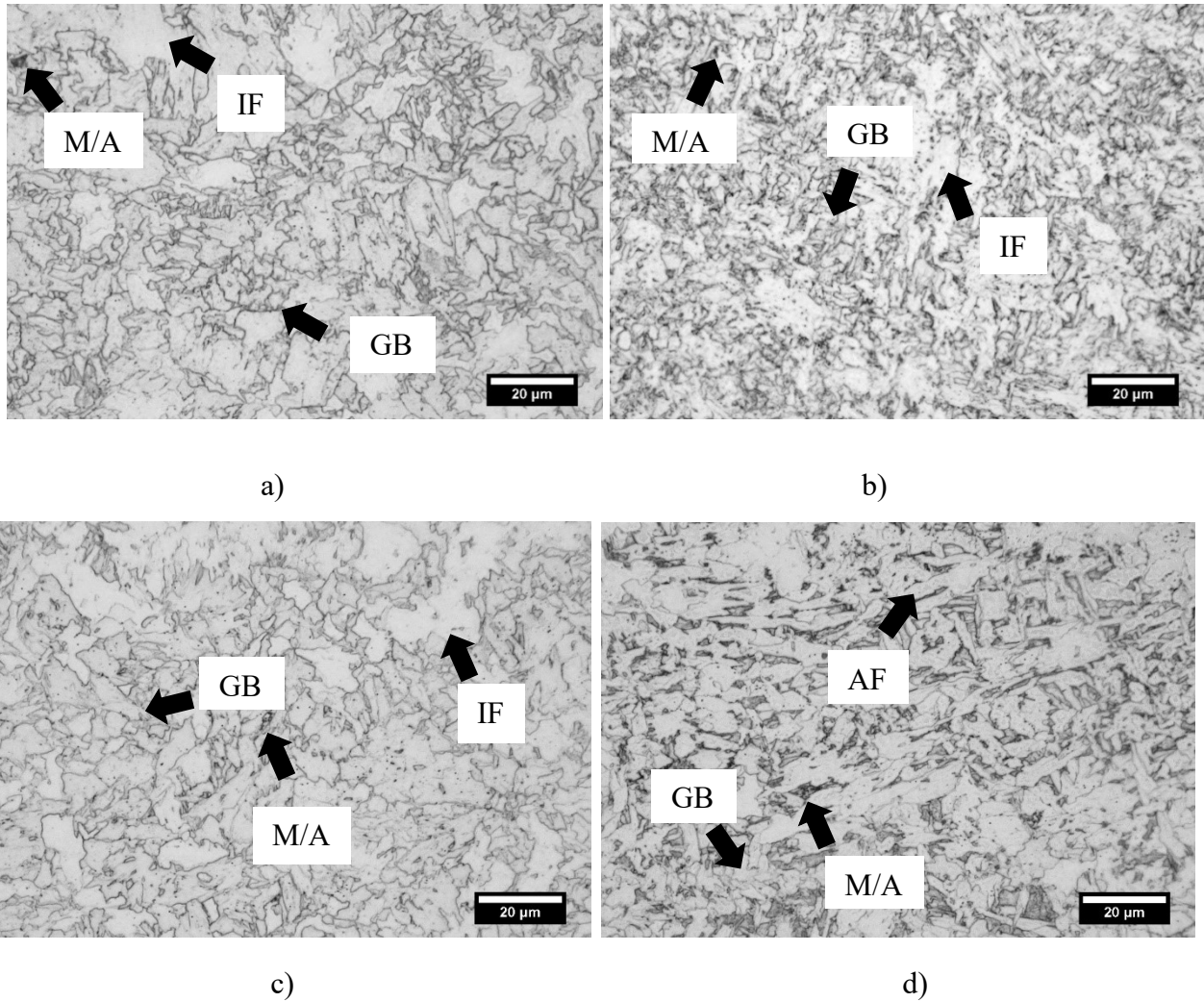
Fig. 4.1 OM images of a) 3E-Coiled, b)3E-Air cooled, c) 3F-Coiled and d) 3F-Water quenched

The morphology of M/A constituents of each sample are clearly shown by SEM in Fig. 4.2. In 3E-Coiled, 3E-Air cooled and 3F-Coiled, M/A constituents are mostly in the form of "islands" at triple point junctions or in the form of layers between bainitic ferrite laths; whereas in 3F-Water quenched, large M/A blocks are found with austenite frame and interior martensite lath structure.

a)

b)

c)
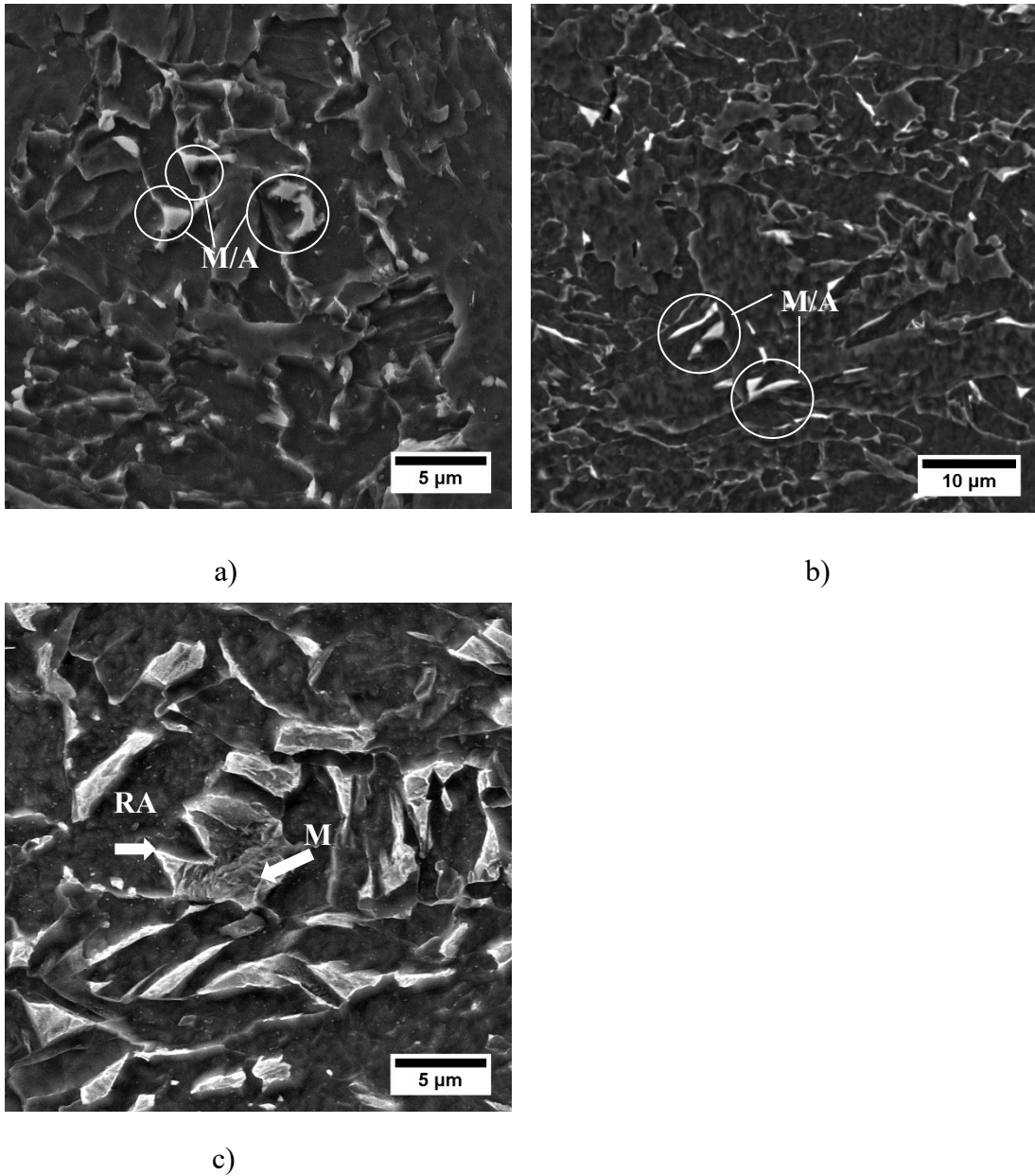
Fig. 4.2 Morphology of M/A constituents in a) 3E-Air cooled, b) 3F-Coiled and c) 3F-Water quenched by SEM (2% Nital etched)

4.1.2 *Quantitative evaluation of microstructure via EBSD and OM*

To estimate the volume fraction of each phase, EBSD band contrast (BC) maps and OM images were used for the measurement. EBSD BC maps of all Group I samples at different locations are presented in Fig.4.3 and Fig 4.4. In these BC maps, M/A constituents can be easily distinguished due to the low imaged quality (IQ) value, which is caused by high dislocation density in martensite and the presence of complex carbides. Based on these BC maps, the volume fraction of ferrite, bainite and M/A constituents or retained austenite (RA) are quantitatively evaluated, and the results are listed in Table 4.1. The evaluation method was presented in section 3.2.3. Devolution curves and colored BC maps showing the evaluation process can be found in Appendix B-2.

a)

b)

c)

d)
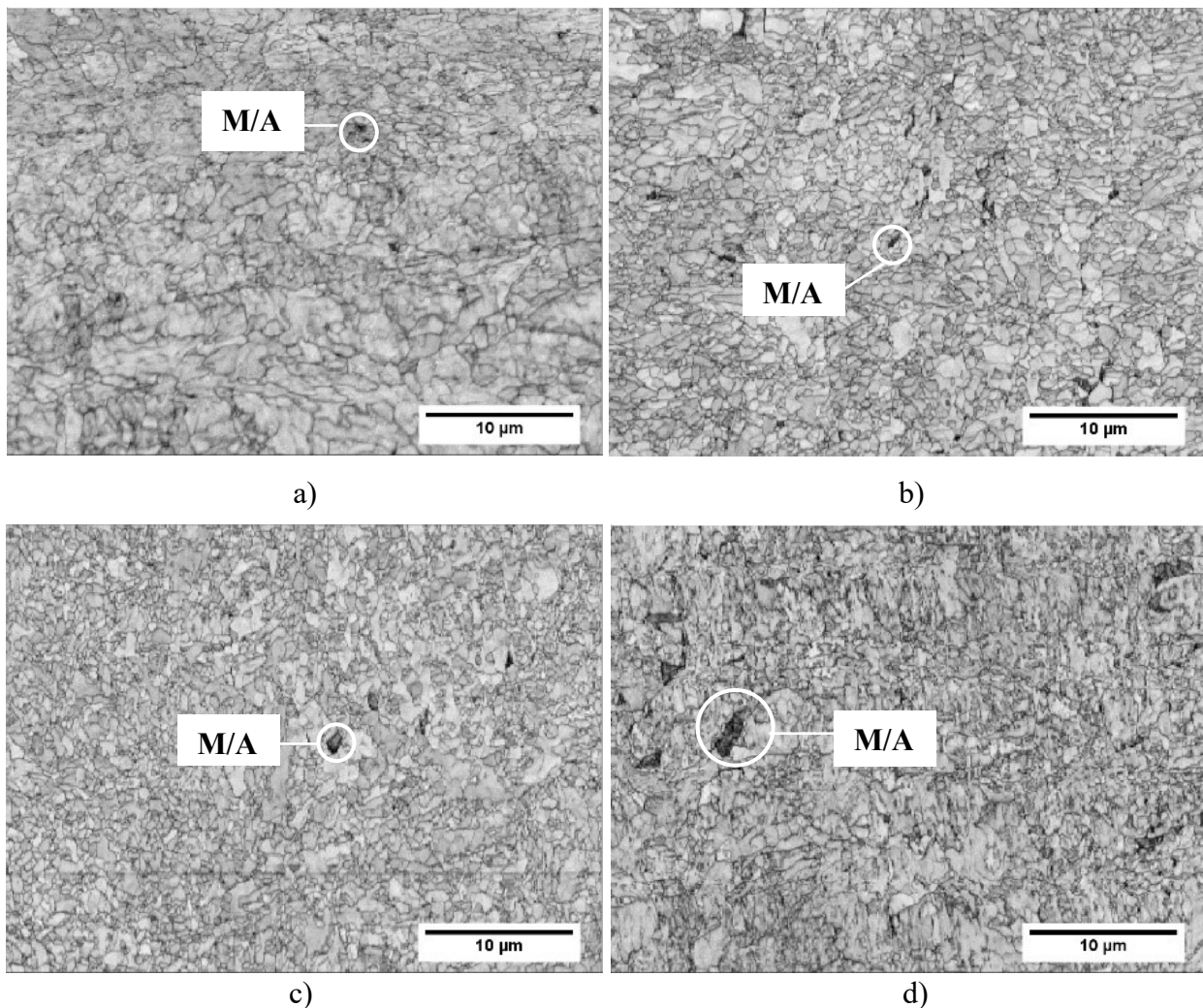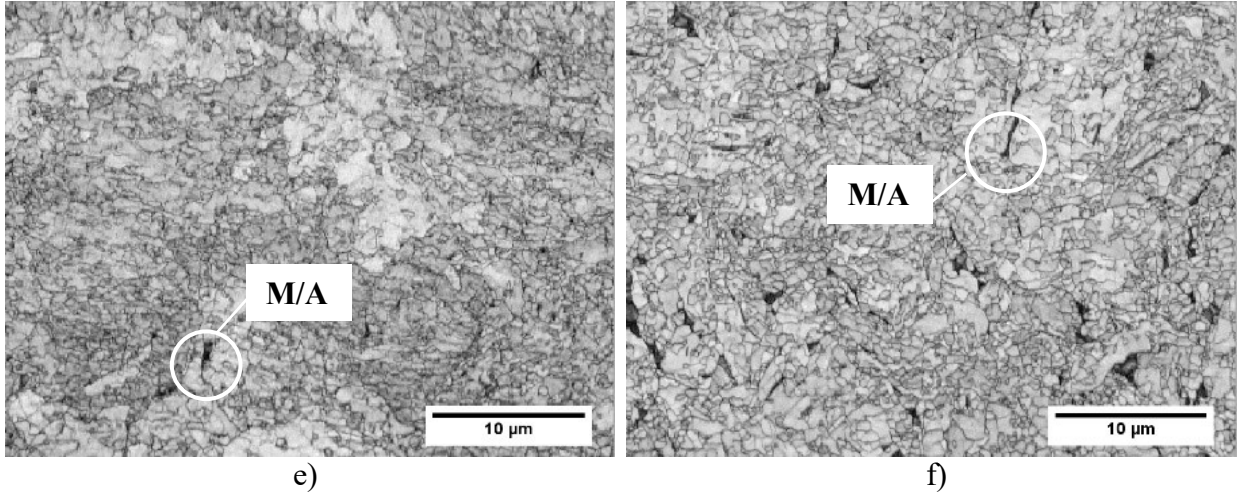
Fig. 4.3 Image quality map of 3E-Coiled at a) surface, c) ¼ distance, e) centerline and 3E-Air cooled at b) surface, d) ¼ distance, f) centerline by EBSD.
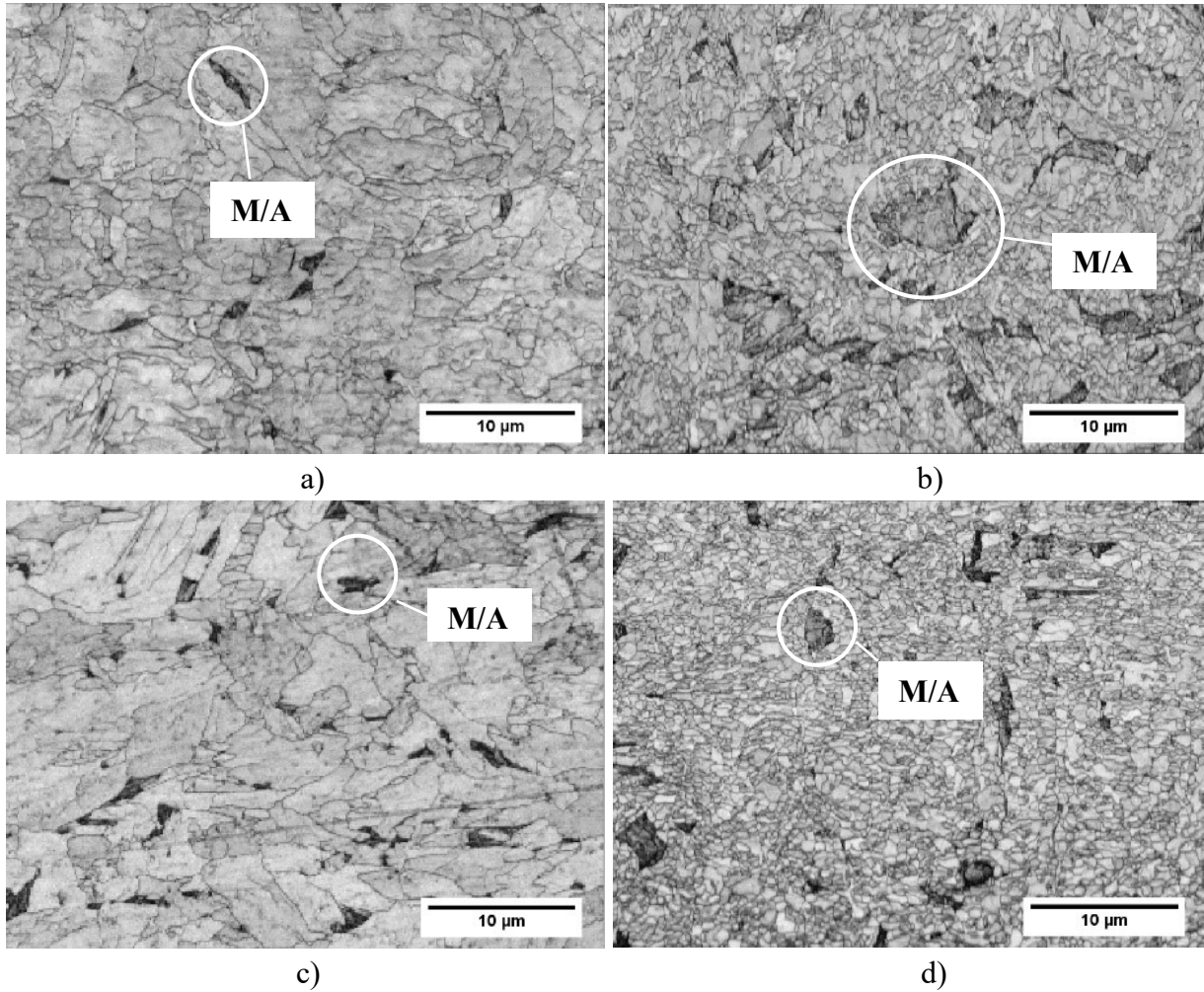
Fig. 4.4 Image quality map of 3F-Coiled at a) surface, c) centerline and 3F-Water quenched at b) surface, d) centerline by EBSD.

Table 4-1 tabulates lower fraction of M/A presented in 3E-Coiled (1.26-2.08%) than in 3E-Air cooled (2.91-5.29%), which might be caused by austenite decomposition in the former during coiling as well as more austenite transformed into martensite in the later due to higher cooling rate. Also, the volume fraction of M/A is higher in 3F-Coiled (3.35-6.91%) than in 3E-Coiled and 3E-Air cooled. This can be explained by the higher finish rolling temperature of 3F skelp (850°C) than 3E skelp (800°C), which facilitated carbon partitioning and segregation before bainite transformation.

Different explanations have been proposed for this phenomenon. Wang suggests that at lower finish rolling temperature, larger strain is accumulated in austenite during deformation, which increases the free energy of austenite and hence increases the critical carbon concentration C_0 (i.e., the carbon concentration lower than which no bainite transformation can occur). Consequently, the formation of bainite is enhanced, and the amount of residual austenite is reduced[174]. However, Liang believes that this is related to carbon diffusion in austenite before the bainite transformation. It is argued that after deformation, carbon atoms preferentially segregated at areas with high stored energy, such as PAG boundaries and some defects, leading to high local carbon concentration. As bainite transformation at these areas stops once carbon concentration exceeds C_0, the remaining untransformed austenite subsequently transforms into M/A constituents. Therefore, higher finish rolling temperature means more sufficient partition and segregation of carbon, and in turn gives rise to larger amount of M/A[175].

In all these three plates, martensite accounts for a small proportion of the M/A constituent, and hence, the dark areas (low IQ value) in EBSD BC map were used to estimate the volume fraction of M/A constituents. However, in 3F-Water quenched, a large proportion of remaining austenite transformed into martensite during water quench process with only a small amount of austenite retained at the edge of the martensite blocks. This can be confirmed by the EBSD Kernel Average Misorientation (KAM) maps of 3F-Water quenched samples (Fig.4.5c and Fig.4.6c), which clearly shows the high dislocation density in martensite blocks. As a result of the high proportion of martensite in M/A and the evidently different contrast of martensite and austenite in EBSD BC map, the evaluation results based on BC maps only represent the retained austenite (RA) part of M/A constituent in 3F-Water quenched samples, as seen in Fig.4.5b and Fig.4.6b. However, these M/A blocks can be measured on OM images of 2% Nital etched samples using imageJ

software (Fig.4.7 and Fig 4.8). And by the following equation, the volume fractions of martensite in 3F-Water quenched samples can be obtained.

$$f_m = f_{M/A} - f_{RA} \tag{4-1}$$

Wherein $f_m, f_{M/A}$ and f_{RA} are volume fraction of martensite, M/A and RA, respectively. $f_{M/A}$ and f_{RA} were obtained from OM image and EBSD BC map, respectively.

a)

b) RA

c)
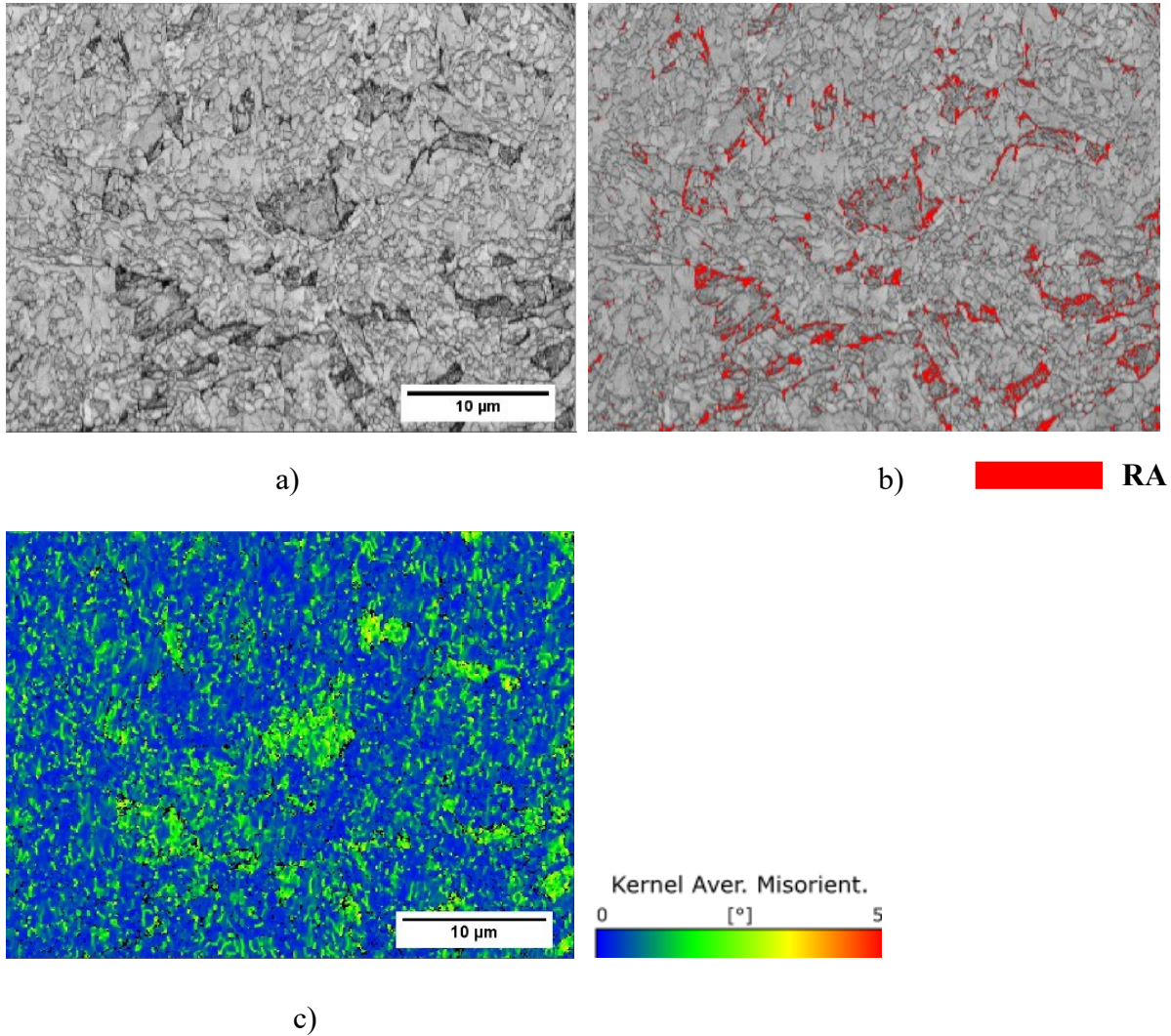
Fig. 4.5 M/A constituents of 3F-Water quenched-Surface in EBSD maps. a) BC map; b) Estimation of RA volume fraction; c)KAM map.

a)   b)   ████ **RA**

Kernel Aver. Misorient.

0   [°]   5
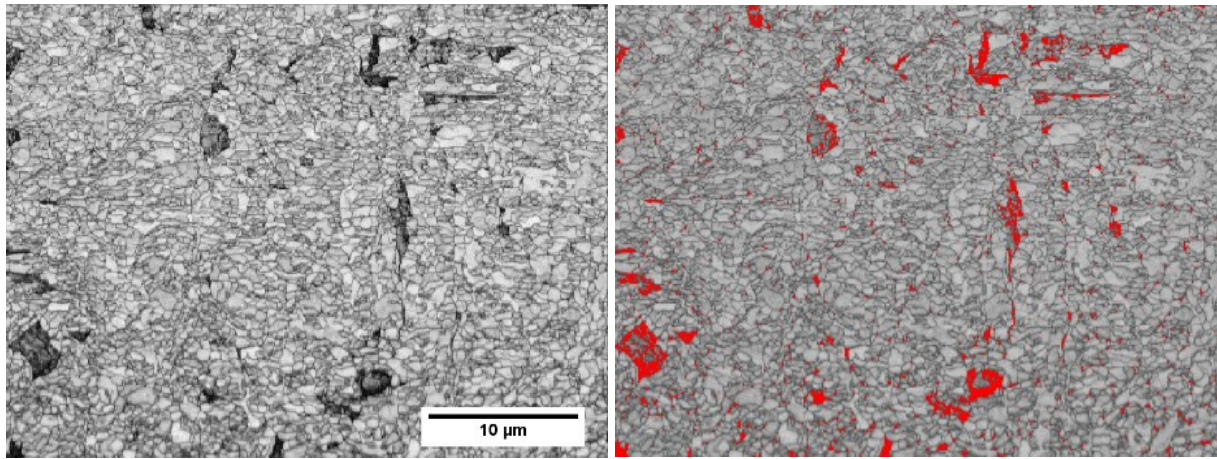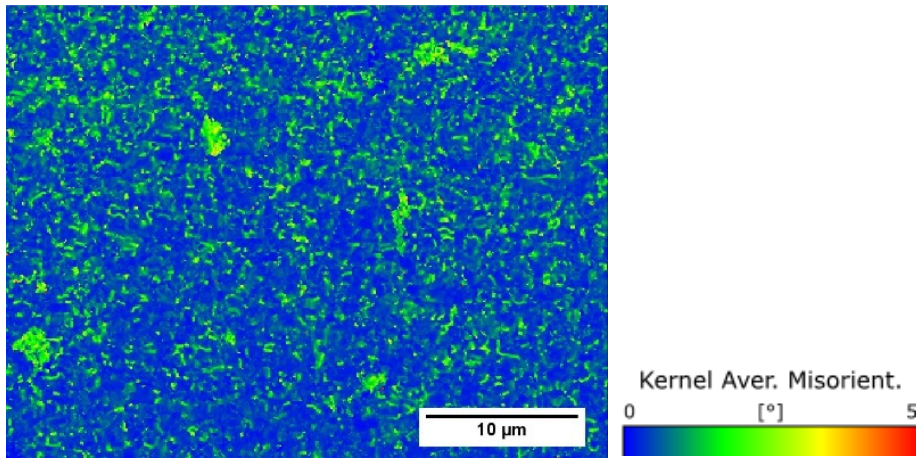
c)

Fig. 4.6 M/A constituents of 3F-Water quenched-Centerline in EBSD maps. a) BC map; b) Estimation of RA volume fraction; c)KAM map
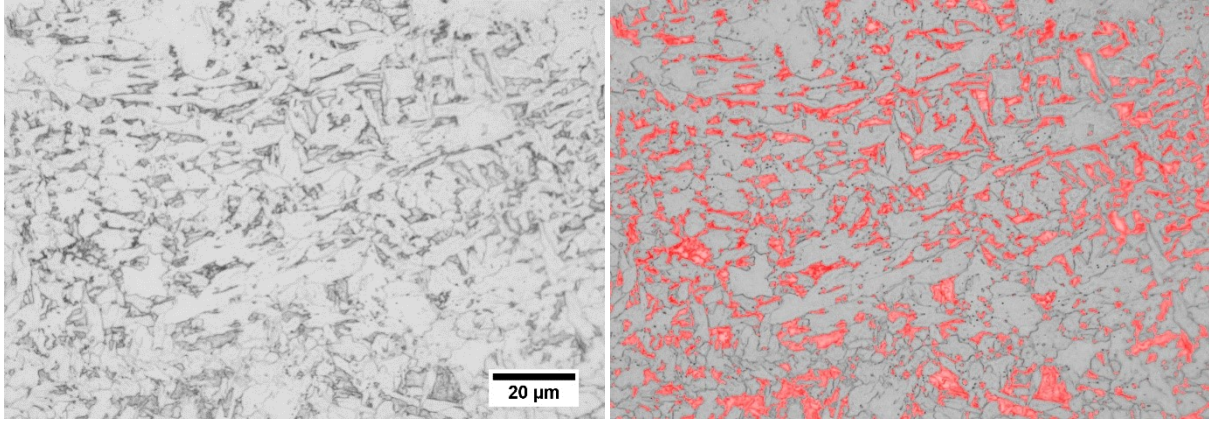
a)　　　　　　　　　　　　　　b) ▬ **M/A**

Fig. 4.7 M/A constituents of 3F-Water quenched-Surface in OM image (2% Nital etched).a) OM image; b) processed OM image showing measured M/A constituents in red.
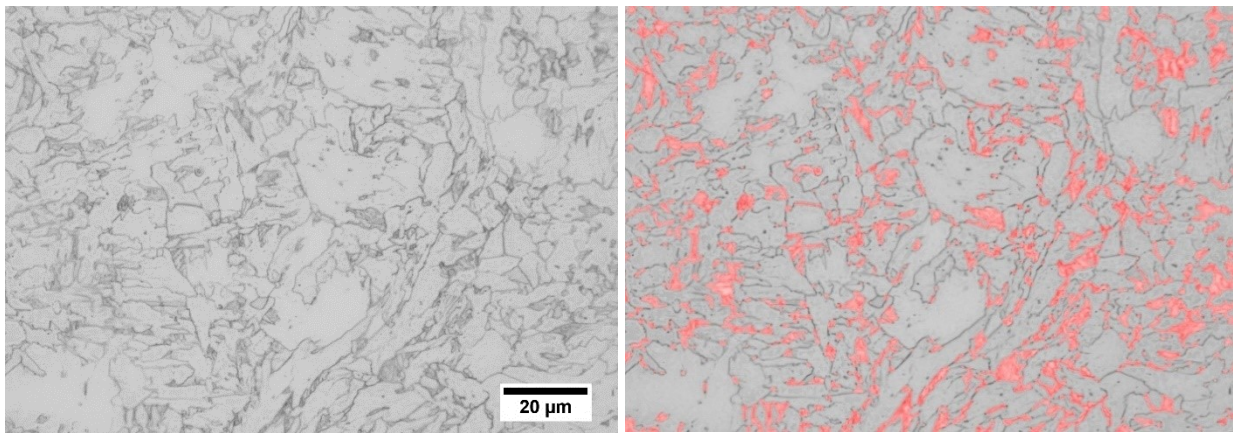
a)　　　　　　　　　　　　　　b) ▬ **M/A**

Fig. 4.8 M/A constituents of 3F-Water quenched-Centerline in OM image (2% Nital etched). a) OM image; b) processed OM image showing measured M/A constituents in red.

Table 4-1 Area fractions of phases obtained via BC map and OM image (%)

Plate	Location	Ferrite	Bainite	M/A	
3E-Coiled	Surface	58.2	39.2	1.3	
	¼ distance	49.2	49.1	1.6	
	Centerline	41.1	55.3	2.1	
3E-Air cooled	Surface	51.8	45.3	2.9	
	¼ distance	39.1	57.1	3.6	
	Centerline	47.4	47.3	5.3	
3F-Coiled	Surface	62.5	33.9	3.4	
	Centerline	66.9	26.7	6.2	
3F-Water quenched				Martensite	RA
	Surface	41.9	36.8	17.9	3.3
	Centerline	33.6	49.5	12.8	3.8

The amount of M/A constituents in 3E-Coiled is extremely small, as it is shown in Fig.4.3a,c,e and in Table 4.1. To further confirm the estimates of M/A constituents based on BC maps, Lepera etchant was applied to polished 3E-Coiled samples in order to reveal the M/A constituents under OM. The OM images processed by software imageJ (Fig.4.9) clearly show that the amount of M/A constituents increases from surface to centerline (measured area are coloured in red). The measured data based on five images for each sample are listed in Table 4-2. The values in Table 4-2 are slightly smaller than the corresponding results based on BC maps (Table 4-1), which might be due to poor surface condition of etched samples and low resolution of OM as compared with EBSD technique. Nevertheless, these data confirmed that the estimates of volume fraction of M/A in 3E-Coiled samples based on BC maps are reasonable.
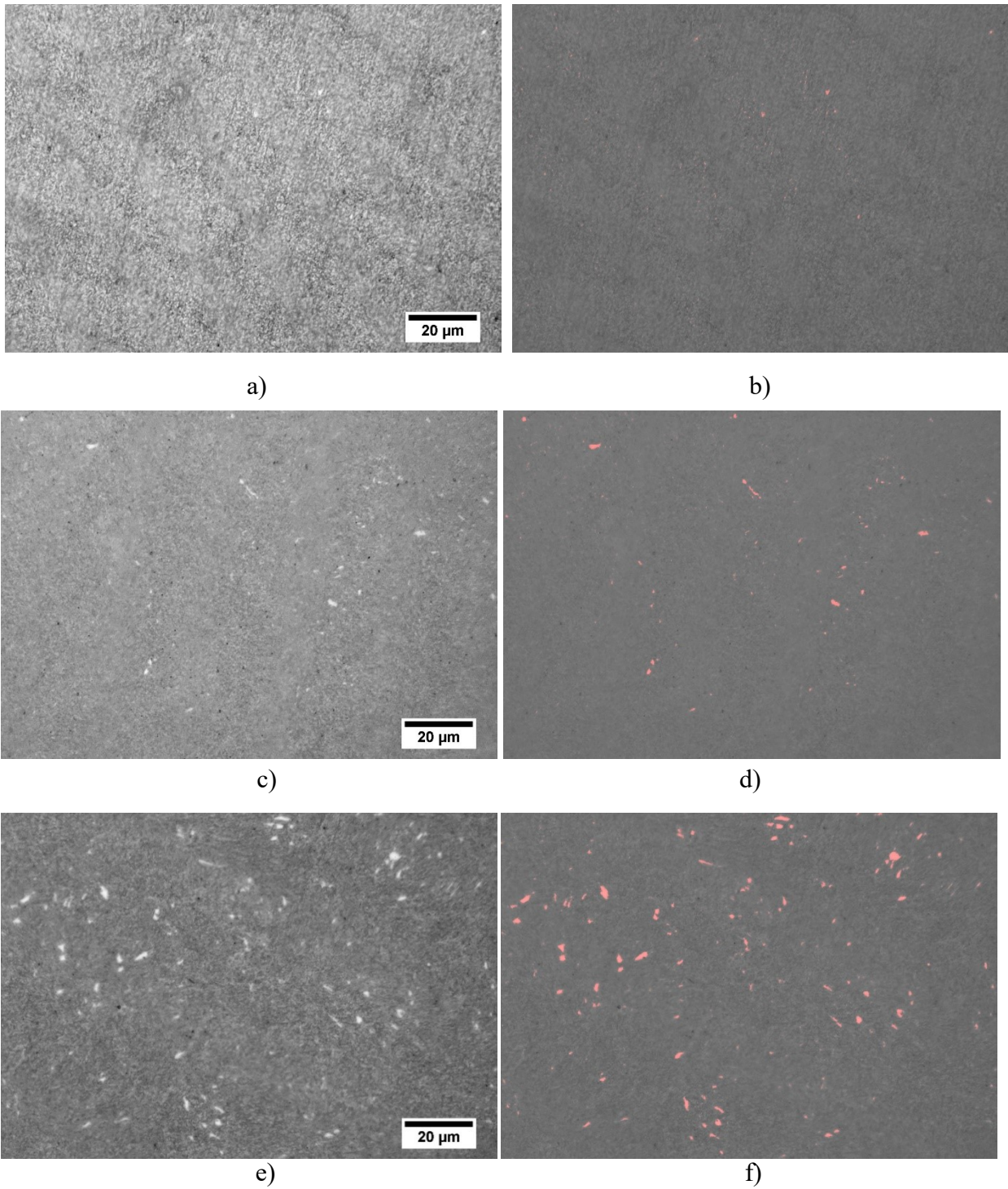
Fig. 4.9 OM images of M/A constituents at different locations of 3E-Coiled (Lepera etched).

a,b) surface; c,d) ¼ distance; e,f) centerline. Colored images have been processed to show the measured area.

Table 4-2 Area fraction of M/A constituents in 3E-Coiled at different locations based on OM images (Lepera etched) (%).

No. of image	Surface	¼ distance	Centerline
1	0.14	0.68	1.30
2	0.16	0.50	1.05
3	0.14	0.60	2.33
4	0.21	0.70	1.20
5	0.12	0.50	1.04
Average	0.16	0.59	1.38

In all four plates, area fraction of M/A (or RA for 3F-WQ) increases through thickness from surface to centerline region, as shown in Fig.4.10. A previous work shows centerline segregation of Mn in X70 pipeline steel[176]. As an austenite stabilizer, the enrichment of Mn can lower the temperature at which austenite begins to decompose and favors the formation of martensite. Therefore, the variation in volume fraction of M/A constituents at different locations of the plate might be caused by the macro segregation of microalloying elements such as Mn.
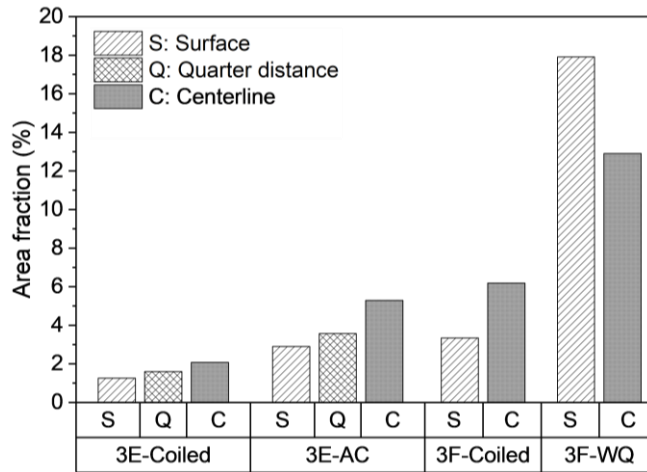
Fig. 4.10 Area fraction of M/A of Group I plates at different locations.

4.1.3 M/A constituents

The inverse pole figure (IPF)+grain boundaries (GB) maps in Fig.4.10a-b) show that M/A constituents are formed distributing along the grain boundaries/sub-grain boundaries or at the triple

junctions of grain boundaries/sub-grain boundaries. Fig.4.11c shows detailed information about the labeled area in Fig.4.11b, indicating that M/A constituents contain high angle grain boundaries (HAGBs), high density of dislocations and complex carbides (unindexed points). Moreover, Fig.4.11d indicates higher fraction of misorientation >50 deg at centerline and higher fraction of misorientation <15 deg near surface in 3F-Coiled. As it is shown in Table 4.1, the volume fraction of M/A in 3F-Coiled at centerline region (6.19%) is higher than that near surface (3.35%), whereas bainite shows the opposite trend (about 33.9% at surface and about 26.7% at centerline). Therefore, it is indicated that the abundance of M/A constituents in centerline contributes to the higher fraction of high angle grain boundaries (HAGBs), and bainite contains more low angle grain boundaries (LAGBs) than the other phases.

a)   b)

c)   d)
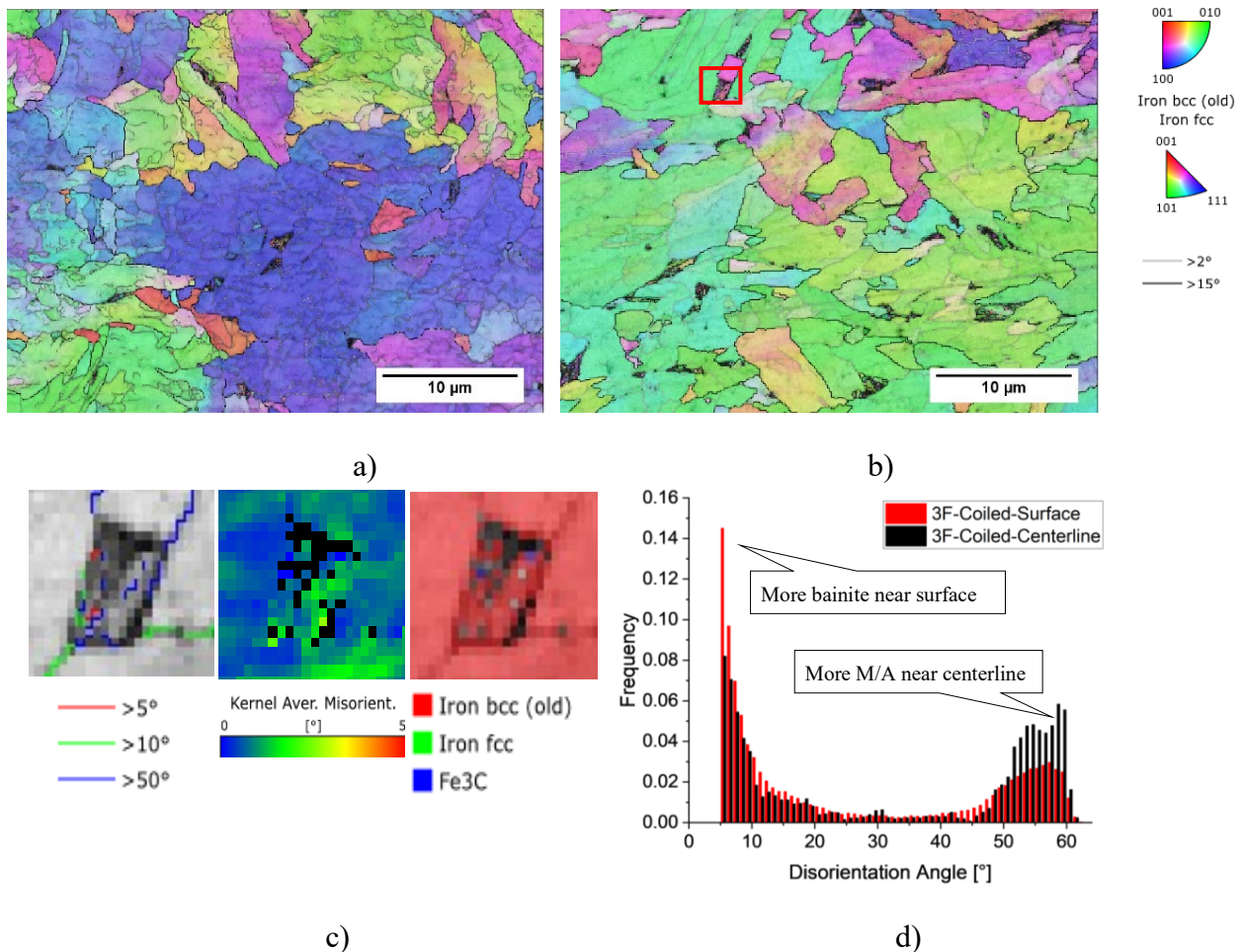
Fig. 4.11 EBSD maps of M/A constituents in 3F-Coiled-Surface/Centerline. a,b) IPF + GB map of 3F-Coiled-Surface/Centerline; c) GB + BC map, KAM map, phase map of M/A island in labeled area in b);d) misorientation distribution

4.1.4 Grain boundaries

Grain size of Group I plates at surface, centerline and/or quarter distance were measured by EBSD with misorientation ≥ 15 defined as grain boundaries. As it is shown Fig. 4.12, the grain size distributions of all samples are similar at all three dislocations. The results were fitted to lognormal equations presented in section 3, and the statistical parameters of the fitted curves are listed in Table 4.3, which further confirm the similarity of grain size in Group I samples. The fitted grain size distribution curves of individual samples are provided in Appendix B-3.

a)   b)

c)
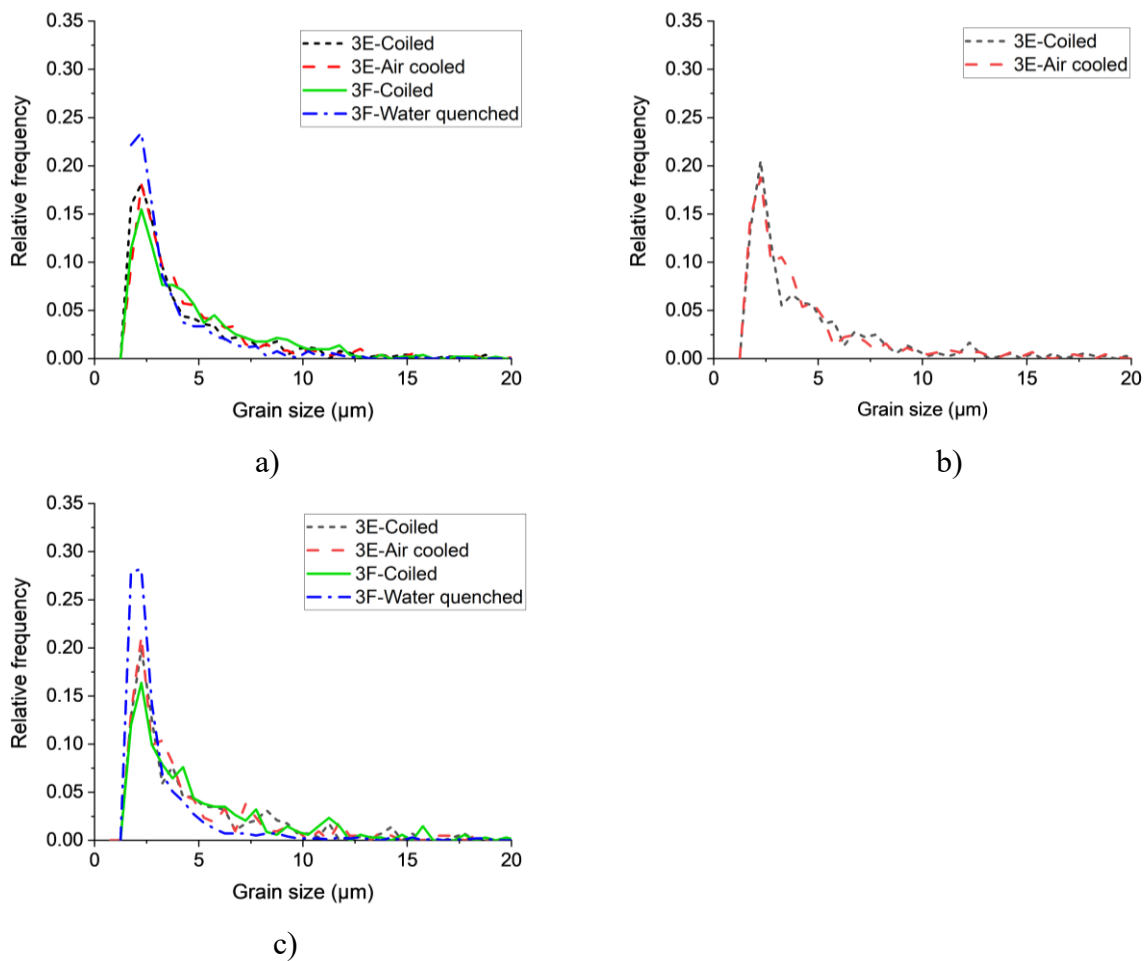
Fig. 4.12 Grain size distribution of Group I samples at surface a), quarter distance b), and centerline c).

Table 4-3 shows the mean, mode, median and standard deviation of the fitted lognormal curve of grain size distributions. By comparing the medians of grain size distribution, we can find that median grain size in 3E-Coiled and 3E-Air cooled are similar (about 2.5-3.0 μm) whereas the median value for 3F-Coiled is slightly larger (3.22 μm and 3.07 μm for surface and centerline respectively) and for 3F-Water quenched is smaller (2.23 μm and 2.17 μm for surface and centerline respectively). For all plates, grain size decreases slightly through thickness from surface to centerline, which might be caused by the macro segregation of microalloying elements such as Nb, Ti, V in centerline region. These elements can improve grain size refinement by retarding recrystallization when they are in solid solution and by pinning effect in form of precipitates. According to Lee's research[177], the contribution of hydrogen trapped at grain boundaries to HE phenomenon decreased to a negligible level as the grain size is smaller than 10 μm.

Table 4-3 Parameters of lognormal fitting curves of grain size distribution for Group I plates.

Plate no.	Location	Mode (μm)	Mean (μm)	Median (μm)	Standard Deviation (μm)
3E-Coiled	surface	2.29	2.75	2.59	0.35
	1/4 distance	2.25	2.62	2.49	0.32
	centerline	2.28	2.68	2.54	0.33
3E-Air cooled	surface	2.54	3.26	3.00	0.41
	1/4 distance	2.38	3.05	2.64	0.32
	centerline	2.32	2.81	2.64	0.36
3F-Coiled	surface	2.53	3.16	3.22	0.49
	centerline	2.44	3.44	3.07	0.48
3F-Water quenched	surface	1.70	2.55	2.23	0.52
	centerline	2.05	2.23	2.17	0.24

4.1.5 Summary

The results of microstructure analysis of Group I plates are summarized as follows:

1) The microstructure of plates in Group I consist of IF, AF/GB and M/A constituents.

2) In 3E-Coiled, 3E-Air cooled and 3F-Coiled, the area fraction of M/A constituents increases through thickness from surface to centerline.

3) In 3F-Water quenched, M/A constituents consist of large martensite blocks and small amounts of RA on the edge, which is different from the M/A in the other three plates.

4) In 3F-Water quenched, although the total area fraction of M/A is lower at surface than at centerline, the fraction of RA slightly increased from the former to the latter.

5) EBSD results indicate that M/A constituents contain HAGBs, high density of dislocations and complex carbides.

6) The grain size distributions of the four plates are similar with the mean values ranging from 2.23 µm to 3.34 µm.

4.2 *Non-metallic inclusion analysis*

Non-metallic inclusions (NMIs) play an important role in hydrogen permeation process as irreversible traps and may have significant influence on hydrogen-induced cracking of pipeline steel[43, 121, 160]. NMIs were characterized based on morphology and chemistry (EDX/SEM), In addition, the area fraction size distribution and count density were determined from OM images. Although the four Group I plates have been through different TMCP process, all these plates were produced from the same casting. Therefore, the types of non-metal inclusions of all Group I plates should be the same, as well as the chemistry of the NMIs. As a result, only 3E-Coiled sample is used for chemistry analysis via SEM/EDS. In addition, since 3E plates (3E-Coiled and 3E-Air cooled) and 3F plates (3F-Coiled and 3F-Water quenched) have been through different hot rolling processes, which might have influence on the size and distribution of NMIs, 3E-Coiled and 3F-Coiled were investigated to quantitatively assess the inclusions in 3E and 3F plates, based on the assumption that no further changes of NMIs occur after runout table.

4.2.1 *Morphology and composition of non-metallic inclusions*

SEM images of selected NMIs in 3E-C are shown in Fig. 4.13. It is observed that most of the inclusions are globular or faceted in shape with size < 20 µm. In addition, EDX spectrum for each inclusion are included. The composition of these inclusions mainly consists of Al, S, Ca, O, Si and Mg, indicating they are mostly complex oxides, e.g., $CaO \cdot Al_2O_3$, $MgO \cdot Al_2O_3$, MnO, SiO or sulfides, e.g., CaS. According to reference [178, 179], these inclusions, falling into the category of indigenous inclusions, are deoxidation products that originate from the reaction between dissolved oxygen and added deoxidants, such as, Al, Ca and Si. The NMIs in the investigated steel are mostly complex oxides, e.g., $CaO \cdot Al_2O_3$, $MgO \cdot Al_2O_3$, MnO, SiO or sulfides, e.g., CaS. And the observed morphology of inclusions, i.e., globular and faceted, reflects the composition, where the former consists of simple sulfide/oxysulfide (Fig.4.13b) and the latter is heavily deoxidized with aluminum (Fig.4.13c)[180]. These inclusions are formed during converter and ladle treatment processes of continuous casting of the steel[181].
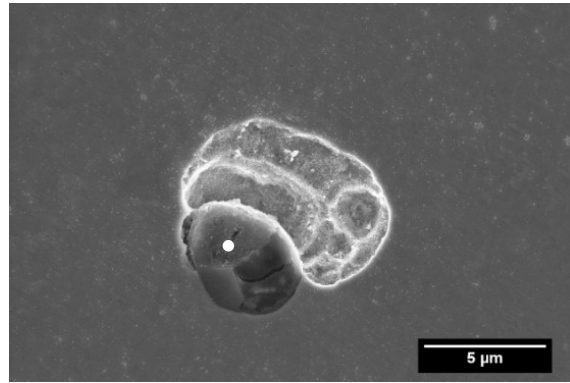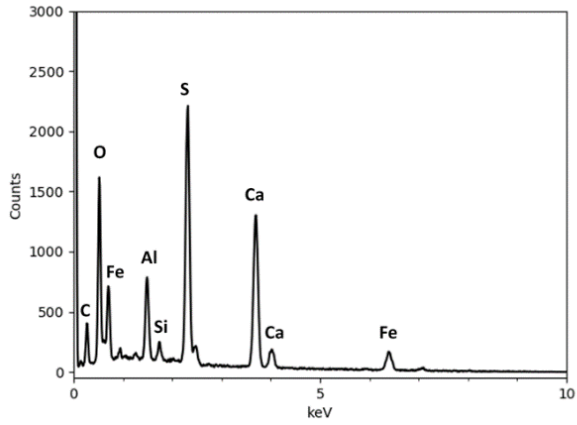
a)
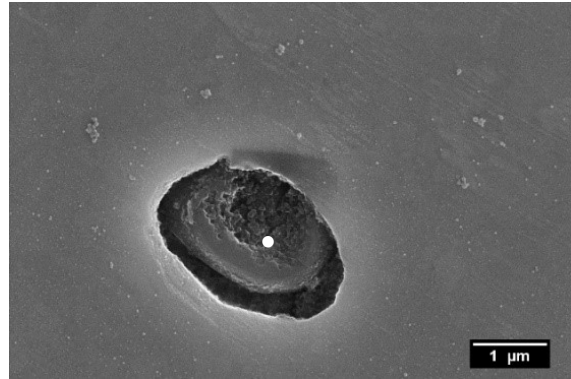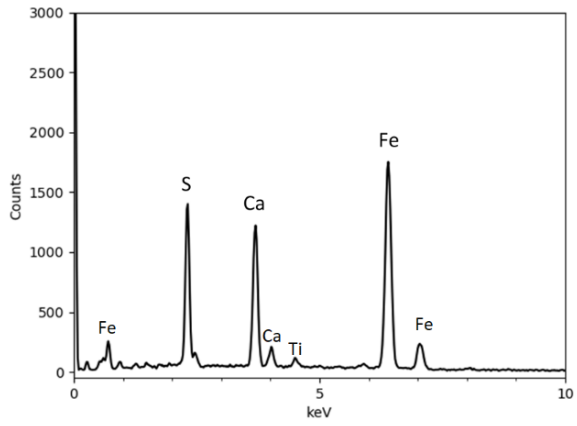
b)
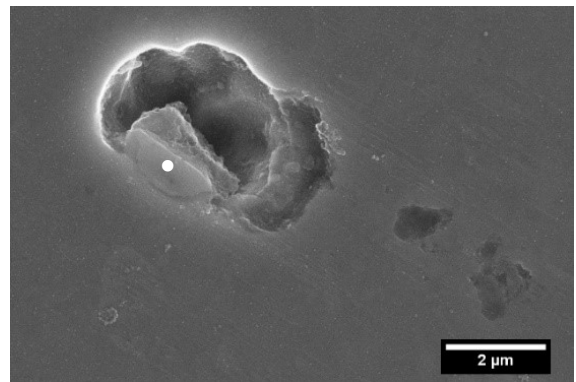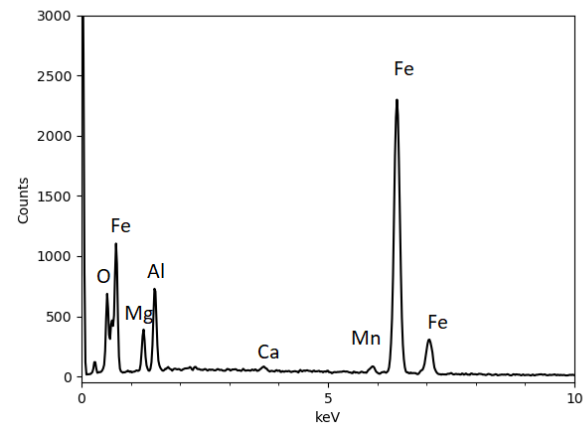
c)
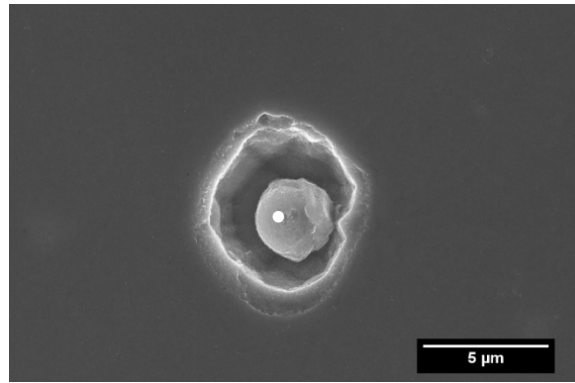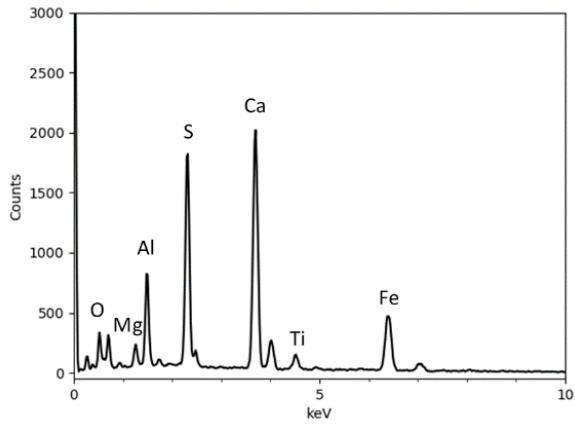
d)
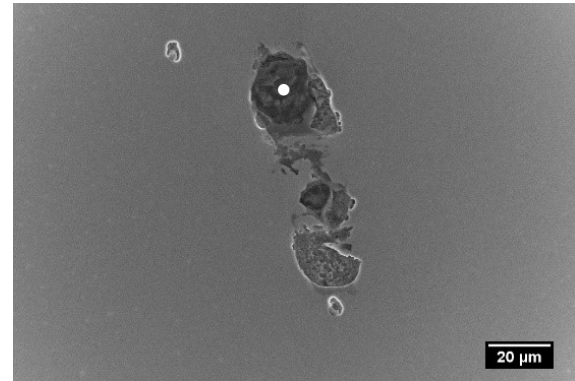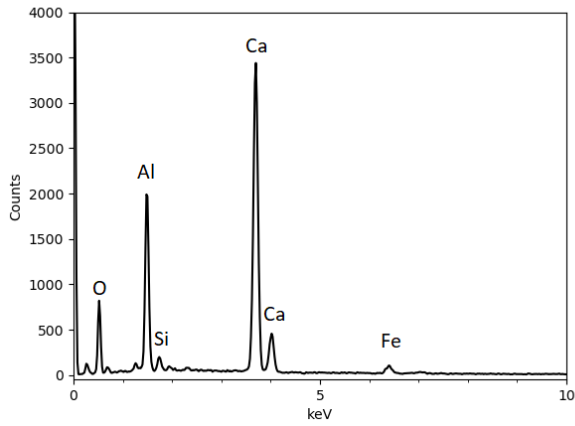
e)
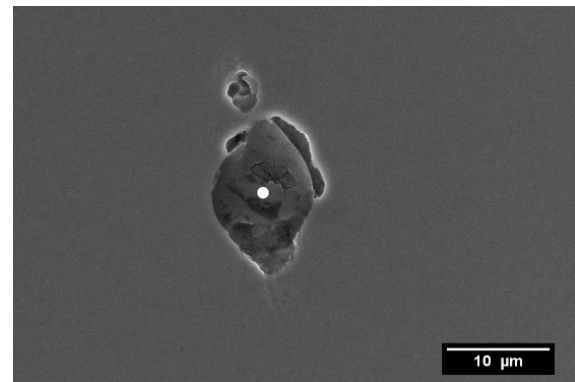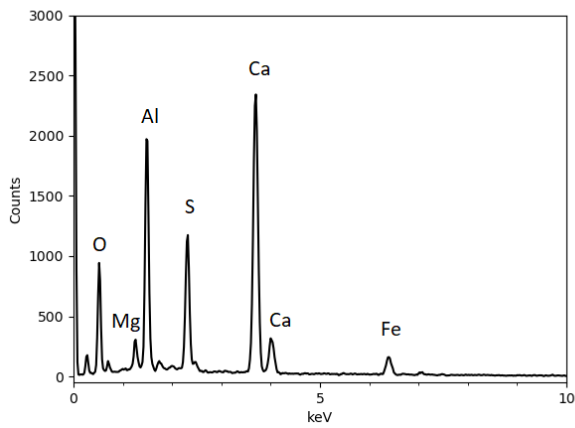
f)
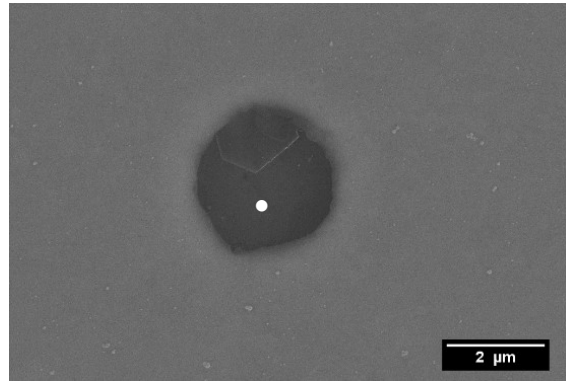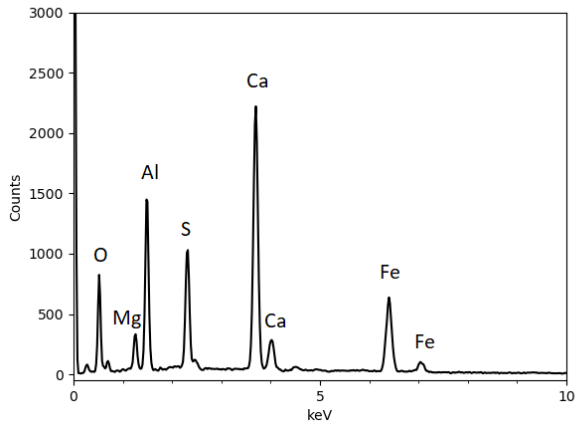
g)
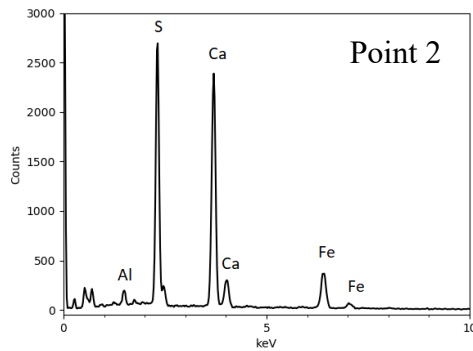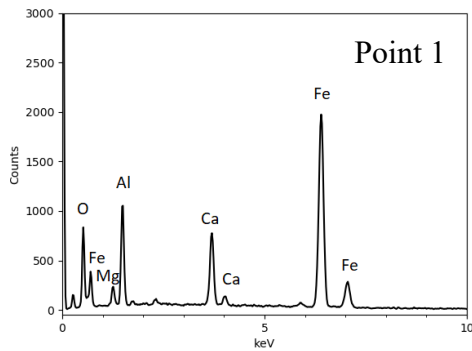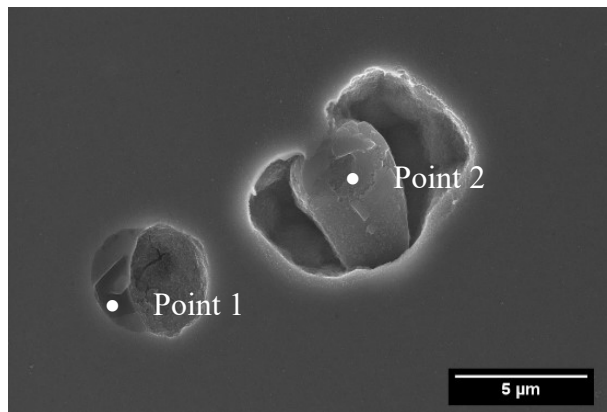
h)

Fig. 4.13 Morphology and composition of inclusions by SEM/EDS.

4.2.2   Quantitative assessment of non-metallic inclusions

3E-Coiled and 3F-Coiled plates are adopted to quantitatively study the NMIs in skelps 3E (surface, ¼ distance and centerline) and 3F (surface and centerline), respectively. Area fraction, size distribution and count density of NMIs in each sample were measured based on ten (10) OM images. These OM images of inclusions in 3E-Coiled and 3F-Coiled at various locations were processed by software imageJ and used for quantitative analysis. Statistically analyzed data of the inclusions are shown in Fig.4.14 and Table 4-4.

For both 3E and 3F, the area fraction and count density of NMIs at centerline are significantly higher than those of other locations indicating the existence of centerline segregation. As it is reported[179], NMIs tend to agglomerate in centerline region mainly due to the fact that it is the last portion of the slab to solidify during casting. As the slab solidify from the outer surfaces, inclusions are pushed inward and trapped in the centerline region. This is especially true for inclusions with lower melting point, such as sulfide, which remains in liquid portion until the solidification process is completed. Also, increased number of large inclusions were found in centerline region in both skelps leading to the size distribution shifting to larger size with higher mean values, although the trend is more obvious in 3E than in 3F.

Comparing the NMIs in 3E and 3F, the area fraction of inclusions at surface and at centerline in 3F are quite close to those in 3E. Nevertheless, the count density of the former is considerably higher than that of the latter. This means that the inclusions in 3F are finer than those in 3E, as it is also shown by the mean value of size distribution.

4.2.3   Summary

The analysis results of inclusions in 3E and 3F are summarized as follows:

1)   EDS results show that the NMIs in the investigated steel are mainly complex oxides such as $CaO•Al_2O_3$, $MgO•Al_2O_3$, MnO, SiO, and sulfide, such as CaS.

2) Significantly higher area fraction and count density of NMIs at centerline than those of other locations indicates the existence of centerline segregation that formed during solidification.

3) NMIs in 3F are finer than those in 3E since the area fractions of the plates are similar at the same location while the count density is much higher in the former than in the latter, which is also confirmed by the mean of the size distribution.

Table 4-4 Statistical analysis results of area fraction and size distribution of NMIs in 3E-Coiled.

			Surface	¼ distance	Centerline
Area fraction %	3E	Mean	4.1	5.4	15.2
		STD	0.6	0.5	2.0
	3F	Mean	5.7	/	14.1
		STD	0.9	/	1.2
Inclusion size (diameter) μm	3E	Mean	2.3	2.27	3.5
		STD	1.4	1.45	2.4
	3F	Mean	2.2	/	2.5
		STD	1.1	/	1.3
Count density count/ mm^2	3E	Mean	73.1	96.5	110.8
		STD	14.4	17.5	26.3
	3F	Mean	119.6	/	224.0
		STD	21.2	/	30.2
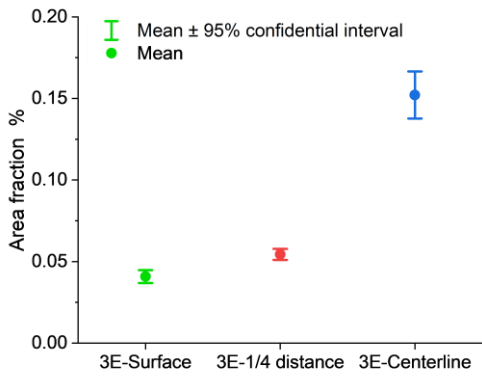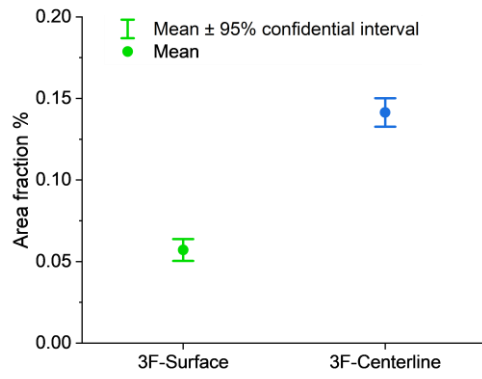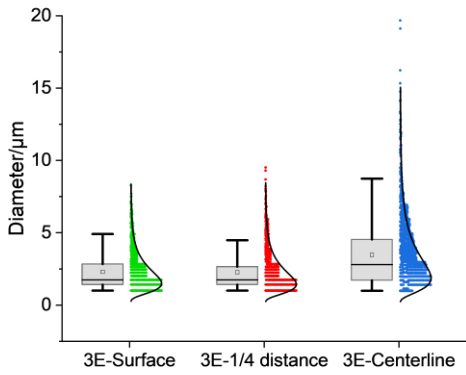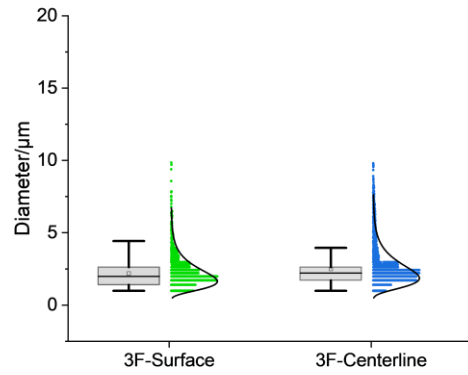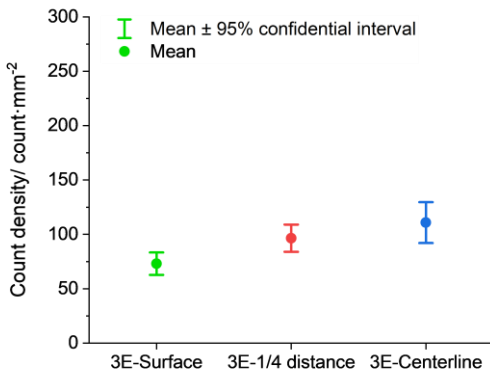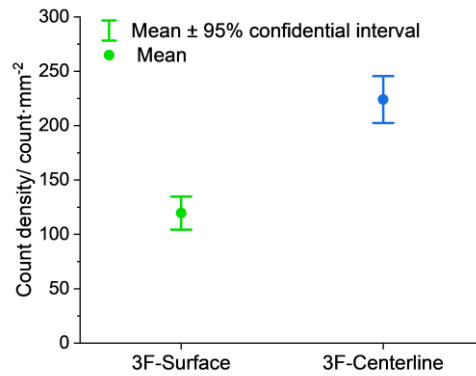
Fig. 4.14 Area fraction (a,b), size distribution(c,d) and count density(e,f) of non-metallic inclusions at different locations of 3E and 3F.

4.3   Precipitate analysis

In pipeline steel, precipitates not only improve mechanical properties of the steel but also might have an interaction with hydrogen when exposed to hydrogen resources. In this section, precipitates in Group I plates are extracted by carbon replica extraction technique and studied via TEM/EDS. Different types of precipitates are found and analyzed with a special focus on fine NbC precipitates (< 20 nm) as they are the main contributor to hydrogen trapping. The composition of these precipitates is confirmed by measuring the lattice distance on high resolution STEM (HR-STEM) images as it is hard for the application of EDS mapping due to their small size. And the size distribution of these fine precipitates in four Group I plates are measured and analyzed based on 15 STEM images for each sample at the magnification of 1M. Composition and morphology of large precipitates (>20 nm) are characterized by EDS and TEM, respectively.

4.3.1   Types of precipitates

Four types of precipitates were observed in all four plates as it is shown in Fig. 4.15, including irregular Ti (C, N) $_x$ (~100nm) formed during solidification process (Fig.4.15a), cuboidal TiN with NbC nucleated on which are formed during rough rolling process (Fig.4.15b), large NbC (>20 nm) formed during finish rolling process (Fig.4.15c) and nano-size NbC (<20 nm) (Fig.4.15d).

4.3.2   Nano-sized precipitates

For each Group I plate, nano-sized precipitates on 14 STEM (bright field, 1M×) images are measured and counted. The morphology and size distribution of the precipitates in the four plates (all surface samples) are shown in Fig.4.16. To evaluate the size distribution of these precipitates, a normalized value N(D) is introduced which is defined by equation (4-2).

$$N(D) = N_0 \left(\frac{1}{\alpha \cdot D \cdot \sqrt{2 \cdot \pi}} \; exp \left[-\frac{1}{2} \left(\frac{ln(D/D_0)}{\alpha} \right)^2 \right] \right) \tag{4-2}$$

Where N_0 is the total number of precipitates in the distribution, D_0 is the precipitate diameter at the maximum of distribution, and α is a fitting parameter related to the width of the distribution via the relationship

$$\alpha = \frac{\beta}{D_0} \qquad\qquad (4\text{-}3)$$

wherein β is the width of the distribution.
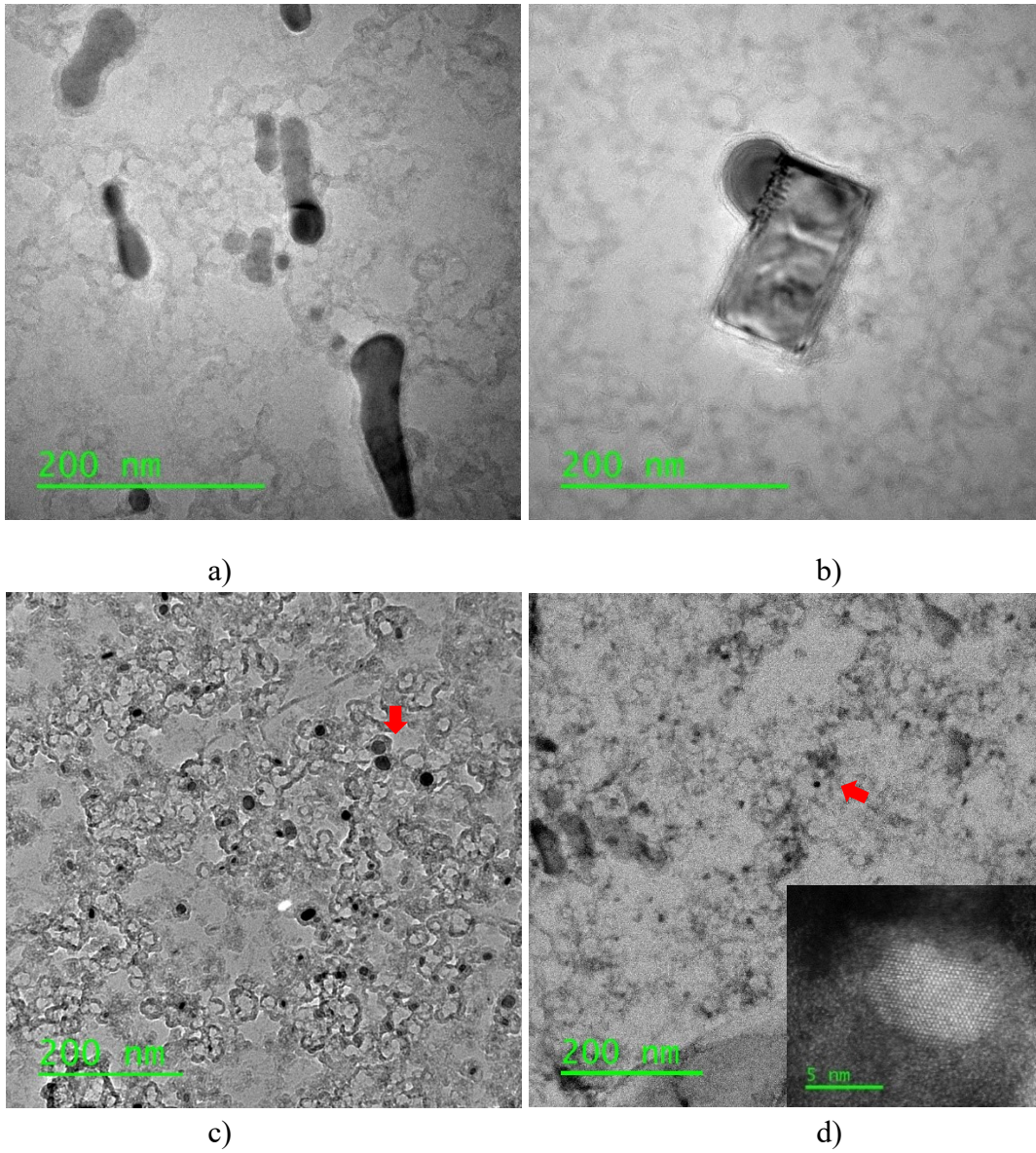
Fig. 4.15 TEM images of four types of precipitates in 3E-Coiled-Surface.

From D_0 and α, the standard deviation of the precipitate size distribution, σ, and the mean value of the diameter, D_m, can be derived according to equations (4-4) and (4-5), respectively.

$$\sigma^2 = D_0^2\, exp(\alpha^2)\, [exp\,(\alpha^2) - 1] \qquad (4\text{-}4)$$

$$D_m = D_0 exp\left(\frac{\alpha^2}{2}\right) \qquad (4\text{-}5)$$

By means of peak fitting function in Origin software, the distribution curves are fitted with the equations (4-2) and (4-3), and the values of N_0 , D_0, α, D_m and σ are listed in Table 4-5. Nano-sized precipitates in 3E-Air cooled and 3F-Water quenched are mainly formed during laminar cooling with a unimodal log-normal size distribution (Fig.4.16d and Fig.4.16h). However, for 3E-Coiled and 3F-Coiled, bimodal distribution calculations show a reasonably good fit with the measured data (Fig.4.16b,f) indicating that the precipitates are formed during two TMCP processes, i.e., laminar cooling and coiling, corresponding to peak 1 and peak 2 of the fitting size distribution. The dual distribution characteristics of the precipitates caused by precipitation at two different temperatures during TMCP was also discovered by Nayak[182] and Wiskel[183].

For both 3E and 3F skelps, D_0 of the non-coiled samples (3E-Air cooled and 3F-Water quenched) are smaller than the $D_{0,1}$ but larger than $D_{0,2}$ of the corresponding coiled sample (3E-Coiled and 3F-Coiled), as shown in Fig.4.17a (herein $D_{0,1}$ and $D_{0,2}$ represent D_0 of peak 1 and peak 2, respectively). This indicates that precipitates formed during laminar cooling coarsened during coiling, and precipitates formed during coiling are finer than those formed during laminar cooling due to lower precipitation temperature. It is also shown in Fig. 4.17 that D_0 value of the precipitates formed during laminar cooling is increased as the cooling rate after laminar cooling decreases. For example, D_0 of 3E-Air cooled is larger than D_0 of 3F-Water quenched, and $D_{0,1}$ of 3E-Coiled is larger than $D_{0,1}$ of 3F-Coiled. (Note: 3E is thicker than 3F, and hence the cooling rate of the former should be lower than the later during simulated coiling, i.e., furnace cooling).

Comparing the two coiled samples, significantly larger amount of peak 2 precipitates (finer precipitates) is found in 3E-Coiled than in 3F-Coiled, as seen in Fig.4.17b. This considerable disparity in nucleation rate of the strain-induced precipitation during coiling may result from the difference in crystal defects density in 3E and 3F, since 3E has been through more hot rolling passes (10 rough rolling + 8 finish rolling) than 3F (7 rough rolling + 7 finish rolling). Generated

during hot rolling process, these crystal defects, such as dislocations and subgrain boundaries, act as nucleation sites of these nano-sized precipitates during coiling.
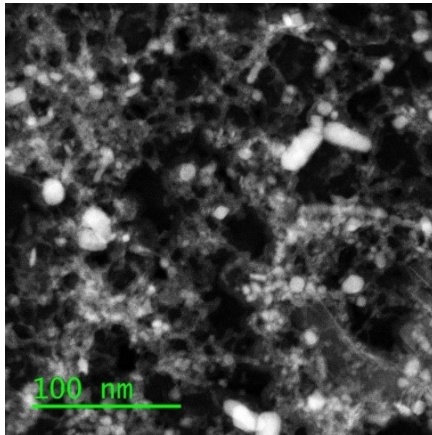
a)
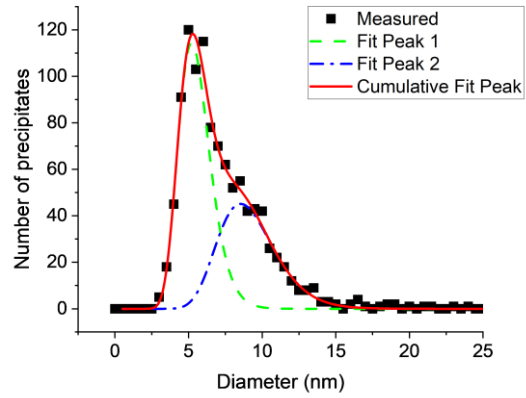
b)
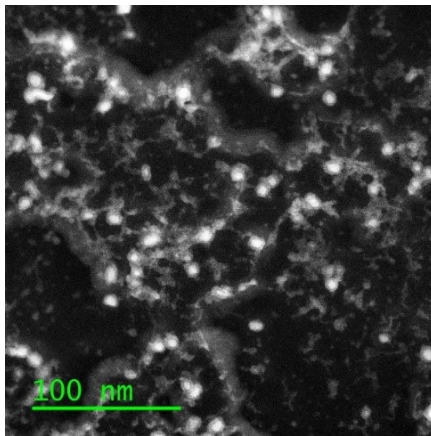
c)
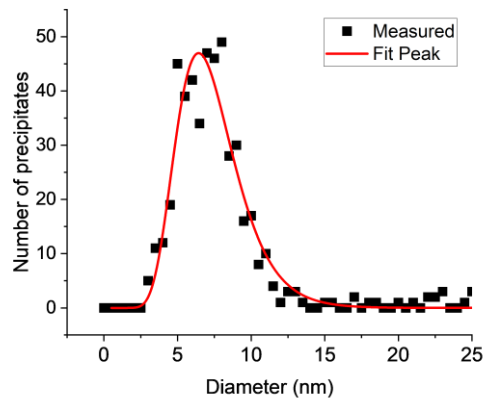
d)
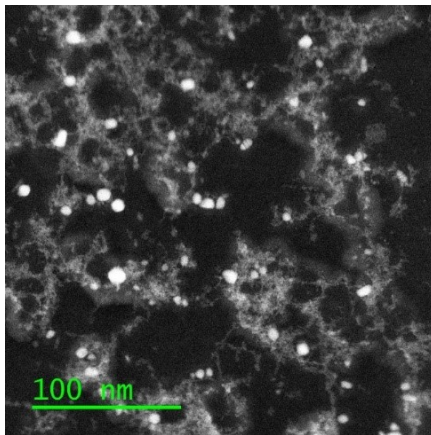
e)
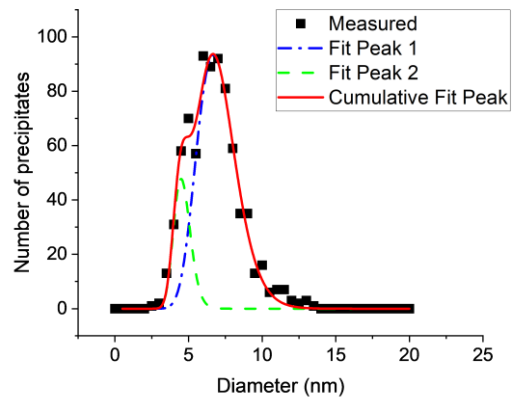
f)
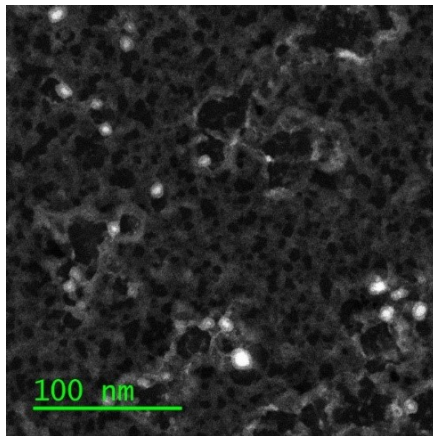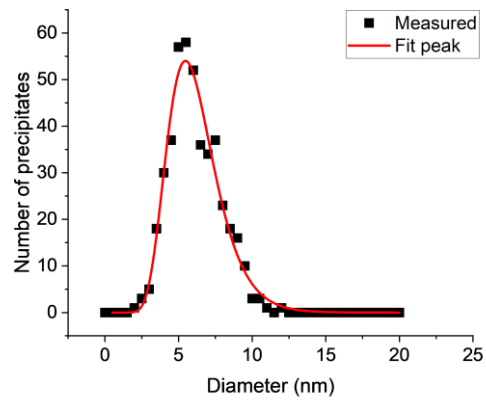
g)   h)

Fig. 4.16 STEM image and size distribution of nano-size precipitates at the surface region of

3E-Coiled (a,b), 3E-Air cooled (c,d), 3F-Coiled (e,f) and 3F-Water quenched (g,h).

Table 4-5 Distribution data of precipitates size in Group I plates (near surface) obtained by curve fitting with equations (4-2) and (4-3).

Sample		N_0	D_0/nm	α/nm	D_m/nm	σ/nm
3E-Coiled	Peak 1	218	9.0	0.2	9.2	2.0
	Peak 2	309	5.4	0.2	5.5	1.1
3E-Air cooled		240	7.1	0.3	7.4	2.3
3F-Coiled	Peak 1	283	7.0	0.2	7.1	1.4
	Peak 2	59	4.6	0.1	4.6	0.5
3F-Water quenched		223	6.0	0.3	6.2	1.8
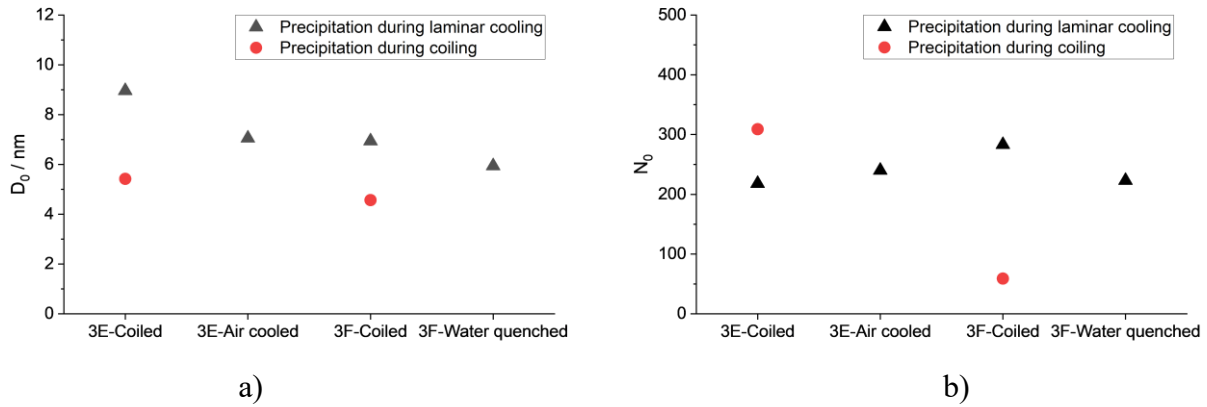
Fig. 4.17 D_0 a) and N_0 b) of the size distribution of nano-sized precipitates in Group I plates.

Based on STEM images of precipitates in Group I samples, count density of nano-sized precipitates is measured manually and statistically illustrated in Fig.4.18. It is shown that more nano-sized precipitates are generated in coiled samples than in non-coiled samples, and that 3E plates contain more of these precipitates than 3F plates. As discussed above, precipitation during coiling is the main cause of the difference in total count density of nano-sized precipitates between coiled and non-coiled samples. The statistical data for Fig. 4.18 are listed in Appendix B-5.
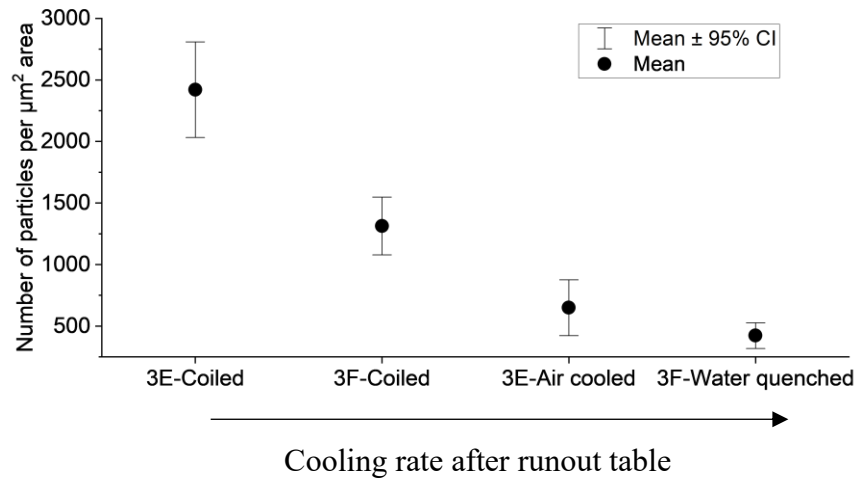
Fig. 4.18 Count density of nano-sized precipitates in Group I samples (near surface region).

In addition, the nano-sized precipitates in 3E-Coiled at centerline region were investigated and analyzed in the same way. As it is shown in Fig. 4.19 and Table 4-6, nano-sized precipitates

at centerline show unimodal size distribution with a D_0 of 6.31nm, which is between the D_0 values of the two peaks at surface region (i.e., 9.03 nm and 5.46 nm). This indicates that all the nano-sized precipitates at centerline are formed during one process, i.e., laminar cooling, which is also when peak 1 precipitates of the surface sample are formed, however, the growth rate of the precipitates at centerline is lower than that of the precipitates near the surface. And no finer precipitates were formed during coiling at centerline. Moreover, the count density of nano-sized precipitates at centerline of 3E-Coiled is considerably lower than that at the surface, as shown in Fig. 4.20. The distinct precipitation behavior at centerline might be associated with other precipitation event and will be discussed in section 4.3.3.
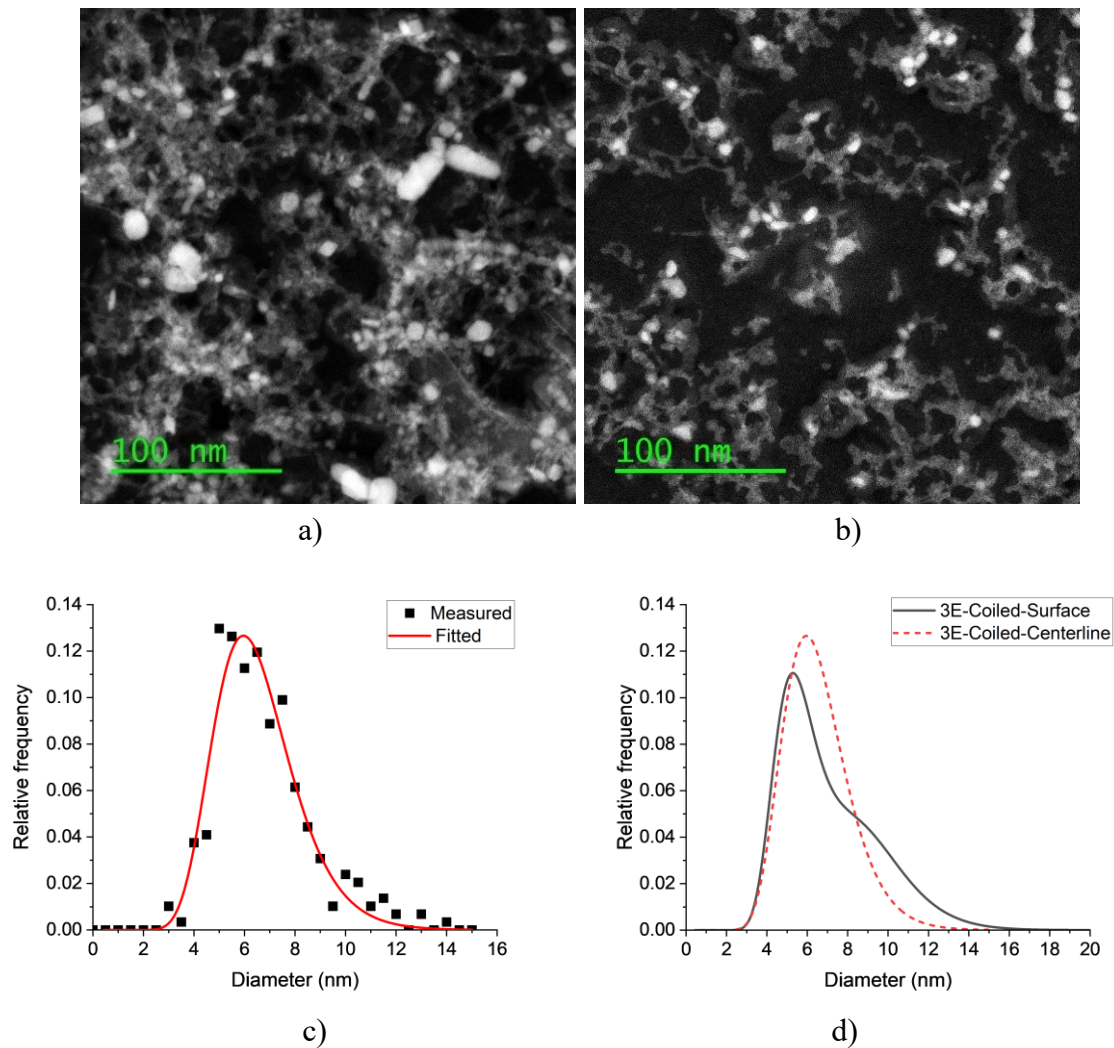
Fig. 4.19 STEM image of nano-sized precipitates in 3E-Coiledat surface (a) and centerline (b); size distribution of nano-sized precipitates in 3E-Coiled at centerline (c) and comparison with that at surface (d).

Table 4-6 Distribution data of precipitates size in 3E-Coiled obtained by curve fitting with equations (4-2) and (4-3).

Sample		N_0	D_0/nm	α/nm	D_m/nm	σ/nm
Surface	Peak 1	218	9.0	0.2	9.2	2.0
	Peak 2	309	5.42	0.2	5.5	1.1
Centerline		137	6.31	0.2	6.5	1.6
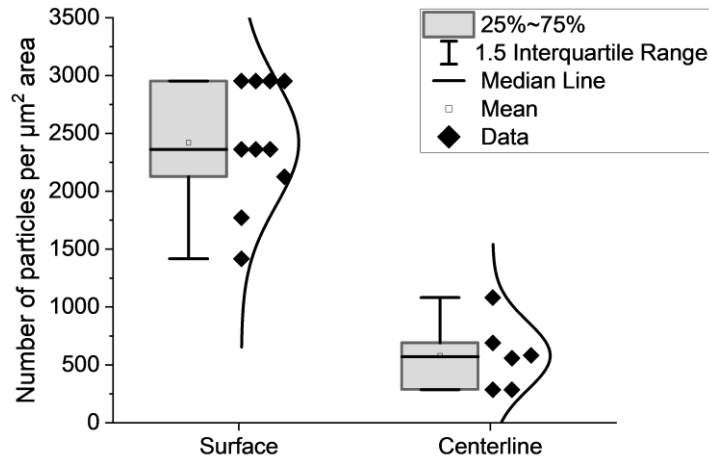
Fig. 4.20 Count density of nano-sized precipitates in 3E-Coiled at surface and centerline.

As a result of the small size of nano-sized precipitates, the composition cannot be determined by EDS precisely. Therefore, lattice parameter obtained by HR-TEM is used to confirm the crystal structure of these fine precipitates. The lattice distance of nano-sized precipitates with different sizes shows that all these precipitates are NbC (d=0.2602 nm, (hkl)=(111)), as seen in Fig.4.21.

a)   b)

c)   d)
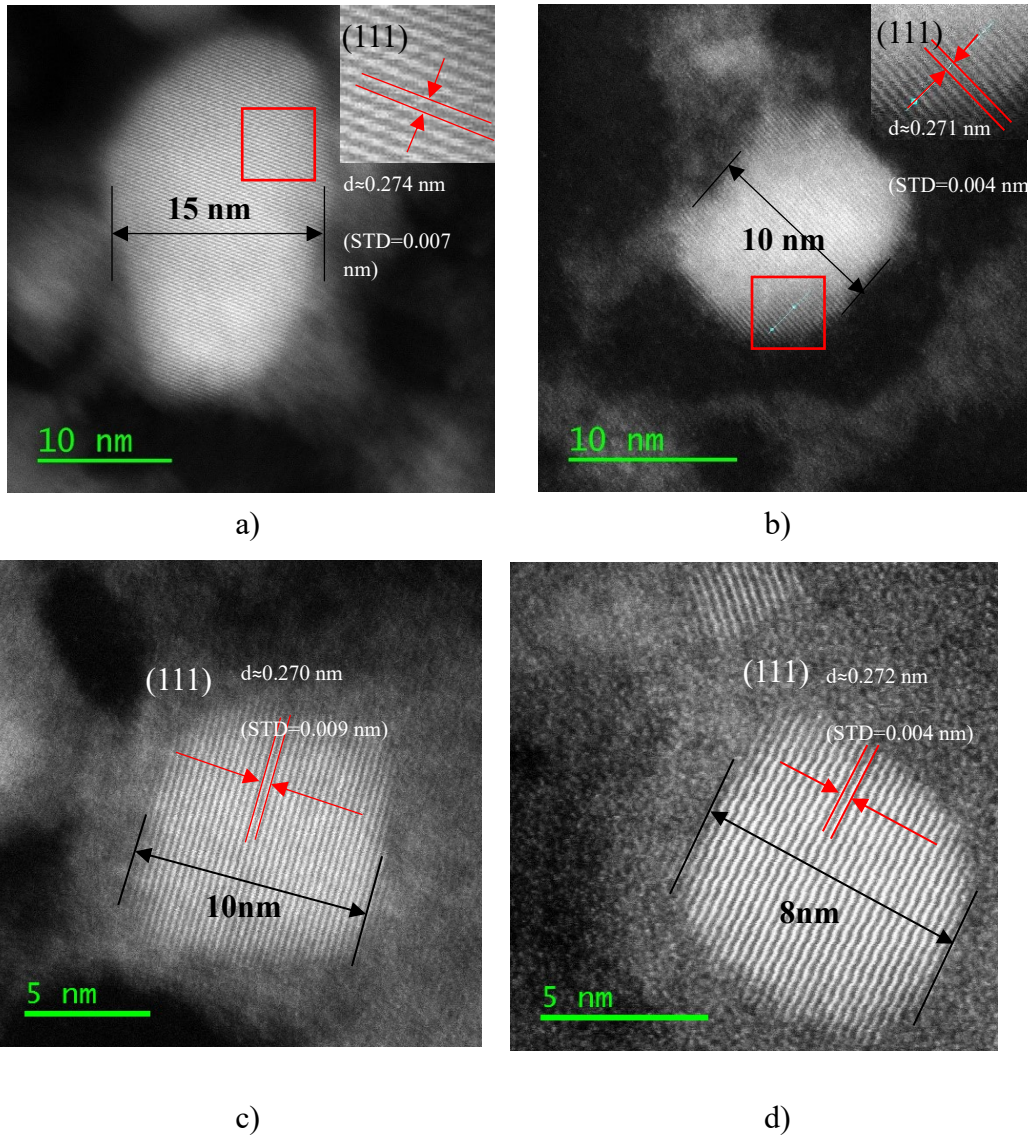
Fig. 4.21 Lattice distance of NbC precipitates with different size (plane (111))

4.3.3 NbC-TiN complex precipitates

In addition to the nano-sized NbC precipitates, large (50~100nm) cuboidal TiN with globular NbC cap are observed in all Group I plates, as it is shown in Fig. 4.22. It is believed that TiN precipitation occurs during solidification since its precipitation temperature approaches to the solidus temperature of microalloy steels[184]. And these pre-existing TiN precipitates act as nucleation sites for NbC, which has much lower precipitation temperature than TiN, during rough rolling process (1000~1100°C). (The epitaxial growth of NbC on TiN cube was observed in Group II samples and is reported in Chapter 5 in detail). This heterogenous nucleation of NbC on TiN

precipitates is preferred due to the absence of interfacial free energy and strain energy between NbC and the matrix[185]. It is reported that the co-precipitation of NbC on TiN can deplete the solute Nb in matrix, and hence strongly decrease the amount of Nb available for subsequent precipitation[185, 186]. As compared with surface region, larger and higher volume fraction of TiN are formed at the centerline region due to the segregation of Ti and N[48, 181, 187]. Therefore, more Nb are consumed at the centerline by the formation of NbC/TiN complex precipitates leading to lower Nb content for NbC precipitation during finish rolling, accelerate cooling and coiling. This explains the discrepancy in count density and size distribution of the nano-sized NbC precipitates between centerline and surface region shown in section 4.3.2.
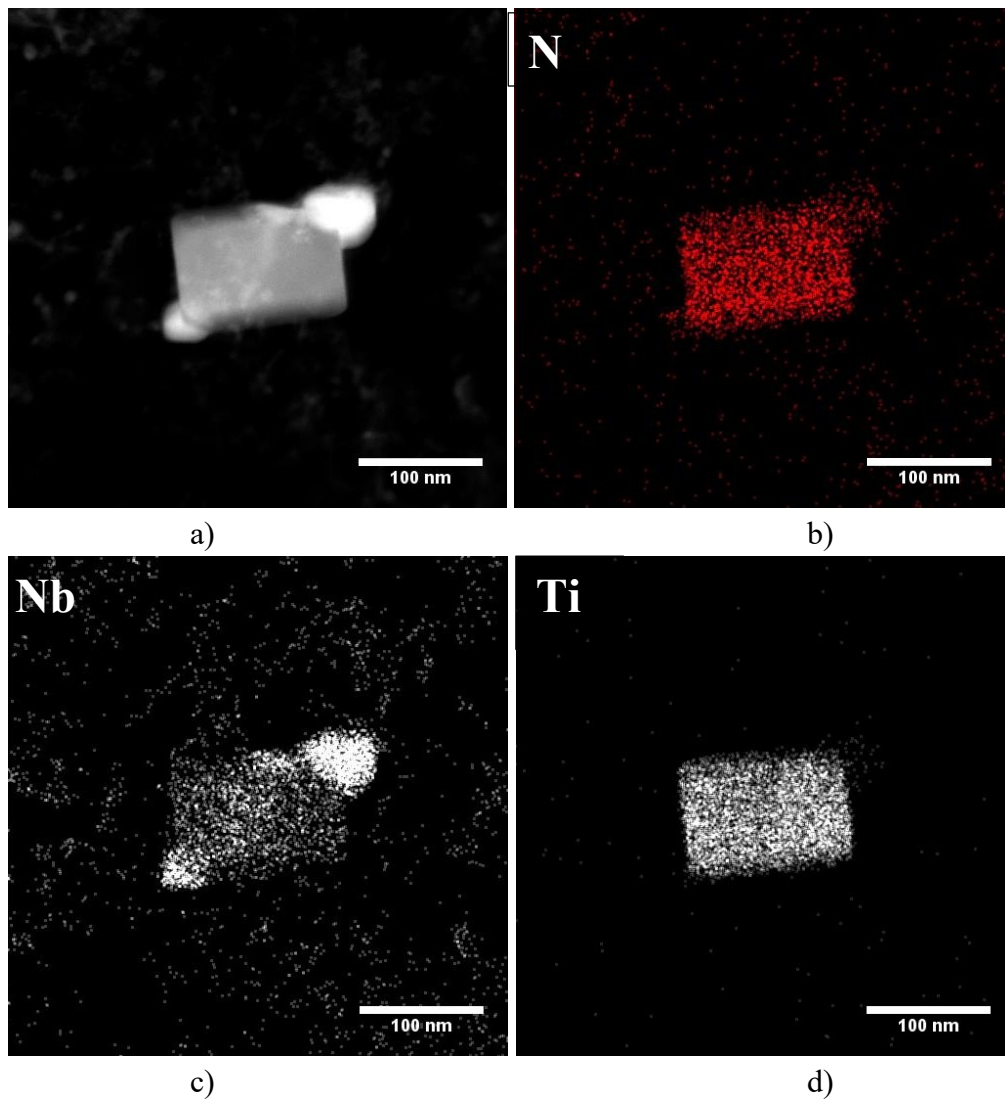
Fig. 4.22 TEM Bright Field (BF) mode image a) and EDX mapping b-d) of cuboidal TiN with globular NbC.

4.3.4 Summary

Based on the analysis above, we can obtain the following conclusions about precipitates in Group I plates:

1) Four types of precipitates are found in all Group I plates, including irregular NbC precipitates (>100nm) formed during solidification, complex precipitates that consist of undissolved cuboidal (Ti,Nb)N and spherical NbC nucleated during rough rolling, large NbC precipitates (>20 nm) formed during finish rolling, and nano-sized NbC precipitates (<20 nm) formed during laminar cooling and coiling.

2) The nano-sized precipitates in coiled plates and in non-coiled plates show unimodal and bimodal size distribution, respectively, indicating the existence of two separate precipitation events. The NbC precipitates formed during coiling are finer than those formed during laminar cooling due to the lower temperature as well as the coarsening of the latter during coiling.

3) The hot rolling process has an effect on the density of nano-sized NbC precipitates by introducing dislocations and subgrain boundaries that act as nucleation sites for strain-induced precipitation. This leads to significantly larger number of nano-sized precipitates in 3E-Coiled than in 3F-Coiled nucleated during coiling.

4) D_0 of nano-sized precipitates that formed during laminar cooling is increased as the cooling rate after runout table decreases. For example, D_0 of 3E-Air cooled is larger than D_0 of 3F-Water quenched, and $D_{0,1}$ of 3E-Coiled is larger than $D_{0,1}$ of 3F-Coiled.

5) At the centerline of 3E-Coiled, nano-sized precipitates shows unimodal size distribution indicating no precipitation during coiling as well as smaller size and lower count density of nano-sized precipitates than those at the surface.

4.4 Hydrogen permeation test

Double-cell electrochemical hydrogen permeation tests were carried on Group I samples. Dimensions, locations, and preparation of the samples as well as test conditions and process refer to section 3.3. Two methods, i.e., time-lag method and curve fitting method, are used to calculate the effective diffusion coefficient (D_{eff}) with the results listed and compared. Oriani-Dong's model is applied to determine total the trap density[1] (N_t) during 1st and 2nd transient, based on which reversible/irreversible trap density ($N_{t,r}/N_{t,ir}$) are obtained. Detailed analysis process and pre-processing of the experimental data can be found in section 3.3.5. The original testing results are shown in Appendix B-6.

4.4.1 Data analysis using time-lag method

Fig. 4.23 shows the normalized hydrogen permeation curves of Group I samples. For all samples, the current curve reaches to a plateau sooner during 2nd transient than during 1st transient. Effective diffusion coefficients (D_{eff}) of these samples are determined by using time-lag method and the results are listed in Table 4-7. As it is shown in Fig. 4.23, D_{eff} of the 1st transient is about 1 order of magnitude lower than that of the 2nd transient since all irreversible traps are occupied and hence not active during the 2nd transient. And this indicates the existence of large volume of irreversible traps in all samples.

To better characterize the traps in these samples, Oriani-Dong's model is adopted to calculate reversible and irreversible trap density with the results shown in Fig. 4.24. In the following part, the reversible and irreversible traps will be discussed separately. In combination with microstructure characterization results reported in section 4.1, these findings can give us some insights on the trapping behaviors of various microstructures.

---

[1] Trap density means the number of traps per unit volume (unit: $mol \cdot cm^{-3}$).

a) b)

c) d)
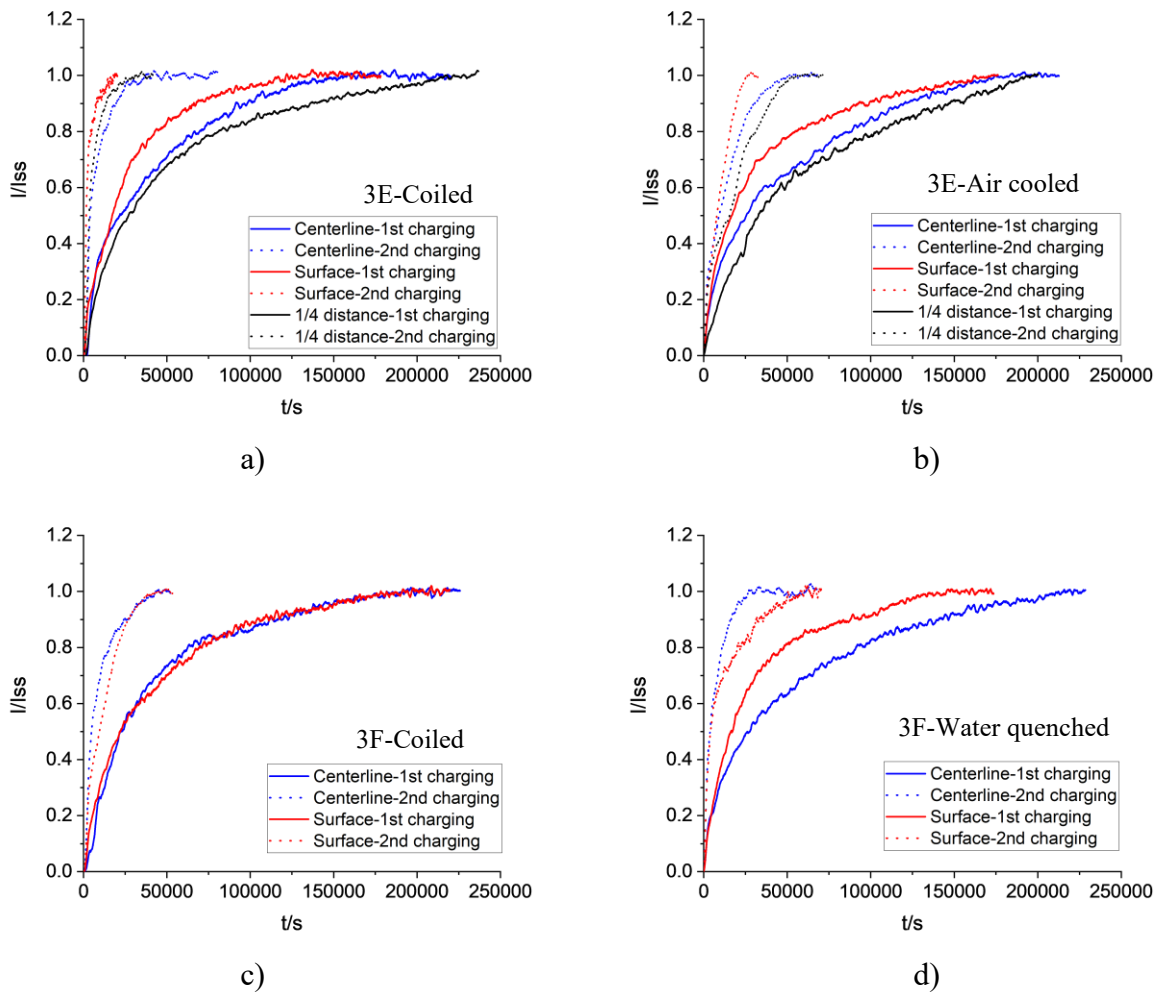
Fig. 4.23 Normalized hydrogen permeation curves (1st and 2nd transient) of Group I samples.

Table 4-7 Hydrogen permeation parameters of Group I samples in 1st and 2nd transient.

Sample	Transient	t_{lag} 10^3 s	D_{eff} 10^{-7} $cm^2 \cdot s^{-1}$	c_{app} 10^{-5} $mol \cdot cm^{-3}$	N_t 10^{-5} $mol \cdot cm^{-3}$	$N_{t,ir}$ 10^{-5} $mol \cdot cm^{-3}$	$N_{t, r}$ 10^{-5} $mol \cdot cm^{-3}$
3E-Coiled-Surface	1st	24.4	2.96	5.13	45.97	41.7	4.28
	2nd	2.32	31.05	0.34	4.28		
3E-Coiled-1/4 distance	1st	43.1	1.67	9.38	81.47	72.9	8.61
	2nd	4.61	15.63	0.64	8.61		
3E-Coiled-Centerline	1st	36.5	1.97	5.59	68.98	57.1	11.9
	2nd	6.34	11.35	0.83	11.89		
3E-Air cooled-Surface	1st	26.5	2.71	4.75	50.12	29.5	20.6
	2nd	10.9	6.58	2.11	20.59		
3E-Air cooled-1/4 distance	1st	29.5	3.37	2.23	55.66	17.1	38.6
	2nd	20.5	3.52	2.70	38.59		
3E-Air cooled-Centerline	1st	44.3	1.62	9.40	83.78	56.7	27.13
	2nd	14.4	5.01	3.23	27.11		
3F-Coiled-Surface-1	1st	38.0	1.90	7.14	71.75	/	/
3F-Coiled-Surface-2	1st	38.0	1.91	0.77	71.15	45.0	26.1
	2nd	13.9	5.20	6.95	26.12		
3F-Coiled-Centerline	1st	34.5	2.09	3.16	65.12	50.1	15.0
	2nd	7.98	9.02	4.74	14.99		
3F-Water quenched-Surface-1	1st	24.8	2.91	0.91	46.76	/	/
3F- Water quenched-Surface-2	1st	29.9	2.41	6.15	56.51	38.4	18.1
	2nd	9.65	7.47	2.27	18.14		
3F- Water quenched-Centerline	1st	45.9	1.57	6.78	86.82	75.0	11.8
	2nd	6.29	11.44	0.82	11.80		
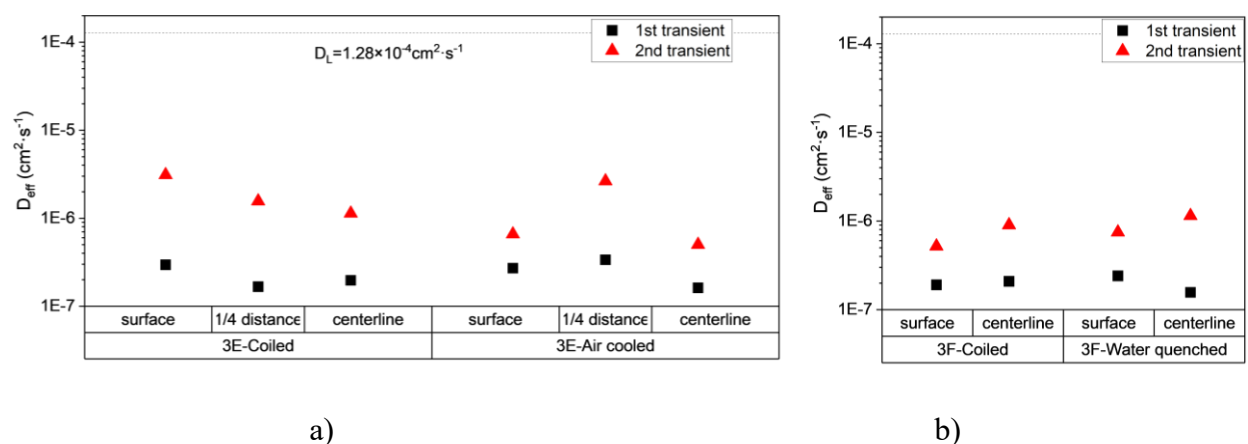
Fig. 4.24 Effective diffusion coefficient of Group I samples in 1st and 2nd transient. a) 3E; b) 3F

4.4.1.1 Reversible traps

Fig.4.25a shows that in 3E samples, the reversible trap density ($N_{t,r}$) increases from surface to centerline, whereas an opposite trend can be found in 3F samples (as seen in Fig. 4.25b). First, density of reversible traps is closely related to the density of dislocations and subgrain boundaries which varies from phase to phase. In 3E samples, $N_{t,r}$ is increased consistently and sharply with increasing fraction of M/A constituents, as shown in Fig. 4.26a, which suggests a strong reversible trapping effect of M/A. However, $N_{t,r}$ increases slowly with fraction of bainite as seen in Fig.4.26b and even decreases with fraction of ferrite increases (while fraction of M/A and/or bainite decreases), which means bainite and ferrite provide much fewer trapping sites than M/A. The trapping ability of these phases follow the sequence of M/A>bainite>ferrite.

For both 3F-Coiled and 3F-Water quenched, higher density of reversible traps at the surface than at the centerline results from the higher fraction of low temperature formed phases, i.e., bainite and martensite, respectively, as shown in Fig.4.27.
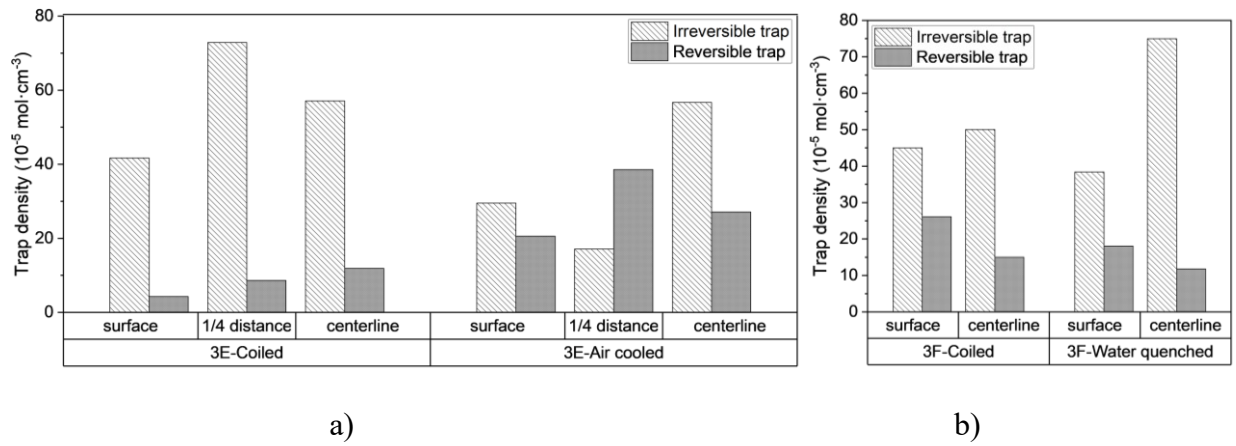
Fig. 4.25 Reversible and irreversible trap density of Group I samples. a) 3E; b) 3F
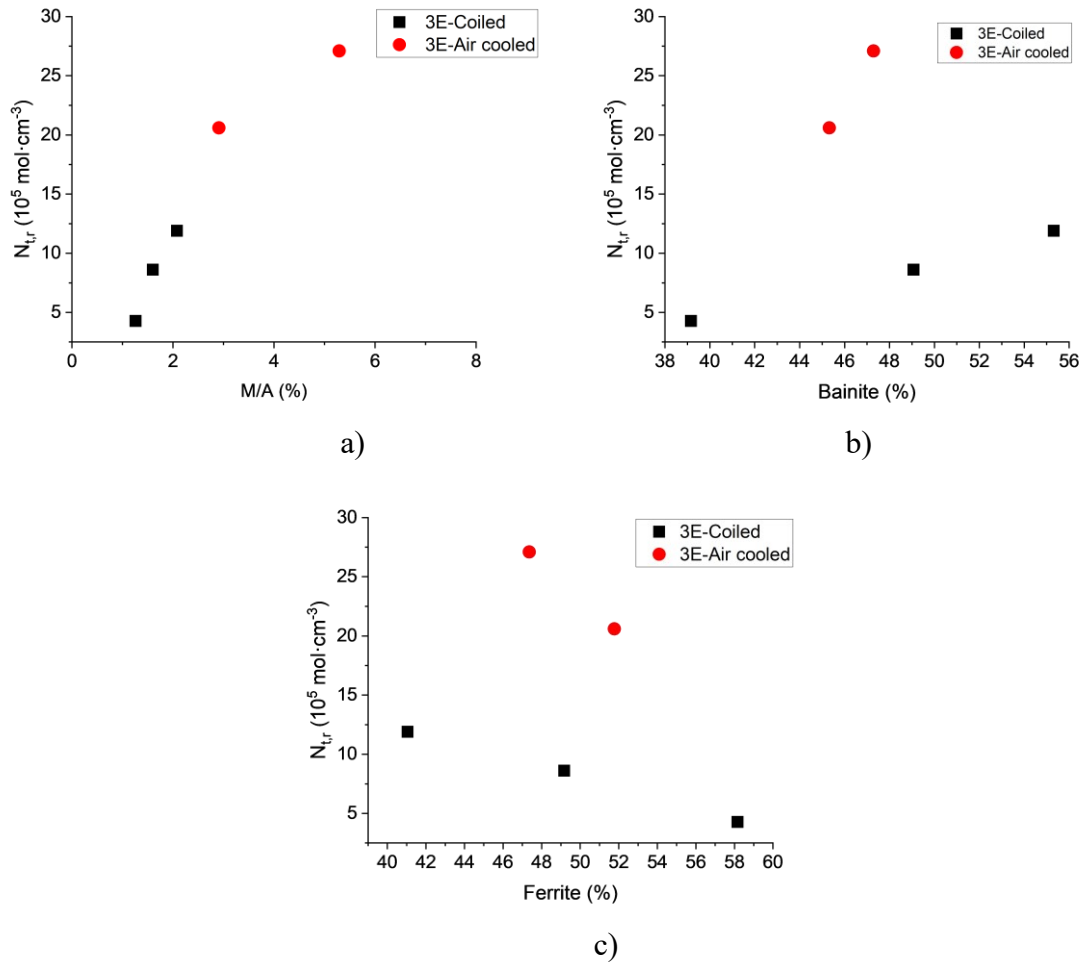
Fig. 4.26 Reversible trap density changing with fractions of M/A constituents a), bainite b) and ferrite c) in 3E samples.
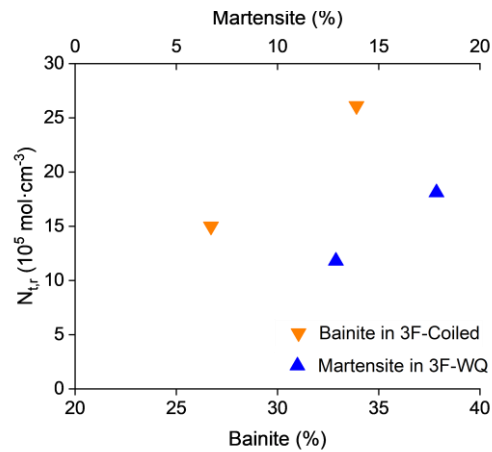
Fig. 4.27 $N_{t,r}$ of 3F-Coiled and 3F-Water quenched increases with fraction of bainite and martensite, respectively.

4.4.1.2 Irreversible traps

The irreversible trap density ($N_{t,ir}$) at centerline is higher than that near the surface in all samples. As reported in section 4.3, unlike the nano-sized precipitates at surface, those at centerline shows a unimodal size distribution with much lower density. On the contrary, inclusion segregation was found at centerline in section 4.2. Therefore, in the region near the centerline, inclusions are the main contributor of irreversible traps instead of nano-sized precipitates.

Since all Group I samples come from the same casting skelp, it is reasonable to assume that the density and chemistry of non-metal inclusions at centerline should be identical for centerline samples. However, it is shown in Fig.4.25 that although $N_{t,ir}$ of 3E-Coiled, 3E-Air cooled and 3F-Coiled are quite close ranging from 50.1×10^{-5} mol·cm^{-3} to 57.1×10^{-5} mol·cm^{-3}, $N_{t,ir}$ of 3F-Water quenched at centerline is obviously much higher (75×10^{-5} mol·cm^{-3}).

To understand the reason behind the abnormally high $N_{t,ir}$ of 3F-Water quenched samples, surface and centerline HPT samples of all plates were sectioned after hydrogen permeation test, and observed by SEM. Fig. 4.28 shows that cracks along inclusions were found in 3F-Water quenched samples at both surface and centerline, whereas no cracks were found in samples from other plate. Although it is uncertain if these cracks were caused by the high cooling rate during water quench or the HEDE mechanism during hydrogen permeation process, their existence can

significantly decrease the D_{eff}. The powerful irreversible trapping effect of micro-cracks has also been found by other researchers [188].

Considering the trapping effect of micro-cracks, $N_{t,ir}$ of 3F-Water quenched samples are recalculated to reveal the influence of inclusions as well as nano-sized precipitates. Two assumptions are taken for the recalculation: 1) the trapping effect of NMIs overwhelms that of nano-size NbC precipitates at centerline due to the segregation; 2) the size distribution and density of NMIs in 3F-Water quench is the same as that in 3F-Coiled; 3) the number of micro-cracks is proportional to the number of NMIs. The trap density of 3F-Water quench after recalculation is shown in Fig. 4.28.

$$N'_{wq,cl} = N_{c,cl} \tag{4-6}$$

$$N_{wq,cl} - N'_{wq,cl} = n_{wq,cl} \tag{4-7}$$

$$n_{wq,cl} / n_{wq,s} = c_{in,cl} / c_{in,s} \tag{4-8}$$

$$N'_{wq,s} = N_{wq,cl} - n_{wq,s} \tag{4-9}$$

Wherein the $N_{c,cl}$ and $N_{wq,cl}$ are the irreversible trap density in 3F-Coiled-Centerline and 3F-Water quench-Centerline (calculated by Dong's model); $N'_{wq,cl}$ and $N'_{wq,s}$ are the updated irreversible trap density in 3F-Water quench-Centerline and 3F-Water quench-Surface; $n_{wq,cl}$ and $n_{wq,s}$ are the trap density caused by micro-cracks in 3F-Water quench-Centerline and 3F-Water quench-Surface; $c_{in,cl}$ and $c_{in,s}$ are the NMIs density in 3F-Water quench-Centerline and 3F-Water quench-Surface.

a)   b)
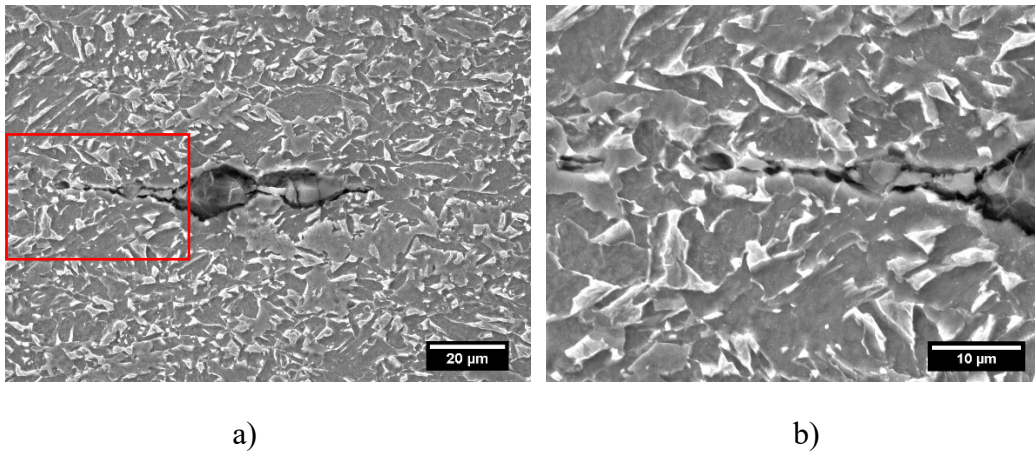
Fig. 4.28 Cracks in 3F-WQ at centerline after hydrogen permeation test.

$N_{t,ir}$ at the ¼ distance of 3E-Coiled is higher than that at both the surface and the centerline. The $N_{t,ir}$ at the centerline is quite close in all samples except in 3F-Water quenched, which shows much higher irreversible trap density.

Within the same skelp, $N_{t,ir}$ at the surface is obviously higher in the coiled plate than in the non-coiled one, i.e., $N_{t,ir}$ (3E-Coiled)> $N_{t,ir}$ (3E-Air cooled), and $N_{t,ir}$ (3F-Coiled)> $N_{t,ir}$ (3F-Water quenched). Herein, the inclusion effect can be excluded based on the assumption that inclusion density at the same location should be the same for both coiled and non-coiled samples. Therefore, the higher $N_{t,ir}$ in coiled samples should be attributed to the higher density of nano-sized precipitates as compared with those non-coiled samples, as it is shown in Fig.4.29. This indicates that the nano-size NbC precipitates are irreversible hydrogen traps, which is consistent with Wallaert's [119]and Chen's[110] results obtained from thermal desorption spectroscopy (TDS) and atom probe tomography (APT), respectively.
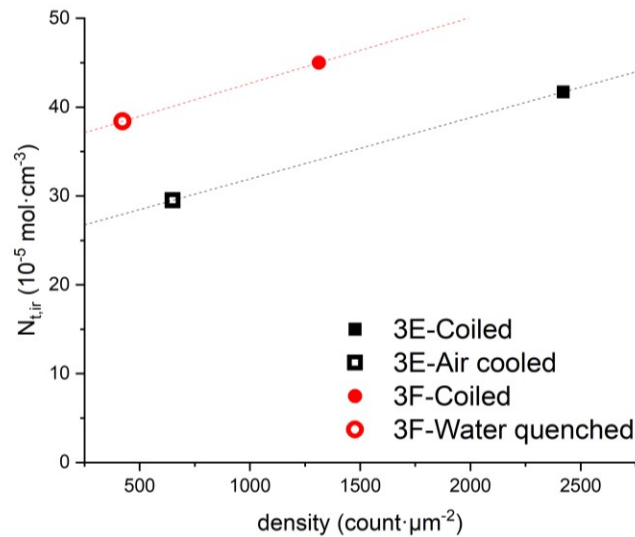
Fig. 4.29 Effect of nano-sized precipitates on irreversible trap density.

4.4.2 Data analysis using curve-fitting method

Another commonly used method to analyze hydrogen permeation curve is curve-fitting method. In this method, the experimental hydrogen permeation curves are fitting with equations (3-4) and (3-5), which are the solutions to Fick's Second Law based on boundary conditions of constant flux and constant concentration on the entrance side of the sample. Detailed analysis procedure and equations can be found in Section 3.3.5.2. The curve-fitting results are shown in

Fig.4.30. (The curve-fitting results on logarithmic scale are in Appendix B-6.) The diffusion coefficient (D_{eff}) values obtained by curve-fitting are listed in Table 4-8, along with those D_{eff} calculated by time-lag method for comparison.

As seen in Fig.4.30, all experimental data fits the equation based on constant flux boundary condition better than that based on constant concentration boundary condition. Also, Table 4-8 shows that for each round of test, the relative standard error (RSE) of the former is smaller than the latter indicating a better accuracy of fitting with constant flux model. These founding leads to the conclusion that for double-cell hydrogen permeation test using galvanostat as the charging equipment, constant flux of hydrogen at the entrance side should be selected as the boundary condition when analyzing the experimental data, which verified *Carvalho*'s recommendation[173].

Moreover, as shown in Fig. 4.30, for both boundary conditions, experimental data fits the equations better in 2nd transient than in 1st transient. This is because in Fick's second law, the "missing" hydrogen atoms that captured by irreversible traps are not considered.

3E-Coiled-1/4 distance-1st charging

3E-Coiled-1/4 distance-2nd charging

3E-Coiled-Centerline-1st charging

3E-Coiled-Centerline-2nd charging

3E-Air cooled-Surface-1st charging

3E-Air cooled-Surface-2nd charging

107
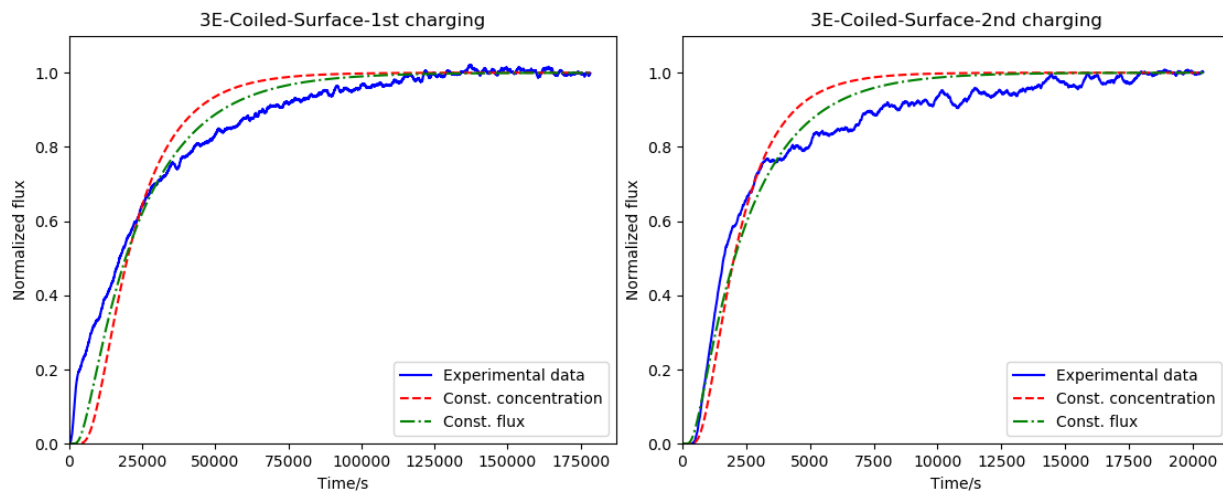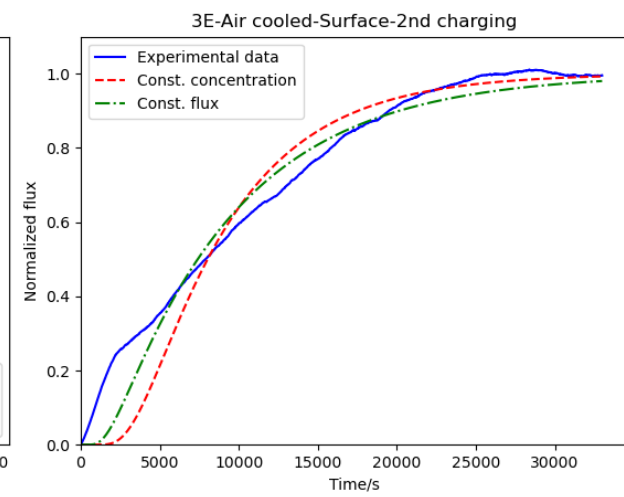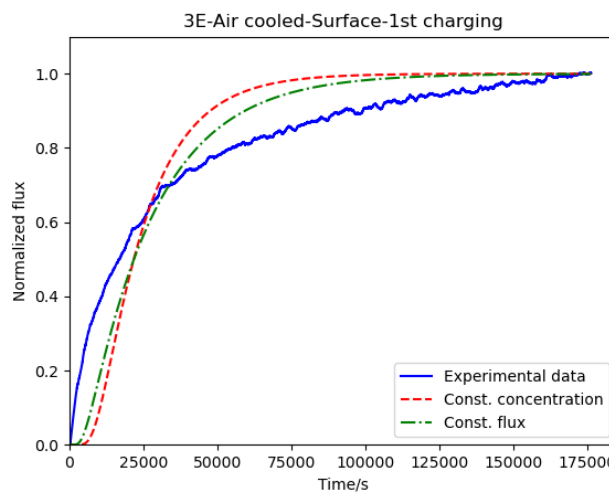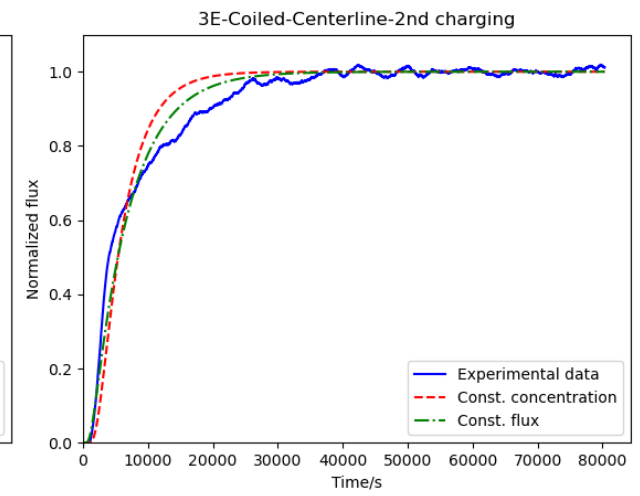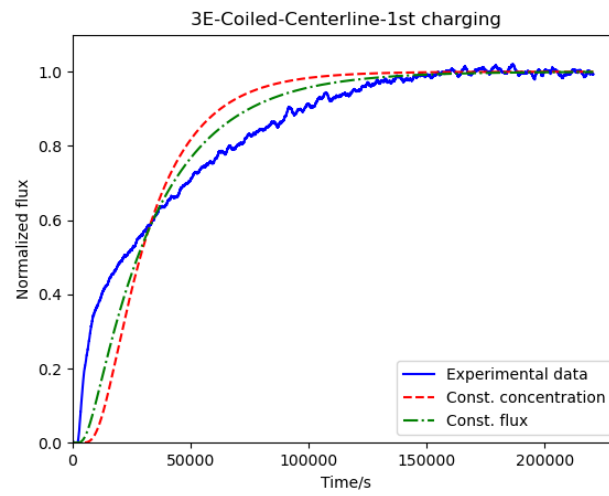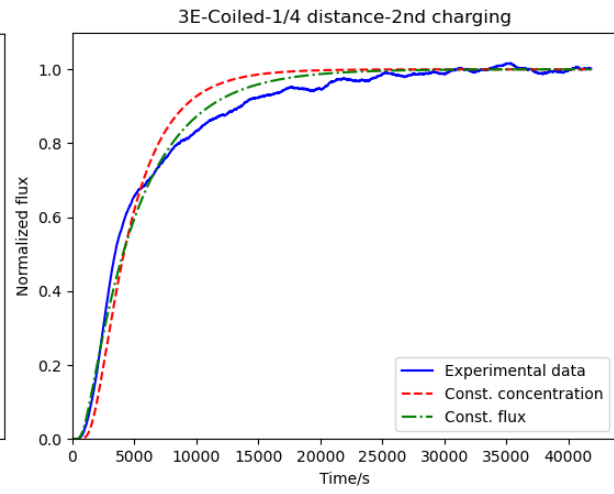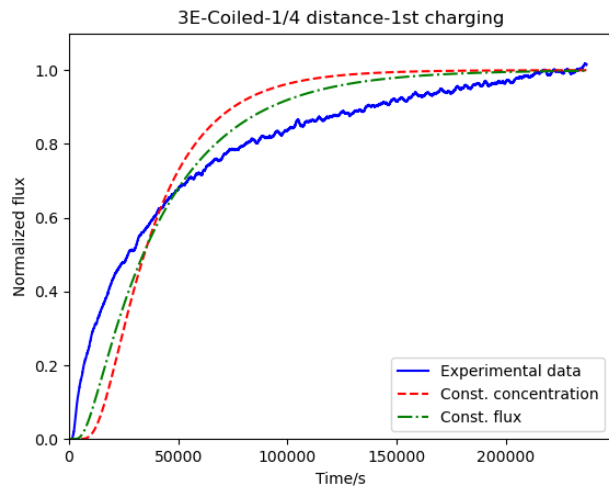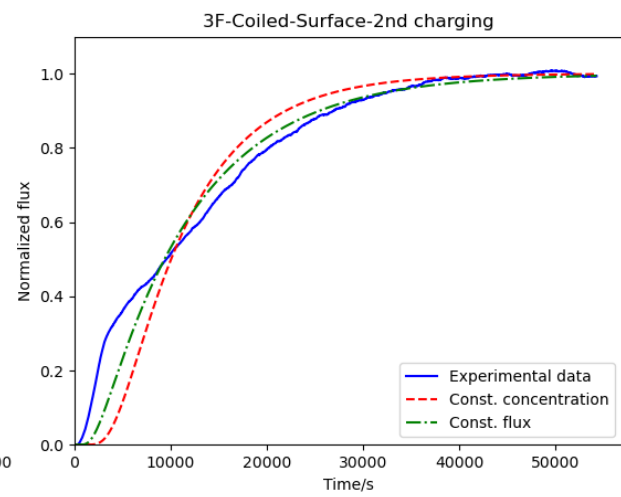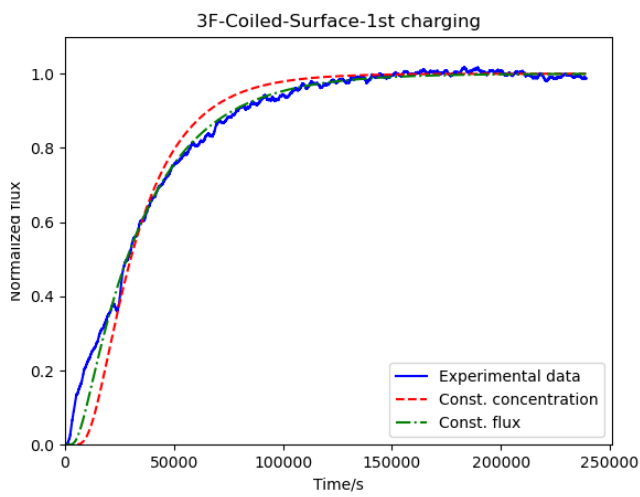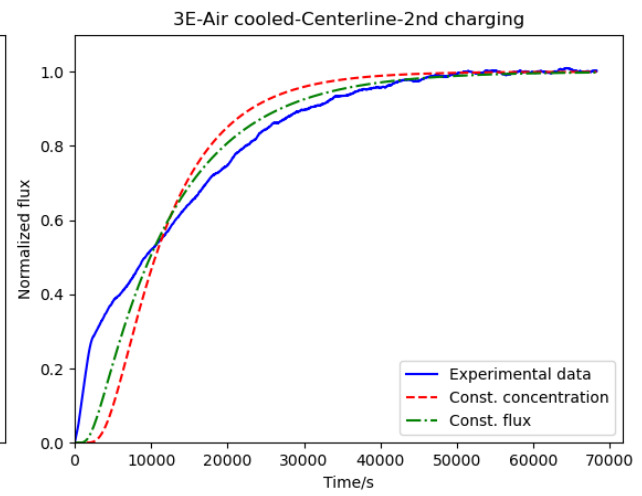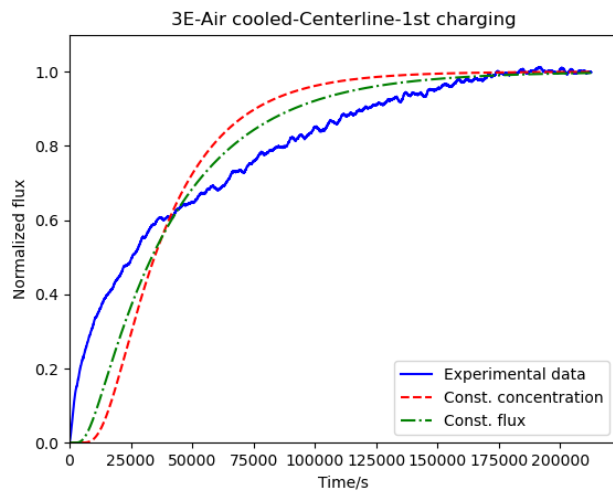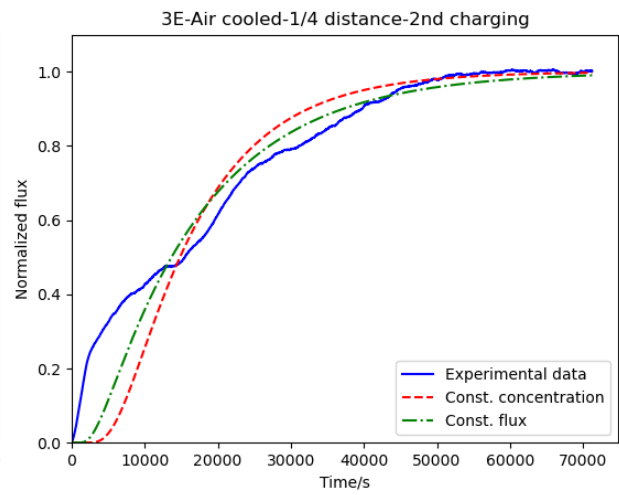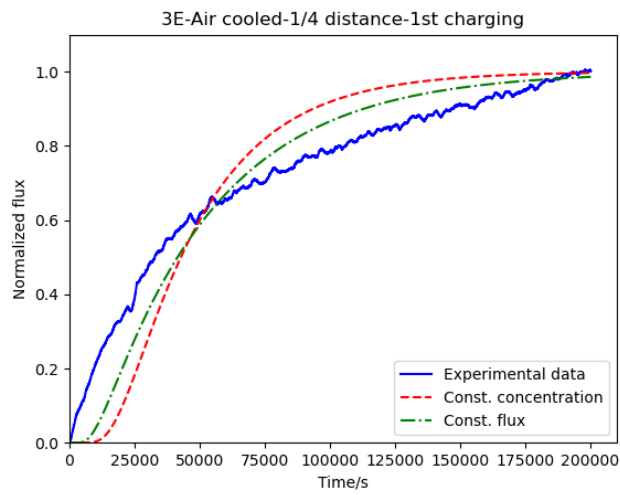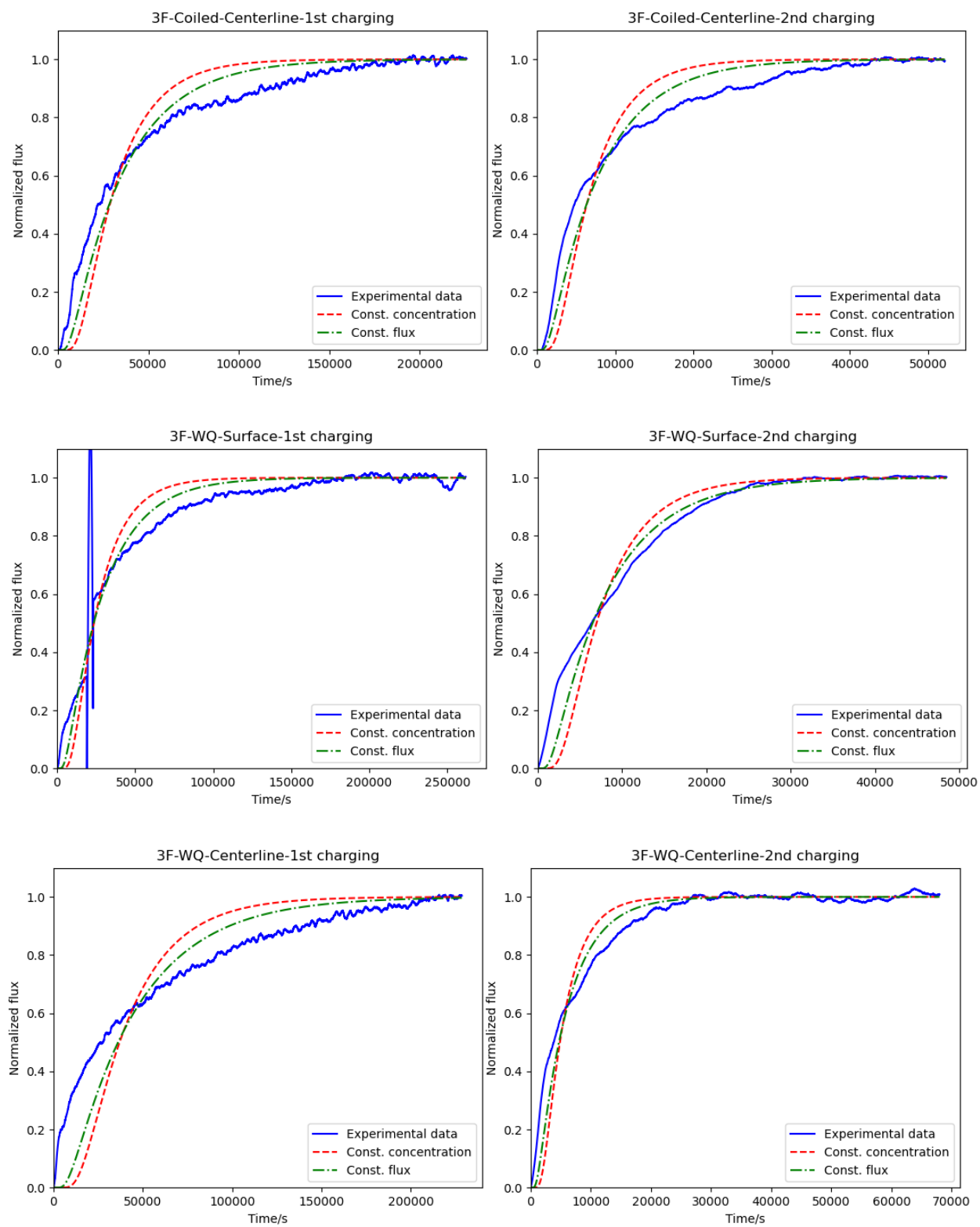
Fig. 4.30 Curve-fitting of experimental hydrogen permeation data with constant concentration and constant flux boundary conditions.

Table 4-8 D_{eff} of Group I samples obtained by curve-fitting method in comparation with D_{eff} calculated by time-lag method.

| Plate | Location | Transient | Curve-fitting method | | | | Time-lag method |
| | | | Const. concentration | | Const. flux | | |
			D_{eff} $10^{-7}cm^2 \cdot s^{-1}$	RSE[2]	D_{eff} $10^{-7}cm^2 \cdot s^{-1}$	RSE	D_{eff} $10^{-7}cm^2 \cdot s^{-1}$
3E-Coiled	Surface	1st	1.00	0.24%	2.84	0.18%	2.96
		2nd	9.88	0.69%	26.7	0.55%	31.1
	¼ distance	1st	0.581	0.25%	1.61	0.20%	1.67
		2nd	4.83	0.35%	13.4	0.20%	15.6
	Centerline	1st	0.698	0.26%	1.98	0.20%	1.97
		2nd	37.2	0.34%	10.2	0.23%	11.4
3E-Air cooled	Surface	1st	0.920	0.33%	2.51	0.27%	2.71
		2nd	2.49	0.41%	7.37	0.31%	6.58
	¼ distance	1st	0.854	0.30%	2.32	0.25%	3.37
		2nd	1.35	0.37%	3.99	0.30%	3.52
	Centerline	1st	0.577	0.29%	1.63	0.23%	1.62
		2nd	1.89	0.40%	5.52	0.30%	5.01
3F-Coiled	Surface	1st	0.665	0.13%	1.93	0.07%	1.91
		2nd	1.99	0.37%	5.84	0.25%	5.20
	Centerline	1st	0.697	0.23%	1.9	0.17%	2.09
		2nd	3.15	0.49%	8.62	0.35%	9.02
3F-Water quenched	Surface	1st	8.45	0.26%	2.30	0.23%	2.41
		2nd	2.87	0.41%	8.40	0.28%	7.47
	Centerline	1st	0.541	0.28%	1.51	0.23%	1.57
		2nd	4.12	0.43%	11.6	0.31%	11.4

---

[2] RSE: Relative standard error, is equal to the standard error of a survey estimate divided by the survey estimate and then multiplied by 100.

4.4.3   Summary

The results and analysis of hydrogen permeation test of Group I samples are listed as follows:

1)   Trapping ability of the phases in 3E samples follows the sequence of M/A>bainite>ferrite.

2)   For 3F-Coiled and 3F-Water quenched, reversible traps with higher density are found at the surface than at the centerline due to higher fraction of low temperature formed phases, i.e., bainite and martensite, respectively.

3)   Inclusions are the main irreversible traps at centerline region due to centerline segregation

4)   Nano-sized NbC precipitates are the major contributors of irreversible trapping at the surface since much less Nb solute are consumed before coiling at the surface than at the centerline.

5)   Micro-cracks, which act as irreversible traps, are observed at 3F-Water quenched samples at both surface and centerline.

6)   Size distribution of inclusions has strong effect on trapping efficiency, i.e., fine size inclusions are more effective irreversible traps than large ones (equal volume fraction).

7)   Curve-fitting equation with constant flux boundary condition fit the HPT curves better than that with constant concentration boundary condition.

5 Microstructure and hydrogen trapping ability of Group II steels

In this Chapter, seven (7) X70 pipeline steel plates went through different rough rolling process before accelerated cooling/water quench are studied. Since no finish rolling or coiling was applied on these plates, the analysis of Group II steels exclusively reveals the influence of rough rolling process on the hydrogen diffusion behavior through the effect on different types of traps. The TMCP and rough rolling schedule of these plates are illustrated in Fig.3.1b) and Appendix C-1, respectively. Only surface sample of Group II plates are used (as shown in Fig.3.2c) to rule out the overwhelming influence of inclusion segregation at centerline. Besides, the cooling rate of these plates during each cooling process can be considered as equivalent due to the same thickness after (15.2 mm) rough rolling.

The microstructure of these plates was studied by means of OM and EBSD, which revealed the effect of TMCP schedule on microstructural features such as phase morphology, PAG size, misorientation distribution, etc. In addition, precipitates in Group II plates were characterized by TEM in terms of morphology, density, size distribution, lattice parameters and chemistry. And double-cell hydrogen permeation test (HPT) was conducted on surface samples of all Group II plates which gives information such as hydrogen diffusivity, trap density and hydrogen solubility. Finally, the influence of microstructure and precipitates on hydrogen diffusivity/trap density is discussed based on the results of characterization tests and HPT.

5.1 *Microstructure analysis*

The microstructure of Group II plates was studied via OM. 2% Nital and PAG etchant were used to reveal the phases and PAG boundaries, respectively. Composition of the etchants is shown in Table 3-2. In addition, EBSD technique was used to study the effect of increased rough rolling passes to the microstructure of Group II plates in terms of morphology of phases, PAG size, distribution of disorientation, etc.

5.1.1 *Phases revealed by 2% Nital*

As shown in Fig.5.1, the microstructure of 3F-0P, 3B-1P, 3E-3P, 3B-5P and 3E-5P-4MIN, mainly consist of lower lath bainite (LB) due to the high cooling rate of water quenching, whereas

in 3E-5P-OLAC and 3E-4P-1P-OLAC, in addition to lower lath bainite, upper bainite (UB) with blocks of M/A constituents between the interlocked ferrite lath/along coarse ferrite lath is also presented. The complex microstructure in 3E-5P-OLAC and 3E-4P-1P-OLAC is caused by the double-stage cooling process: UB were formed during OLAC (from 1000~1100°C to 550~600°C) due to the lower cooling rate and the remain untransformed austenite were decomposed into LB during the subsequent water quenching.

Although having been through the same cooling process, the microstructure of 3E-5P-OLAC and 3E-4P-1P-OLAC are quite different: 3E-4P-1P-OLAC contains much more UB than 3E-5P-OLAC, especially coarse UB, which is observed in the former rather than in the latter. This can be attributed to the great difference in PAG size between 3E-4P-1P-OLAC (65.1 μm) and 3E-5P-OLAC (37.3 μm) (see Table 5-1). It has been reported [189] that under relatively low cooling rate, bainite transformation at relatively high temperature consists of two stages: the first stage is associated with primary bainitic ferrite (BF) nucleating at the austenite boundaries and growing inwards; during second stage, secondary BF nucleates on the primary plates and grows in a different direction from that of the first stage. As the primary BF grows into the austenite grains, the carbon concentration in adjacent region is lower in large PAGs than in small PAGs, because in small PAGs, the carbon diffusion fields next to pre-exist BF tend to overlap with each other and lead to increase of carbon concentration, as shown in Fig. 5.2. Therefore, the secondary BF are more likely to grow within large PAGs due to the lower carbon level that allows generation of BF. [190]

According to Ohtani[191], bainite can be classified into three types based on carbon distribution: Type I is carbon free bainite, which is formed at such a high temperature that carbon diffuses into untransformed austenite without cementite participation. Type II has fine cementite layers lying between laths and Type III has carbides parallel to a specific ferrite plane in the interior, which are formed at intermediate and lower temperature, respectively. However, in low carbon microalloyed steel as the investigated X70 pipeline steel, M/A constituents are formed instead of carbide due to the low carbon concentration. This type of upper/lower bainite with inter/intra-lath M/A rather than carbide is called degenerated upper/lower bainite by Zajac[192]. Therefore, based on Ohtani's classification, the coarse UB and intricated UB observed in 3E-4P-

1P-OLAC fall into the category of Type I and Type II bainite, respectively, and LB is Type II bainite.

a)

b)

c)

d)

e)

f)

g)

h)

i)

j)

k)

l)

m)　　　　　　　　　　　　　　　　　　　　n)
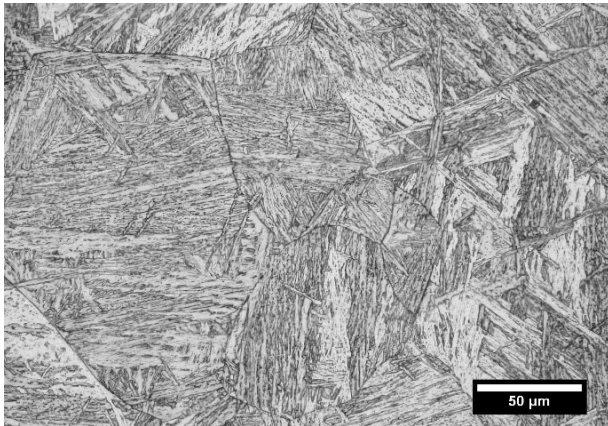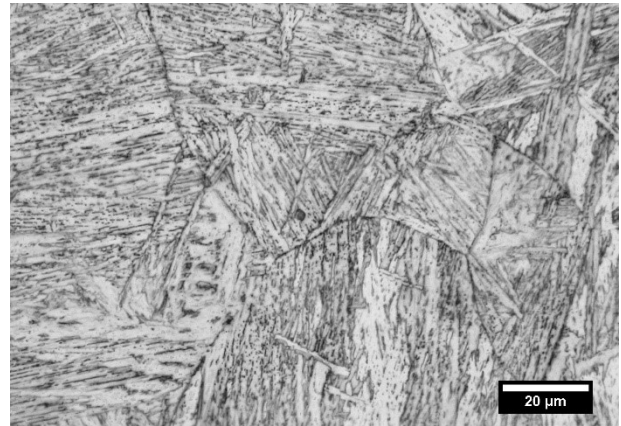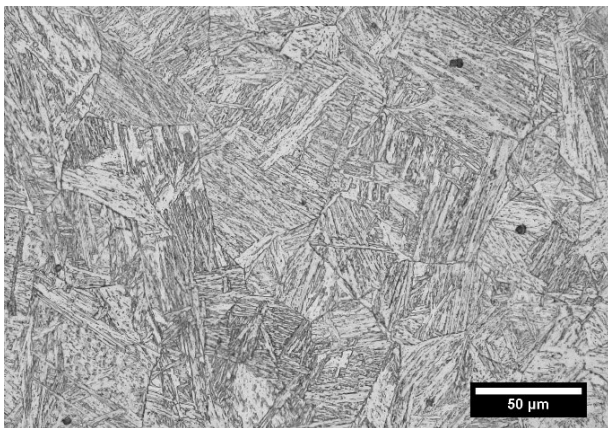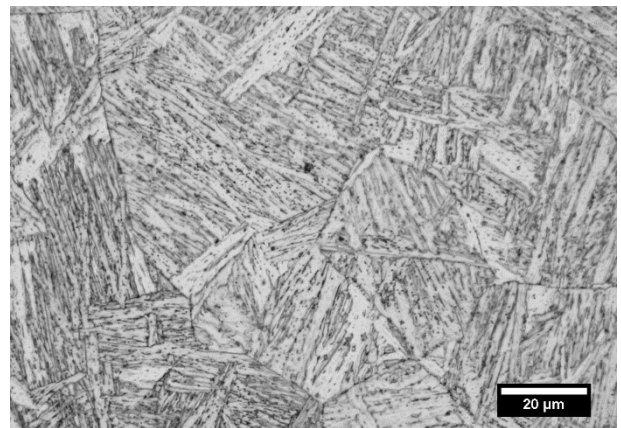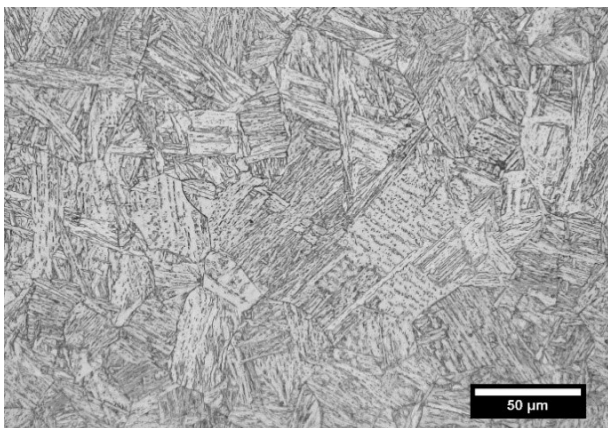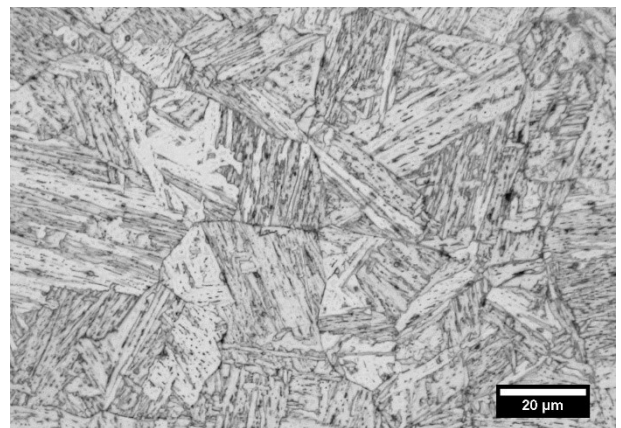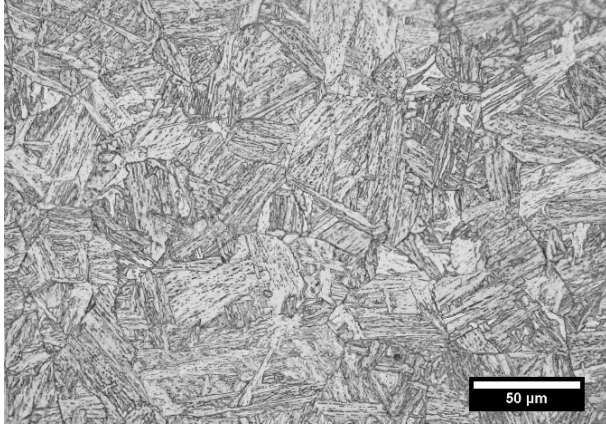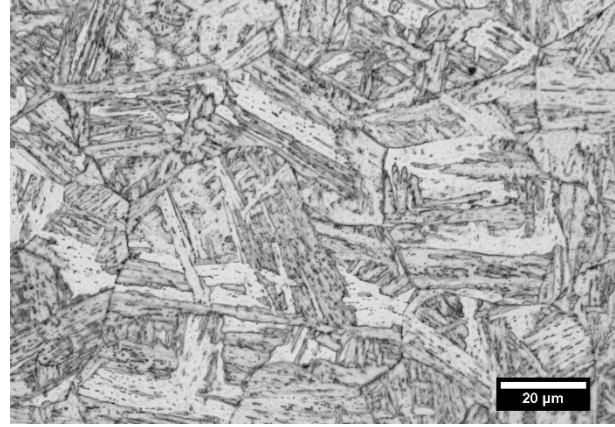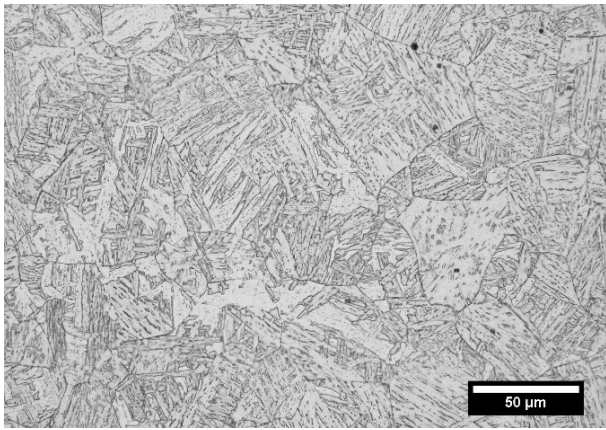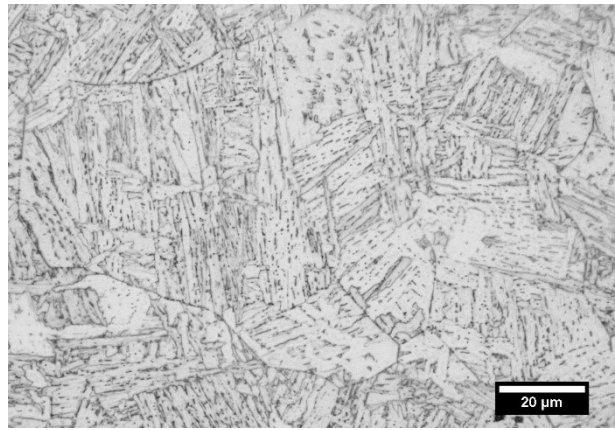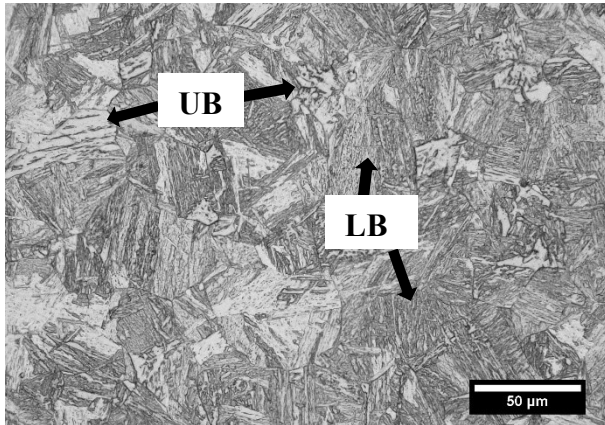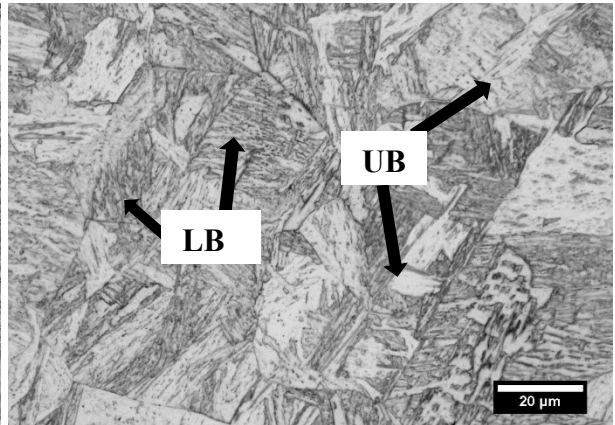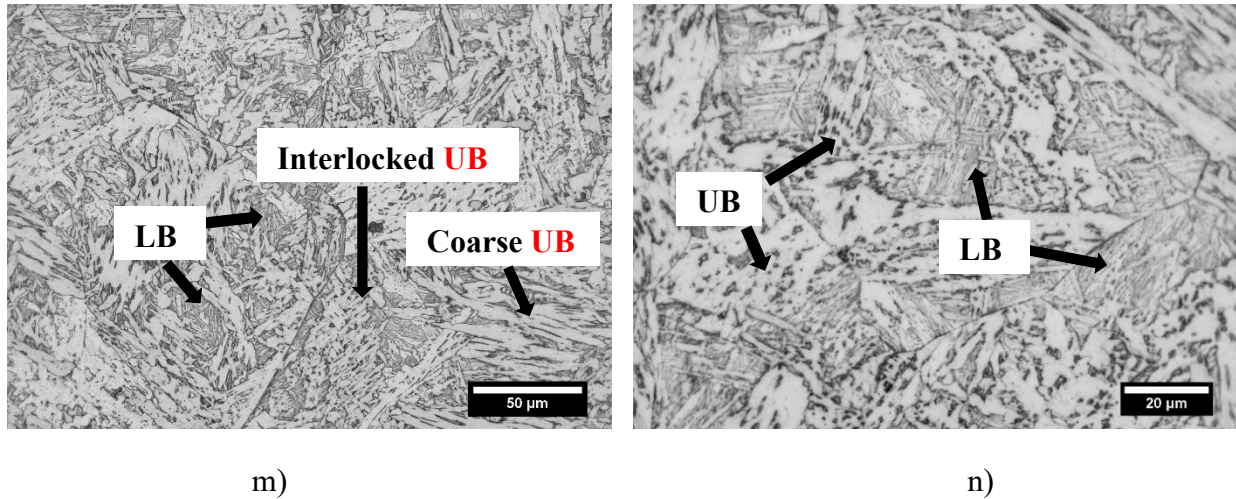
Fig. 5.1 OM images of 3F-0P (a,b); 3B-1P (c,d); 3B-1P (e,f); 3B-5P (g,h); 3E-5P-4MIN (i,j); 3E-5P-OLAC (k,l); 3E-4P-1P-OLAC (m,n).
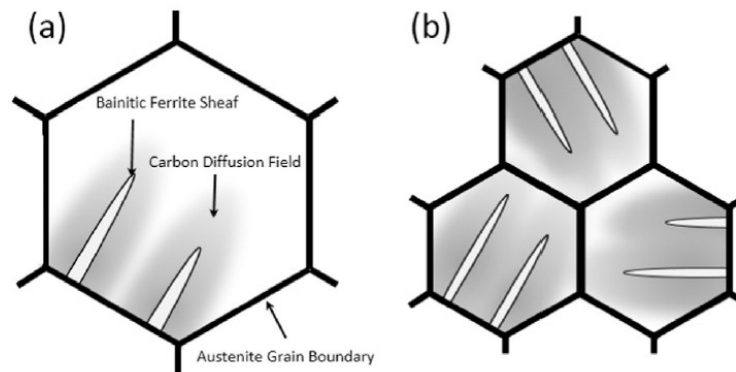
Fig. 5.2 Schematic illustration of the difference in carbon diffusion fields in the austenite with (a) large and (b) small PAGs.[190]

5.1.2　PAG size

PAG size of Group II plates were measured using Lineal Intercept Procedure according to ASTM E112-13[193]. The composition of the etchant used to reveal PAGs is listed in section 3.3.2 Table 3-2. The measurement was conducted on OM images at a magnification of 200× or 500×, depending on the PAG size of the sample. Typical OM images of Group II plates used for PAG size measurement are shown in Appendix C-1. For each sample, OM images of eleven (11) areas are tested, and the number of intercepts on five (5) straight lines at different directions are counted on each of the images. The mean lineal intercept length (MLIL) and standard deviation of measurements on Group II samples are shown in Fig. 5.3 and Table 5-1.

116

The effect of rough rolling on PAG size is obvious: as the number of rough rolling passes increased from 0 to 5, the MLIL decreases from 83.3 μm to 33.5 μm due to increasingly sufficient crystallization. And the PAG size increased slightly during holding at the rough rolling temperature for 4 min (from 33.5 μm to 39.1 μm). The MLIL of 3E-5P-OLAC is marginally larger than that of 3E-5P, which might be due to the slower cooling rate of OLAC than that of water quench. However, the MLIL of 3E-4P-1P-OLAC (65.1 μm) is significantly larger than that of either 3E-5P-OLAC or 3B-1P as a result of grain coarsening during reheating to 1200°C.
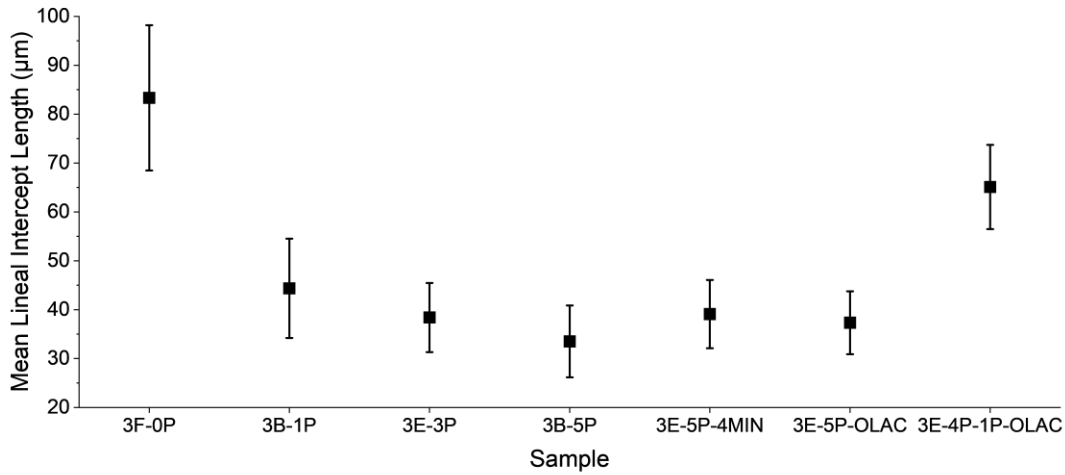
Fig. 5.3 Mean lineal intercept length of PAGs in Group II samples.

Table 5-1 Lineal intercept length of PAGs in Group II samples.

Sample	Mean (μm)	Standard deviation (μm)
3F-0P	83.3	14.9
3B-1P	44.4	10.2
3E-3P	38.4	7.1
3B-5P	33.5	7.4
3E-5P-4MIN	39.1	7.0
3E-5P-OLAC	37.3	6.4
3E-4P-1P-OLAC	65.1	8.6

As discussed in section 5.1.1, the large PAG size in 3E-4P-1P-OLAC leads to the formation of coarse UB. This is also disclosed in Zhao's work[190] and explained by the lower carbon concentration in the austenite near the existing bainitic ferrite (BF) laths in large-grained austenite than that in small-grained austenite, where carbon diffusion fields of adjacent BF laths are more likely to overlap. Moreover, Hu[194] reported that the width and length of bainitic ferrite is larger in specimens with coarse austenite grain than those with finer ones due to the reduced nucleation density provided by grain boundary and decreased hard impingement during the growth of bainite sheaves.

It is worth mentioning that although the PAG size of 3F-0P is even larger than that of 3E-4P-1P-OLAC, no coarse bainite lath was observed in 3F-0P. This is because the cooling rate of 3F-0P is much higher, since it has been water quenched directly from soaking temperature (1260°C), whereas 3E-4P-1P-OLAC was cooled on runout table from rough rolling temperature (1100~1000°C) to 550~600°C before water quenched.

5.1.3 EBSD results

EBSD technique is used to reveal the microstructural features of Group II plates, such as misorientation distribution, packet/block boundaries of bainite. It is shown in Fig. 5.4 (overlapped band contrast map, inverse polar figure and grain boundaries map) that the bainite laths in 3B-5P is shorter and thicker than those in 3B-1P. And Fig. 5.5 shows that the morphology of retained austenite (RA) in these samples are also different: in 3B-5P, RA films lie between the thin and long bainitic laths, whereas RA islands disperse between thick and short bainitic laths or at triple point junctions in 3B-1P. It is believed that the difference in morphology of bainite and RA is related to the difference of PAG size between 3B-1P (44.4 μm) and 3B-5P (33.5 μm). Similar results has also been reported by Singh [195], which shows significant effect of PAG size on bainitic lath thickness and morphology of RA. Singh attributed this effect to the more frequent impingement of bainitic lath and subsequent lateral growth of bainitic sheaves in small PAGs. However, further study shows that the orientation selection during the nucleation of bainite should be a more reasonable mechanism for this phenomenon.
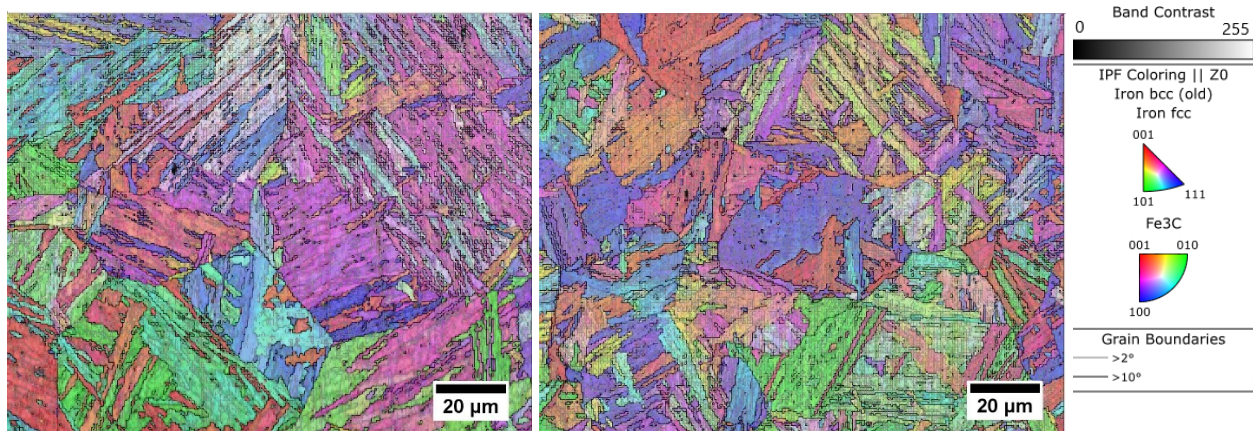
Fig. 5.4 EBSD BC+IPF+GB map of 3B-1P a) and 3B-5P b)
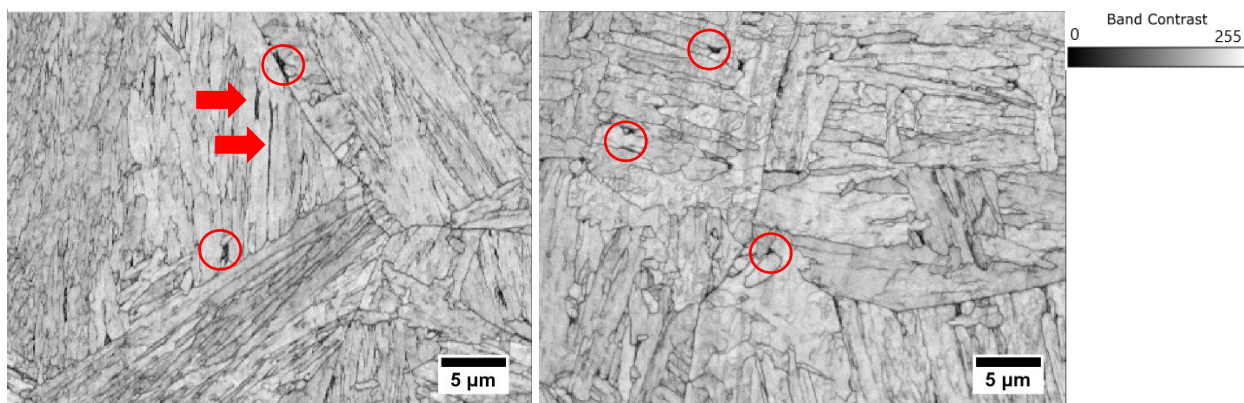
Fig. 5.5 EBSD BC map of 3B-1P a) and 3B-5P b) showing RA morphology.

In Fig. 5.6, misorientation of 3B-1P a) and 3B-5P b) in the ranges of 5~30°, 30~50° and >50° is shown in red, black and green lines, corresponding to lath boundary, PAG and packet/block boundary, respectively. The definition of lath boundary, PAG boundary and packet/block boundary is illustrated in Fig.5.7. As a product of displacive transformation, lath bainite has a similar structure with lath martensite: a PAG is divided into several packets, each of which consists of laths with the same habit plane (or the same parallel close-packed planes relationship) with respect to austenite; each packet is further divided into blocks, and laths in each blocks share the same orientation[196].
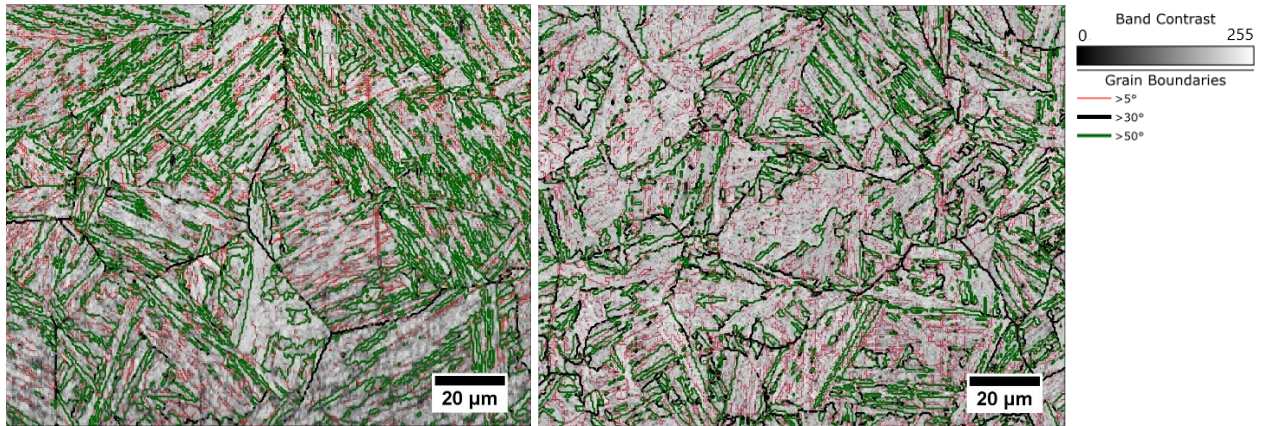
a)   b)

Fig. 5.6 EBSD BC+GB map of 3B-1P a) and 3B-5P b).
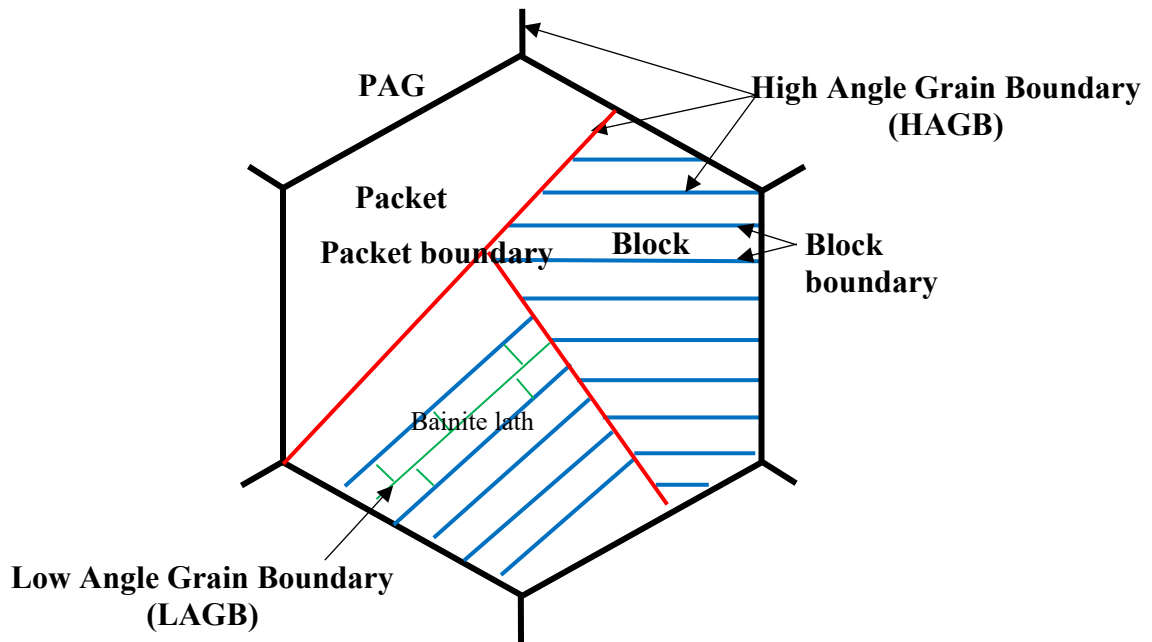
Fig. 5.7 Schematic illustration describing structure of lath bainite.

It has been reported [190, 197-199] that large driving force of transformation, such as high cooling rate/low transformation temperature, large undercooling, low carbon content, can lead to formation of more BF variants during nucleation to reduce the system energy by introducing less strain and interfacial energy to the system, which leads to fine blocks within the same packet. On

the contrary, small driving force, such as low cooling rate/high transformation temperature, small undercooling, high carbon content, gives rise to strong variant selection, and hence the formation of preferred variants is enhanced resulting in coarse bainite blocks (as shown in Fig. 5.8).
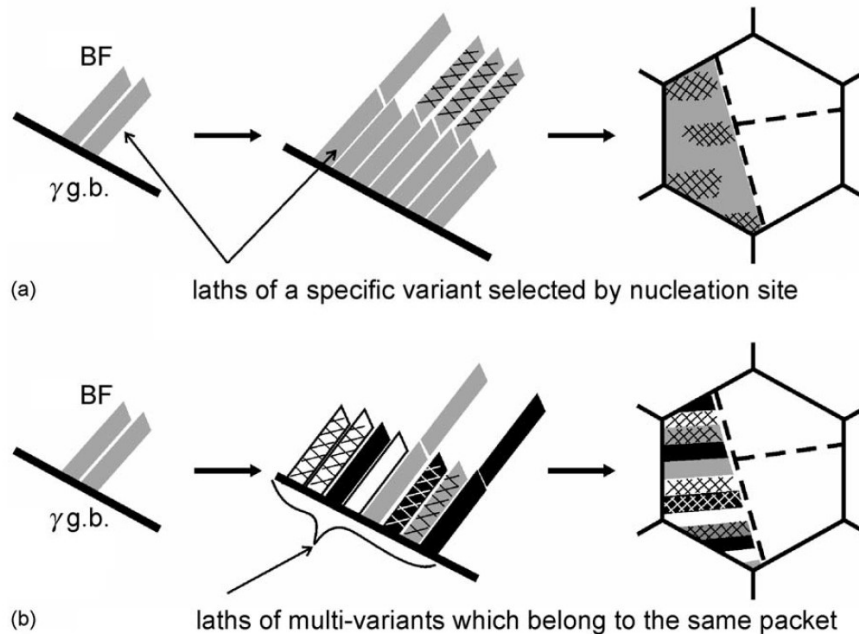
Fig. 5.8 Schematic illustration describing the formation of a bainite packet: a) for a small driving force and b) for a large driving force.[197]

According to Chen [200], the bainite transformation in sample with small PAG is retarded with increased incubation time and slow transformation velocity, indicating small driving force as compared with large PAG. Mandal [201] recently found that PAG size has a great influence on bainitic transformation kinetics: the higher PAG size the faster the transformation kinetics. Therefore, for the same reason mentioned above, PAG size has an influence on the variant selection and thickness of bainite blocks: large PAG size leads to BF with more variants and refined bainite blocks (3B-1P); small PAG size results in few variants and thick bainite blocks (3B-5P). This effect has been also observed by Zhao[190].

Beladi's work[199] shows that more variants with high misorientation angles (50°, 53.7°,60°) are selected at lower transformation temperature (higher driving force). This indicates that these variants are selected only when the driving force is high enough and self-accommodation of the transformation strain is encouraged. This explains the higher fraction of misorientation >50°

in 3B-1P than in 3B-5P shown in Fig.5.9: the PAG size of 3B-1P is larger than that of 3B-5P, which means higher driving force for 3B-1P as discussed above, and hence more variants with high misorientation angles were selected during the nucleation of bainitic ferrite.
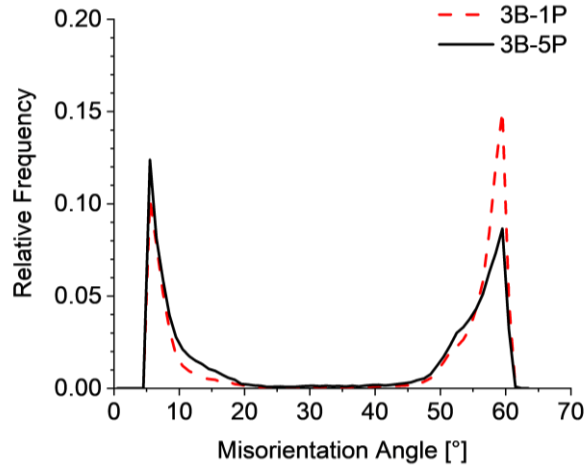
Fig. 5.9 Misorientation distribution of 3B-1P and 3B-5P.

However, it is observed that the morphology and misorientation distribution of bainite in 3E-4P-1P-OLAC is quite different from that of the bainite in 3B-1P and 3B-5P. As shown in Fig.5.10, the UB in 3E-4P-1P-OLAC are intricated bainitic ferrite with blocks of M/A constituents. And Fig.5.11 shows that the misorientation distribution of 3E-4P-1P-OLAC contains high fraction of low angle grain boundary (<20°) and low fraction of high angel grain boundary (45~60°). As mentioned above, 3E-4P-1P-OLAC has been through double-stage cooling process. The cooling rate during OLAC should be lower than that during water quench, and hence, led to formation of UB with strong variants selection due to small driving force. Therefore, variants with high misorientation angles are not preferred during nucleation in 3E-4P-1P-OLAC.
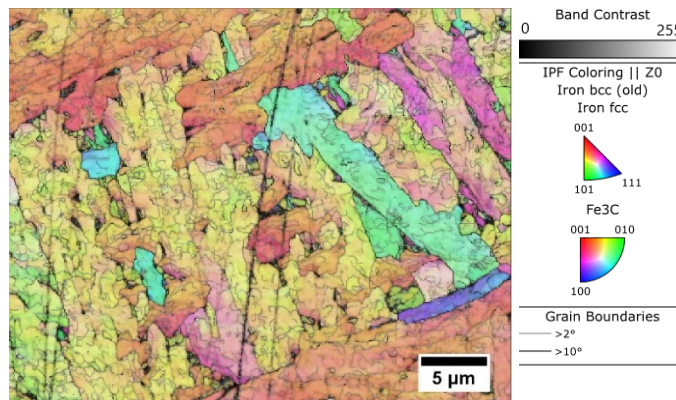
Fig. 5.10 EBSD BC+IPF+GB map of UB in 3E-4P-1P-OLAC
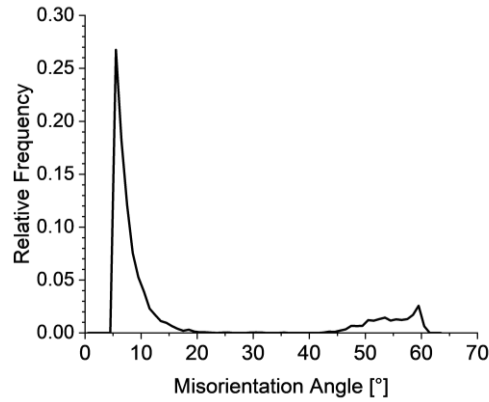
Fig. 5.11 Disorientation distribution in UB of 3E-4P-1P-OLAC (area shown in Fig.5.10)

According to Zajac[202], lower bainite (LB) and upper bainite (UB) can be reliably distinguished by the distribution of misorientations: LB contains high proportion of misorientation in the range of 50°~60° and low proportion in the range of <20°; whereas UB shows the opposite distribution mode (Fig. 5.12). This classification of bainite can be explained by the variant selection mechanism as mentioned above and is consistent with the observation in the present study.
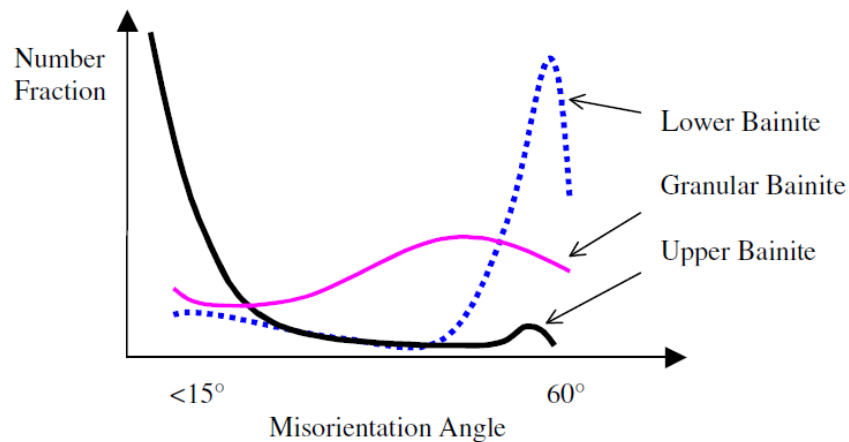
Fig. 5.12 Definition of bainite based on misorientation of distribution angles between grains/laths.[202]

Meanwhile, the large M/A blocks were formed in 3E-4P-1P-OLAC due to the relatively low cooling rate during OLAC, which results in sufficient dwelling time at high temperature for carbon diffusing into austenite; whereas in the plates that were directly water quenched from rough rolling temperature (1100°C) or soaking temperature (1250°C), only RA films or islands are present due to the high cooling rate.

5.1.4   Summary

The characterization results of Group II samples are summarized as below:

1) The microstructure of 3F-0P, 3B-1P, 3E-3P, 3B-5P and 3E-5P-4MIN consists of lower lath bainite and fine RA constituents between the laths; in 3E-5P-OLAC and 3E-4P-1P-OLAC, upper lath bainite with intricated or coarse bainitic ferrite is revealed in addition to LB and M/A.

2) The PAG size of Group II samples (except 3E-4P-1P-OLAC) decreases as the number of rough rolling passes increases due to crystallization; PAG size of 3E-4P-1P-OLAC is significantly larger than that of 3B-1P due to the grain coarsening during reheating after 4 passes of rough rolling.

3) PAG size has strong effect on morphology of lower lath bainite through variant selection mechanism: samples with large PAG size tend to have fine blocks since more variants, especially those with high angle misorientation, are selected during nucleation because of the high driving force of transformation, and vice versa.

4) PAG size has effect on morphology of upper lath bainite through carbon concentration mechanism: larger amount of coarse upper bainite laths is observed in 3E-4P-1P-OLAC with large PAGs as compared with 3E-5P-OLAC with small PAGs, which is attributed to the lower carbon concentration adjacent to bainitic ferrite within large PAG during transformation.

5) Cooling rate can affect the variant selection during nucleation: low cooling rate leads to formation of UB with limited number of variant selection (with low angle misorientation) due to the small driving force for transformation; whereas variants with high angle misorientation are also selected when transformation to LB occurred under high cooling rate.

5.2 Precipitates Analysis

Depending on the coherency between precipitates and matrix, some precipitates, such as nano-size NbC in Group I plates, are strong hydrogen irreversible traps, whereas some others have no trapping effect at all. As no nano-size NbC precipitates exist in Group II plates, the focus of this section is on large $(Nb,Ti)_x(C,N)_y$ precipitates, which are investigated by TEM and SEM in terms of morphology, size distribution and count density. Besides, the composition of the precipitates is also studied by means of EDS and Selected Area Electron Diffraction (SEAD) technique.

5.2.1 Morphology of precipitates

In 3F-0P, as it is shown in Fig.5.13a), only cuboidal TiN precipitates are observed, which means that no NbC precipitates was generated at soaking temperature. Fig.5.13 also shows the morphology of TiN precipitate in 3F-0P a) and NbC-TiN complex precipitates in 3B-1P b), 3E-3P c), 3B-5P d), and 3E-5P-4MIN e,f), indicating heterogenous nucleation of NbC on pre-existing TiN precipitates for lower free energy of the nucleation. These TEM images reveal the growing process of NbC nucleated on cuboidal TiN during rough rolling process and the extensive growth of NbC in 3E-5P-4MIN when the plate was hold at rough rolling temperature (~1000°C). It is shown that the NbC precipitates grow as the number of rough rolling pass increased or as the holding time extended. Besides, unlike in Group I plates, which have been through finish rolling and OLAC process, neither large NbC (>20 nm) nor nano-size NbC (<20 nm) precipitates were observed in these Group II plates. This means the driving force for homogenous nucleation of NbC is not reached at this temperature. Some researchers supposed that the epitaxial growth of NbC on pre-existing TiN could lead to depletion of solute Nb in matrix and hence suppress the precipitation of NbC in successive processes. [185, 186] Therefore, the rough rolling process can still influence hydrogen resistance of the steel by affecting the concentration of solute Nb in matrix for the precipitation of nano-size NbC.
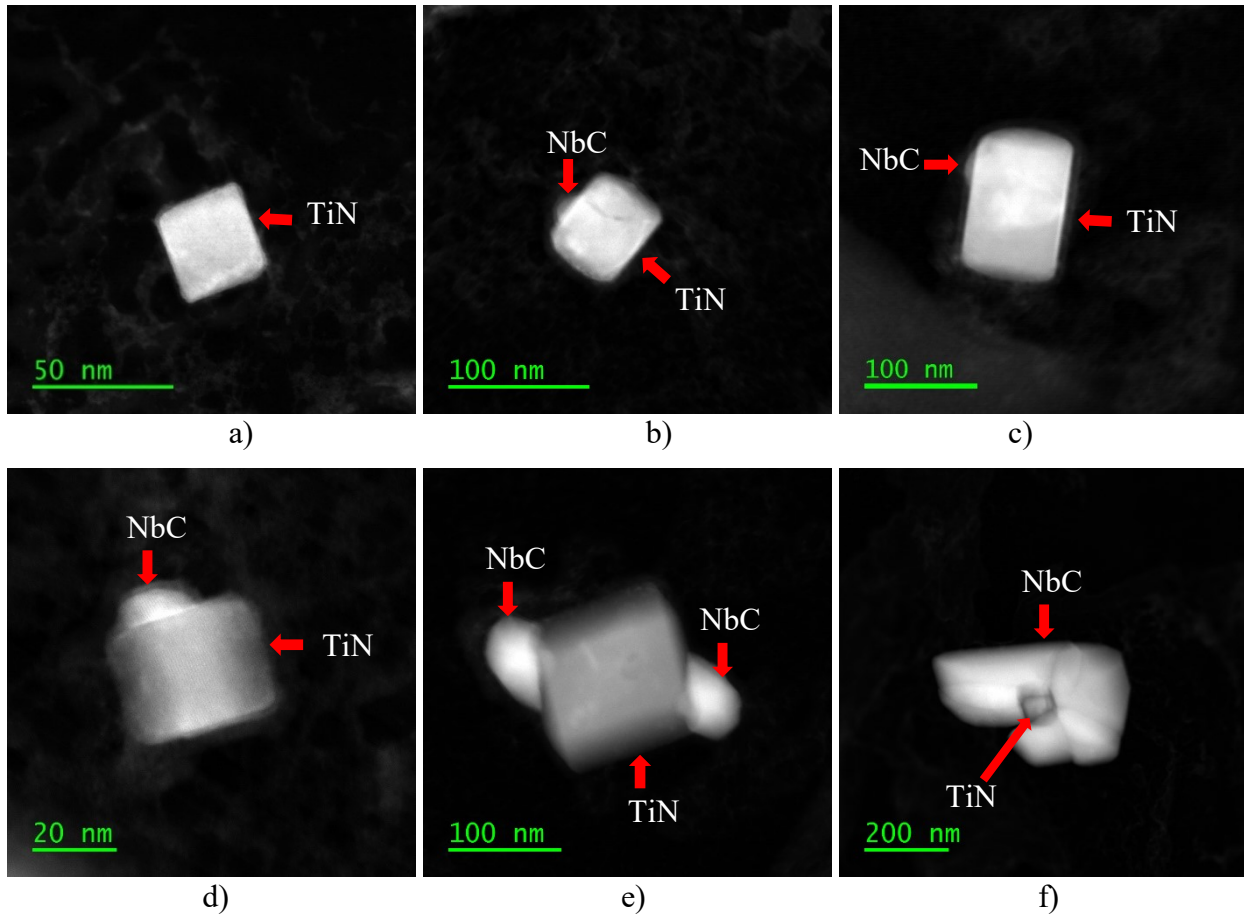
Fig. 5.13 Morphology of TiN precipitate in 3F-0P a) and NbC-TiN complex precipitates in 3B-1P b); 3E-3P c); 3B-5P d); 3E-5P-4MIN e,f).

5.2.2 Composition of precipitates

The composition of the complex precipitates was analyzed by EDX. It is shown that the cuboidal precipitates are Ti-rich and the heterogeneously nucleated spherical precipitates are Nb-rich (as seen in Fig. 5.14-15). As TiN precipitation temperature (~1500°C) is close to the solidus temperature of microalloy steel, these cuboidal precipitates are formed during solidification of the steel and survived the soaking process (1260°C). Since NbC starts to precipitate at about 1140°C[184], when temperature dropped to 1100 °C during rough rolling, NbC co-precipitated on the habit plane of pre-existing TiN particles and coarsened with increased rough rolling pass/time.
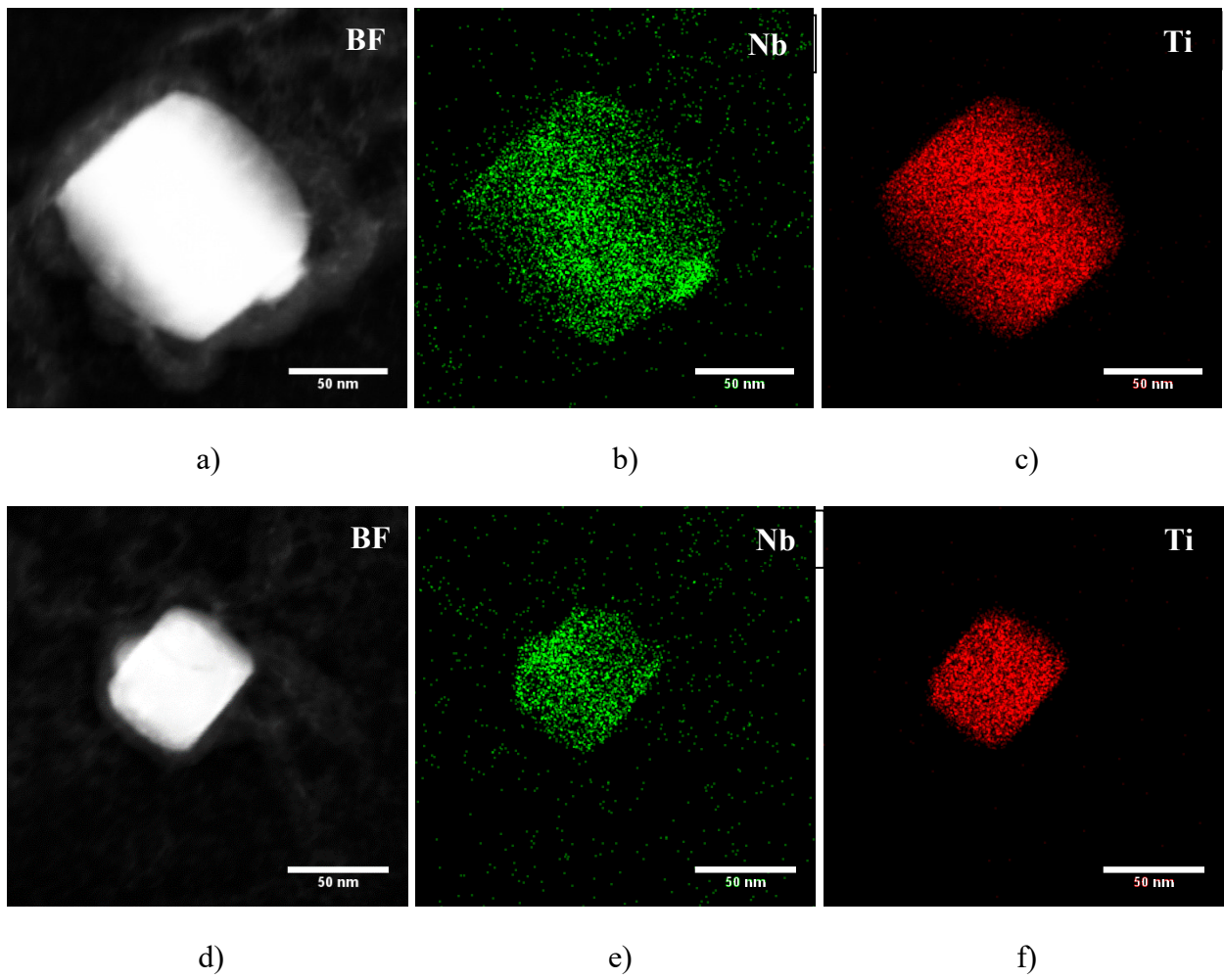
Fig. 5.14 EDX composition mapping of NbC-TiN complex precipitates in 3B-1P.
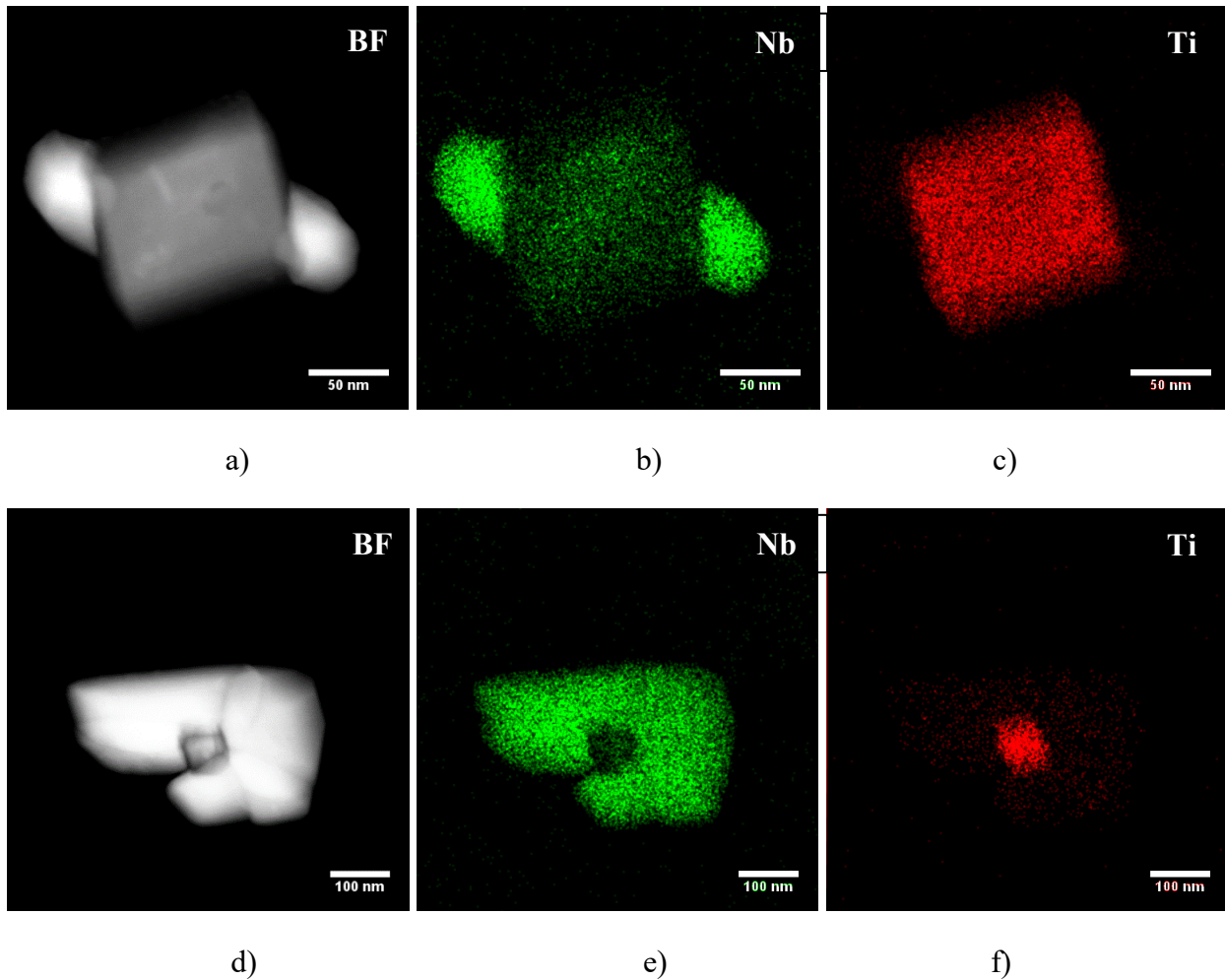
Fig. 5.15 EDX composition mapping of NbC-TiN complex precipitates in 3E-5P-4MIN.

Fig. 5.16 shows the SAED patterns of precipitates in 3F-0P, indicating that both the small cuboidal particles (~100 nm) and the large, elongated ones (~2 µm) are TiN precipitates, which might be formed during solidification process and pre-exist in liquid steel, respectively. As only one diffraction pattern is shown, it can be confirmed that no other crystal structure co-exists with TiN at the soaking temperature. By contrast, after 5 passes rough rolling and 4 min holding at 1100~1000 °C (3E-5P-4MIN), the diffraction pattern for NbC is shown in both the ring pattern of a group of complex precipitates and the spot pattern of a single NbC/TiN precipitate (as seen in Fig. 5.17). It is also suggested that NbC nucleated on the (111) plane of TiN (Fig.5.17d), which is consistent with the prediction that (111) plane is the NbC/TiN heterogeneous nucleation interface with highest priority based on first principles calculation[203].
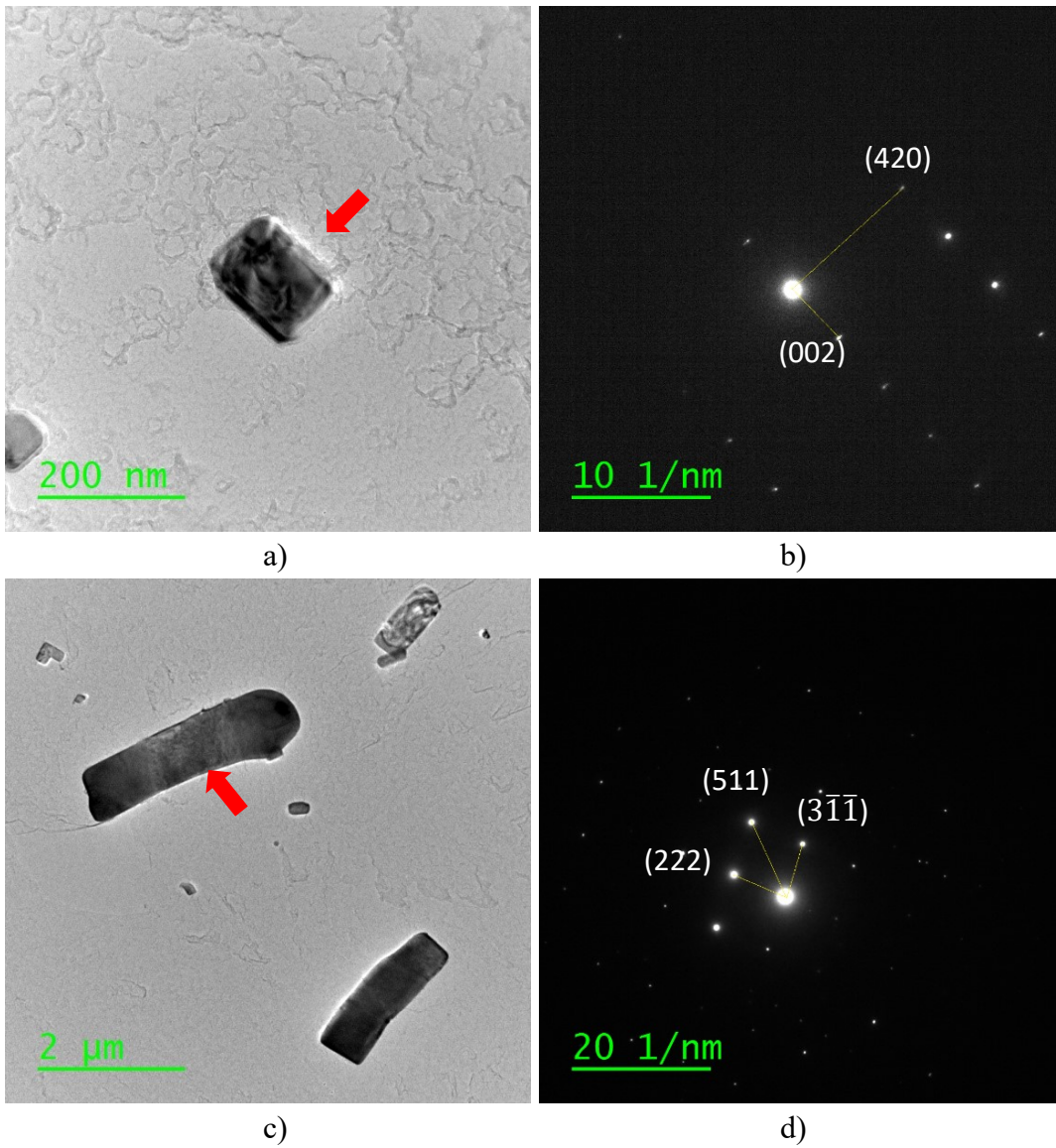
Fig. 5.16 SAED patterns b,d) of selected small a) and large b) TiN precipitates in 3F-0P.
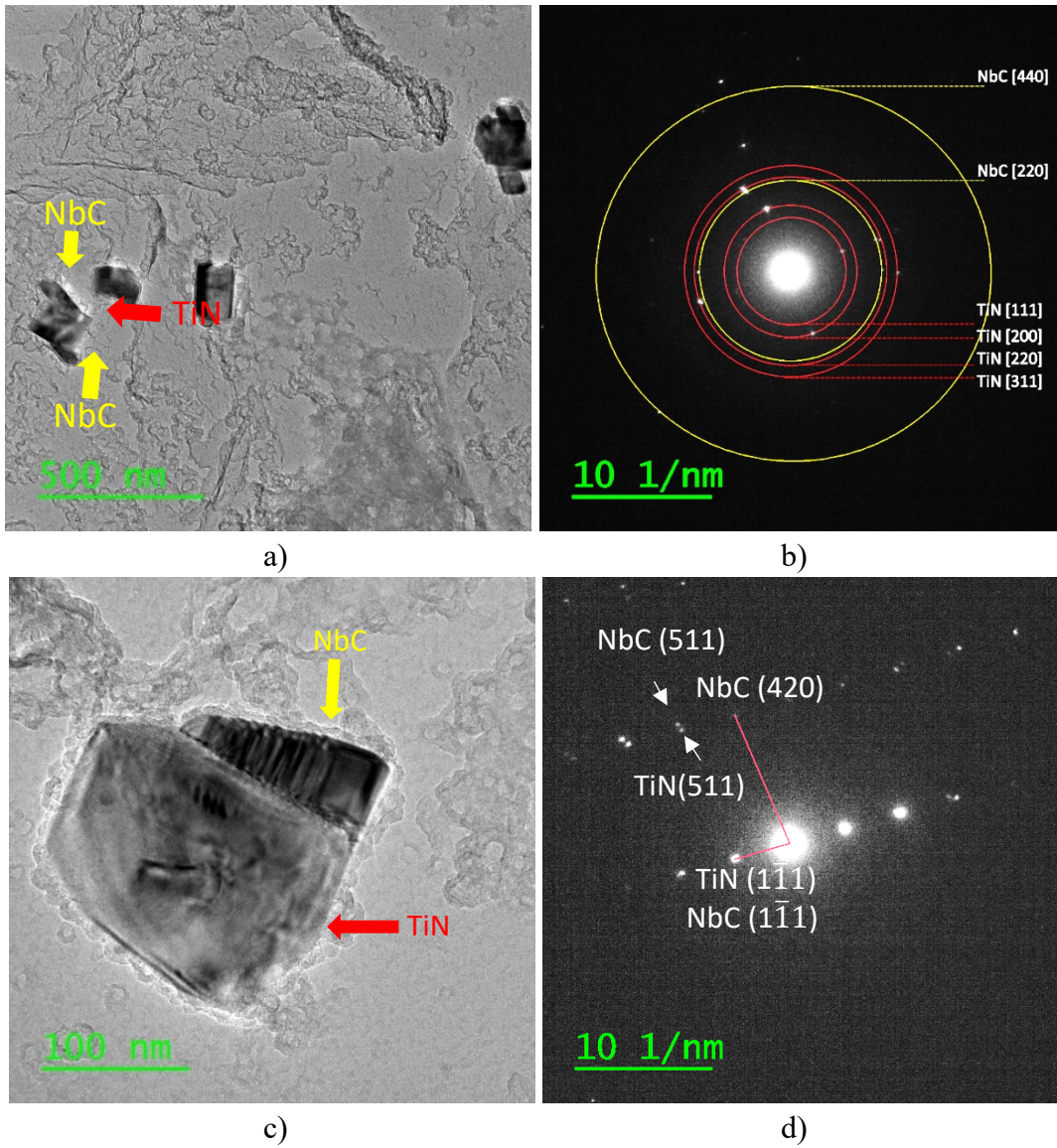
Fig. 5.17 SAED ring pattern b) of a group of NbC-TiN precipitates a) and SAED spot pattern d) of single NbC-TiN precipitate c) in 3E-5P-4MIN.

5.2.3   Size and density of precipitates

The size of these TiN/NbC-TiN precipitates was measured via Gatan® software using threshold method (detailed procedure about the measurement is described in section 3.2.2). Fig. 5.18 shows size distribution data and lognormal fitting curve of plates 3F-0P, 3B-1P, 3E-3P, 3B-5P and 3E-5P-4MIN. The mean values of these precipitates obtained by lognormal fit are listed in Table 5-2. As it is shown in Table 5-2, the size of these TiN/NbC-TiN precipitate slightly increased during the rough rolling process due to the growth of TiN precipitates as well as the heterogenous nucleation of NbC.

Table 5-2 Mean value of diameter of TiN/ NbC-TiN precipitates by lognormal fitting.

Sample	Mean/nm	STD/nm
3F-0P	96.0	1.4
3B-1P	119.0	3.3
3E-3P	121.2	3.5
3B-5P	121.3	4.2
3E-5P-4MIN	121.5	0.2

Count density (i.e., number of precipitates per unit area) of TiN/complex precipitates in each Group II sample was measured on 5 SEM images (30k ×, in-lens detector), and the statistically analyzed results are shown in Fig. 5.19. The count density gradually increases with the number of rough rolling passes, and almost doubled after holding for 4 minutes. Therefore, the precipitation of TiN continues during rough rolling and holding process. (Typical SEM images for the count density measurement are shown in Appendix C-3).
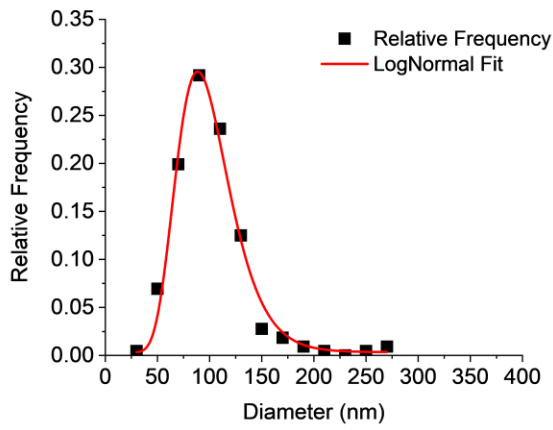
a)
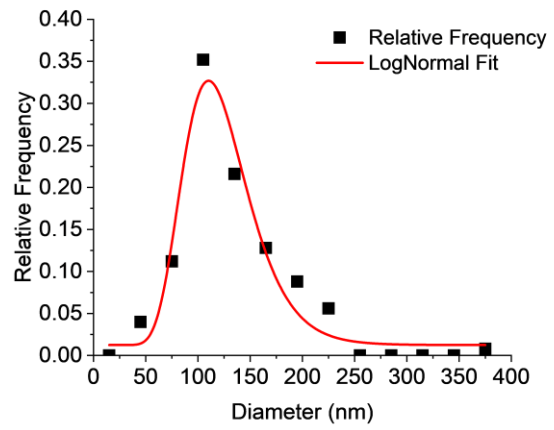
b)
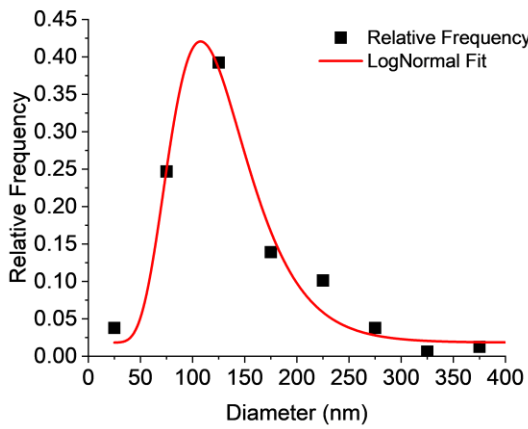
c)
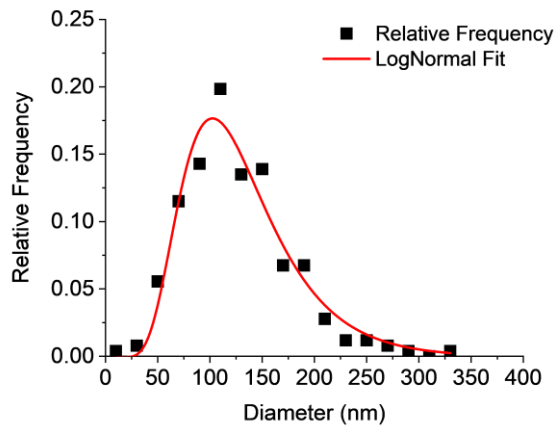
d)
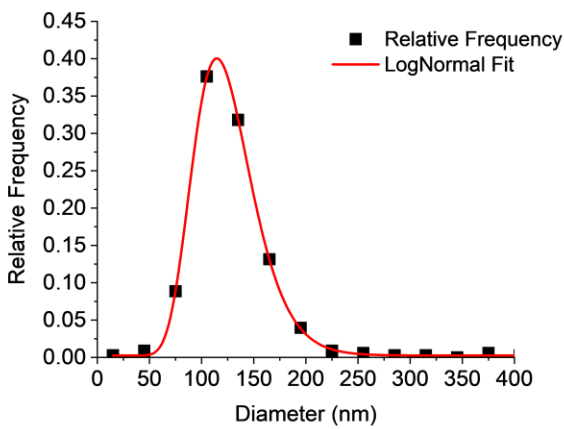
e)

Fig. 5.18 Size distribution of TiN precipitates in 3F-0P a) and complex NbC-TiN precipitates in 3B-1P b), 3E-3P c), 3B-5P d) and 3E-5P-4MIN e).

Count density (i.e., number of precipitates per unit area) of TiN/complex precipitates in each Group II sample was measured on 5 SEM images (30k ×, in-lens detector), and the statistically analyzed results are shown in Fig. 5.19. The count density gradually increases with the number of rough rolling passes, and almost doubled after holding for 4 minutes. Therefore, the precipitation of TiN continues during rough rolling and holding process. (Typical SEM images for the count density measurement are shown in Appendix C-3).

Sample	3F-0P	3B-1P	3E-3P	3B-5P	3E-5P-4MIN
Count Density	0.5	0.56	0.71	0.91	1.82
STD	0.04	0.07	0.14	0.32	0.22
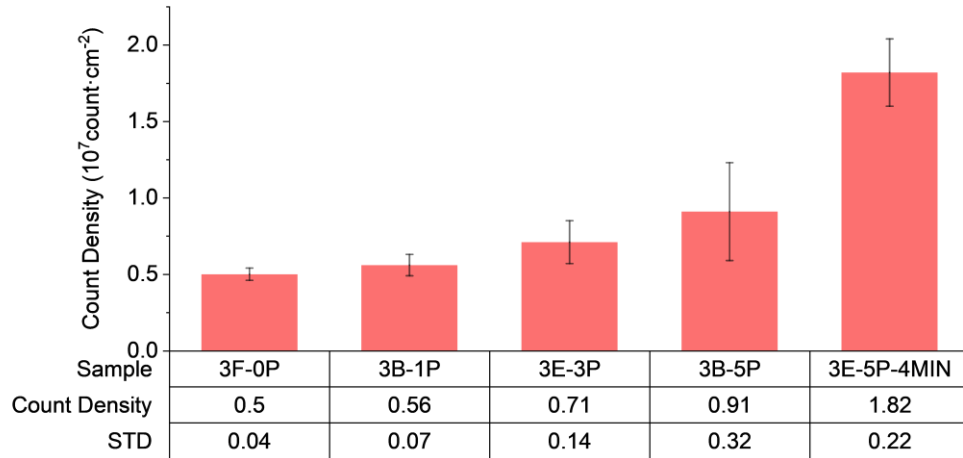
Fig. 5.19 Count density of TiN/complex precipitates in Group II samples.

5.2.4 Summary

The characterization results of TiN/complex precipitates in Group II samples are summarized as below:

1)   No homogeneously nucleated NbC precipitate is found in Group II samples, however, it is shown that as the temperature dropped to about 1100 °C during rough rolling process, NbC co-precipitated on (111) habit plane of pre-existing TiN particles and coarsened with increased rough rolling pass/time.

2)   The size of the complex TiN-NbC precipitates is obviously larger than the pre-existing TiN precipitates and grows slowly during rough rolling process.

3)   Although TEM images show considerable coarsening of NbC, the average size of the complex precipitates did not change much after being hold at rough rolling temperature for 4

min, which is probably because it is averaged out by large amount of small TiN precipitates that just nucleated.

4)   The count density of these $(Nb,Ti)_x(C,N)_y$ precipitates increased gradually with the rough rolling pass, and almost doubled after holding for 4 min.

5.3   Hydrogen permeation test (HPT) results

According to HPT results of Group I plates, centerline segregation has great influence on H diffusivity. Therefore, in this section, HPT was only carried on surface samples of Group II plates far away from centerline region. The experimental data were analyzed using two methods, i.e., lag time method and curve-fitting method, which give parameters such as effective diffusion coefficient (D_{eff}) and trap density (N_t). Based on these results, the effect of precipitates, PAG, phases were evaluated and associated with TMCP parameters. The original testing results are shown in Appendix B-6.

5.3.1   Data analysis using time-lag method

Figure 5.20 shows a typical normalized oxidation current curve of surface sample of 3E-5P-4MIN, wherein I represents oxidation current and I_{ss} represents the oxidation current at steady state. (The normalized oxidation current curves of other plates are shown in Appendix C-4). For all samples, the oxidation current starts to rise (i.e., break-through time) and reach to steady state much earlier during the 2nd transient than during the 1st transient, indicating the existence of large amounts of irreversible traps in the sample, which only trapped H atoms and delay the diffusion of H flux during the 1st transient and are occupied and inactive during the second transient. Based on these curves, the effective diffusion coefficients (D_{eff}) are calculated by time-lag method and tabulated in Table 5-3. Apparent surface concentration (c_{app}), total trap density (N_t), irreversible trap density ($N_{t,ir}$) and reversible trap density ($N_{t,r}$) are also calculated according to the method shown in section 3.3.5.

Table 5-3 Hydrogen permeation parameters of Group II samples in 1st and 2nd transient.

Sample	Transient	t_{lag} 10^3 s	D_{eff} 10^{-7} cm^2·s^{-1}	c_{app} 10^{-5} mol·cm^{-3}	N_t 10^{-4} mol·cm^{-3}	$N_{t,ir}$ 10^{-4} mol·cm^{-3}	$N_{t, r}$ 10^{-4} mol·cm^{-3}
3F-0P	1st	48.8	1.47	12.72	9.23	7.52	1.70
	2nd	9.06	7.95	2.32	1.70		
3B-1P	1st	37.3	1.93	6.12	7.05	5.42	1.62
	2nd	8.64	8.33	1.28	1.62		
3E-3P	1st	30.6	2.35	3.34	5.78	3.57	2.21
	2nd	11.8	6.13	1.94	2.21		
3B-5P	1st	26.5	2.71	4.52	5.01	2.88	2.13
	2nd	11.3	6.35	1.69	2.13		
3E-5P-4MIN	1st	27.1	2.66	5.50	5.12	3.10	2.01
	2nd	10.7	6.73	2.05	2.01		
3E-5P-OLAC	1st	30.7	2.35	3.62	5.79	3.17	2.62
	2nd	13.9	5.17	2.05	2.62		
3E-4P-1P-OLAC	1st	37.5	1.92	2.47	7.08	5.63	1.45
	2nd	7.73	9.32	0.53	1.45		

a)   b)
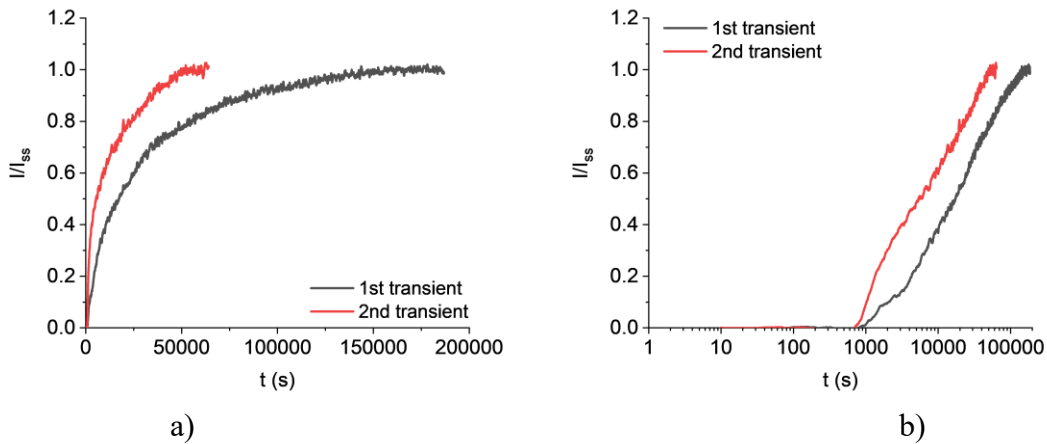
Fig. 5.20 Normalized hydrogen permeation curve of 3E-5P-4MIN during 1st and 2nd transient on a) linear scale and b) logarithmic scale.

For all Group II samples, the D_{eff} during the 2nd transient is considerably higher than that during 1st transient as seen in Fig. 5.21. However, the variation mode of the D_{eff} during 1st and during 2nd transient are different, since the TMCP parameters affect the reversible traps and irreversible traps in different ways. As shown in Fig. 5.22, the reversible trap density varied slightly between 1.45×10^{-4} mol·cm^{-3} and 2.62×10^{-4} mol·cm^{-3}; whereas the irreversible trap density substantially decreased from 7.10×10^{-4} mol·cm^{-3} to 2.18×10^{-4} mol·cm^{-3} as the number of rough rolling passes increased from 0 to 5.
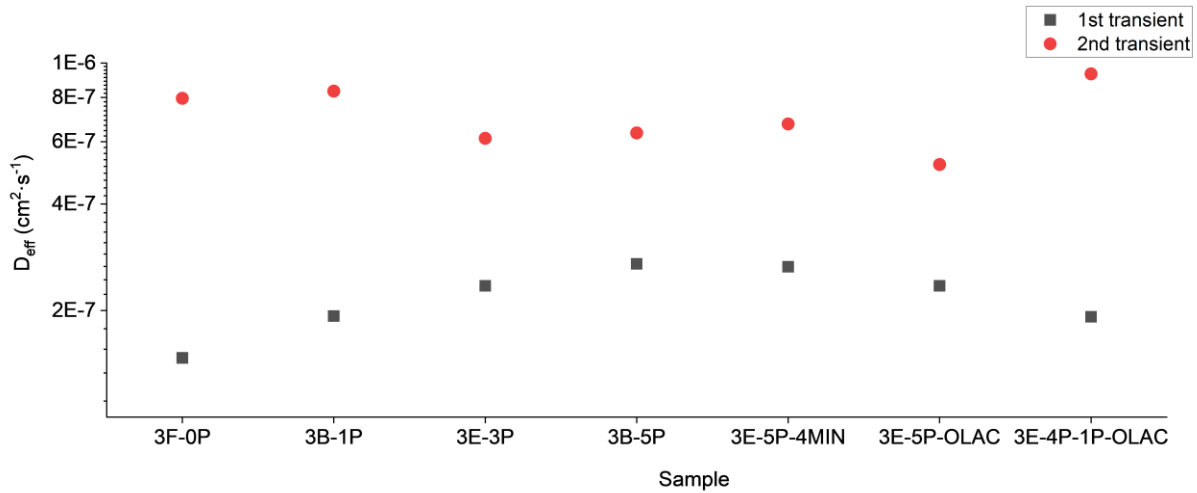
Fig. 5.21 Effective diffusion coefficient (D_{eff}) of Group II samples during 1st and 2nd transient.
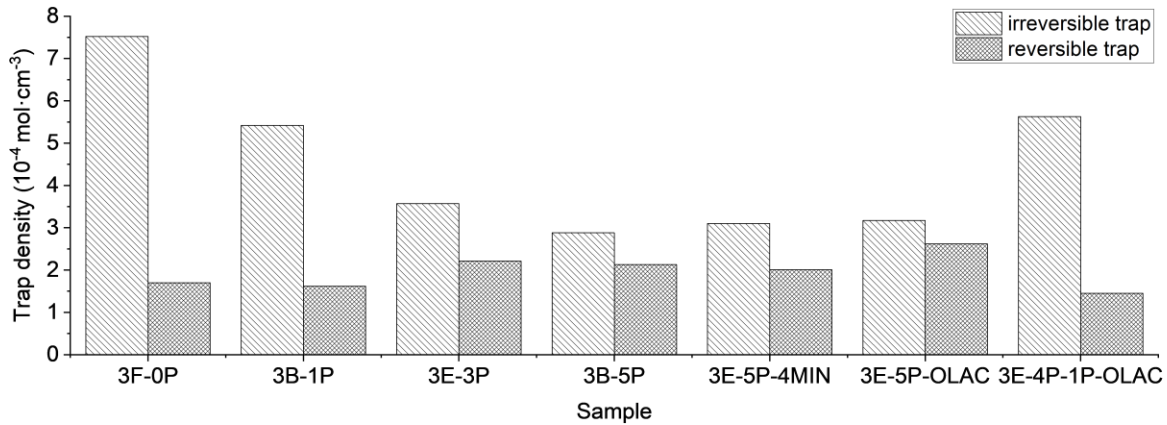
Fig. 5.22 Irreversible and reversible trap density of Group II samples.

In Fig. 5.23, the irreversible trap density of Group II plates exponentially decreased with the number of rolling passes with consistency: points of 3E-5P-4MIN and 3E-5P-OLAC almost overlap the point of 3E-5P. It should be noted that both 3E-4P-1P-OLAC and 3E-5P-OLAC contain certain fractions of UB in addition to LB, whereas all the other Group II plates mainly consist of lath LB. However, as LB is still the dominant phase in 3E-5P-OLAC, $N_{t,ir}$ of the plate still follows the exponentially decreasing trend shown in Fig. 5.23.

Using irreversible trap density of 3F-0P, 3B-1P, 3E-3P and 3B-5P, a semi-empirical equation is obtained as follows by curve fitting:

$$N_{t,ir} = N_0 + A_{ir} \times e^{b_{ir} \times n_{roll}} \tag{5-1}$$

Wherein $N_{t,ir}$ is irreversible trap density; n_{roll} is number of rough rolling passes; N_0 is the density of other types of irreversible traps such as inclusions and equals to 2.57×10^{-4} mol·cm^{-3}; A_{ir} and b_{ir} are constants, which equal to 4.9×10^{-4} and -0.54, respectively. As the number of rough rolling passes increased, $N_{t,ir}$ gradually approaches to 2.57×10^{-4} mol·cm^{-3}, which can be seen as the influence of inclusions.

As mentioned in section 5.1.2, increasing number of rough rolling passes leads to more sufficient crystallization and finer PAGs. And EBSD results suggested that the PAG size has effect on thickness of bainite blocks through variant selection mechanisms, i.e. smaller PAG gives rise

137

to thicker bainite blocks, and vice versa. Moreover, EBSD GB map shows that the block/packet boundaries are high angle grain boundaries (HAGBs) with misorientation angle larger than 50°, which was also found by some other researchers[165, 169]. It is reported that the binding energy of these block/packet boundaries is about 47.4 kJ/mol and classified as irreversible traps[165, 204]. Therefore, increasing rough rolling passes can eventually lead to decrease in irreversible trap density and increase in hydrogen diffusivity, as it is shown in Fig.5.24.

Since all Group II samples for hydrogen permeation test were machined from close to surface region, the inclusion density in all samples is reasonably considered to be equal. Besides, no nano-sized precipitates are observed in any Group II plates as they have been directly cooled down from rough rolling temperature without sufficient time for initiation/growth of fine NbC precipitates. Also, both size and density of complex NbC/TiN precipitates increased with rough rolling passes and holding time, which shows opposite trend with the irreversible trap density obtained by hydrogen permeation test, indicating that the complex NbC/TiN precipitates did not act as irreversible traps. As the effect of all the other microstructural features have been excluded, the variation of measured irreversible trap density exclusively reflects the trapping effect of HAGBs, i.e., packet/block boundaries.

Moreover, it is also shown in Fig. 5.22 that the irreversible trap density of 3E-1P-4P-OLAC is obviously higher than that of 3E-5P-OLAC, which is associated with the higher fraction of UB in the former. During OLAC process, the relatively low cooling rate (as compared with WQ) results in the formation of UB with M/A constituents dispersed between laths. The M/A-UB interface, classified as second phase interphase, act as irreversible traps during HPT, significantly increasing the $N_{t,ir}$. Therefore, the discrepancy of $N_{t,ir}$ in 3E-4P-1P-OLAC and 3E-5P-OLAC basically reflects the different irreversible trapping ability of UB and LB, i.e., UB>LB. Similar conclusion has also been drawn by Chan [133] in his study about the hydrogen trapping ability of different microstructures in steels, wherein UB was found to contain larger amount of residual hydrogen than LB after being charged with hydrogen gas and stored for two weeks/heated in a vacuum.

In sum, under high cooling rate of water quenching, PAG boundary can impede growth of lower bainite lath and hence reduce the number of HAGBs (i.e., block/packet boundaries) per volume, whereas during OLAC, small PAG size gives rise to lower fraction of UB, which contains

large amount of M/A-ferritic lath interface as irreversible traps. Therefore, in general, PAG size is positively correlated to the $N_{t,ir}$ in both UB and LB, as shown in Fig.5.22, although via different mechanisms.

On the other hand, as seen in Fig. 5.22, the difference in reversible trap density of most Group II plates (except 3E-4P-1P-OLAC) is minor and beyond the accuracy of HPT, although as the rough rolling pass increases the PAGs size is reduced, and more dislocation were introduced into the skelp, both leading to higher $N_{t,r}$. However, the $N_{t,r}$ of 3E-4P-1P-OLAC is obviously lower than that of 3E-5P-OLAC, which is probably due to the lower reversible trapping efficiency of UB (higher fraction in the former) than that of LB (higher fraction in the latter). Since LB transformation occurs at a lower temperature than UB, the carbon atoms and other solute atoms are more likely to retain inside LB laths rather than diffuse out of the laths. This gives rise to increasing amount of lattice imperfections, which are ideal reversible trapping sites within ferritic laths. Therefore, on the contrary to irreversible trapping ability, the reversible trapping efficiency of LB is higher than that of UB.
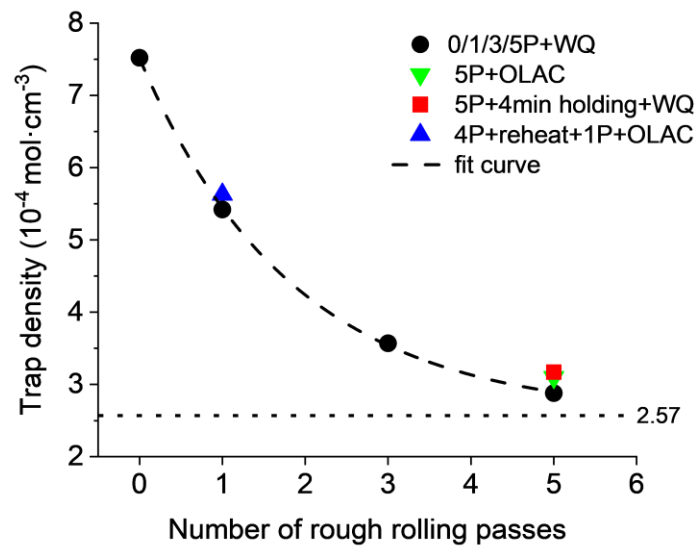
Fig. 5.23 Effect of rough rolling passes on irreversible trap density.
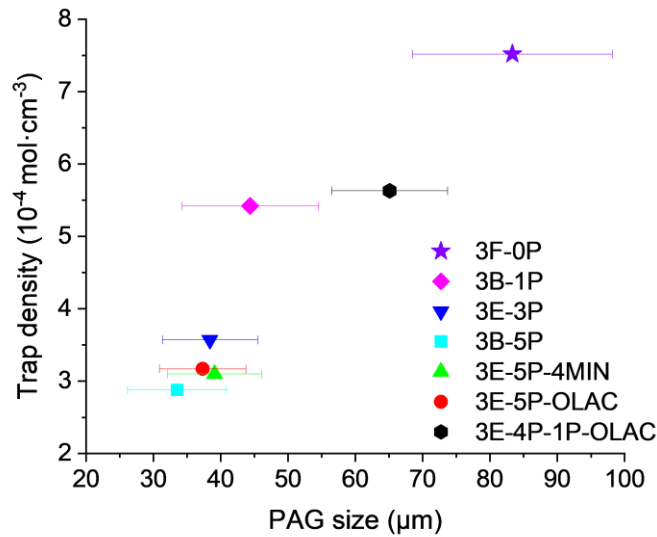
Fig. 5.24 Relationship between PAG size and irreversible trap density of Group II plates.

5.3.2 *Data analysis using curve-fitting method*

In this section, the hydrogen permeation curves of Group II samples are analyzed by curve-fitting method using equations (3-3) and (3-4), which are the solutions to Fick's Second Law based on boundary conditions of constant flux and constant concentration on the entrance side of the sample, respectively. The curve-fitting results of 1st transient and 2nd transient of 3F-0P sample is shown in Fig.5.25 on both linear scale and logarithmic scale as an example. (The curve-fitting results of other Group II samples are in Appendix C-4). And the diffusion coefficient (D_{eff}) values obtained by curve-fitting are listed in Table 5-4, along with the D_{eff} calculated by time-lag method for comparison.

By comparing the D_{eff} values obtained based on two boundary conditions, i.e., constant flux and constant concentration, we can find that the relative standard error (RSE) of the former is always smaller than that of the latter, except in the 2nd transient of 3E-1P-4P-OLAC, where RSE under the two conditions are the same. This indicates that the constant flux should be reasonably accepted as the boundary condition for the hydrogen permeation test that use galvanolstat to provide constant current during the charging process. This is constant with the conclusion drawn from the hydrogen permeation results of Group I samples in Chapter 4.
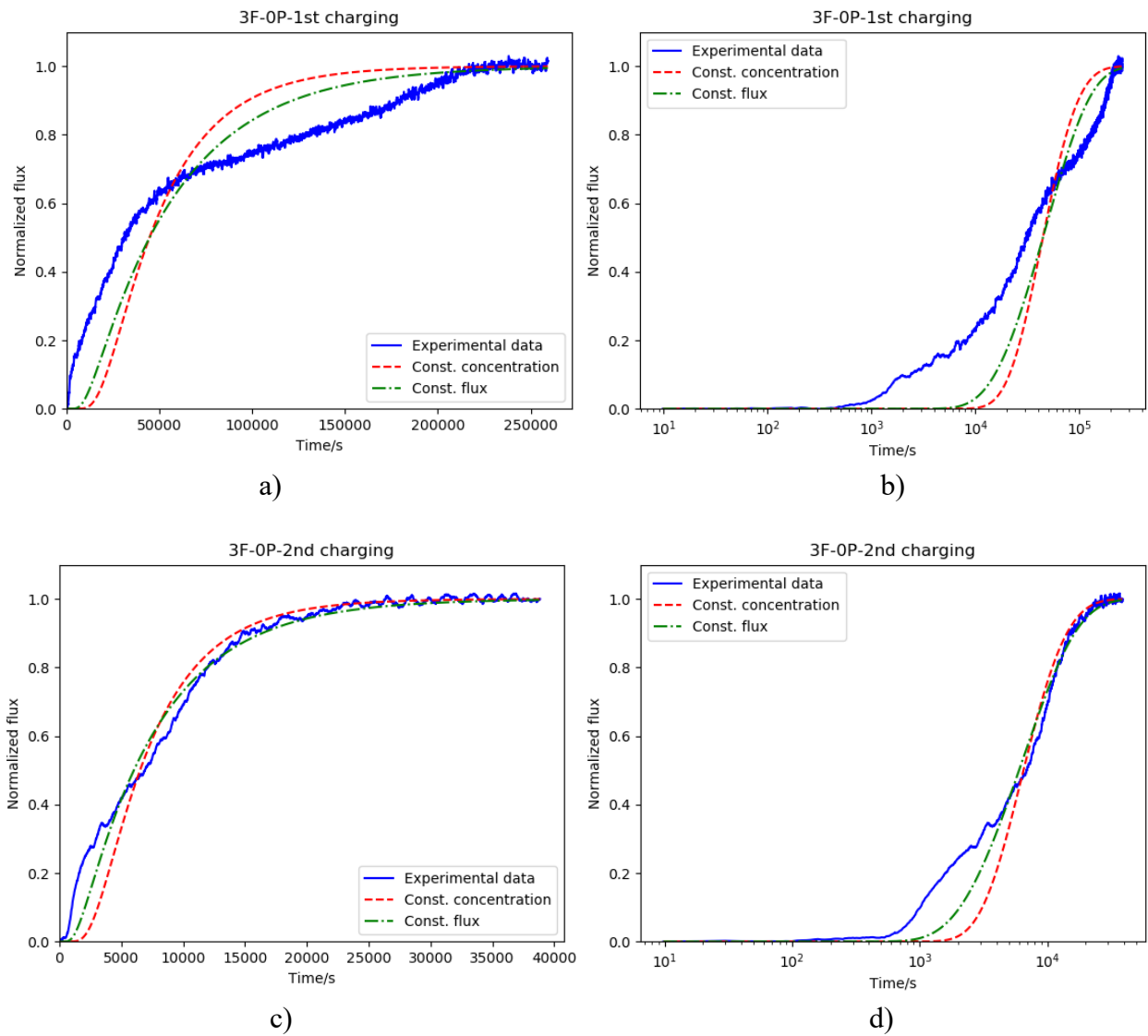
Fig. 5.25 Curve-fitting of experimental hydrogen permeation data with constant concentration and constant flux boundary conditions (3F-0P).

Table 5-4 D_{eff} of Group II samples obtained by curve-fitting method in comparation with D_{eff} calculated by time-lag method.

Plate	Transient	Curve-fitting method				Time-lag method (Const. flux)
		Const. concentration		Const. flux		
		D_{eff} $10^{-7}cm^2 \cdot s^{-1}$	RSE[3]	D_{eff} $10^{-7}cm^2 \cdot s^{-1}$	RSE	D_{eff} $10^{-7}cm^2 \cdot s^{-1}$
3F-0P	1st	0.45	0.27%	1.22	0.22%	1.47
	2nd	3.07	0.35%	9.07	0.25%	7.95
3B-1P	1st	0.63	0.23%	1.78	0.17%	1.93
	2nd	2.78	0.70%	7.29	0.61%	8.33
3E-3P	1st	0.78	0.37%	2.14	0.33%	2.35
	2nd	2.27	0.49%	6.42	0.39%	6.13
3B-5P	1st	0.95	0.25%	2.68	0.18%	2.71
	2nd	2.18	0.53%	5.91	0.43%	6.35
3E-5P-4MIN	1st	0.89	0.29%	2.52	0.23%	2.66
	2nd	2.24	0.59%	6.43	0.48%	6.73
3E-5P-OLAC	1st	0.78	0.28%	2.23	0.23%	2.35
	2nd	1.72	0.51%	6.08	0.40%	5.17
3E-4P-1P-OLAC	1st	0.64	0.27%	8.69	0.21%	9.32
	2nd	3.11	0.38%	9.40	0.38%	10.00

---

[3] RSE: Relative standard error, is equal to the standard error of a survey estimate divided by the survey estimate and then multiplied by 100.

5.3.3 *Summary*

The results and analysis of hydrogen permeation tests for Group II samples are summarized as follows:

1) For LB dominated plates, the irreversible trap density decreases exponentially with rough rolling passes.

2) In addition to inclusions, block/packet boundaries of lath bainite and M/A-ferritic lath interface are the main irreversible traps in LB and UB, respectively.

3) PAG size is positively correlated with irreversible trap density in both LB and UB.

4) Large TiN precipitates/NbC-TiN complex precipitates (~100 nm) are not effective hydrogen traps.

5) Curve-fitting equation with constant flux boundary condition fits the HPT curves better than that with constant concentration boundary condition.

6 Hydrogen trapping models

In this chapter, two hydrogen diffusion models are proposed based on the hydrogen permeation test results and characterization results in chapter 4 and 5. The trapping efficiency model is established to quantitatively evaluate the trapping efficiency of different phases, including ferrite, bainite, martensite and M/A constituents. The second model is a numerical simulation model that consists of two parts: reversible trapping and irreversible trapping. This model reveals how the trap density and binding energy of reversible/irreversible traps affect the hydrogen diffusion process during 1st and 2nd transient of hydrogen permeation test, and with experimental data, can be used to estimate the effective diffusion coefficient (D_{eff}) during the 2nd transient and the trap density ($N_{t,ir}$) and binding energy of irreversible traps (E_i).

6.1 Trapping efficiency model

The present model aims to estimate the trapping efficiency[4] of each phase in X70 pipeline steel, i.e., ferrite, bainite, martensite and M/A constituents, based on the assumption that the trapping ability of each phase in the same plate is constant.

6.1.1 Theory of the model

Hydrogen diffusivity in multi-phase steel is closely related to the type of phases and the proportion of each phase. Hydrogen diffusion behavior in a phase is determined by the lattice structure of the phase since the main hydrogen diffusion mechanism in steel is lattice diffusion by interstitial jumps. Ferritic structure (bcc) has higher diffusion rate and lower solubility than austenitic structure (fcc); whereas the diffusion rate in martensite (bct) is between ferritic and austenitic structure[205]. Moreover, from the perspective of hydrogen trapping effect, microstructural imperfections such as dislocations, voids, grain boundaries, solute atoms, etc., are all effective traps that could significantly influence the diffusivity, the amount of which varies from phase to phase. For example, martensitic structure provides large amount of trapping site due to the high dislocation density; lath boundaries in martensite and bainite act as strong traps; solutes

---

[4] Trapping efficiency, in the present study, is defined as the number of hydrogen traps provided by per unit volume of the phase.

like Cr and Mo in remained austenite may also contribute to the trapping effect[45, 133, 136, 206]. It is reported that the existence of small amount of M/A constituent, which is a combination of martensite and retained austenite, can considerably decrease the hydrogen diffusivity[139, 207]. Park listed degenerated pearlite (DP), acicular ferrite (AF), bainite (B) and M/A constituents as the key microstructures that affect hydrogen diffusivity in high strength pipeline steels[45].

The trapping ability of these phases have been qualitatively compared by many researchers. Park concluded that acicular ferrite has higher trapping efficiency than bainite[45]. However, few of them evaluated the trapping efficiency of different phases quantitatively. In this section, a semi-empirical model is proposed to quantitatively evaluate the trapping efficiency of ferrite, bainite, M/A and martensite and to estimate the diffusivity of multi-phase pipeline steel based on the characterization results and hydrogen permeation results of Group I plates. Only data of 2nd transient of hydrogen permeation tests are adopted to exclude the influence of irreversible traps such as inclusions and precipitates.

Gesnouin et al.[208] proposed a model estimating hydrogen diffusivity of duplex microstructure steels with two extreme patterns:

a. Parallel configuration: $\emptyset = \emptyset_\gamma X_\gamma + \emptyset_\alpha (1 - X_\gamma)$ (6-1)

b. Series configuration: $\emptyset = \dfrac{1}{\frac{X_\gamma}{\emptyset_\gamma} + \frac{1 - X_\gamma}{\emptyset_\alpha}}$ (6-2)

where $\emptyset$ is the global permeation coefficient of the biphasic material, $\emptyset_\alpha$ and $\emptyset_\gamma$ are the permeation coefficients of the martensite and austenite phases, respectively, and X_γ is the global volume fraction of austenite.

However, from trapping effect point of view, it seems more reasonable to establish the model based on trap density. Therefore, the following equation is proposed:

$$\sum_{i=1}^{n} a_i \times x_i + b = N_{t,total}$$ (6-3)

Wherein a_i represents the trapping efficiency factor of a phase i, and x_i represents the area fraction of the phase i; b is a constant that is unique for each TMCP process (until the end of transformation); $N_{t,total}$ is the total reversible trap density.

In the scenario of Group I plates, the equations for 3E-Coiled and 3E-Air cooled can be written as follows:

$$a_f \times x_f^s + a_b \times x_b^s + a_a \times x_a^s + b = N_t^s$$

$$a_f \times x_f^q + a_b \times x_b^q + a_a \times x_a^q + b = N_t^q \qquad (6\text{-}4)$$

$$a_f \times x_f^c + a_b \times x_b^c + a_a \times x_a^c + b = N_t^c$$

Wherein the superscripts s, q and c represent the surface, quarter distance and centerline of the plate; the subscripts f, b and a represent ferrite, bainite and M/A.

The equation set of a plate can also be written as matrix:

$$\bar{A} = \begin{bmatrix} a_f \\ a_b \\ a_a \end{bmatrix} \qquad \chi = \begin{bmatrix} x_f^s & x_b^s & x_a^s \\ x_f^q & x_b^q & x_a^q \\ x_f^c & x_b^c & x_a^c \end{bmatrix} \qquad \Psi = \begin{bmatrix} N_t^s \\ N_t^q \\ N_t^c \end{bmatrix}$$

$$\chi \times \bar{A} + b = \Psi \qquad (6\text{-}5)$$

Values in χ, i.e., area fraction of each phase, were obtained through EBSD Band Contrast maps and distribution curves; and values in Ψ, i.e., reversible trap density can be obtained by hydrogen permeation test. The trapping efficiency factors, i.e., a_f, a_b, a_a, remain the same for 3E-Coiled, 3E-Air cooled, and 3F-Coiled; however, constant b varies for different skelps. And it should be noted that for 3F plates only surface and centerline samples were tested.

Similarly, equation set and matrix for 3F-Water quench are as follows:

$$a_f \times x_f^s + a_b \times x_b^s + a_a \times x_a^s + a_m \times x_m^s + b = N_t^s$$

$$a_f \times x_f^q + a_b \times x_b^q + a_a \times x_a^q + a_m \times x_m^q + b = N_t^q \qquad (6\text{-}6)$$

$$a_f \times x_f^c + a_b \times x_b^c + a_a \times x_a^c + a_m \times x_m^c + b = N_t^c$$

$$\bar{A} = \begin{bmatrix} a_f \\ a_b \\ a_a \\ a_m \end{bmatrix} \qquad \chi = \begin{bmatrix} x_f^s & x_b^s & x_a^s & x_m^s \\ x_f^q & x_b^q & x_a^q & x_m^q \\ x_f^c & x_b^c & x_a^c & x_m^c \end{bmatrix} \qquad \Psi = \begin{bmatrix} N_t^s \\ N_t^q \\ N_t^c \end{bmatrix}$$

$$\chi \times \bar{A} + b = \Psi \tag{6-7}$$

6.1.2 Calculation with experimental data

The experimental data of Group I plates are used as input for the present model, including phase area fraction obtained from EBSD band contrast map and reversible trap density calculated via time lag method, as shown in Table 6-1.

Table 6-1 Phase area fractions and reversible trap density of Group I plates.

Plate	Location	Phase area fraction (%)				Reversible trap density (10^{-5} mol·cm^{-3})
		Ferrite (x_f)	Bainite (x_b)	M/A (x_a)	Martensite (x_m)	
3E-Coiled	Surface	58.2	39.2	1.3	/	4.3
	¼ distance	49.2	49.1	1.6	/	8.6
	Centerline	41.1	55.3	2.1	/	11.9
3E-Air cooled	Surface	51.8	45.3	2.9	/	20.6
	¼ distance	39.1	57.1	3.6	/	38.6
	Centerline	47.4	47.3	5.3	/	27.1
3F-Coiled	Surface	62.5	33.9	3.4	/	26.1
	Centerline	66.9	26.7	6.2	/	15.0
3F-Water quenched	Surface	41.9	36.8	3.3	17.9	18.1
	Centerline	33.6	49.5	3.8	12.8	11.8

To calculate the trapping efficiency factors matrix A, multiple regression is used. Multiple regression is a statistical technique that can be used to analyze the relationship between a single

dependent variable and several independent variables. Herein, the reversible trap density is taken as the dependent variable and the area fraction of phases are independent variables. As more testing data of 3E skelp (including 3E-Coiled and 3E-Air cooled) were obtained than 3F, in this section, only 3E is applied for the calculation. The regression coefficient, i.e., trapping efficiency factors of each phase in 3E plates, as well as the interception, i.e., constant b, are listed in Table 6-2.

Table 6-2 Trapping efficiency factor of phases and Constant b by multiple regression

Trapping efficiency factor				Constant b	
Ferrite (a_f)	Bainite (a_b)	M/A (a_a)	Martensite (a_m)	3E	3F
4.16	4.93	8.94	3.72	-446.00	-442.06

As shown in Table 6-2, the trapping efficiency of bainite is slightly higher than that of ferrite, whereas M/A constituents, with a trapping efficiency factor about twice of the other two phases, is the most effective trapping phase among the three. This result is consistent with some researchers' findings that mentioned previously.

Assuming that the trapping efficiency of ferrite, bainite and M/A are independent of TMCP of the plate, the constant b and trapping efficiency factor of martensite in 3F skelps (including 3F-Coiled and 3F-Water quenched) are evaluated by the same method. It is worth mentioning that the M/A constituents in 3E-Coiled, 3E-Air cooled and 3F-Coiled mainly consist of retained austenite. Therefore, the value of trapping efficiency of M/A in 3E plates that calculated previously is adopted as the trapping efficiency of RA in 3F-Water quenched. As shown in Table 6-2, the constant b for 3F plates is close to that of 3E plates. It is also shown that the trapping efficiency factor of martensite is smaller than that of ferrite, however, some researchers claim that martensite act as efficient reversible traps due to the high dislocation density, lath structure and high lattice strain in martensitic structure[136]. This discrepancy might be caused by the small sample size for the calculation of martensite trapping efficiency factor, as only two samples with martensite are included. Nevertheless, the result shows that the trapping efficiency of martensite is close to that of ferrite and bainite and much lower than that of remained austenite (or M/A), which is reasonable and acceptable.

6.2 *Numerical simulation model of hydrogen trapping*

Hydrogen trapping is complicated process considering the various types of traps with different binding energies, densities, interaction behavior with H, etc., existing in steels, which makes it difficult to analyze the hydrogen trapping capability of a steel simply by solving Fick's diffusion equations numerically. Most of models that proposed in recent decades to describe the trapping process are generally based on the model established by McNabb and Foster[15] and modified by Oriani [16]. The basic assumptions of the model are that a dynamic equilibrium is maintained between trapped hydrogen and lattice hydrogen and that the traps under concern are saturable. However, most these models either do not consider irreversible traps or set parameters arbitrarily that cannot be suitable for all types of traps or conditions.

In this section, a two-stage numerical simulation model of hydrogen trapping is proposed to analyze the reversible and irreversible trapping effect based on the 2nd and 1st transient of oxidation curve obtained by double-cell hydrogen permeation test, respectively. By this model, D_{eff} (effective diffusion coefficient) of reversible and irreversible taps are obtained separately and compared with the D_{eff} values calculated by lag-time method and curve-fitting method; the effect of binding energy (E_b) and trap density (N_t) of reversible and irreversible traps on the shape of oxidation curve are analyzed.

6.2.1 *Reversible trapping part*

The first part of the model only involves reversible trapping and should be applied to the 2nd transient of the double-cell hydrogen permeation test during which the irreversible trapping effect is excluded. The simulation is based on McNabb and Foster's model[15] for saturable hydrogen traps with simple kinetic laws for trapping and detrapping and Oriani's hypothesis of local equilibrium[16]. To simplify the simulation, only one type of reversible trap and unidirectional diffusion is assumed. Finally, the experimental data of 3E-Coiled-surface sample is used for evaluation of D_{eff}.

6.2.1.1 Theory of the model

According to McNabb and Foster[15], hydrogen atoms diffuse through the crystal lattice in accordance with Fick's first and second law and the reversible traps that can release trapped hydrogen atoms should also be considered as a H source in Fick's equations. Therefore, the partial differential equation (6-8) describes the diffusion process.

$$\frac{\partial c_l}{\partial t} + N\frac{\partial \theta}{\partial t} = D_L\frac{\partial^2 c_l}{\partial x^2} \tag{6-8}$$

Wherein c_l is the lattice H concentration, t is time, D_L is the lattice diffusion coefficient, x is the spatial coordinate, N is the trap density, θ is the fraction of reversible traps that are occupied by H.

Also, considering the interchange of H atom between the traps and adjacent lattice, the difference between capture and release rate of H should equal to the accumulating rate of H in the traps. Hence,

$$\frac{\partial \theta}{\partial t} = kc_l\,(1-\theta) - p\theta \tag{6-9}$$

Wherein k and p are the trapping and detrapping constants, which represent the probability of a H atom jumping in and out of the trap, respectively.

Combining equations (6-8) and (6-9), we have equation (6-10):

$$\frac{\partial c_l}{\partial t} + kc_l\,(1-\theta)N - p\theta N = D_L\frac{\partial^2 c_l}{\partial x^2} \tag{6-10}$$

According to Oriani, Fick's first law for the flux of H can be written both in forms of the occupied normal sites and in forms of the total concentration gradient, as shown in equation (6-11).

$$J = -D_L\frac{dc_l}{dx} = -D_{eff}\frac{dc_T}{dx} \tag{6-11}$$

$$c_T = c_l + c_x \tag{6-12}$$

$$c_l = N_L\theta_L \tag{6-13}$$

$$c_x = N\theta \tag{6-14}$$

Wherein D_L and D_{eff} are the diffusivity in normal lattice and the effective diffusivity; c_x, c_T are the H concentration in traps and the total H concentration, respectively; θ_L and N_L are the fraction of occupied sites and the density of H sites in normal lattice.

Based on local equilibrium assumption, the equilibrium constant K is introduced by Oriani, which is the ratio of activity of hydrogen on the trapping site (a_x) and on the normal lattice sites (a_L). And a_x and a_L can be expressed in terms of fractional occupancies as shown in equation (6-15). Since the H concentration in normal lattice is rather low, $\theta_L \to 0$, $1-\theta_L \to 1$.

$$K = \frac{a_x}{a_L} = \frac{\theta/(1-\theta)}{\theta_L/(1-\theta_L)} \approx \frac{\theta/(1-\theta)}{\theta_L} = \frac{\theta}{\theta_L(1-\theta)} \tag{6-15}$$

$$K^0 = K/N_L \tag{6-16}$$

Then we can get equation (6-17) by combining equations (6-8), (6-15) and (6-16).

$$\frac{\partial c_l}{\partial t} + N\frac{\partial}{\partial t}\left(\frac{K^0 c_l}{1+K^0 c_l}\right) = D_L\frac{\partial^2 c_l}{\partial x^2} \tag{6-17}$$

Also, by equations (6-11)~(6-15), equation (6-18) can be obtained.

$$D_{eff} = D_L\frac{dc_l}{dc_T} = D_L\left[1 + \frac{NN_L K}{(N_L+Kc_l)^2}\right]^{-1} \tag{6-18}$$

When only reversible traps are considered, one can assume that $\theta \ll 1$ and $K\theta_L \ll 1$ ($Kc_L \ll 1$). Therefore, equation (6-18) becomes

$$D_{eff} = D_L(1 + KN/N_L)^{-1} \tag{6-19}$$

And since $K^0 = K/N_L$ equation (6-19) can be rewritten as

$$D_{eff} = D_L(1 + K^0 N)^{-1} = D_L(1 + K_r N_r)^{-1} \tag{6-20}$$

Wherein the subscript "r" is used to denote "reversible".

This means that D_{eff} is determined by the product of K_r and N_r, and hence, it is not possible to get the binding energy and trap density of the reversible traps by a single oxidation curve since unlimited pairs of K_r and N_r yield the same D_{eff} as well as the same curve. Moreover,

as the second term of equation (6-17) turns out to be 0 under the assumption that $Kc_L \ll 1$, the existence of reversible traps cannot change the shape of the hydrogen diffusion curve[209].

According to Oraini[16], c_L and c_T satisfy equation (6-21) in low θ domain. Therefore, Equation (6-22) is obtained by combining equations (6-17), (6-20) and (6-21) and assuming the second term in equation (6-17) is close to 0, based on which the reversible trapping model is established.

$$c_T = c_l + c_x = c_l(1 + K_r N_r)^{-1} \qquad (6\text{-}21)$$

$$\frac{\partial c_T}{\partial t} = D_{eff}\frac{\partial^2 c_T}{\partial x^2} \qquad (6\text{-}22)$$

6.2.1.2 Numerical simulation

To simulate the hydrogen permeation process during 2nd transient, a 1-D finite element model is established. In this model, the diffusion path through the sample is divided into n′ slices with a thickness of L/n′ for both interior slices and the surface slices (L is the thickness of the sample). The concentrations of H at different locations are denoted as shown in Fig. 6.1.
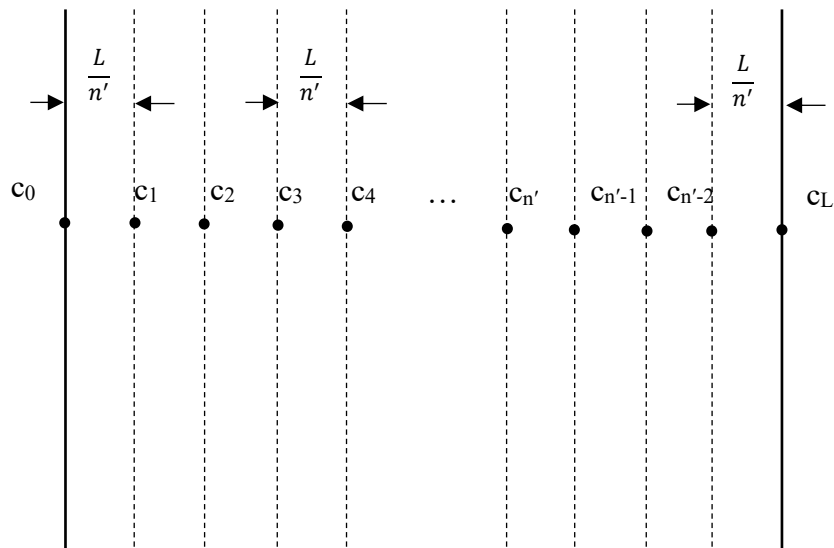

Fig. 6.1 Construction of finite elements in reversible trapping model.

The second order partial derivatives of equation (6-22) are approximated by finite element increment, and hence the gradient of H concentration at slice i can be calculated by equation (6-23) (The total H concentration is denoted as c instead of c_T for simplicity.)

$$\frac{\Delta c}{\Delta t} = D_{eff} \frac{\frac{c_2-c_1}{L/n'}-\frac{c_1-c_0}{L/n'}}{\frac{L}{n}} = D_{eff}\frac{(c_2+c_0-2c_1)}{(L/n')^2} \qquad (i=1)$$

$$\frac{\Delta c}{\Delta t} = D_{eff} \frac{\frac{c_{i+1}-c_i}{L/n}-\frac{c_i-c_{i-1}}{L/n}}{L/n'} = D_{eff}\frac{(c_{i+1}+c_{i-1}-2c_i)}{(L/n')^2} \qquad (2 \le i \le n'-1) \qquad (6\text{-}23)$$

$$\frac{\Delta c}{\Delta t} = D_{eff} \frac{\frac{c_L-c_{n'}}{L/n}-\frac{c_{n'}-c_{n'-1}}{L/n}}{\frac{L}{n}} = D_{eff}\frac{(c_L+c_{n'-1}-2c_{n'})}{(L/n')^2} \qquad (i=n')$$

In the present study, during the hydrogen permeation test a gavanolstat is used to generate hydrogen on the entrance side of the sample at a constant current and a potentiostat is applied to the sample to make sure all H atoms that reach the exit side are oxidized into H^+. Therefore, constant flux of H atoms is assumed as the boundary condition at the entrance side, and c_0 can be obtained by the first Fick's Law, as shown in equation (6-24). On the other hand, $c_L = 0$ should be taken as the boundary condition at the exit side.

$$J_{ss} = -D_{eff}\frac{\partial c}{\partial x} \cong -D_{eff}\frac{\Delta c}{\Delta x} = -D_{eff}\frac{c_1-c_0}{L/2n'} \qquad (6\text{-}24)$$

Thomas[210] introduce the mesh ratio "r" to evaluate the accuracy and efficiency of a simulation in MacNabb-Foster-Caskey system, which is defined by the x-step h and the time-step k, as shown in equation (6-25). It is suggested that the mesh ratio r and the number of elements n_e should be r=0.2 and n_e=40 to guarantee sufficient accuracy of the simulation results[209, 210], which are adopted in this study and determine the value of Δt.

$$r = \frac{\Delta T}{\Delta X^2} = \frac{\Delta t}{D_{eff}\Delta x^2} = \frac{D_{eff}\cdot\Delta t}{(\frac{L}{n_e})^2} \qquad (6\text{-}25)$$

6.2.1.3 Simulation results

Fig.6.2 shows the simulated normalized H flux on linear scale and logarithmic scale, when $D_{eff} = 3.1\times10^{-6}$ cm$^2\cdot$s^{-1}, 2.0×10^{-6} cm$^2\cdot$s^{-1}, 1.0×10^{-6} cm$^2\cdot$s^{-1}, 1.0×10^{-7} cm$^2\cdot$s^{-1}, 1.0×10^{-8} cm$^2\cdot$s^{-1}. As seen in Fig.6.2b), the position of the flux curve moves to the right as D_{eff} increases, but the shape of the flux curves does not change with D_{eff}. In Fig. 6.3, the 2nd transient data of 3E-Coiled-surface

are compared with simulation results. It shows that the experimental curve fits well with the curve of $D_{eff} = 2.5 \times 10^{-6}$ cm$^2 \cdot$s^{-1} up till 80% of the J_{ss} (H flux at steady state), which close to the curve of $D_{eff} = 3.1 \times 10^{-6}$ cm$^2 \cdot$s^{-1} that is obtained by lag-time method. However, if we use Mean-Square Error (MSE) as the cost function to find the D_{eff} that can give the simulated hydrogen permeation curve that fit the experimental curve best, the D_{eff} should be 2.2×10^{-6} cm$^2 \cdot$s^{-1}. Therefore, 2.2×10^{-6} cm$^2 \cdot$s^{-1} is taken as the effective diffusion coefficient of 2nd transient and will be used in the simulation of diffusion process with irreversible trapping effect (1st transient).
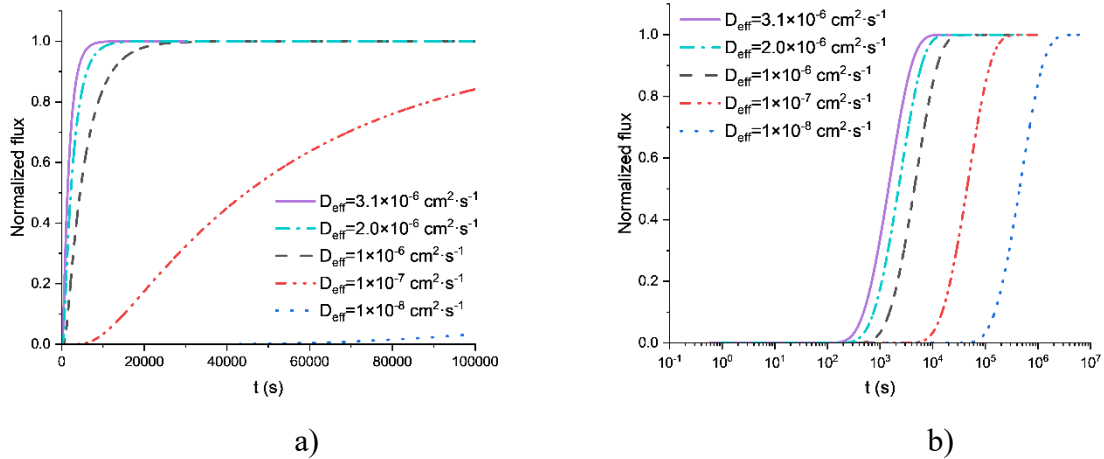

Fig. 6.2 Simulated normalized H flux during 2nd transient with only reversible trapping effect on linear scale a) and logarithmic scale b).
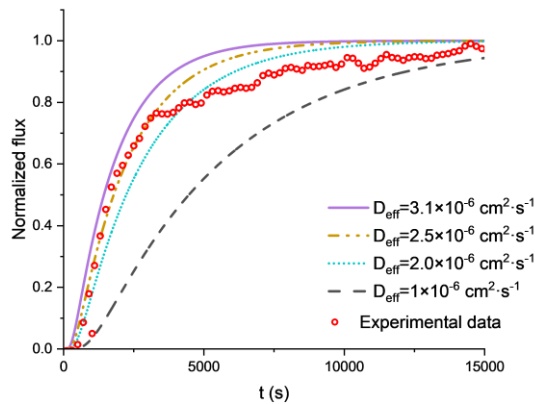

Fig. 6.3 Comparison of simulated normalized H flux with experimental data (3E-Coiled-surface).

6.2.2 Irreversible trapping part

During the 1st transient of hydrogen permeation test, both reversible and irreversible traps are active and capture H atoms. In this section, the irreversible trapping effect is focused and simulated based on the assumption that the reversible traps behave in the same way during the 1st transient as during the 2nd transient.

6.2.2.1 Theory of the model

According Castano's work[209], equation (6-26) can be used to simulate the diffusion process during 1st transient, which explicitly considers the effect of irreversible traps and implicitly reflects the trap density and binding energy of reversible traps in the value of D_{eff}.

$$\frac{\partial c}{\partial t} + N_i \frac{\partial}{\partial t}\left(\frac{K'c}{1+K'c}\right) = D_{eff}\frac{\partial^2 c}{\partial x^2} \tag{6-26}$$

$$K' = \frac{K_i}{1+K_rN_r} \tag{6-27}$$

In equation (6-26), N_i is the irreversible trap density, K' is related to K_i, which is the true equilibrium constant of irreversible traps, by equation (6-27).

Since $\frac{\partial}{\partial t}\left(\frac{K'c}{1+K'c}\right) = \frac{\partial c}{\partial t} \cdot \frac{\partial}{\partial c}\left(\frac{K'c}{1+K'c}\right)$, equation (6-26) can be finally transformed into equation (6-28), which is used in numerical simulation of irreversible trapping effect.

$$\frac{\partial c}{\partial t} = D_{eff}\frac{\partial^2 c}{\partial x^2} \cdot \left[1 + \frac{N_iK'}{(1+K'c)^2}\right]^{-1} \tag{6-28}$$

6.2.2.2 Numerical simulation

The construction of finite elements in irreversible trapping model is similar to that in reversible trapping model as shown in Fig.6.1. And the gradient of H concentration at slice i can be calculated by equation (6-26), considering the effect of reversible traps via $K' = \frac{K_i}{1+K_rN_r}$. Similar to reversible trapping model, the value of Δt is determined by equation (6-25), wherein r=0.2 and n_e=40. The product of K_r and N_r can be obtained by applying reversible trapping model to the 2nd transient of the same sample and calculating via equation (6-20).

$$\frac{\Delta c}{\Delta t} = D_{eff} \frac{(c_2 + c_0 - 2c_1)}{(L/n')^2} \left[1 + \frac{N_i K'}{(1+K'c_1)^2}\right]^{-1} \qquad (i = 1)$$

$$\frac{\Delta c}{\Delta t} = D_{eff} \frac{(c_{i+1} + c_{i-1} - 2c_i)}{(L/n')^2} \left[1 + \frac{N_i K'}{(1+K'c_i)^2}\right]^{-1} \qquad (2 \leq i \leq n' - 1) \qquad (6\text{-}29)$$

$$\frac{\Delta c}{\Delta t} = D_{eff} \frac{(c_L + c_{L-1} - 2c_n)}{(L/n')^2} \left[1 + \frac{N_i K'}{\left(1+K'c_{n'}\right)^2}\right]^{-1} \qquad (i = n')$$

6.2.2.3 Simulation results

Using the irreversible trapping model, the effect of irreversible trap density (N_i), binding energy (E_b) and reversible traps, i.e., effective diffusion coefficient during the 2nd transient (D_w), on the hydrogen permeation curve of 1st transient is analyzed, as shown in Fig. 6.4-6.7. It is shown in Fig.6.4 b) and Fig.6.5 b) that N_i has effect on both position and shape of the curve, whereas E_b of irreversible traps only influences the position of the curve.
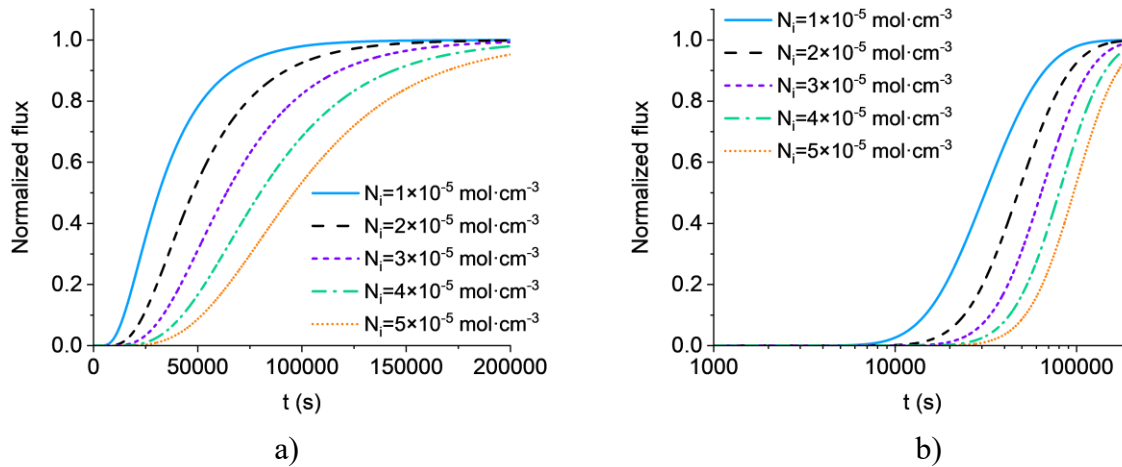

Fig. 6.4 Effect of irreversible trap density (N_i) on hydrogen permeation curve during 1st transient at linear scale a) and logarithmic scale b).
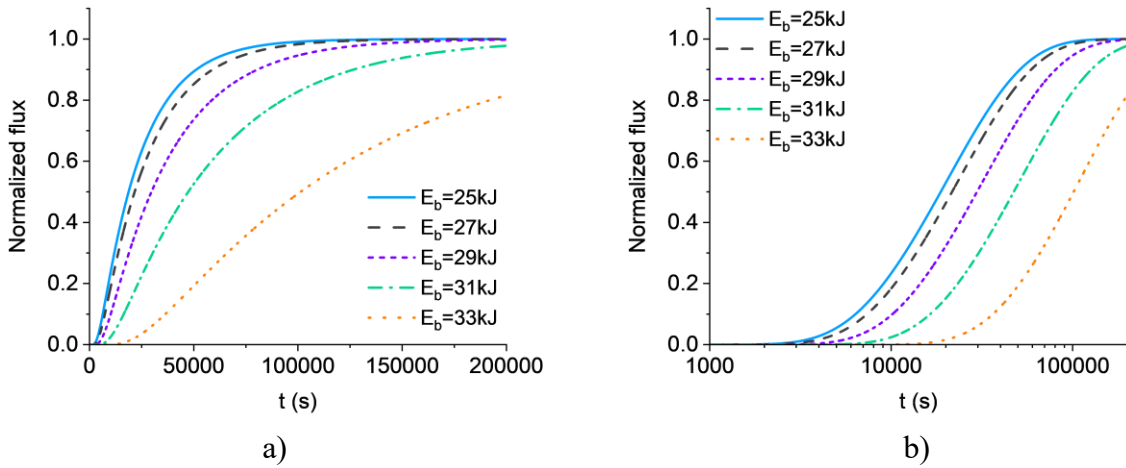
Fig. 6.5 Effect of binding energy (E_b) on hydrogen permeation curve during 1st transient at linear scale a) and logarithmic scale b).

Fig. 6.6 shows that the combined effect of E_b and N_i. For traps with lower E_b, the influence of N_i on the permeation process is very limited as compared with those with high E_b ; the effect of E_b is significantly more prominent when N_i is high. Moreover, as shown in Fig. 6.7, the effect of reversible traps (D_w) on 1st transient is minor when D_w is small enough. In effect, the effective diffusion coefficient calculated from all experimental data in present study is smaller than 1×10^{-6} $cm^2 \cdot s^{-1}$, which means the effect of D_w on 1st transient is negligible.
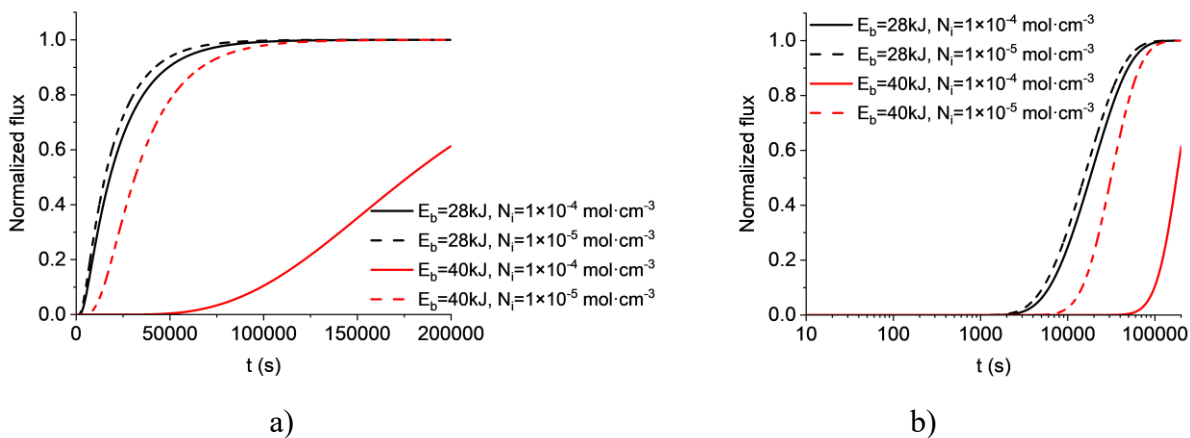

Fig. 6.6 Combined effect of binding energy (E_b) and irreversible trap density (N_i) on hydrogen permeation curve during 1st transient on linear scale a) and logarithmic scale b).
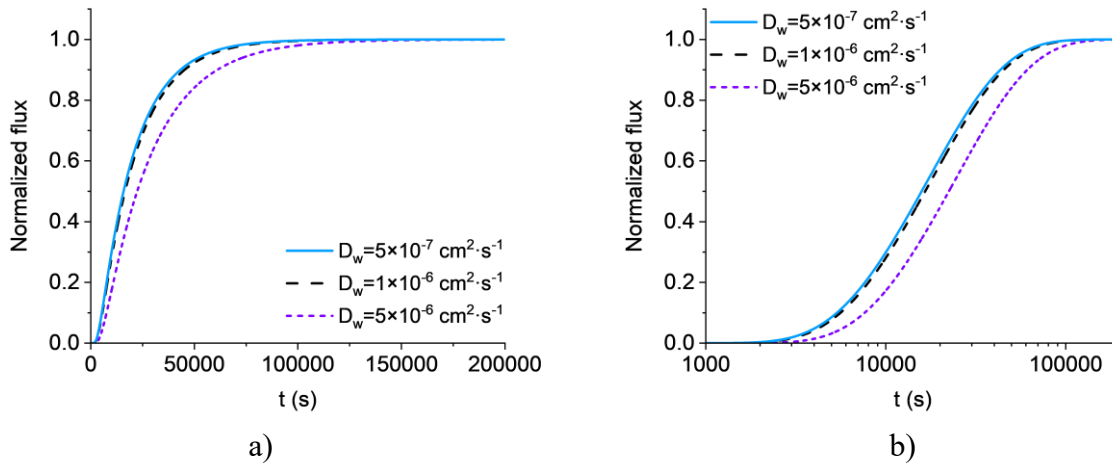
Fig. 6.7 Effect of diffusivity during 2nd transient (D_w) on hydrogen permeation curve during 1st transient on linear scale a) and logarithmic scale b).

In the irreversible trapping part of the model, five variables are needed to simulate the hydrogen permeation curve, i.e., D_w, J_{ss}, D_{eff}, N_i and E_b, among which D_w and J_{ss} can be obtained via reversible trapping part of the model and from experimental data, respectively. Therefore, to get the combination of D_{eff}, N_i and E_b that can make the simulated hydrogen permeation curve best fit experimental data, Bayesian optimization is used to tune the model for lowest Mean-Squared Error (MSE). Based on the hydrogen permeation test results in Chapter 4 and Chapter 5, the range of D_{eff}, N_i and E_b are set as $1\times10^{-7}\sim5\times10^{-7}$ cm$^2\cdot$s^{-1}, $1\times10^{-6}\sim1\times10^{-3}$ mol$\cdot$cm^{-3}, 20~80kJ, respectively. The parameters for best-fit simulation of 3E-Coiled at surface and centerline region are listed in Table 6-3. It is shown that the diffusion coefficients (during both 1st and 2nd transient) obtained by simulation are very close to those calculated using lag-time method for both samples, indicating that the simulation results are reasonable. Furthermore, the N_i of surface sample is higher than that of the centerline sample, which might be due to the high density of nano-size NbC precipitates in the former than the latter according to TEM results in chapter 4. E_b of centerline sample is larger than that of the surface sample, which indicates higher binding energy of precipitates than that of inclusions, since more inclusion are observed at centerline and more precipitates at surface region. Fig.6.8 shows the simulated curve fits well with the experimental hydrogen permeation test data (3E-Coiled-Surface).

Table 6-3 Parameters of irreversible trapping model optimized for best-fit simulation.

Plate	Location	D_w $10^{-6}cm^2 \cdot s^{-1}$		D_{eff} $10^{-7}cm^2 \cdot s^{-1}$		N_i $10^{-5}mol \cdot cm^{-3}$	E_b $kJ \cdot mol^{-1}$
		Simulation result	Lag-time method	Simulation result	Lag-time method		
3E-Coiled	surface	2.20	3.11	2.37	2.96	12.6	77.0
	centerline	0.85	1.14	2.17	1.97	7.9	53.2
3E-Air cooled	surface	0.59	0.66	2.07	2.71	1.12	53.6
	centerline	0.44	0.50	1.26	1.62	9.21	58.1
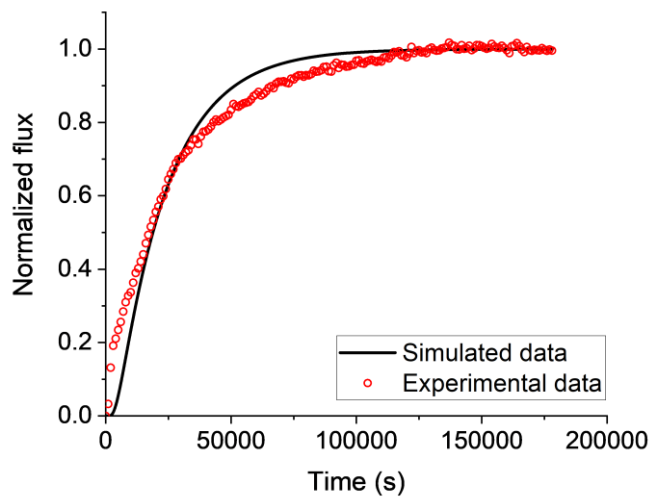
Fig. 6.8 Hydrogen permeation test data and simulated hydrogen permeation curve of 3E-Coiled-Surface.

6.2.3   Summary

The results of reversible and irreversible trapping model are summarized as follows:

1) The effective diffusion coefficient during 1st and 2nd transient can be obtained by the irreversible trapping model and reversible trapping model, respectively, and the values are very close to the ones calculated by time-lag method.

2) The simulated data using the models have a good fit with the experimental data of hydrogen permeation test.

3) As the diffusivity during 2nd transient is determined by the product of K_r and N_r, the density and binding energy of reversible traps cannot be obtained by hydrogen permeation test results under only one temperature scenario.

4) The irreversible trapping model shows larger number of irreversible traps near surface region than at centerline, which is consistent with characterization results in Chapter 4.

5) The irreversible trapping model also shows higher average binding energy of the irreversible traps near surface region than those at centerline, indicating higher binding energy of nano-size NbC precipitates than that of inclusions since the former is more abundant near surface region whereas the latter segregated near centerline.

7 Effect of processing on microstructure

In this chapter, the effect of rough rolling deformation, finish rolling deformation and the temperature-time profile during coiling on precipitate formation, PAG size, inclusion size, and fraction of HAGB and phase types are discussed and correlated to measurements of trap density obtained by hydrogen permeation test.

7.1 *Effect of rough rolling deformation*

In this section, the effect of number of rough rolling passes on the formation of large TiN-NbC complex precipitates, PAG size and irreversible trap density is examined on Group II plates.

7.1.1 *Effect on TiN-NbC precipitation*

The effect of number of rough rolling passes on the size and count density of TiN/TiN-NbC precipitates is shown in Fig. 7.1. It is observed that TiN-NbC precipitates diameter increases from about 95 nm in 0 pass plate (3F-0P) to a plateau of about 120 nm for plates that have been through 1/3/5 passes of rough rolling (3B-1P/3E-3P/3B-5P/3E-5P-4MIN). This is mainly due to the lower solubility of titanium and niobium in austenite matrix at rough rolling temperature (1100~1000°C) than at soaking temperature (1260°C), which leads to the heterogeneous nucleation of NbC upon TiN and coarsening of the complex TiN-NbC precipitates. In addition, the deformation might also play a role in accelerating the precipitation by introducing more dislocations as the nucleation sites [211]. The slight increase of precipitate size with the increasing time/number of rolling passes could be attributed to the nucleation and growth of NbC on TiN, the process of which is observed by TEM images and shown in Fig.5.11. Meanwhile, as it is also shown in Fig. 7.1, the precipitate count density (count/mm^2) increases with the onset of number of rolling passes, and almost doubled when being held for 4 minutes after 5 passes of rolling (3E-5P-4MIN Vs 3B-5P). This means more TiN-NbC complex precipitates nucleated with increased time/rolling passes. On the contrary, the irreversible trap density of these plates decreases as the number of rolling passes increases and show minor difference before and after being held for 4 min. The irrelevancy between the size and density of TiN-NbC and the irreversible trap density

indicates that these precipitates do not act as hydrogen traps. This is similar with the observed results on TiC precipitates, that coarse precipitates loss the trapping ability[155, 212].
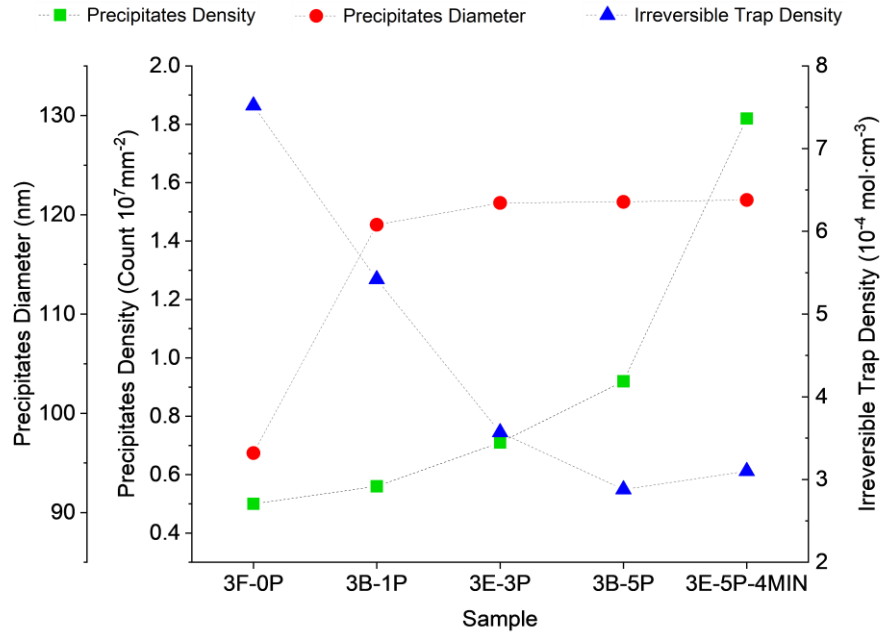

Fig. 7.1 Diameter (mean value) and density of complex TiN-NbC precipitates and irreversible trap density in Group II samples.

7.1.2   *Effect on PAG/HAGB*

In Fig.7.2, the PAG size, which is presented by the mean lineal intercept length (MLIL) of PAGs, is plotted against the number of rough rolling passes. It is shown that the PAG size dramatically reduced from 83 µm (3F-0P) to 44 µm (3B-1P) at the onset of rough rolling and continued to decrease as the number of rough rolling passes increases. This is due to the recrystallization of austenite grains during rough rolling process. It is also observed that the austenite grain size significantly increased when the plate was reheated to soaking temperature (1260 °C) after 4 rolling passes (3E-4P-1P-OLAC). And the discrepancy in PAG size between 3E-4P-1P-OLAC and 3E-5P-OLAC leads to the formation of different types of bainite during subsequent cooling process: in addition to lower lath bainite, large amount of upper bainite with coarse ferritic lath is observed in the former, but only a few in the latter (as shown in Fig.5.1k-n).

This could be caused by the lower carbon concentration adjacent to ferritic lath in larger PAGs, where the areas rich in carbon (rejected from ferritic lath) is less likely to overlap with each other as compared with those in smaller PAGs.
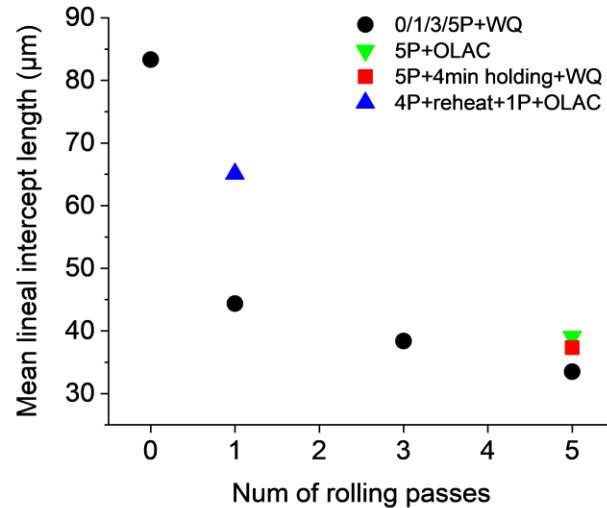

Fig. 7.2 Effect of rough rolling passes on PAG size (MLIL).

Similarly, the irreversible trap density of the plates that directly water quenched after rough rolling exponentially decreases with the number of rolling passes as shown in Fig. 7.3. It is believed that these irreversible traps are provided by HAGBs, i.e., packet/block boundaries of lath lower bainite. As it is shown in EBSD grain boundary maps (Fig.5.6), the fraction of HAGB in 3B-1P is higher than that in 3B-5P. According to the variant selection mechanism[190, 197-199], large driving force of transformation, such as high cooling rate/low transformation temperature, large undercooling, low carbon content, can lead to formation of more BF variants during nucleation to reduce the system energy by introducing less strain and interfacial energy to the system, which leads to fine blocks within the same packet. It is reported[200] that the bainite transformation in sample with small PAG is retarded with increased incubation time and slow transformation velocity, indicating small driving force as compared with large PAG. Therefore, more variants with high angle misorientations (>50°C) are selected during nucleation of bainite in large PAGs than in small PAGs due to the higher driving force of transformation, leading to formation of bainite with thinner bainite blocks and higher fraction of HAGBs, and hence higher density of irreversible traps.

It is also shown in Fig. 7.3 that the irreversible trap density of 3E-4P-1P-OLAC is much higher than that of 3E-5P-OLAC. This should be mainly caused by their different fractions of upper bainite, which contains the interface between M/A and ferrite as more effective irreversible traps. As it is discussed earlier, due to the large PAG size, higher fraction of upper bainite is observed in 3E-4P-1P-OLAC than in 3E-5P-OLAC, which gives rise to higher density of irreversible traps.
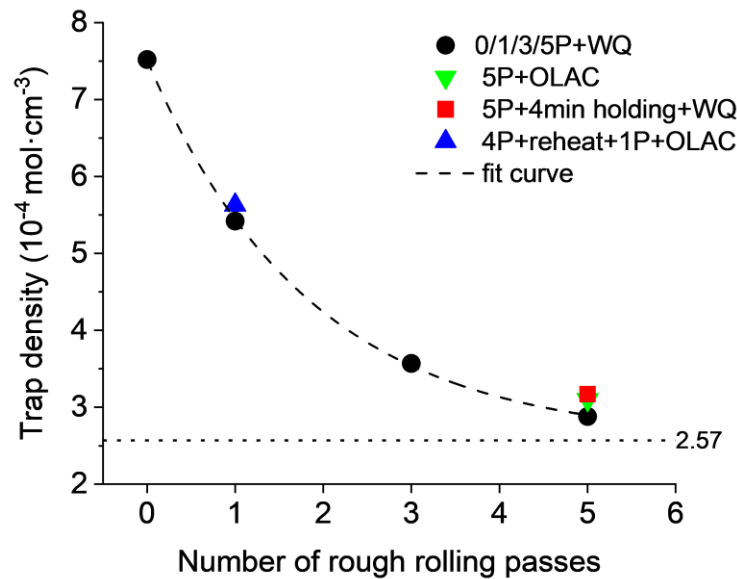

Fig. 7.3 Effect of rough rolling passes on irreversible trap density.

7.2   *Effect of rolling process on non-metallic inclusions (NMIs)*

Characterization results of NMIs in Group I plates show that rolling process (including rough rolling and finish rolling) have influence on the size distribution of NMIs, which, in turn, affect the irreversible trap density and H diffusivity of the plates.

It is observed in Fig. 7.4 that the count density of NMIs in 3E is much higher than that in 3F at both surface and centerline of the plate, although the area fraction of NMIs in both plates is quite close. This means the NMIs in 3F is finer than those in 3E, which is due to the different rolling processes of the plates. As shown in Table 7-1, the reduction rate of 3E and 3F during rolling process is almost the same, but fewer rolling passes were applied to 3F than to 3E, leading

to higher reduction of each pass for 3F. In addition, EDS analysis results show that these NMIs are mainly complex oxides and sulfides, such as $CaO \cdot Al_2O_3$, $MgO \cdot Al_2O_3$, MnO, SiO_2 and CaS, which are rigid non-deformable inclusions that can fracture during hot rolling. Therefore, the NMIs in 3F were subjected to higher compressive stress and crushed into finer grains during rolling.

As a result of the discrepancy in NMIs size distribution between 3E and 3F, the irreversible trap density contributed by NMIs is higher in the latter than in the former, which is shown in Fig. 7.5. In this figure, the influence of nano-size precipitates can be excluded by extrapolating the lines determined by the points of experimental data to obtain the intercepts (35×10^{-5} mol·cm^{-3} for 3F and 25×10^{-5} mol·cm^{-3} for 3E). Assuming that nano-size precipitates and NMIs are the only contributors of irreversible traps in these plates, the higher density of NMIs in 3F gives rise to the higher density of irreversible traps in the plate as compared with those in 3E. This indicates that by increasing the rolling deformation stress, the NIMs can be crushed down to finer particles and become more effective irreversible traps, and hence decrease the hydrogen diffusivity in the plate.
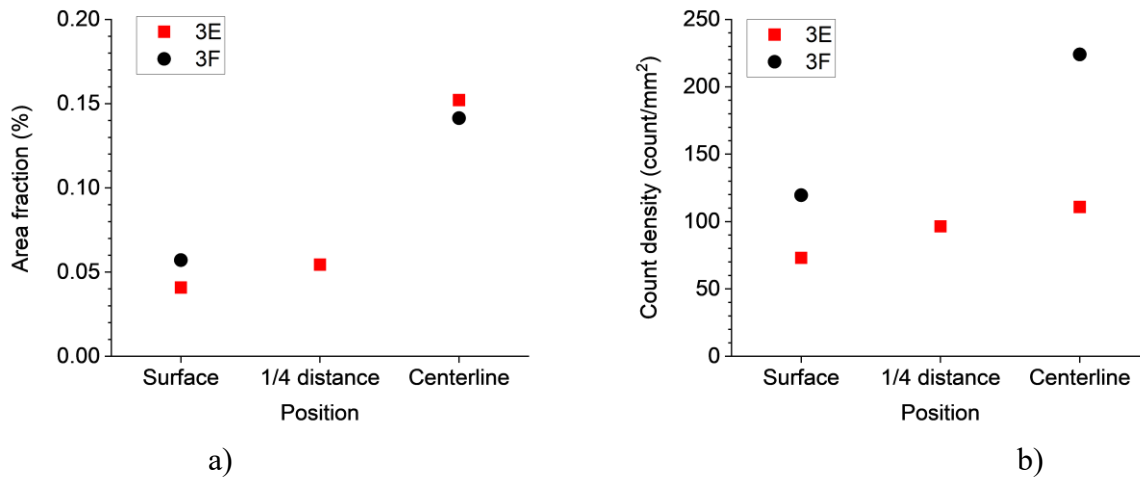
Fig. 7.4 Area fraction a) and count density b) of NMIs in 3E and 3F.

Table 7-1 Rolling parameters of Group I 3E and 3F plates.

Plate No.	Rolling type	Num of passes	Plate thickness (mm)		Reduction (%)	Total reduction (%)
			Entry	Exit		
3E	Roughing	10	259.1	78.7	69.6	92.6
	Finishing	8	78.7	19.3	75.5	
3F	Roughing	7	203.2	62.2	69.4	92.3
	Finishing	7	62.2	15.7	74.8	
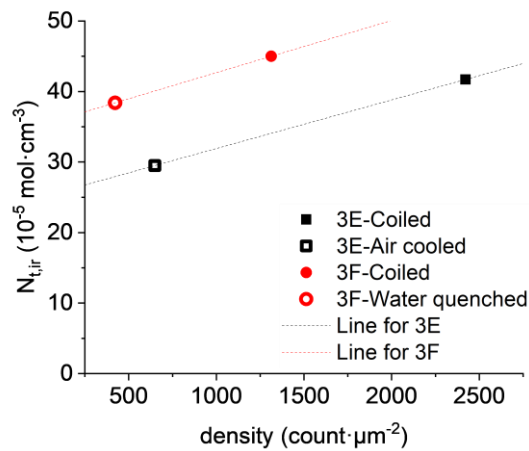
Fig. 7.5 The relationship between density of irreversible traps and density of nano-size precipitates in coiled and uncoiled surface samples of 3E and 3F.

Table 7-2 Intercept and slope of lines in Fig.7.5.

	Intercept	Slope
Line for 3E	25	0.0074
Line for 3F	35	0.0069

It is reported that HIC can be initiated at oxide inclusions rich in Al, Si and Ca, which are hard and incoherent with the matrix[12, 132]. And microcracks initiated from these oxide inclusions are also observed in the present study (Fig.4.35) in 3F-WQ before hydrogen permeation test. Thus, these oxide inclusions can potentially be harmful to the safety of pipelines, especially when exposed to hydrogen flux or after experiencing fast cooling rate. Moreover, these inclusions segregate at the centerline, where fewer nano-size precipitates present (see discussion in section 7.4), making the region a weak area in terms of HIC resistance and mechanical property. As the stress concentration of rigid inclusions like NMIs decreases with the size of the inclusions, smaller size NMIs should be preferred to improve HIC resistance and other properties, such as ductility, toughness, fatigue strength. And this can be obtained by proper TMCP design, for example, increasing the rolling force.

7.3 *Effect of coiling process on nano-size NbC precipitates*

Nano-size NbC precipitates in Group I plates were characterized by TEM/STEM using carbon replica technique and measured manually on STEM images. The results show that nano-size NbC precipitates are formed during accelerated cooling (OLAC) and subsequent coiling process with different size distributions. It is observed that the fine NbC precipitates in coiled plates (i.e., 3E-Coiled and 3F-Coiled) show bimodal size distribution, whereas those in non-coiled plates (i.e., 3E-Air cooled and 3F-Water quenched) show unimodal size distribution, as seen in Fig. 7.6. By lognormal curve fitting, the average precipitate diameter is obtained for each peak (Table 4-5), and it is found that precipitates formed during coiling are finer than those formed during laminar cooling (Fig.7.7). This is due to the slow kinetic of NbC precipitation under the lower temperature during coiling as well as the coarsening of those precipitates formed during laminar cooling.

The evolution process of nano-size NbC precipitates is clearly revealed by Fig.7.7. It is shown in Fig.7.7a) that in both 3E-Coiled and 3F-Coiled, the fine NbC precipitates generated during OLAC were coarsened in subsequent coiling process, assuming that they barely grew during water quench and air-cooling process due to the high cooling rates (3E-Air cooled and 3F-Water quenched) and their size distribution in coiled and corresponding non-coiled plates should

be the same after OLAC (shown as "estimated D_0 after OLAC" in Fig.7.7 a). It is also observed that the growth rate of the NbC in 3E is higher than those in 3F due to the lower cooling rate of 3E during simulated coiling (i.e., furnace cooling) since 3E plate (19 mm) is thicker than 3F plate (15 mm). For the same reason, more and larger NbC precipitates were nucleated during coiling in 3E than in 3F, as seen in Fig.7.7b). In addition, this might also be attributed to the larger number of dislocations introduced by rolling process in 3E, which are nucleation sites for NbC precipitates.

In effect, the cooling rate after OLAC has consistent influence on the count density of nano-size Nb precipitates, i.e., count density decreases with increasing cooling rate, as it is shown in Fig.7.8. The cooling rates of the four Group I plates follow the sequence: 3E-Coiled<3F-Coiled<3E-Air cooled<3F-Water quenched.

a)   b)

c)   d)
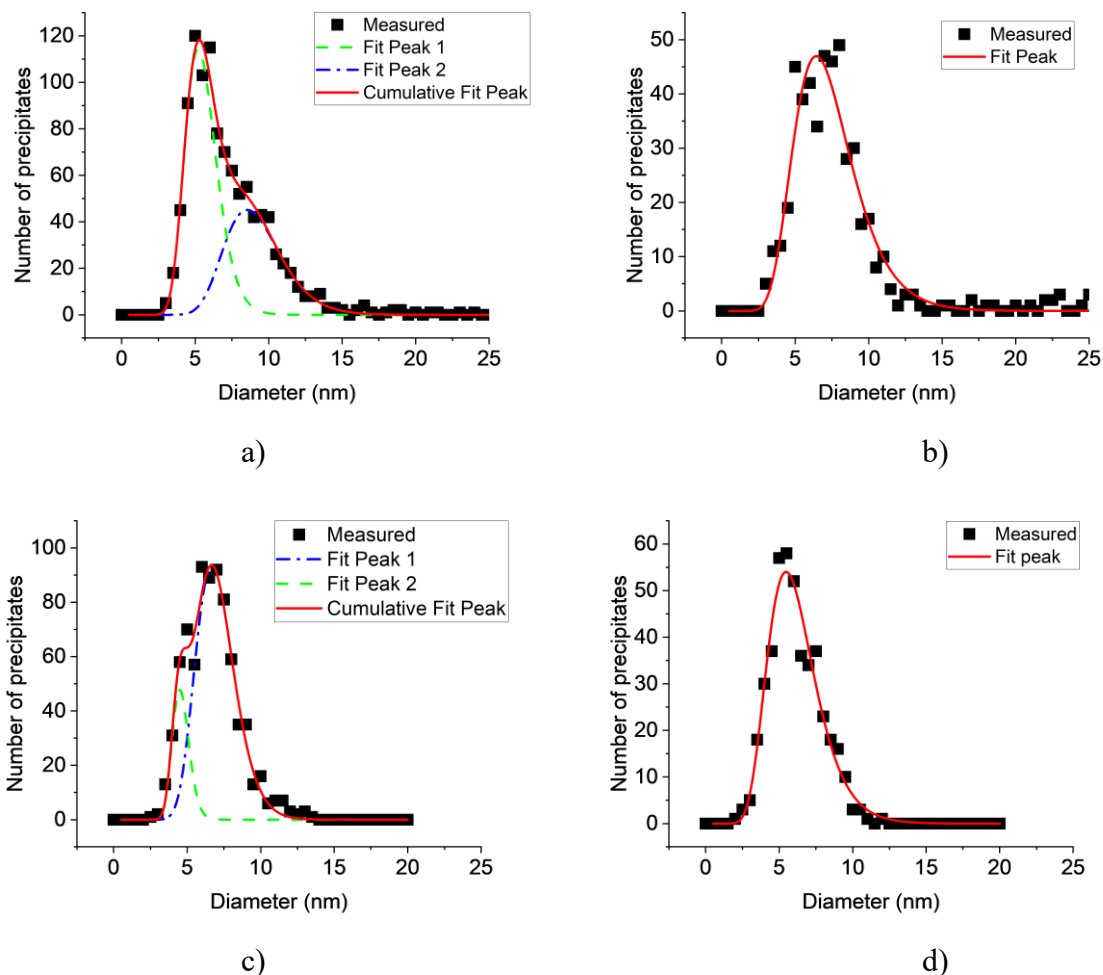
Fig. 7.6 Size distribution of nano-size NbC precipitates in 3E-Coiled a), 3E-Air cooled b), 3F-Coiled c) and 3F-Water quenched d).

168
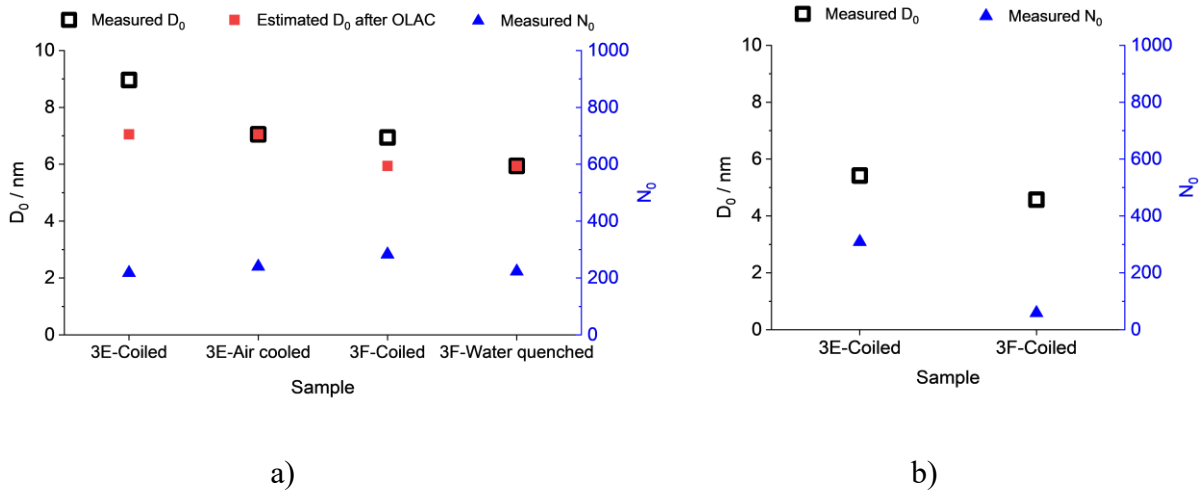
Fig. 7.7 D_0 and N_0 of nano-size NbC precipitates size distribution[5]. a) NbC formed during laminar cooling process; b) NbC formed during coiling process.
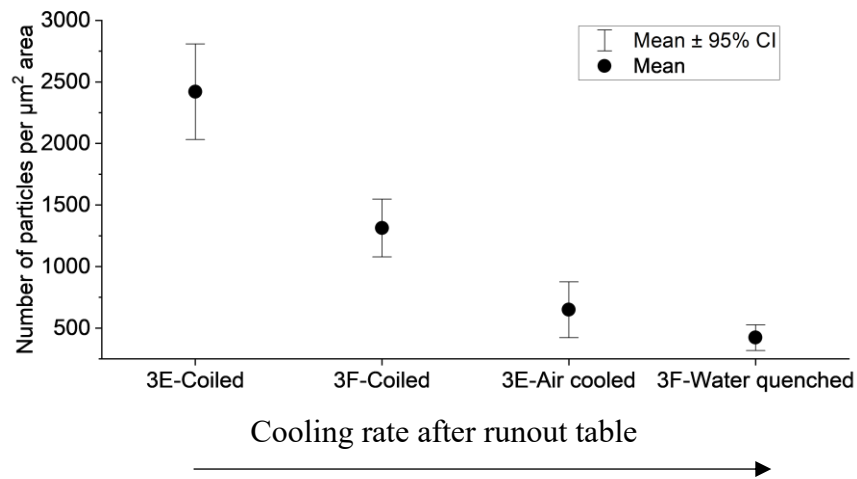
Fig. 7.8 Influence of cooling rate after OLAC on the count density of nano-size NbC precipitates in Group I samples (near surface region).

---

[5] D_0 and N_0 are obtained by curve fitting with equation 4-2. D_0 represents the precipitate diameter at the maximum of distribution; N_0 is the total number of precipitates in the distribution, which can be used for evaluation of count density since the total measured area for each sample is the same.

7.4   Effect of TMCP on M/A constituents

Characterization tests via OM and EBSD revealed the presence of M/A constituents in all Group I plates at surface, quarter distance and centerline. Quantitative analysis of OM images and EBSD band contrast map shows the effect of cooling rate (after OLAC) and finish rolling temperature on the area fraction and size of M/A constituents.

In Fig.7.9 a), the area fraction of M/A is higher in 3E-Air cooled than in 3E-Coiled at surface, quarter distance and centerline of the plates. Since both plates have been through the same OLAC process, this should be due to the different cooling rate after accelerated cooling. After OLAC, 3E-Coiled was cooled down from 565°C at a much slower rate than 3E-Air cooled, which caused the decomposition of the remain austenite in M/A[144]. This is because at such low temperature (<565°C) the diffusion rate of carbon is still high enough for diffusion with grains, although the reconstructive movement of large substitutional atoms is difficult[175].

It can be observed in Fig.7.9 b) that the area fraction of M/A in 3F-Coiled is higher than those in 3E-Coiled at both surface and centerline of the plates. Moreover, EBSD Band Contrast maps (Fig.7.10) show that the size of M/A constituents in the former are obviously larger than those in the latter. Similar results have also been reported by some other researchers[174, 213]. This can be explained by the higher finish rolling temperature of 3F skelp (850~950°C) than 3E skelp (800~920°C), which facilitated carbon partitioning and segregation before bainite transformation (see section 4.1.2 for detailed discussion). Therefore, the amount and size of M/A constituents increases with the increase of finish rolling temperature.

It is also shown in Fig. 7.9. that in all the three plates, i.e., 3E-Coiled, 3E-Air cooled and 3F-Coiled, the area fraction of M/A increases through the thickness from surface to centerline. This is believed to owe to the centerline segregation of austenite stabilizers, such as Mn and C, which lower the decomposition temperature of austenite and favor the formation of martensite. The positive segregation of Mn and C towards the center of the slab is due to the redistribution of these solute atoms between liquid and solid during solidification and has been observed by many researchers[176, 214, 215].

Hydrogen permeation test results of these plates show the strong trapping ability of M/A constituents as reversible traps. Based on the area fractions of phases in Group I plates and the

reversible trap density obtained by hydrogen permeation test, a trap efficiency model is established and shows that the trapping ability of M/A constituents is much higher than that of ferrite and bainite (Section 6.1). The trapped hydrogen atoms lead to the build-up of local hydrogen concentration and increase the risk of HIC [216]. Therefore, agglomerated M/A constituents, like those in 3F-Coiled, should be avoided to enhance the HIC resistance of the plate.
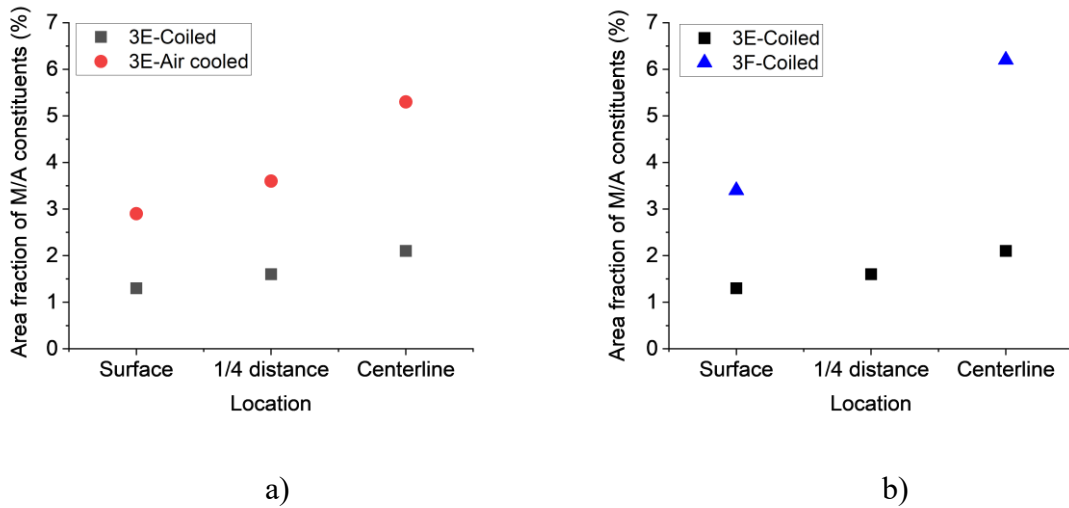

a)

b)

Fig. 7.9 Comparison of area fraction of M/A constituents in Group I samples. a) 3E-Coiled and 3E-Air cooled, b) 3E-Coiled and 3F-Coiled.

a)

b)
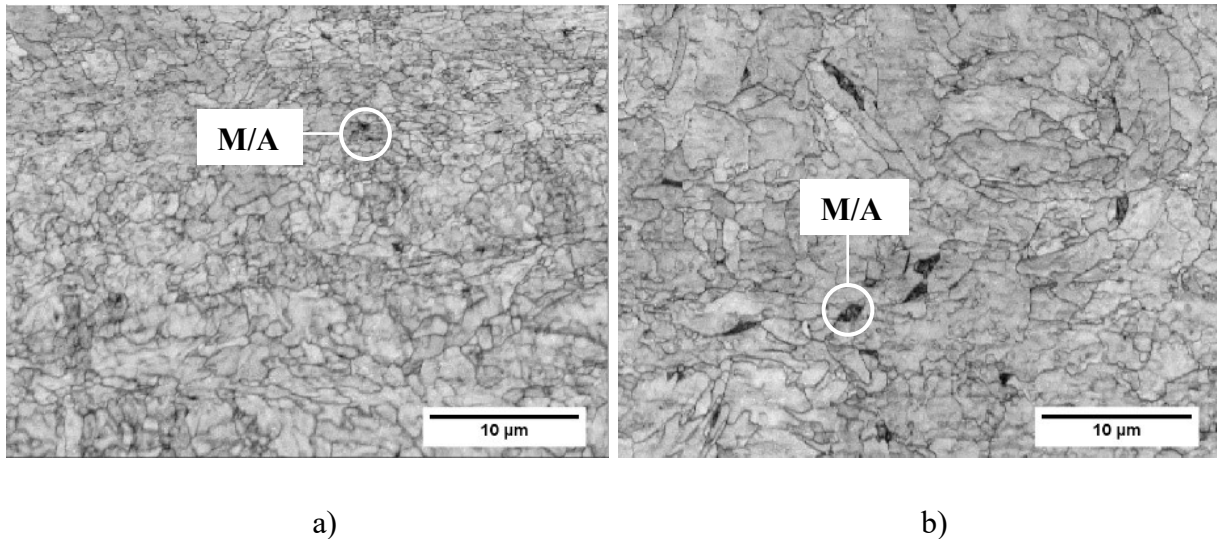
Fig. 7.10 EBSD band contrast map of 3E-Coiled a) and 3F-Coiled b) at surface.

8 Conclusions

The work presented in this study focused on effect of microstructure of X70 steels on the hydrogen diffusion and trapping. A variety of different microstructural features, such as phase composition, precipitates, non-metallic inclusions, and high angle grain boundaries, were obtained by altering TMCP parameters and sample locations through the plate thickness. By comparing hydrogen trapping behavior among samples, the effect of TMCP such as controlled rolling and coiling on formation of various microstructural features, for example, precipitates, inclusions, HAGBs, etc., are observed and discussed. The conclusions filled the knowledge gap about the relationship between TMCP and hydrogen traps in pipeline steel. Moreover, the reversible trapping ability of different phases was estimated quantitatively using a linear-regression model, which gives trapping efficiency of each phase. In addition, a numerical simulation model of hydrogen diffusion was developed based on the McNabb and Foster's theory and can be applied to obtain diffusivity, trap density and binding energy of hydrogen traps in pipeline steel. The conclusions are summarized as follows:

1) Nano-sized NbC precipitates are irreversible traps for hydrogen that decrease the amount of diffusible hydrogen.

2) A reduced cooling rate after OLAC leads to a higher count density of the nano-sized NbC precipitates.

3) The higher the count density of the nano-size NbC precipitates, the lower the diffusivity of hydrogen.

4) Non-metallic inclusions (NMIs), such as CaS and Al_2O_3, are strong irreversible hydrogen traps.

5) A lower average size of NMIs reduces hydrogen diffusivity due to the larger total surface area of the fine NMI.

6) An increase in overall rolling deformation resulted in a finer NMI size distribution.

7) The count density distribution of nano-sized NbC precipitates decreased from surface to the centerline, whereas that of NMIs are opposite, especially large ones. As a consequence, nano-sized NbC precipitates can be used to delay the hydrogen flux diffused to centerline region.

8) Based on the trapping efficiency model, the <u>reversible</u> trapping ability of phases in X70 steels rank in the order of M/A > bainite > ferrite.

9) The block/packet boundaries of lath bainite and M/A-ferritic lath interface are the main irreversible traps in LB and UB, respectively.

10) For the LB dominated microstructure, an increase in the number of rough rolling passes leads to decreased PAG size, lower density of block/packet boundaries, and hence lower density of irreversible traps.

11) Large (> 100 nm) TiN precipitates (including complex NbC/TiN precipitates), were not effective hydrogen traps.

12) The effective diffusion coefficients during 1st and 2nd transient obtained by the hydrogen diffusion model are similar to the values calculated by time-lag method.

13) The hydrogen diffusion models applied to sample 3E-plate, shows that both density and binding energy of irreversible traps are higher at surface region than near centerline region.

9 Future works

As the chemical composition and microstructure of pipeline steel is very complicated, and the mechanism of hydrogen induced cracking is still not fully understood, more efforts are needed for better prediction about the HIC susceptibility of the steel and accurate designing of steels with improved HIC resistance. Based on the present work, some aspects for future study are suggested as follows.

1) Effect of various kinds of hydrogen traps on the mechanical property degradation of pipeline stees: Although some general conclusions about classification of beneficial and harmful traps have been reported, the effects of each type of hydrogen traps on mechanical property degradation remains unclear. Slow strain rate test (SSRT) in high pressure hydrogen gas or under cathodic charging are recommended for this purpose.

2) Application of TDS: the hydrogen permeation simulation models in Chapter 6 provides estimation on average binding energy of both reversible and irreversible traps in samples. TDS technique, which gives desorption activation energy of each type of traps in steel, can be used to evaluate the accuracy of these models.

3) Other pipeline steel with different compositions: it is worth applying the similar study process on more pipeline steels with different compositions that can offer microstructures that are not studied in the present work, such as pearlite.

4) TMCP effect: To better control the HIC resistance of pipeline steel, the effect of TMCP on formation of different types of hydrogen traps, especially those harmful ones, need to be further studied.

Reference

1. Ohaeri, E., U. Eduok, and J. Szpunar, *Hydrogen related degradation in pipeline steel: A review.* International Journal of Hydrogen Energy, 2018. **43**(31): p. 14584-14617.
2. Yalçì, H.K. and D.V. Edmonds, *Application of the hydrogen microprint and the microautoradiography techniques to a duplex stainless steel.* Materials Characterization, 1995. **34**(2): p. 97-104.
3. Ovejero-García, J., *Hydrogen microprint technique in the study of hydrogen in steels.* Journal of Materials Science, 1985. **20**: p. 2623-2629.
4. Ogura, S. and K. Fukutani, *Thermal Desorption Spectroscopy*, in *Compendium of Surface and Interface Analysis*, J. The Surface Science Society of, Editor. 2018, Springer Singapore: Singapore. p. 719-724.
5. Hultquist, G., et al., *Hydrogen in metals studied by Thermal Desorption Spectroscopy (TDS).* Corrosion Science, 2015. **93**: p. 324-326.
6. Verbeken, K., *2 - Analysing hydrogen in metals: bulk thermal desorption spectroscopy (TDS) methods*, in *Gaseous Hydrogen Embrittlement of Materials in Energy Technologies*, R.P. Gangloff and B.P. Somerday, Editors. 2012, Woodhead Publishing. p. 27-55.
7. Boes, N. and H. Züchner, *Electrochemical methods for studying diffusion, permeation and solubility of hydrogen in metals.* Journal of the Less Common Metals, 1976. **49**: p. 223-240.
8. Devanathan, M. and Z. Stachurski, *The adsorption and diffusion of electrolytic hydrogen in palladium.* Proceedings of the Royal Society of London. Series A. Mathematical and Physical Sciences, 1962. **270**(1340): p. 90-102.
9. McBreen, J., L. Nonis, and W. Beck, *A method for determination of the permeation rate of hydrogen through metal membranes.* Journal of the electrochemical society, 1966. **113**(11): p. 1218-1222.
10. Zakroczymski, T. and J. Flis, *Impedance characterization of the activation of iron surface for hydrogen entry from alkaline solution.* Electrochimica Acta, 1996. **41**(7): p. 1245-1250.
11. Takahashi, J., et al., *The first direct observation of hydrogen trapping sites in TiC precipitation-hardening steel through atom probe tomography.* Scripta Materialia, 2010. **63**(3): p. 261-264.
12. Ghosh, G., et al., *Hydrogen induced cracking of pipeline and pressure vessel steels: A review.* Engineering Fracture Mechanics, 2018. **199**: p. 609-618.
13. Robertson, I.M., et al., *Hydrogen embrittlement understood.* Metallurgical and Materials Transactions B, 2015. **46**(3): p. 1085-1103.
14. Krom, A.H.M. and A. Bakker, *Hydrogen trapping models in steel.* Metallurgical and Materials Transactions B, 2000. **31**(6): p. 1475-1482.
15. Foster, A.M.a.P.K., *A New Analysis of the Diffusion of Hydrogen in Iron and Ferritic Steels.* Trans. Metall. Soc. AIME, 1963. **227**: p. 618-627.
16. Oriani, R.A., *The diffusion and trapping of hydrogen in steel.* Acta Metallurgica, 1970. **18**(1): p. 147-157.
17. Dong, C.F., et al., *Effects of hydrogen-charging on the susceptibility of X100 pipeline steel to hydrogen-induced cracking.* International Journal of Hydrogen Energy, 2009. **34**(24): p. 9879-9884.
18. Kumnick, A.J. and H.H. Johnson, *Hydrogen transport through annealed and deformed armco iron.* Metallurgical Transactions, 1974. **5**(5): p. 1199-1206.
19. Haq, A.J., et al., *Effect of microstructure and composition on hydrogen permeation in X70 pipeline steels.* International Journal of Hydrogen Energy, 2013. **38**(5): p. 2544-2556.
20. Fischer, F.D., G. Mori, and J. Svoboda, *Modelling the influence of trapping on hydrogen permeation in metals.* Corrosion Science, 2013. **76**: p. 382-389.

21. Vecchi, L., et al., *Modelling of hydrogen permeation experiments in iron alloys: Characterization of the accessible parameters–Part I–The entry side.* Electrochimica Acta, 2018. **262**: p. 57-65.

22. Yazdipour, N., et al., *2D modelling of the effect of grain size on hydrogen diffusion in X70 steel.* Computational Materials Science, 2012. **56**: p. 49-57.

23. Johnson, W.H., *On Some Remarkable Changes Produced in Iron and Steel by the Action of Hydrogen and Acids.* Nature, 1875. **11**(281): p. 393-393.

24. Sadananda, K. and A.K. Vasudevan, *Review of Environmentally Assisted Cracking.* Metallurgical and Materials Transactions A, 2011. **42**(2): p. 279-295.

25. Sun, B., et al., *Current Challenges and Opportunities Toward Understanding Hydrogen Embrittlement Mechanisms in Advanced High-Strength Steels: A Review.* Acta Metallurgica Sinica (English Letters), 2021. **34**(6): p. 741-754.

26. H.K.D.H.Bhadeshia, *Prevention of hydrogen embrittlement in steels.* ISIJ International, 2016. **56**.

27. Nishioka, K. and K. Ichikawa, *Progress in thermomechanical control of steel plates and their commercialization.* Science and technology of advanced materials, 2012. **13**(2): p. 023001-023001.

28. Endo, S. and N. Nakata, *Development of Thermo-Mechanical Control Process (TMCP) and high performance steel in JFE Steel.* 2015: p. 1-7.

29. Imao Tamura, C.O., Tomo Tanaka, Hiroshi Sekine, *Thermomechanical Processing of High-Strength Low-Alloy Steels*. 1988.

30. Graux, A., et al., *Design and Development of Complex Phase Steels with Improved Combination of Strength and Stretch-Flangeability.* Metals, 2020. **10**(6): p. 824.

31. D. Bai, e.a., *Process for making high strength micro-alloy steel*. 2004.

32. Jansto, S.G., *High Quality TMCP Production and Metallurgy of Niobium Bearing Steels.* Materials Science Forum, 2017. **879**: p. 820-825.

33. Cui, Q., et al., *Effect of nanosized nbc precipitates on hydrogen diffusion in x80 pipeline steel.* Materials, 2017. **10**(7): p. 721.

34. Wei, F.-G., T. Hara, and K. Tsuzaki. *Nano-Preciptates Design with Hydrogen Trapping Character in High Strength Steel*. in *Advanced Steels*. 2011. Berlin, Heidelberg: Springer Berlin Heidelberg.

35. Cheng, S., et al., *Effect of coiling temperature on microstructure and properties of X100 pipeline steel.* Materials Science and Engineering: A, 2016. **666**: p. 156-164.

36. Xue, J., et al., *Effects of rolling and coiling temperature on the microstructure and mechanical properties of hot-rolled high strength complex phase steel.* Materials Research Express, 2019. **6**(9): p. 0965c8.

37. Militzer, M., E.B. Hawbolt, and T.R. Meadowcroft, *Microstructural model for hot strip rolling of high-strength low-alloy steels.* Metallurgical and Materials Transactions A, 2000. **31**(4): p. 1247-1259.

38. Murakami, Y., *21 - Hydrogen embrittlement*, in *Metal Fatigue (Second Edition)*, Y. Murakami, Editor. 2019, Academic Press. p. 567-607.

39. Esaklul, K.A., *13 - Hydrogen damage*, in *Trends in Oil and Gas Corrosion Research and Technologies*, A.M. El-Sherik, Editor. 2017, Woodhead Publishing: Boston. p. 315-340.

40. Raja, V. and T. Shoji, *Stress corrosion cracking: theory and practice*. 2011: Elsevier.

41. Popov, B.N., J.-W. Lee, and M.B. Djukic, *Chapter 7 - Hydrogen Permeation and Hydrogen-Induced Cracking*, in *Handbook of Environmental Degradation of Materials (Third Edition)*, M. Kutz, Editor. 2018, William Andrew Publishing. p. 133-162.

42. !!! INVALID CITATION !!! {}.

43. Jin, T.Y., Z.Y. Liu, and Y.F. Cheng, *Effect of non-metallic inclusions on hydrogen-induced cracking of API5L X100 steel.* International Journal of Hydrogen Energy, 2010. **35**(15): p. 8014-8021.

44.   Du, X.S., et al., *Effect of microstructures and inclusions on hydrogen-induced cracking and blistering of A537 steel.* Materials Science and Engineering: A, 2015. **642**: p. 181-186.

45.   Park, G.T., et al., *Effect of microstructure on the hydrogen trapping efficiency and hydrogen induced cracking of linepipe steel.* Corrosion Science, 2008. **50**(7): p. 1865-1871.

46.   Zhang, S., et al., *Dual role of nanosized NbC precipitates in hydrogen embrittlement susceptibility of lath martensitic steel.* Corrosion Science, 2020. **164**: p. 108345.

47.   Fan, E.-d., et al., *Effect of nanosized NbC precipitates on hydrogen-induced cracking of high-strength low-alloy steel.* International Journal of Minerals, Metallurgy, and Materials, 2021. **28**: p. 249.

48.   Moon, J., C. Park, and S.-J. Kim, *Influence of Ti addition on the hydrogen induced cracking of API 5L X70 hot-rolled pipeline steel in acid sour media.* Metals and Materials International, 2012. **18**(4): p. 613-617.

49.   Huang, F., et al., *Hydrogen-induced cracking susceptibility and hydrogen trapping efficiency of different microstructure X80 pipeline steel.* Journal of Materials Science, 2011. **46**(3): p. 715-722.

50.   Beidokhti, B., A. Dolati, and A.H. Koukabi, *Effects of alloying elements and microstructure on the susceptibility of the welded HSLA steel to hydrogen-induced cracking and sulfide stress cracking.* Materials Science and Engineering: A, 2009. **507**(1): p. 167-173.

51.   Carneiro, R.A., R.C. Ratnapuli, and V. de Freitas Cunha Lins, *The influence of chemical composition and microstructure of API linepipe steels on hydrogen induced cracking and sulfide stress corrosion cracking.* Materials Science and Engineering: A, 2003. **357**(1): p. 104-110.

52.   Liou, H.-Y., et al., *Roles of Microalloying Elements in Hydrogen Induced Cracking Resistant Property of HSLA Steels.* Corrosion, 1993. **49**(5): p. 389-398.

53.   Smith, V., et al. *Hydrogen induced cracking safe materials operating limits*. in *CORROSION 2015*. 2015. OnePetro.

54.   McEvily, A.J. and I. Le May, *Hydrogen-assisted cracking.* Materials Characterization, 1991. **26**(4): p. 253-268.

55.   Zhang, G.A. and Y.F. Cheng, *Micro-electrochemical characterization of corrosion of welded X70 pipeline steel in near-neutral pH solution.* Corrosion Science, 2009. **51**(8): p. 1714-1724.

56.   Chen, W., *An Overview of Near-Neutral pH Stress Corrosion Cracking in Pipelines and Mitigation Strategies for Its Initiation and Growth.* Corrosion, 2016. **72**(7): p. 962-977.

57.   Zhao, Q., et al., *Understanding the Effect of Nanosized NbC Precipitates on the Stress Corrosion Cracking of High-Strength Low-Alloy Steel in a Simulated Deep-Sea Environment.* Journal of Materials Engineering and Performance, 2021. **30**(3): p. 2159-2173.

58.   Hirth, J.P., *Effects of hydrogen on the properties of iron and steel.* Metallurgical Transactions A, 1980. **11**(6): p. 861-890.

59.   Troiano, A.R., *The Role of Hydrogen and Other Interstitials in the Mechanical Behavior of Metals.* Metallography, Microstructure, and Analysis, 2016. **5**(6): p. 557-569.

60.   Oriani, R.A., *A mechanistic theory of hydrogen embrittlement of steels.* Berichte der Bunsengesellschaft für physikalische Chemie, 1972. **76**(8): p. 848-857.

61.   Wei, X., et al., *The effect of hydrogen on the evolution of intergranular cracking: a cross-scale study using first-principles and cohesive finite element methods.* RSC advances, 2016. **6**(33): p. 27282-27292.

62.   Martin, M.L., et al., *Hydrogen-induced intergranular failure in nickel revisited.* Acta Materialia, 2012. **60**(6): p. 2739-2745.

63.   Li, X., et al., *Review of Hydrogen Embrittlement in Metals: Hydrogen Diffusion, Hydrogen Characterization, Hydrogen Embrittlement Mechanism and Prevention.* Acta Metallurgica Sinica (English Letters), 2020. **33**(6): p. 759-773.

64.   Johnson, H., J. Morlet, and A. Troiano, *Hydrogen, crack initiation, and delayed failure in steel.* Trans. Met. Soc. AIME, 1958. **212**.

65.   Martin, M.L., et al., *Enumeration of the hydrogen-enhanced localized plasticity mechanism for hydrogen embrittlement in structural materials.* Acta Materialia, 2019. **165**: p. 734-750.

66.   Birnbaum, H.K. and P. Sofronis, *Hydrogen-enhanced localized plasticity—a mechanism for hydrogen-related fracture.* Materials Science and Engineering: A, 1994. **176**(1): p. 191-202.

67.   Martin, M.L., I.M. Robertson, and P. Sofronis, *Interpreting hydrogen-induced fracture surfaces in terms of deformation processes: A new approach.* Acta Materialia, 2011. **59**(9): p. 3680-3687.

68.   Ferrin, P., et al., *Hydrogen adsorption, absorption and diffusion on and in transition metal surfaces: A DFT study.* Surface Science, 2012. **606**: p. 679-689.

69.   Dwivedi, S.K. and M. Vishwakarma, *Hydrogen embrittlement in different materials: A review.* International Journal of Hydrogen Energy, 2018. **43**(46): p. 21603-21616.

70.   Vollman, K., A. Côte-Verhaaf, and R. Illing, *Public inquiry concerning stress corrosion cracking on Canadian oil and gas pipelines.* 1996.

71.   Chen, X., et al., *Effect of cathodic protection on corrosion of pipeline steel under disbonded coating.* Corrosion Science, 2009. **51**(9): p. 2242-2245.

72.   Liang, P., et al., *Stress corrosion cracking of X80 pipeline steel in simulated alkaline soil solution.* Materials & Design, 2009. **30**(5): p. 1712-1717.

73.   van Renssen, S., *The hydrogen solution?* Nature Climate Change, 2020. **10**(9): p. 799-801.

74.   Findlay, C. *Repurposing gas infrastructure for hydrogen* 2020; Available from: https://www.siemens-energy.com/global/en/news/magazine/2020/repurposing-natural-gas-infrastructure-for-hydrogen.html.

75.   *Transporting Pure Hydrogen by Repurposing Existing Gas Infrastructure: Overview of existing studies and reflections on the conditions for repurposing*. 2021, European Union Agency for the Cooperation of Energy Regulators.

76.   Addach, H., et al., *Hydrogen permeation in iron at different temperatures.* Materials Letters, 2005. **59**(11): p. 1347-1351.

77.   Zakroczymski, T., *Adaptation of the electrochemical permeation technique for studying entry, transport and trapping of hydrogen in metals.* Electrochimica Acta, 2006. **51**(11): p. 2261-2266.

78.   Cheng, Y.F., *Analysis of electrochemical hydrogen permeation through X-65 pipeline steel and its implications on pipeline stress corrosion cracking.* International Journal of Hydrogen Energy, 2007. **32**(9): p. 1269-1276.

79.   Akiyama, E. and S. Li, *Electrochemical hydrogen permeation tests under galvanostatic hydrogen charging conditions conventionally used for hydrogen embrittlement study.* Corrosion Reviews, 2016. **34**(1-2): p. 103-112.

80.   Liu, Z.-y., et al., *Local additional potential model for effect of strain rate on SCC of pipeline steel in an acidic soil solution.* Corrosion Science - CORROS SCI, 2009. **51**: p. 2863-2871.

81.   Driver, R., *Electrodeposition of Palladium on Iron and Steel for Electrochemical Hydrogen Permeation Studies.* Journal of Electroanalytical Chemistry, 1981. **128**(11).

82.   Manolatos, P. and M. Jerome, *A thin palladium coating on iron for hydrogen permeation studies.* Electrochimica Acta, 1996. **41**(3): p. 359-365.

83.   Chen, S.C., et al., *Preparation of palladium membrane by electroplating on AISI 316L porous stainless steel supports and its use for methanol steam reformer.* Journal of Membrane Science, 2008. **314**(1): p. 5-14.

84.   Zakroczymski, T. and Z. Szklarska-Smialowska, *Activation of the iron surface to hydrogen absorption resulting from a long cathodic treatment in NaOH solution.* Journal of the Electrochemical Society, 1985. **132**(11): p. 2548-2552.

85.   Casanova, T. and J. Crousier, *The influence of an oxide layer on hydrogen permeation through steel.* Corrosion Science, 1996. **38**(9): p. 1535-1544.

86.   Elhamid, M.A., B. Ateya, and H. Pickering, *The effect of iodide ions on the kinetics of hydrogen absorption by iron.* Journal of the Electrochemical Society, 2000. **147**(6): p. 2258-2262.

87.   Zakroczymski, T., Z. Szklarska-śmiałowska, and M. Śmiałowski, *Effect of Promoters on the Permeation of electrolytic hydrogen through steel.* Materials and Corrosion, 1976. **27**(9): p. 625-630.

88.   Lillard, R.S., D.G. Enos, and J.R. Scully, *Calcium Hydroxide as a Promoter of Hydrogen Absorption in 99.5% Fe and a Fully Pearlitic 0.8% C Steel during Electrochemical Reduction of Water.* CORROSION, 2000. **56**(11): p. 1119-1132.

89.   Flis, J., et al., *Changes in hydrogen entry rate and in surface of iron during cathodic polarisation in alkaline solutions.* Electrochimica Acta, 1999. **44**(23): p. 3989-3997.

90.   Zakroczymski, T., V. Kleshnya, and J. Flis, *Evolution and entry of hydrogen into iron during cathodic charging in alkaline solution with ethylenediaminetetraacetic acid.* Journal of The Electrochemical Society, 1998. **145**(4): p. 1142-1148.

91.   Flis-Kabulska, I., T. Zakroczymski, and J. Flis, *Accelerated entry of hydrogen into iron from NaOH solutions at low cathodic and low anodic polarisations.* Electrochimica Acta, 2007. **52**(9): p. 2966-2977.

92.   Gabrielli, C., et al., *Transfer function analysis of hydrogen permeation through a metallic membrane in a Devanathan cell: Part II: Experimental investigation on iron membrane.* Journal of Electroanalytical Chemistry, 2006. **590**(1): p. 15-25.

93.   ISO, *ISO 17081 Method of measurement of hydrogen permeation and determination of hydrogen uptake and transport in metals by an electrochemical technique*. 2014.

94.   ASTM, *Standard Practice for Evaluation of Hydrogen Uptake, Permeation, and Transport in Metals by an Electrochemical Technique*. 2018.

95.   McKibben, R., et al., *A potentiostatic double-step method for measuring hydrogen atom diffusion and trapping in metal electrodes—I. Theory.* Acta Metallurgica, 1987. **35**(1): p. 253-262.

96.   Crank, J., *The Mathematics of diffusion*. 1975: Oxford University Press.

97.   Standardization, I.O.f., *ISO 17081 Method of measurement of hydrogen permeation and determination of hydrogen uptake and transport in metals by an electrochemical technique*. 2014.

98.   Turnbull, A., M. Saenz de Santa Maria, and N.D. Thomas, *The effect of H2S concentration and pH on hydrogen permeation in AISI 410 stainless steel in 5% NaCl.* Corrosion Science, 1989. **29**(1): p. 89-104.

99.   Izadi, H., M. Tavakoli, and M.H. Moayed, *Effect of thermomechanical processing on hydrogen permeation in API X70 pipeline steel.* Materials Chemistry and Physics, 2018. **220**: p. 360-365.

100.   McNabb, A. and P. Foster, *A new analysis of the diffusion of hydrogen in iron and ferritic steels.* Trans. Metall. Soc. AIME, 1963. **227**(3): p. 618-627.

101.   Castro, F.J. and G. Meyer, *Thermal desorption spectroscopy (TDS) method for hydrogen desorption characterization (I): theoretical aspects.* Journal of Alloys and Compounds, 2002. **330-332**: p. 59-63.

102.   Silverstein, R., D. Eliezer, and E. Tal-Gutelmacher, *Hydrogen trapping in alloys studied by thermal desorption spectrometry.* Journal of Alloys and Compounds, 2018. **747**: p. 511-522.

103.   Frappart, S., et al., *Hydrogen trapping in martensitic steel investigated using electrochemical permeation and thermal desorption spectroscopy.* Scripta Materialia, 2011. **65**(10): p. 859-862.

104.   Pérez Escobar, D., et al., *Thermal desorption spectroscopy study of the interaction between hydrogen and different microstructural constituents in lab cast Fe–C alloys.* Corrosion Science, 2012. **65**: p. 199-208.

105. Depover, T. and K. Verbeken, *Understanding the Interaction Between a Steel Microstructure and Hydrogen: The Key to Develop More Hydrogen Resistant Materials*, in *The 28th International Ocean and Polar Engineering Conference*. 2018, International Society of Offshore and Polar Engineers: Sapporo, Japan. p. 8.

106. Ichitani, K., M. Kanno, and S. Kuramoto, *Recent development in hydrogen microprint technique and its application to hydrogen embrittlement.* ISIJ international, 2003. **43**(4): p. 496-504.

107. Thomas, A. and J.A. Szpunar, *Hydrogen diffusion and trapping in X70 pipeline steel.* International Journal of Hydrogen Energy, 2020. **45**(3): p. 2390-2404.

108. Nagao, A., et al., *Visualization of hydrogen transport in high strength steels affected by stress fields and hydrogen trapping.* Scripta materialia, 2001. **45**(10): p. 1227-1232.

109. Ohnuma, M., et al., *Direct observation of hydrogen trapped by NbC in steel using small-angle neutron scattering.* Scripta Materialia, 2008. **58**(2): p. 142-145.

110. Chen, Y.S., et al., *Direct observation of individual hydrogen atoms at trapping sites in a ferritic steel.* Science, 2017. **355**(6330): p. 1196.

111. Ivanov, E.S., et al., *Use of impedance spectroscopy for evaluating pipe steel susceptibility towards hydrogenation and hydrogen cracking.* Metallurgist, 2012. **56**(7): p. 597-603.

112. Johnson, H.H., *Hydrogen in iron.* Metallurgical Transactions B, 1988. **19**(5): p. 691-707.

113. Wert, C.A., *Trapping of hydrogen in metals*. 1978.

114. Liu, Q. and A. Atrens, *Reversible hydrogen trapping in a 3.5NiCrMoV medium strength steel.* Corrosion Science, 2015. **96**: p. 112-120.

115. Liang, Y., et al., *Effect of hydrogen trapping on void growth and coalescence in metals and alloys.* Mechanics of Materials, 2008. **40**(3): p. 115-132.

116. Raymond, L., *Hydrogen embrittlement: prevention and control*. Vol. 962. 1988: ASTM International.

117. Pressouyre, G.M., *Trap theory of Hydrogen embrittlement.* Acta Metallurgica, 1980. **28**(7): p. 895-911.

118. Maroef, I., et al., *Hydrogen trapping in ferritic steel weld metal.* International Materials Reviews, 2002. **47**(4): p. 191-223.

119. Wallaert, E., et al., *Thermal Desorption Spectroscopy Evaluation of the Hydrogen-Trapping Capacity of NbC and NbN Precipitates.* Metallurgical and Materials Transactions A, 2014. **45**(5): p. 2412-2420.

120. Lee, H.G. and J.-Y. Lee, *Hydrogen trapping by TiC particles in iron.* Acta Metallurgica, 1984. **32**(1): p. 131-136.

121. Xue, H.B. and Y.F. Cheng, *Characterization of inclusions of X80 pipeline steel and its correlation with hydrogen-induced cracking.* Corrosion Science, 2011. **53**(4): p. 1201-1208.

122. Takai, K. and N. Abe, *Identification of hydrogen desorption peak temperatures, binding energies, and occupation ratios at vacancies, dislocations and grain boundaries in iron and steel.* Proceedings of the International Hydrogen Energy Development Forum 2013, 2013: p. 29-36.

123. Novak, P., et al., *A statistical, physical-based, micro-mechanical model of hydrogen-induced intergranular fracture in steel.* Journal of the Mechanics and Physics of Solids, 2010. **58**(2): p. 206-226.

124. Li, D., R.P. Gangloff, and J.R. Scully, *Hydrogen trap states in ultrahigh-strength AERMET 100 steel.* Metallurgical and materials transactions A, 2004. **35**(3): p. 849-864.

125. Choo, W.Y. and J.Y. Lee, *Thermal analysis of trapped hydrogen in pure iron.* Metallurgical Transactions A, 1982. **13**(1): p. 135-140.

126. Lee, J.L. and J.Y. Lee, *Hydrogen trapping in AISI 4340 steel.* Metal Science, 1983. **17**(9): p. 426-432.

127.   Hong, G.-W. and J.-Y. Lee, *The measurement of the trap binding energy by the thermal analysis technique.* Scripta Metallurgica, 1983. **17**(7): p. 823-826.

128.   Peng, Z., et al., *Comparative study of non-metallic inclusions on the critical size for HIC initiation and its influence on hydrogen trapping.* International Journal of Hydrogen Energy, 2020. **45**(22): p. 12616-12628.

129.   Peng, Z., et al., *The significance of inclusion morphology and composition in governing hydrogen transportation and trapping in steels.* International Journal of Hydrogen Energy, 2021. **46**(56): p. 28811-28822.

130.   Huang, F., et al., *Effect of microstructure and inclusions on hydrogen induced cracking susceptibility and hydrogen trapping efficiency of X120 pipeline steel.* Materials Science and Engineering: A, 2010. **527**(26): p. 6997-7001.

131.   Zhao, M.-C., K. Yang, and Y. Shan, *The effects of thermo-mechanical control process on microstructures and mechanical properties of a commercial pipeline steel.* Materials Science and Engineering: A, 2002. **335**(1): p. 14-20.

132.   Dong, C.F., et al., *Hydrogen-induced cracking and healing behaviour of X70 steel.* Journal of Alloys and Compounds, 2009. **484**(1): p. 966-972.

133.   Chan, S.L.I., *Hydrogen trapping ability of steels with different microstructures.* Journal of the Chinese Institute of Engineers, 1999. **22**(1): p. 43-53.

134.   Luu, W. and J. Wu, *The influence of microstructure on hydrogen transport in carbon steels.* Corrosion Science, 1996. **38**(2): p. 239-245.

135.   Luppo, M.I. and J. Ovejero-Garcia, *The influence of microstructure on the trapping and diffusion of hydrogen in a low carbon steel.* Corrosion Science, 1991. **32**(10): p. 1125-1136.

136.   Parvathavarthini, N., et al., *Studies on hydrogen permeability of 2.25% Cr–1% Mo ferritic steel: correlation with microstructure.* Journal of Nuclear Materials, 2001. **288**(2): p. 187-196.

137.   Mohtadi-Bonab, M.A., et al., *Evaluation of hydrogen induced cracking behavior of API X70 pipeline steel at different heat treatments.* International Journal of Hydrogen Energy, 2014. **39**(11): p. 6076-6088.

138.   Turk, A., et al., *Quantification of hydrogen trapping in multiphase steels: Part II – Effect of austenite morphology.* Acta Materialia, 2020. **197**: p. 253-268.

139.   Chan, S.L.I., H.L. Lee, and J.R. Yang, *Effect of retained austenite on the hydrogen content and effective diffusivity of martensitic structure.* Metallurgical Transactions A, 1991. **22**(11): p. 2579-2586.

140.   Saleh, A.A., et al., *Investigation of the effect of electrolytic hydrogen charging of X70 steel: II. Microstructural and crystallographic analyses of the formation of hydrogen induced cracks and blisters.* International Journal of Hydrogen Energy, 2016. **41**(28): p. 12424-12435.

141.   Wang, M., et al., *Enhancing Hydrogen Embrittlement Resistance of Lath Martensite by Introducing Nano-Films of Interlath Austenite.* Metallurgical and Materials Transactions A, 2015. **46**(9): p. 3797-3802.

142.   Chatzidouros, E.V., V.J. Papazoglou, and D.I. Pantelis, *Hydrogen effect on a low carbon ferritic-bainitic pipeline steel.* International Journal of Hydrogen Energy, 2014. **39**(32): p. 18498-18505.

143.   Arafin, M.A. and J.A. Szpunar, *Effect of bainitic microstructure on the susceptibility of pipeline steels to hydrogen induced cracking.* Materials Science and Engineering: A, 2011. **528**(15): p. 4927-4940.

144.   Kichkina, A.A., et al., *M/A-Constituent in Bainitic Low Carbon High Strength Steel Structure. Part 1.* Metallurgist, 2018. **62**(7): p. 772-782.

145.   Wang, S.H., et al., *Hydrogen permeation in a submerged arc weldment of TMCP steel.* Materials Chemistry and Physics, 2003. **77**(2): p. 447-454.

146. Xing, Y., et al., *Comparative study on hydrogen induced cracking sensitivity of two commercial API 5L X80 steels.* International Journal of Pressure Vessels and Piping, 2022. **196**: p. 104620.

147. Tau, L. and S.L.I. Chan, *Effects of ferrite/pearlite alignment on the hydrogen permeation in a AISI 4130 steel.* Materials Letters, 1996. **29**(1): p. 143-147.

148. Gong, P., E. Palmiere, and W. Rainforth, *Dissolution and precipitation behaviour in steels microalloyed with niobium during thermomechanical process.* Acta Materialia, 2015. **97**: p. 392-403.

149. Wang, Z., et al., *Strain-induced precipitation in a Ti micro-alloyed HSLA steel.* Materials Science and Engineering: A, 2011. **529**: p. 459-467.

150. Depover, T., et al., *Effect of hydrogen charging on the mechanical properties of advanced high strength steels.* International Journal of Hydrogen Energy, 2014. **39**(9): p. 4647-4656.

151. Nagao, A., et al., *The effect of nanosized (Ti,Mo)C precipitates on hydrogen embrittlement of tempered lath martensitic steel.* Acta Materialia, 2014. **74**: p. 244-254.

152. Li, L., et al., *Effects of vanadium precipitates on hydrogen trapping efficiency and hydrogen induced cracking resistance in X80 pipeline steel.* International Journal of Hydrogen Energy, 2018. **43**(36): p. 17353-17363.

153. Miyamura, H., et al., *Enhancement of hydrogen solubility in α-iron by coherent precipitates.* Journal of Alloys and Compounds, 1999. **293-295**: p. 443-445.

154. Stevens, M. and I. Bernstein, *Microstructural trapping effects on hydrogen induced cracking of a microalloyed steel.* Metallurgical Transactions A, 1989. **20**(5): p. 909-919.

155. Wei, F.G. and K. Tsuzaki, *Quantitative analysis on hydrogen trapping of TiC particles in steel.* Metallurgical and Materials Transactions a-Physical Metallurgy and Materials Science, 2006. **37A**(2): p. 331-353.

156. Pérez Escobar, D., et al., *Thermal desorption spectroscopy study of the interaction of hydrogen with TiC precipitates.* Metals and Materials International, 2013. **19**(4): p. 741-748.

157. Malard, B., et al., *Hydrogen trapping by VC precipitates and structural defects in a high strength Fe-Mn-C steel studied by small-angle neutron scattering.* Materials Science and Engineering a-Structural Materials Properties Microstructure and Processing, 2012. **536**: p. 110-116.

158. Asahi, H., D. Hirakami, and S. Yamasaki, *Hydrogen Trapping Behavior in Vanadium-added Steel.* ISIJ International, 2003. **43**(4): p. 527-533.

159. Kim, W.K., et al., *Effect of environmental and metallurgical factors on hydrogen induced cracking of HSLA steels.* Corrosion Science, 2008. **50**(12): p. 3336-3342.

160. Rahman, K.M.M., et al., *New insight into the role of inclusions in hydrogen-induced degradation of fracture toughness: three-dimensional imaging and modeling.* Philosophical Magazine, 2021. **101**(8): p. 976-996.

161. Todoshchenko, O.M.I., et al., *Role of Nonmetallic Inclusions in Hydrogen Embrittlement of High-Strength Carbon Steels with Different Microalloying.* Metallurgical and Materials Transactions A, 2014. **45**(11): p. 4742-4747.

162. Luu, W.C. and J.K. Wu, *Effects of sulfide inclusion on hydrogen transport in steels.* Materials Letters, 1995. **24**(1): p. 175-179.

163. Peng, Z., et al., *Effect of Submicron-Scale MnS Inclusions on Hydrogen Trapping and HIC Susceptibility of X70 Pipeline Steels*. Vol. 89. 2018. 1700566.

164. Martinez-Madrid, M., S.L.I. Chan, and J.A. Charles, *Hydrogen occlusivity and embrittlement in iron – effect of grain structure and cold work.* Materials Science and Technology, 2013. **1**(6): p. 454-460.

165. Shi, R., et al., *Quantitative investigation on deep hydrogen trapping in tempered martensitic steel.* Journal of Alloys and Compounds, 2021. **854**: p. 157218.

166. Ueji, R., et al., *Ultragrain refinement of plain low carbon steel by cold-rolling and annealing of martensite.* Acta Materialia, 2002. **50**(16): p. 4177-4189.

167. Kitahara, H., et al., *Crystallographic features of lath martensite in low-carbon steel.* Acta Materialia, 2006. **54**(5): p. 1279-1288.

168. Morito, S., et al., *The morphology and crystallography of lath martensite in alloy steels.* Acta Materialia, 2006. **54**(19): p. 5323-5331.

169. Nagao, A., et al., *Hydrogen-enhanced-plasticity mediated decohesion for hydrogen-induced intergranular and "quasi-cleavage" fracture of lath martensitic steels.* Journal of the Mechanics and Physics of Solids, 2018. **112**: p. 403-430.

170. Jinghui WU, P.J.W., Calixto I. GARCIA, Mingjian HUA and Anthony J. DEARDO, *Image Quality Analysis: A New Method of Characterizing Microstructures.* ISIJ International, 2005. **45**(2): p. 254-262.

171. Devanathan, M.A.V. and Z. Stachurski, *The Mechanism of Hydrogen Evolution on Iron in Acid Solutions by Determination of Permeation Rates.* Journal of The Electrochemical Society, 1964. **111**(5): p. 619.

172. Manolatos, P., M. Jerome, and J. Galland, *Necessity of a palladium coating to ensure hydrogen oxidation during electrochemical permeation measurements on iron.* Electrochimica Acta, 1995. **40**(7): p. 867-871.

173. Carvalho, J.P.D., E.O. Vilar, and B.A. Araújo, *A critical review and experimental analysis of the equation recommended by ASTM G148-97 and ISO 17081: 2004 for the calculation of the hydrogen diffusivity in metals and alloys.* International Journal of Hydrogen Energy, 2017. **42**(1): p. 681-688.

174. Wang, S.-C. and J.-R. Yang, *Effects of chemical composition, rolling and cooling conditions on the amount of martensite/austenite (M/A) constituent formation in low carbon bainitic steels.* Materials Science and Engineering: A, 1992. **154**(1): p. 43-49.

175. Liang, X.J., M.J. Hua, and A.J. DeArdo, *The Mechanism of Martensite-Austenite Microconstituents Formation during Thermomechanical Controlling Processing in Low Carbon Bainitic Steel.* Materials Science Forum, 2014. **783-786**: p. 704-712.

176. RAj, R., *Segregation and Homogenization of Alloying Elements in X70 Steels*. 2020, University of Alberta.

177. Park, I.-J., et al., *The advantage of grain refinement in the hydrogen embrittlement of Fe–18Mn–0.6C twinning-induced plasticity steel.* Corrosion Science, 2015. **93**: p. 63-69.

178. *The Origins of Oxide Inclusions.*

179. Yang, K.H.J.R.Y. and A. McLean, *Inclusion Detection and Analysis in Pipeline Steel.*

180. Wu, C.P.P., *Inclusion Characterization in High Strength Low Alloy Steel* 2009.

181. Koskenniska, S., et al., *RELATIONSHIP BETWEEN INCLUSIONS AND SEGREGATIONS IN CONTINUOUS CAST ULTRAHIGH-STRENGTH STEEL.*

182. Nayak, S.S., et al., *Microstructure and properties of low manganese and niobium containing HIC pipeline steel.* Materials Science and Engineering: A, 2008. **494**(1): p. 456-463.

183. Wiskel, J.B., D.G. Ivey, and H. Henein. *Nano Precipitate Analysis of X80 Pipeline Steel Using Small Angle Neutron Scattering*. in *2006 International Pipeline Conference*. 2006.

184. Zhang, J.M., et al., *NbC-TiN co-precipitation behavior and mechanical properties of X90 pipeline steels by critical-temperature rolling process.* International Journal of Pressure Vessels and Piping, 2018. **165**: p. 29-33.

185. Ruizhen, W., et al., *Microstructure and Precipitation Behavior of Nb, Ti Complex Microalloyed Steel Produced by Compact Strip Processing.* ISIJ International, 2006. **46**(9): p. 1345-1353.

186.   Lee, Y. and B.C. De Cooman, *TiN/NbC Compound Particle Formation during Thin Slab Direct Rolling of HSLA Steel.* steel research international, 2014. **85**(7): p. 1158-1172.

187.   Nagata, M.T., J.G. Speer, and D.K. Matlock, *Titanium nitride precipitation behavior in thin-slab cast high-strength low-alloy steels.* Metallurgical and Materials Transactions A, 2002. **33**(10): p. 3099-3110.

188.   Solano-Alvarez, W., et al., *Cracks in Martensite Plates as Hydrogen Traps in a Bearing Steel.* Metallurgical and Materials Transactions A, 2014. **46**: p. 665-673.

189.   Lan, L., et al., *Effect of austenite grain size on isothermal bainite transformation in low carbon microalloyed steel.* Materials Science and Technology, 2011. **27**: p. 1657-1663.

190.   Zhao, H., B.P. Wynne, and E.J. Palmiere, *Effect of austenite grain size on the bainitic ferrite morphology and grain refinement of a pipeline steel after continuous cooling.* Materials Characterization, 2017. **123**: p. 128-136.

191.   Ohtani, H., et al., *Morphology and properties of low-carbon bainite.* Metallurgical Transactions A, 1990. **21**(3): p. 877-888.

192.   Zajac, S., V. Schwinn, and K.H. Tacke, *Characterisation and Quantification of Complex Bainitic Microstructures in High and Ultra-High Strength Linepipe Steels.* Materials Science Forum, 2005. **500-501**: p. 387-394.

193.   ASTM, *ASTME112 − 12Standard Test Methods for Determining Average Grain Size*. 2013.

194.   Hu, F., P. Hodgson, and K. Wu, *Acceleration of the super bainite transformation through a coarse austenite grain size.* Materials letters, 2014. **122**: p. 240-243.

195.   Singh, K., A. Kumar, and A. Singh, *Effect of Prior Austenite Grain Size on the Morphology of Nano-Bainitic Steels.* Metallurgical and Materials Transactions A, 2018. **49**(4): p. 1348-1354.

196.   A.R.MARDER, G.K.A., *The Morphology of Martensite in Iron Alloys.* Metallurgical Transactions, 1971. **2**(September).

197.   Furuhara, T., et al., *Crystallography of upper bainite in Fe–Ni–C alloys.* Materials Science and Engineering: A, 2006. **431**(1): p. 228-236.

198.   Takayama, N., G. Miyamoto, and T. Furuhara, *Chemistry and three-dimensional morphology of martensite-austenite constituent in the bainite structure of low-carbon low-alloy steels.* Acta Materialia, 2018. **145**: p. 154-164.

199.   Beladi, H., et al., *Characterization of Nano-Structured Bainitic Steel.* International Journal of Modern Physics Conference Series, 2012. **05**: p. 1-8.

200.   Chen, S., X. Zhao, and W. Xu, *Effect of prior austenite grain size on bainitic transformation above and below Ms in medium Mn steel.* Journal of Physics: Conference Series, 2020. **1653**: p. 012043.

201.   Mandal, S., et al., *Austenite grain growth and effect of austenite grain size on bainitic transformation.* Materials Science and Technology, 2022. **38**(7): p. 409-418.

202.   Zajac, S., V. Schwinn, and K.-H. Tacke, *Characterisation and Quantification of Complex Bainitic Microstructures in High and Ultra-High Strength Linepipe Steels.* Materials Science Forum - MATER SCI FORUM, 2005. **500-501**: p. 387-394.

203.   Zhang, H., et al., *Mechanism of NbC heterogeneous nucleation on TiN in microalloyed steel: A first-principles study.* Computational Materials Science, 2018. **146**: p. 126-133.

204.   Abe, N., et al. *Identification of hydrogen trapping sites, binding energies, and occupation ratios at vacancies, dislocations and grain boundaries in iron of varying carbon content*. in *Materials Science & Technology 2011 Conference and Exhibition (MS&T Partner Societies)*. 2011.

205.   Olden, V., C. Thaulow, and R. Johnsen, *Modelling of hydrogen diffusion and hydrogen induced cracking in supermartensitic and duplex stainless steels.* Materials & Design, 2008. **29**(10): p. 1934-1948.

206.   Park, Y., et al., *Retained austenite as a hydrogen trap in steel welds.* Welding Journal-New York-, 2002. **81**(2): p. 27-S.

207. Turk, A., et al., *Quantification of hydrogen trapping in multiphase steels: Part I – Point traps in martensite.* Acta Materialia, 2020. **194**: p. 118-133.

208. Gesnouin, C., et al., *Effect of post-weld heat treatment on the microstructure and hydrogen permeation of 13CrNiMo steels.* Corrosion Science, 2004. **46**(7): p. 1633-1647.

209. Castaño-Rivera, P., V.P. Ramunni, and P. Bruzzoni, *Numerical Study of Hydrogen Trapping: Application to an API 5L X60 Steel.* ISRN Materials Science, 2012. **2012**: p. 945235.

210. Thomas, P.G. and E.J. Stern, *Efficient numerical modelling of hydrogen diffusion with trapping.* Journal of Materials Science, 1981. **16**(11): p. 3122-3130.

211. Klinkenberg, C., K. Hulka, and W. Bleck, *Niobium Carbide Precipitation in Microalloyed Steel.* Steel Research International, 2004. **75**: p. 744-752.

212. Stevens, M.F. and I.M. Bernstein, *Microstructural trapping effects on hydrogen induced cracking of a microalloyed steel.* Metallurgical Transactions A, 1989. **20**(5): p. 909-919.

213. Guo, B., et al., *Effect of Finish Rolling Temperature on the Microstructure and Tensile Properties of Nb–Ti Microalloyed X90 Pipeline Steel.* Metals, 2016. **6**(12): p. 323.

214. Miyazaki, M., K. Isobe, and T. Murao, *Formation mechanism and modeling of centerline segregation.* Nippon steel technical report, 2013. **104**: p. 48-53.

215. Guo, F., et al., *The Influence of Centerline Segregation on the Mechanical Performance and Microstructure of X70 Pipeline Steel.* steel research international, 2018. **89**(12): p. 1800407.

216. Lukito, H. and Z. Szklarska-Smialowska, *Susceptibility of medium-strength steels to hydrogen-induced cracking.* Corrosion Science, 1997. **39**(12): p. 2151-2169.

217. Liu, Q., et al., *Determination of the hydrogen fugacity during electrolytic charging of steel.* Corrosion Science, 2014. **87**: p. 239-258.

218. encyclopedia, W.t.f. *Savitzky–Golay filter*. [cited 2022; Available from: https://en.wikipedia.org/wiki/Savitzky%E2%80%93Golay_filter.

219. Savitzky, A. and M.J. Golay, *Smoothing and differentiation of data by simplified least squares procedures.* Analytical chemistry, 1964. **36**(8): p. 1627-1639.

220. Schafer, R.W., *What Is a Savitzky-Golay Filter? [Lecture Notes].* IEEE Signal Processing Magazine, 2011. **28**(4): p. 111-117.

221. Lohninger, H., *Fundamentals of statistics.* E-book. Retrieved from, 2012.

222. Onsøien, M., M. M'Hamdi, and A. Mo, *A CCT Diagram for an Offshore Pipeline Steel of X70 Type.* Welding Journal (Miami, Fla), 2009. **88**: p. 1S-6S.

223. Venkatraman, M., O. Mohanty, and R. Ghosh, *Modelling of transformation kinetics in HSLA 100 steel during continuous cooling.* Scandinavian journal of metallurgy, 2001. **30**(1): p. 8-13.

224. Kang, M., et al., *Kinetics and Morphology of Isothermal Transformations at Intermediate Temperature in 15CrMnMoV Steel.* MATERIALS TRANSACTIONS, 2009. **50**(1): p. 123-129.

225. Villa, M. and M.A.J. Somers. *Activation Energy of Time-Dependent Martensite Formation in Steel*. in *Proceedings of the International Conference on Martensitic Transformations: Chicago*. 2018. Cham: Springer International Publishing.

226. Soleimani, M., H. Mirzadeh, and C. Dehghanian, *Phase transformation mechanism and kinetics during step quenching of st37 low carbon steel.* Materials Research Express, 2019. **6**(11): p. 1165f2.

227. Yan, J.-Y., J. Ågren, and J. Jeppsson, *Pearlite in multicomponent steels: Phenomenological steady-state modeling.* Metallurgical and Materials Transactions A, 2020. **51**(5): p. 1978-2001.

228. Zhu, J.G., et al., *Bainite Transformation-Kinetics-Microstructure Characterization of Austempered 4140 Steel.* Metals, 2020. **10**(2): p. 236.

Appendix A-1 Preparation procedure for TEM sample

Carbon replica technique was used to prepare TEM samples. Firstly, the steel cube cut from specific location of a plate was mounted and grounded the same way as OM/SEM samples, then polished with 1µm and 0.25 µm polycrystalline diamond suspension (because the silicon dioxide particles would stay on the sample surface and be extracted to the carbon replica leading to an interference to precipitates characterization). Then, the sample was immersed in a vessel with ethanol and washed in an ultrasound cleaning machine for 10 min. After dried by pressured air flow, the sample was etched with 3% Nital to remove the ferrite matrix and expose precipitates. (Attention: too much over etching might cause focusing problem at lower magnification under STEM mode.) A thin layer of carbon film (8 nm) was evaporated onto the etched surface by Leica AC600 Carbon/Metal coater. The carbon film was sectioned into small squares (about 3mm×3mm) by a paper cutter before immersed in a new 3% Nital solution. When the small pieces of carbon replica detached from the surface of the sample and floated in the solution (after 2-3 hours), a copper grid was used to transfer these replicas into a solution with 50% deionized water and 50% of ethanol to rinse off the Nital solution. Then the replicas were transferred to 100% deionzed water where the replicas unfolded and floated on the surface of the water due to surface tension of water. At last, replicas were collected by 300 mesh copper grids, dried in the air and ready for observation. At least five replicas were prepared for each sample.

Appendix A-2 Python code for phase fraction calculation based on EBSD band contrast map

```python
from matplotlib import image
from matplotlib import pyplot as plt
from PIL import Image
from numpy import asarray
import numpy as np
import math
import pandas as pd

#read band contrast map data; x,y are lists for position coordinates and band_contrast is the list of index.
raw_data = pd.read_csv('Project 1 3F-C-S Site 2 Map Data 2-BC.csv',header = 0)
x = raw_data['X'].values.tolist()
y = raw_data['Y'].values.tolist()
band_contrast = raw_data['Band Contrast'].values.tolist()

#Define a function to clean up the data.
def clean_up_data (x,y,band_contrast):
    x0 = [int (i*10) for i in x]    #transfor pixels to length in μm
    y0 = [int (i*10) for i in y]
    b0 = [int (i) for i in band_contrast]   #new band contrast value list
    a=int(len(x0)-x0[-1] *y0[-1])
    for j in range (0, a):        #get rid of repeat data
        for i in range (0, len(x0)-1):
            if x0[i] == x0[i+1] and y0[i] == y0[i+1]:
                del x0[i]
                del y0[i]
                del b0[i]
                break

    df=pd.DataFrame(list(zip(x0, y0,b0)),columns =['X', 'Y','Band contrast'])
    df.to_csv('cleaned_data.csv',index=False)
    return (x0, y0, b0)

#Define a function to get rid of repeated value
def check_repeat_value (x2, y2):
    for i in range (0, len(x2) - 1):
        if x2[i] == x2[i + 1] and y2[i] == y2[i + 1]:
            print ("repeat")
            break

#Define a function to plot the image using stored data.
def draw_image (filename):
    df = pd.read_csv(filename,header = 0)
```

```python
    y = df['Y'].values.tolist()
    x = df['X'].values.tolist()
    b = df['Band contrast'].values.tolist()

    m=max(x[1:])
    n=max(y[1:])

    image_arr= np.empty([m+1, n+1, 3], dtype=int)

    for i in range (0, len(x)-1):
        image_arr[x[i]][y[i]]=[b[i],b[i],b[i]]

    return (image_arr)

#Define a function to count each pixel as ferrite, bainite or M/A, and get the friction of each phase.
    def count_phase (image_arr, value1, value2):    #value1 and value2 are thresholds to separate
                                                    M/A and bainite, and bainite and Ferrite, respectively
    total=0
    count1=0
    count2=0
    count3=0
    t = image_arr.shape
    m = t[0]
    n = t[1]
    image_arr_1 = np.empty([m, n, 3], dtype=int) #Creat an image array to distinguish the phases

    for i in range (0, m):
        for j in range (0, n):
            k=image_arr[i][j][0]
            total+=1
            if k<value1:
                image_arr_1[i][j] = [255,0,0]
                count1+=1
            elif k > value1 and k< value2:
                image_arr_1[i][j] = [0, 255, 0]
                count2+=1
            elif k> value2:
                image_arr_1[i][j] = [0, 0, 255]
                count3 += 1

    ma_ratio=count1/total*100
    bi_ratio=count2/total*100
    fe_ratio=count3/total*100

    return (image_arr_1, ma_ratio,bi_ratio,fe_ratio)
```

```
#Call functions.
x2, y2, b2=clean_up_data (x,y,band_contrast)
check_repeat_value (x2, y2)
image_arr=draw_image ("cleaned_data.csv")
plt.imshow(image_arr)
plt.show()

image_arr_1, ma_ratio_1, bi_ratio_1, fe_ratio_1=count_phase (image_arr,105,143.5)
print (ma_ratio_1, bi_ratio_1, fe_ratio_1)
plt.imshow (image_arr_1)
plt.show()
```

Appendix A-3 Experimental process of Pd electroplating

The solution used for Pd plating was 5 g $PdCl_2$ dissolved in 1 L 25 wt.% ammonia solution. The Pd plating solution was prepared at least 24 hours before the plating to ensure $PdCl_2$ powders are completely dissolved. This prevented the solution from boiling before heated to the plating temperature. The Pd electroplating experiment was conducted in a fumehood for good ventilation. The setup of the electroplating is present in Fig. A.1 and the electroplating procedures were as follows. Firstly, the sample was cleaned in an oil removal solution (NaOH 16 g, Na_2CO_3 15 g, $Na_3PO_4\cdot12H_2O$ 15 g, detergent 2 ml dissolved in 500 ml deionized water) at 80 °C for 20 min to get rid of contamination on sample surface and enhance the adhesion of Pd layer; then it was washed with deionized water and dried by cool flowing air; the entry side (charging side) of the sample was masked using an adhesive sticker which is sticky enough to prevent contamination of the plating solution but not too sticky so that it can be peeled off without any residues left on the sample surface; the sample was pickled for 60 s in 10 wt% HCl solution and then washed thoroughly with deionized water (this brief cleaning in concentrated hydrochloric acid can remove the oxides on the freshly polished sample just before immersion in the coating solution); the sample was settled in a beaker filled with plating solution and heated in a water bath at 50 °C; a compressed air flow was introduced to the bottom of the beaker to disturb the solution with bubbles continuously (although unstirred condition is also used by some researchers[81, 217], it is proved that the disturbance enables a fine and shiny surface while unstirred condition leads to dull surface with coarse grains as shown in Fig. A.2); then the sample was connected to the negative pole of a power supply, while a platinum electrode was connected with the positive pole of the power supply; when the system was stable, the electroplating process was started by switching on the power supply to a current of 80 mA (electroplating area: 19 cm^2, current density 4.2 mA/cm^2); the plating lasted 20 min, and the sample was rinsed with ethanol and dried with cool flowing air.
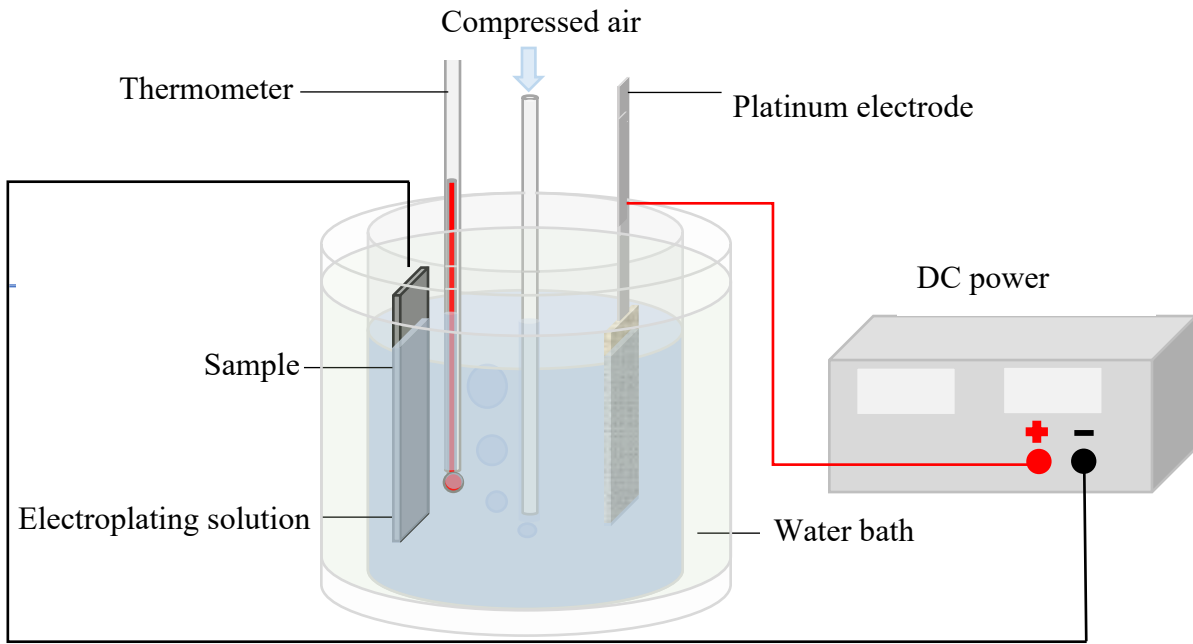
Fig. A. 1 Schematic experimental setup for Pd electroplating.

a)

b)

c)

d)
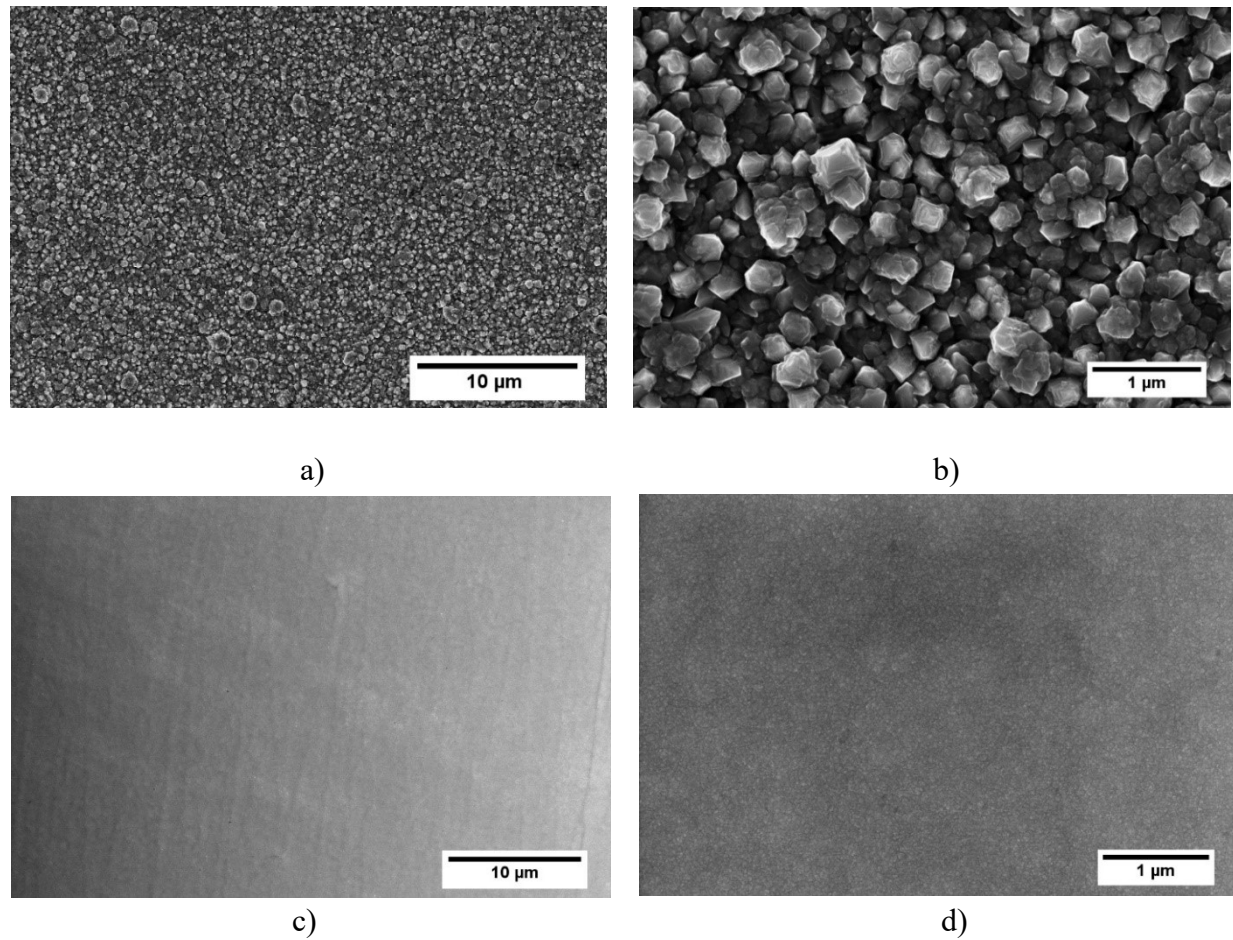
Fig. A. 2 Surface of Pd layer under SEM. a),b): without disturbing; c),d): with disturbing

Appendix A-4 Experiment procedure of hydrogen permeation test

The test procedure is as follows:

1) Prepare the solutions in charging cell and oxidation cell at least 24 hours before use and continuously bubble with N_2 gas to ensure a complete dissolution and deaeration.

2) Conduct sample preparation and electroplating within 2 hours before starting the permeation test to minimize the oxidation of sample surface on the charging side.

3) Put the two cells together with the sample clamped between them by the sample holder (the Pt electrode were fixed onto the cells and sealed with silicon).

4) Fill 0.1M NaOH + 0.01M EDTA in the charging cell and 0.1M NaOH in the oxidation cell with a large syringe through the N_2 inlets.

5) Insert the reference electrode after checking the electrolyte inside (the reference electrode was immersed in 1M NaOH solution when it was not in use, and replenishment was needed when the electrolyte level was too low).

6) Put the double-cell testing system into a Faraday box made by a carboard wrapped with aluminium foil to shield the testing system from external electrical noise.

7) Set up the deaeration system properly with N_2 gas to provide vigorous purging during the test.

8) Connect the galvanostat and the potentiostat to the charging cell and the oxidation cell, respectively (as shown in Fig.3.8).

9) Set the potential of oxidation cell to the control value (401mV) to start the polarization.

10) After 48 hours, when the oxidation current is as low and stable as possible ($< 0.1\mu A/cm^2$), switch on the galvanostat to 0.019A (charging current density: 10 mA/cm^2).

11) Monitor the oxidation curve on potentiostat and stop charging when the current reach to a steady state.

12) Switch off the potentiostat and save the testing data for later analysis.

13) Conduct another round of test on the same sample by repeating steps 9) -12) to distinguish the reversible traps from irreversible traps.

14) Disassemble the testing system, wash the cells, and let them dry in fumehood.

15) Wash the sample in ethanol and dry it with compressed air.

16) Store the sample in a clean and dry place for future use.

Appendix A-5 Derivation of t_{lag}

In hydrogen permeation test during charging process, the time-dependent equalization of hydrogen concentration in the metal is described by Fick's second Law:

$$\frac{\partial c}{\partial t} = D_{eff} \frac{\partial^2 c}{\partial x^2} \qquad \text{(A-1)}$$

Wherein c is the concentration of hydrogen at a specific time t and location x, Dx is a constant called diffusion coefficient.

In the present hydrogen permeation test, the variation of the anodic current at the exit side of the sample can be obtained by a potentiostat, which is determined by Fick's first Law by differentiation of the concentration c(t) at certain location x=s, (q is elementary charge):

$$i(t)_{x=s} = -D_{eff} qF \left(\frac{\partial c_s(t)}{\partial x} \right) \qquad \text{(A-2)}$$

Therefore, since a galvanostat is used for hydrogen charging at the entrance surface of the sample in present investigation, the initial and boundary conditions are as follows:

$$t = 0: c = 0 \ \ for \ \ 0 \le x \le L \qquad \text{(A-3)}$$

$$t > 0: \begin{cases} j_0 = D_{eff} \frac{c_\infty}{L} = const. \\ c_L = 0 \end{cases} \qquad \text{(A-4)}$$

In combination with equations (A-1) ~ (A-4), the solution of the problem is:

$$i_L(t) = i_0 \left(1 - \frac{4}{\pi} \sum_0^\infty \frac{(-1)^m}{2m+1} exp \left(-\frac{(2m+1)^2 \pi^2 D_{eff} t}{4L^2} \right) \right) \qquad \text{(A-5)}$$

$$t_{lag} = \frac{1}{2} \frac{L^2}{D_{eff}} \qquad \text{(A-6)}$$

If the concentration at x=0 (at the entrance side) is maintained (by cathodic polarization using potentiostat) at c0, while at x=L (at the exit side) it is maintained at zero, the initial and boundary conditions should be as follows:

$$t = 0: c = 0 \ \ for \ \ 0 \le x \le L \qquad \text{(A-7)}$$

$$t > 0: c_{x=0} = c_0, \ \ c_{x=L} = 0 \qquad \text{(A-8)}$$

Combing equations (A-7) ~ (A-8) with equations (A-1) ~ (A-2) ,one can obtain equation (A-9) and similarly to the method used in constant flux condition, tlag is given by equation (A-10)[9, 173]:

$$i_L(t) = i_\infty \left(1 + 2 \sum_1^\infty (-1)^m exp \left(-\frac{D_{eff} m^2 \pi^2 t}{L^2} \right) \right) \qquad \text{(A-9)}$$

$$t_{lag} = \frac{1}{6} \frac{L^2}{D_{eff}} \qquad \text{(A-10)}$$

Appendix A-6 Savitzky–Golay filter

A Savitzky-Golay filter is a digital filter that can be applied to a set of digital data points for the purpose of smoothing the data.[218] The method was proposed by Abraham Savitzky and Marcel J. E. Golay[219] based on local least-squares polynomial approximation. It is shown that fitting a polynomial to a set of input samples and then evaluating the resulting polynomial at a single point within the approximation interval is equivalent to discrete convolution with a fixed impulse response[220]. In other words, for each sample in the set of data, fit a polynomial to it with its direct neighbourhood of N neighbours, and then just evaluate the polynomial at its center and repeat this process for the next neighborhood. The basic idea of Savitzky-Golay filter smoothing data is shown in Fig. A.3, wherein the y at t_0 is determined by a polynomial fit with its neighbours. Fig. A. 4 shows an example of Savitzky-Golay filter smoothing using a second order polynomial fit with 25 data points.
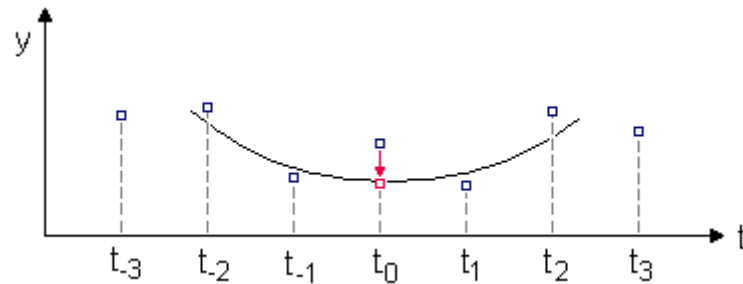
Fig. A. 3 Illustration about the basic idea of Savitzky-Golay filter.[221]
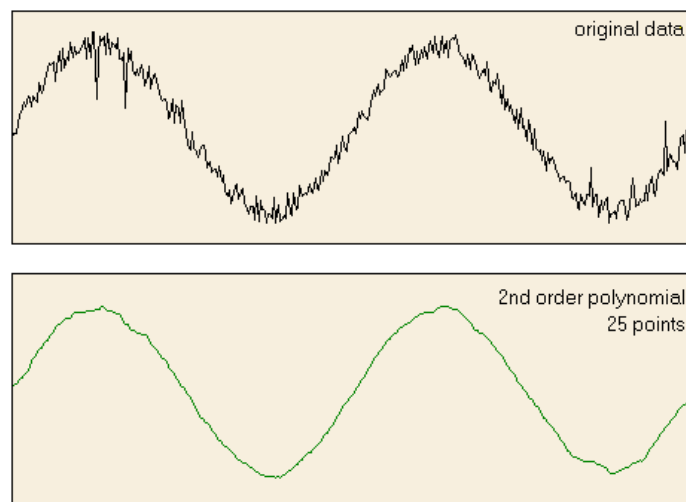
Fig. A. 4 An example of application of Savitzky-Golay filter for smoothing data.[221]

Appendix B-1 OM images of group I samples at various locations

The microstructures of group I samples at surface, quarter distance and centerline for 3E plates and at surface and centerline for 3F plates are revealed by optical microscopy (OM) and shown as follows. As shown in Fig. B.1 and Fig. B.2, ferrite, bainite and M/A constituents are presented in these samples.

a)

b)

c)

d)

e)

f)
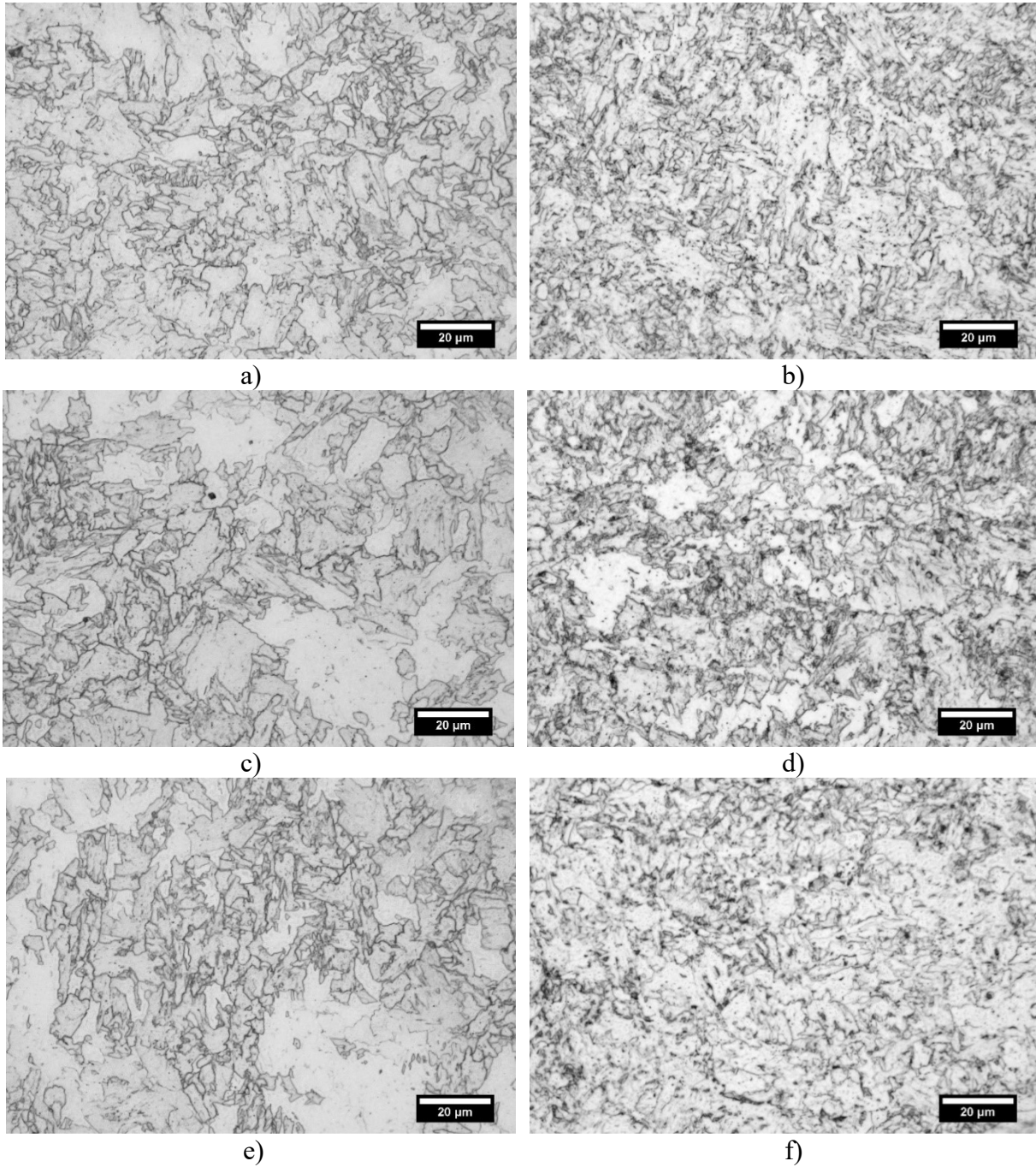
Fig. B. 1 OM image of 3E-Coiled at a) surface, b) ¼ distance, c) centerline and 3E-Air cooled at d) surface, e) ¼ distance, f) centerline.
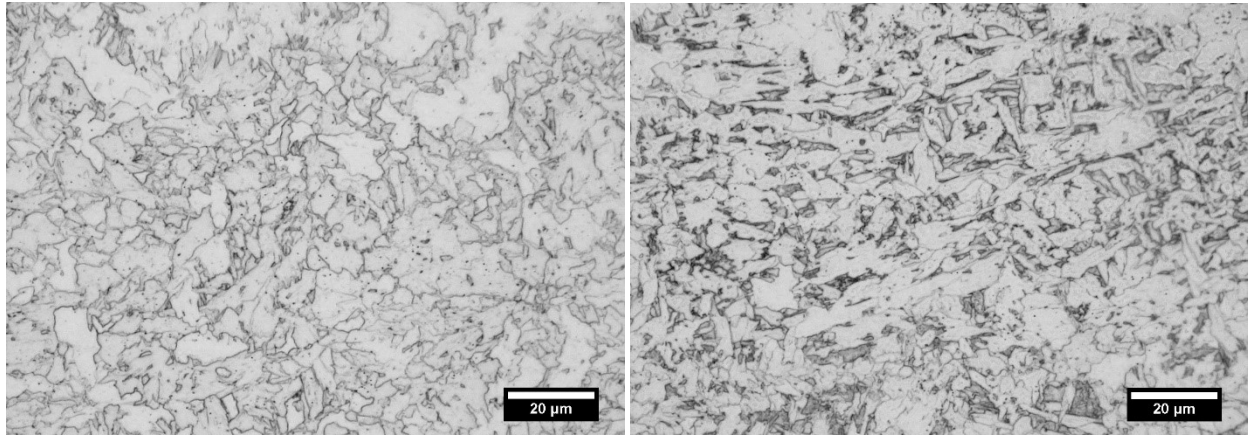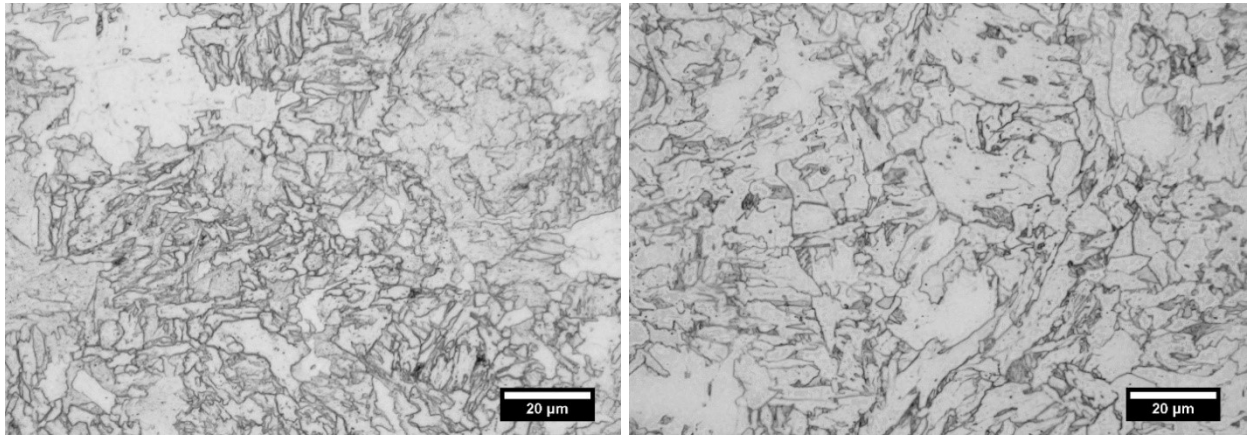
Fig. B. 2 OM image of 3F-Coiled at a) surface, c) centerline and 3F-Water quenched at b) surface, d) centerline.

Appendix B-2 Quantitatively evaluation of phases in group I samples via EBSD BC map

The phase fraction of group I samples are quantitatively evaluated via EBSD Band Contrast (BC) map and band contrast distribution curve (Fig. B.3). The analysis procedure is described in section 3.2.3.
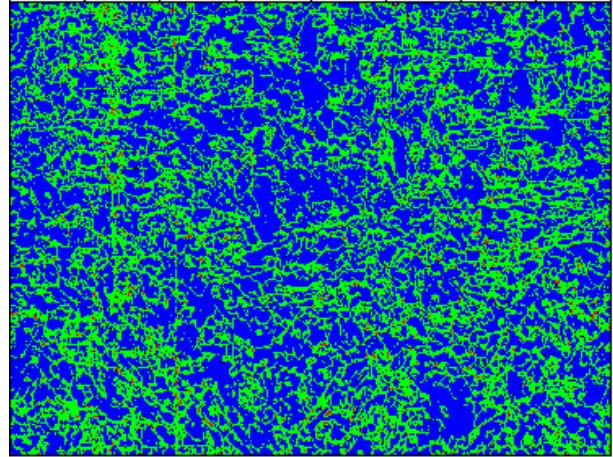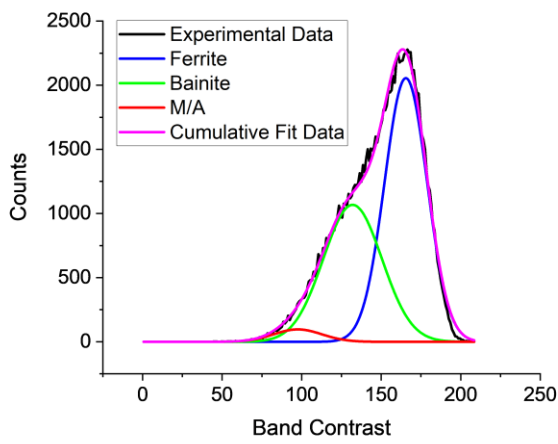
a)
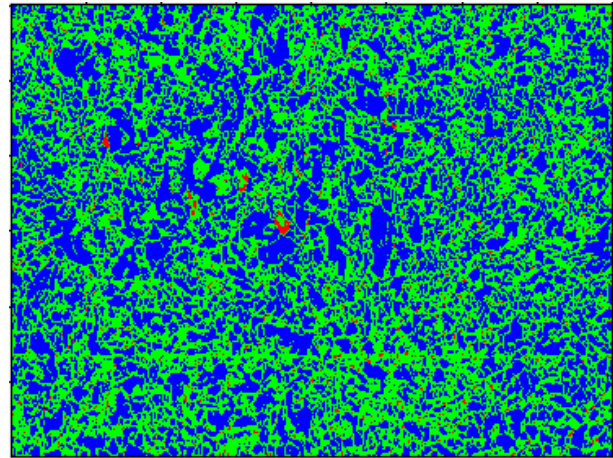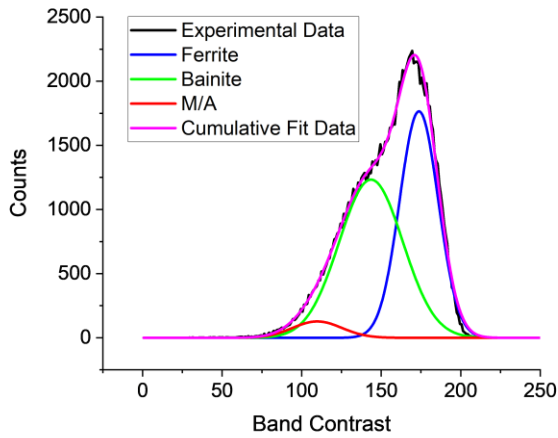
b)
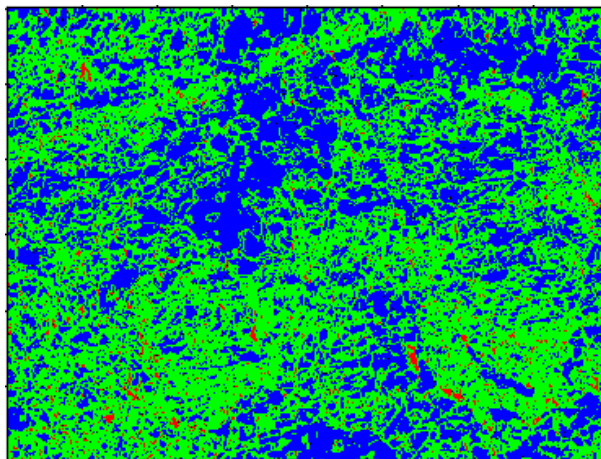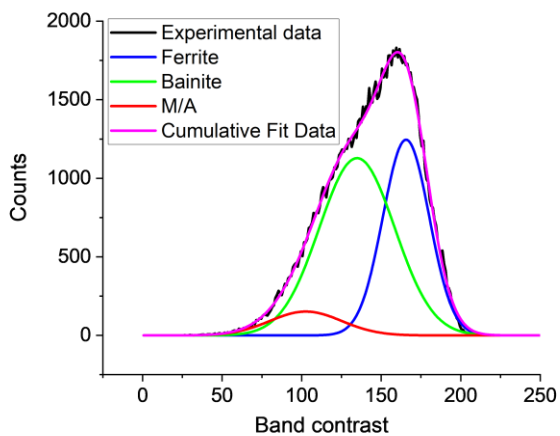
c)
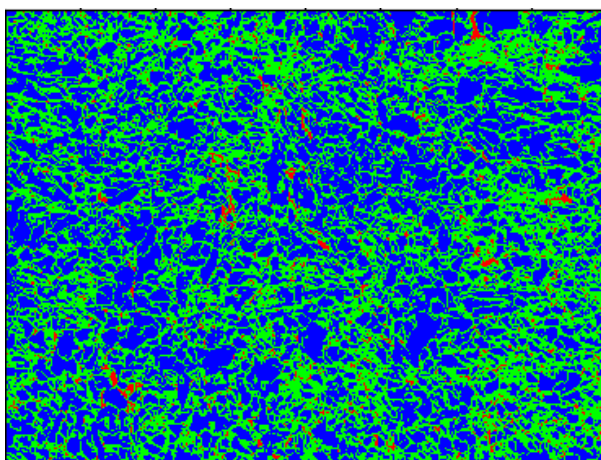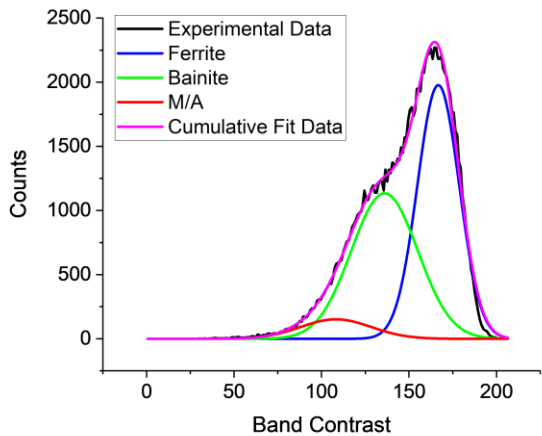
d)
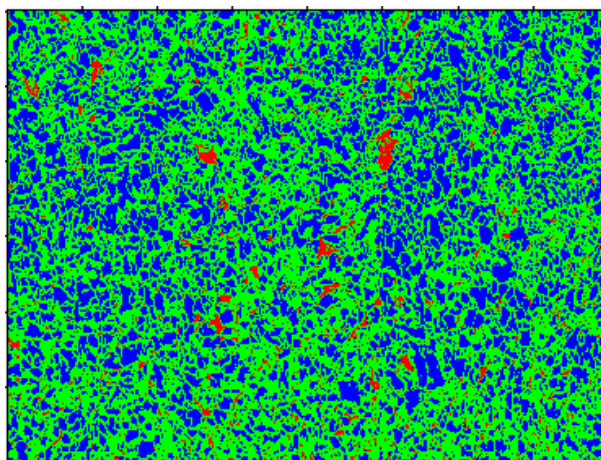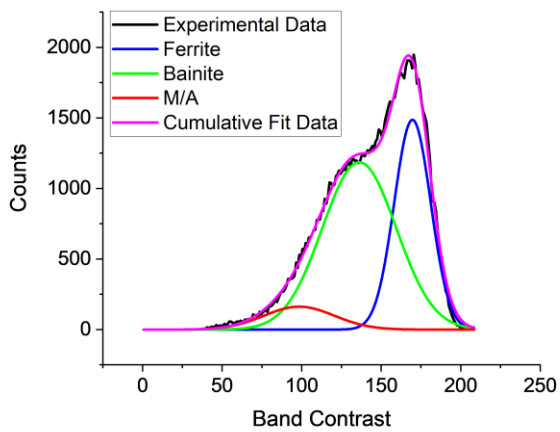
e)
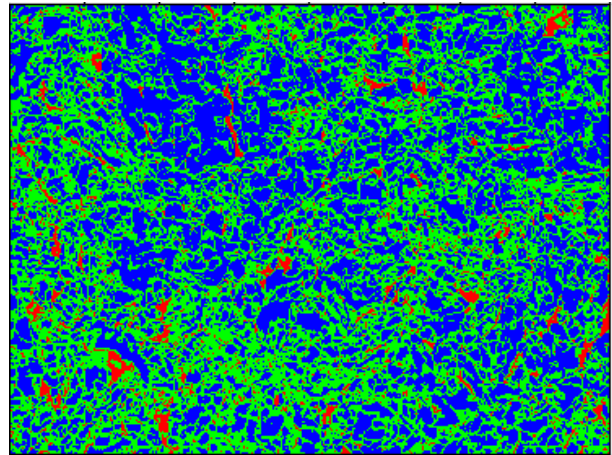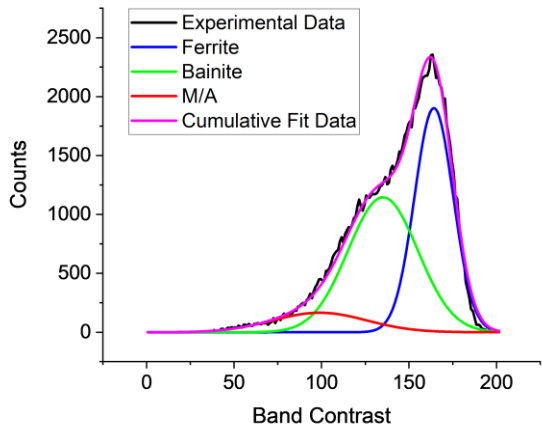
f)
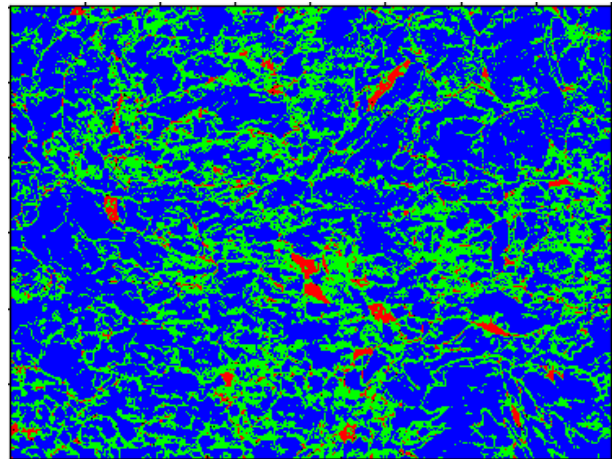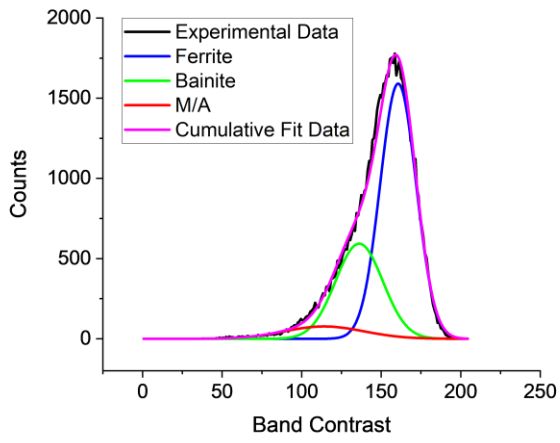
g)
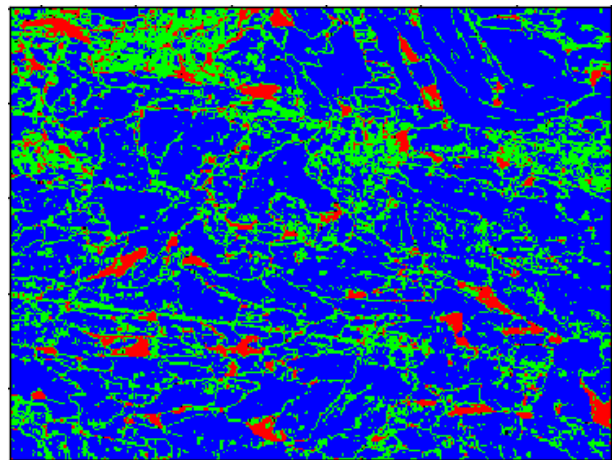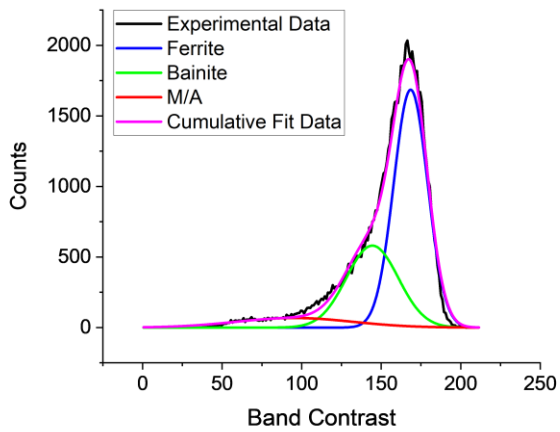
h)
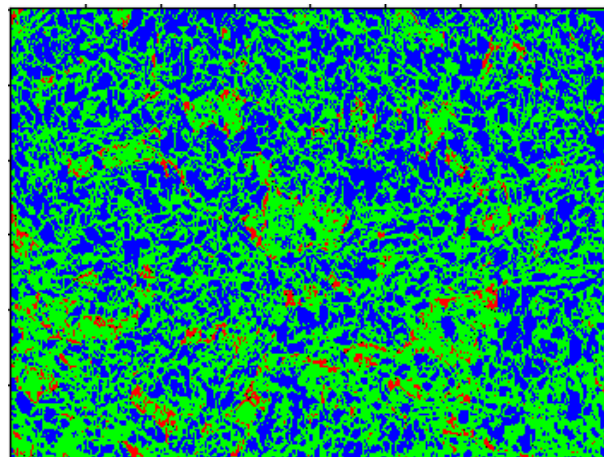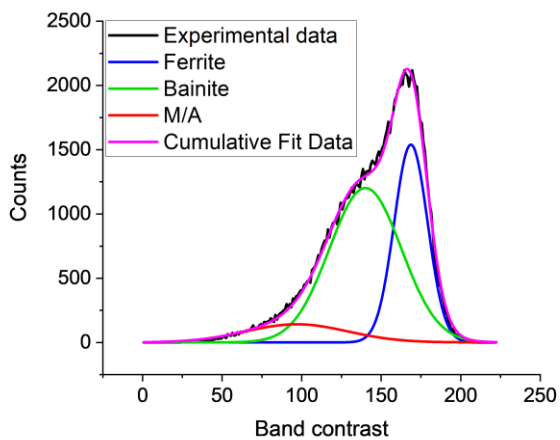
i)
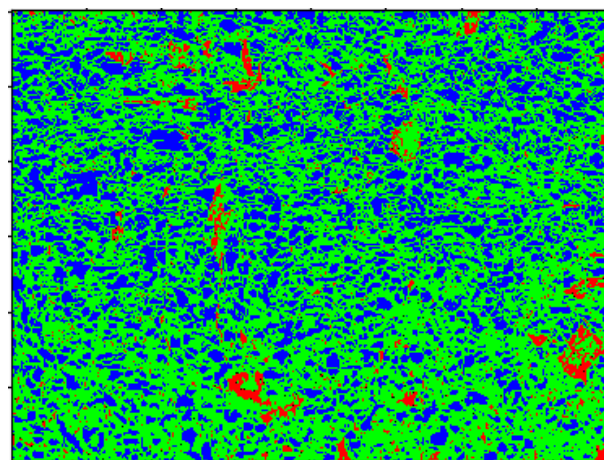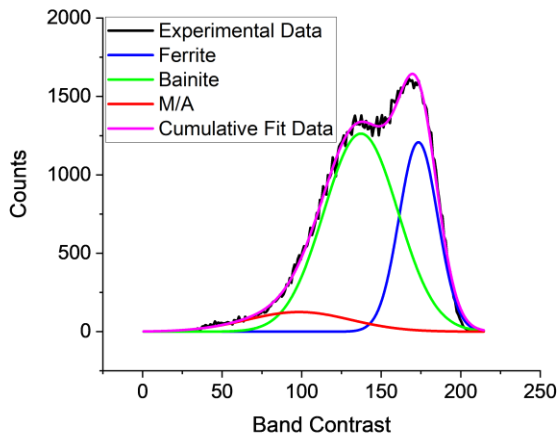
j)

Fig. B. 3 Devolution of band contrast curve and colored phase map of 3E-Coiled at surface a), ¼ distance b), centerline c), 3E-Air cooled at surface d), ¼ distance e), centerline f), 3F-Coiled at surface g), centerline h), and 3F-Water quenched at surface i), centerline j). In the colored phase maps, ferrite, bainite and M/A are shown in blue, green and red. (Note: for 3F-Water quenched sample, bainite and martensite cannot be distinguished due to their similar contrast in BC map, and are colored in green together, and RA is colored in red.)

Appendix B-3 Grain size distribution in Group I samples

The grain size distribution in Group I samples at various dislocations are measured by EBSD (grain boundary is set as misorientation >= 15 degree) and shown as follows in Fig. B.4 and Fig. B.5. The lognormal curve fitting results are listed in Table 4-3.

a)

b)

c)

d)

e)

f)
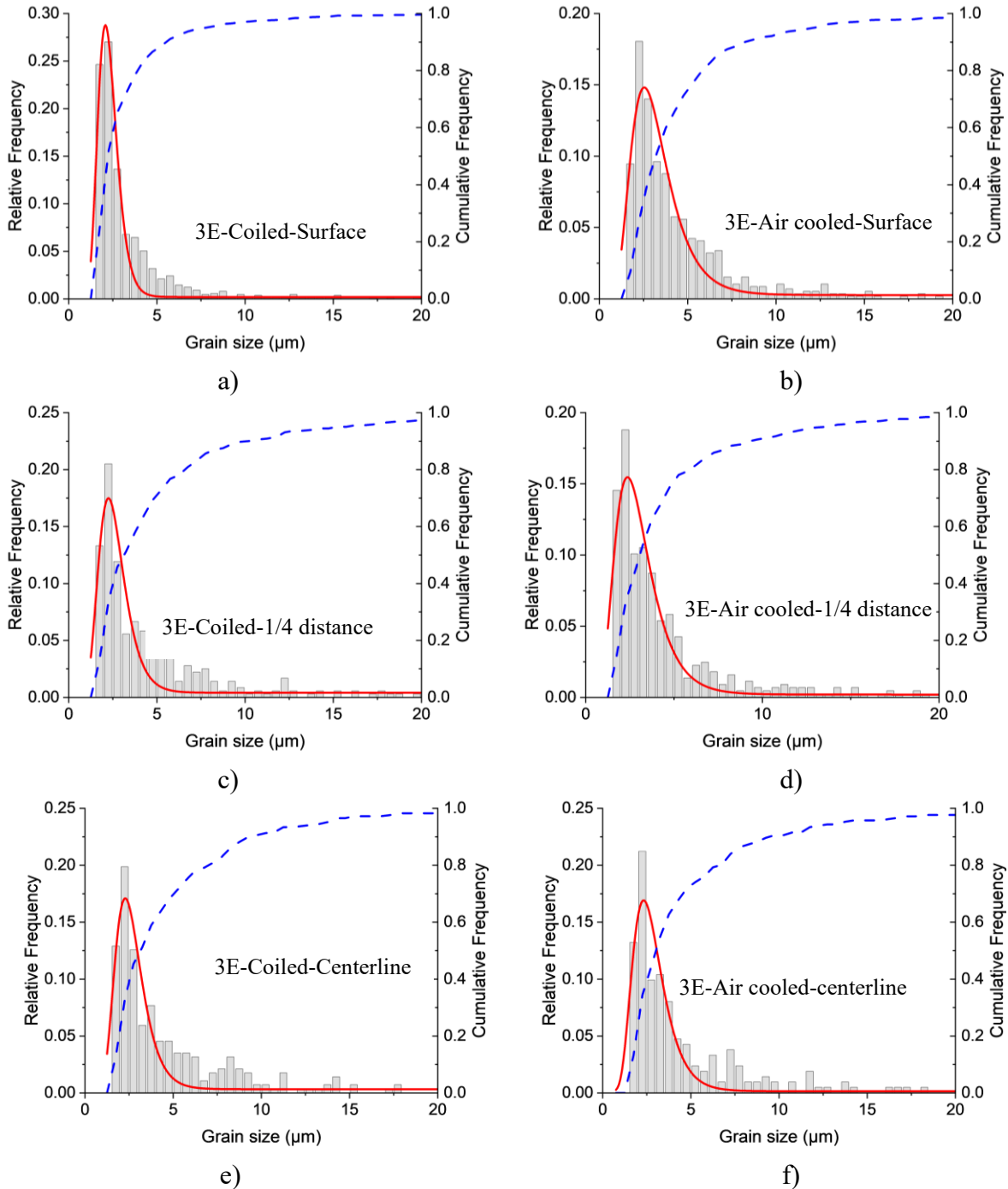
Fig. B. 4 Grain size distribution of 3E-Coiled and 3E-Air cooled. Histogram: relative frequency; solid line: lognormal fitting curve; dashed line: cumulative frequency.
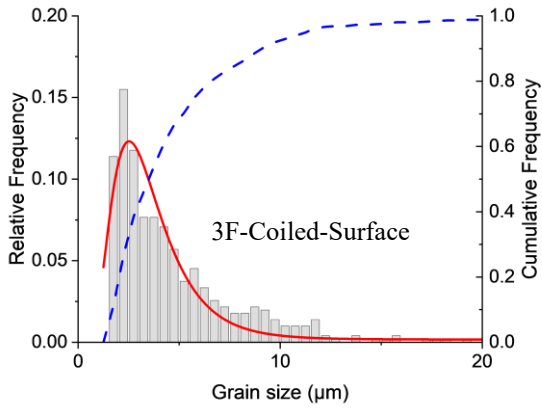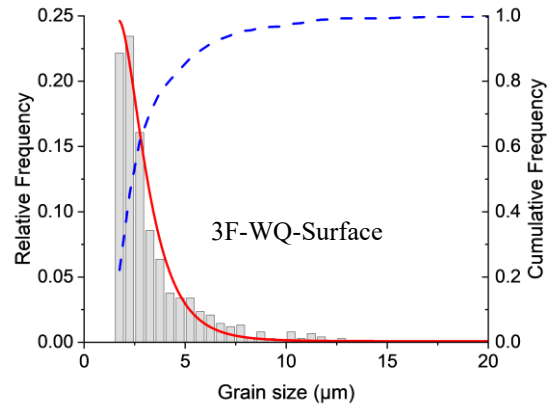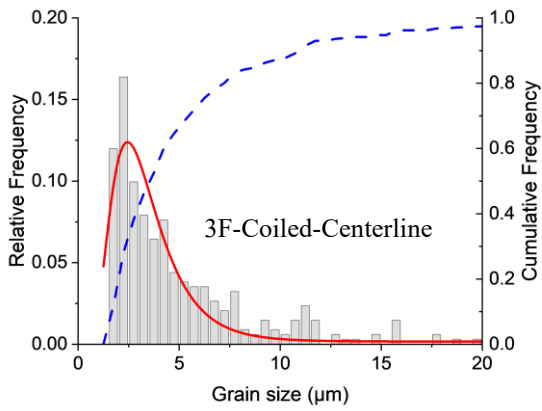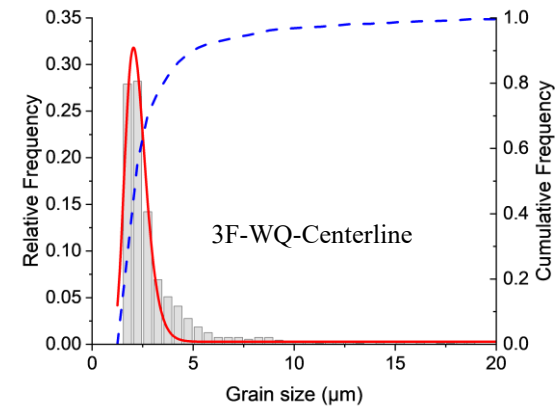
Fig. B. 5 Grain size distribution of 3F-Coiled and 3F-Water quenched. Histogram: relative frequency; solid line: lognormal fitting curve; dashed line: cumulative frequency.

Appendix B-4 Count density of nano-sized precipitates in Group I plates

The count density of nano-sized NbC precipitates in Group I plates are manually measured on STEM images. The measuring method is described in section 3.2.2. The statistical results are shown in Table B-1.

Table B- 1 Statistical parameters for measurement of count density of nano-sized NbC precipitates in Group I plates (No. of particles per μm^2 area).

Sample	Mean	Standard Deviation	Median
3E-Coiled	2421	543	2362
3F-Coiled	650	316	768
3E-Air cooled	1313	328	1287
3F-Water quenched	423	147	461

Appendix B-5 Curve-fitting results of hydrogen permeation curves of Group I samples

The hydrogen permeation curves of Group I samples are fitted with equations (3-4) and (3-5) for constant concentration condition and constant flux condition, respectively. The results plotted on logarithmic scale are as follows (Fig. B.6), which show the hydrogen flux at initial stage more clearly than the figures plotted on linear scale (Fig. 4.30).
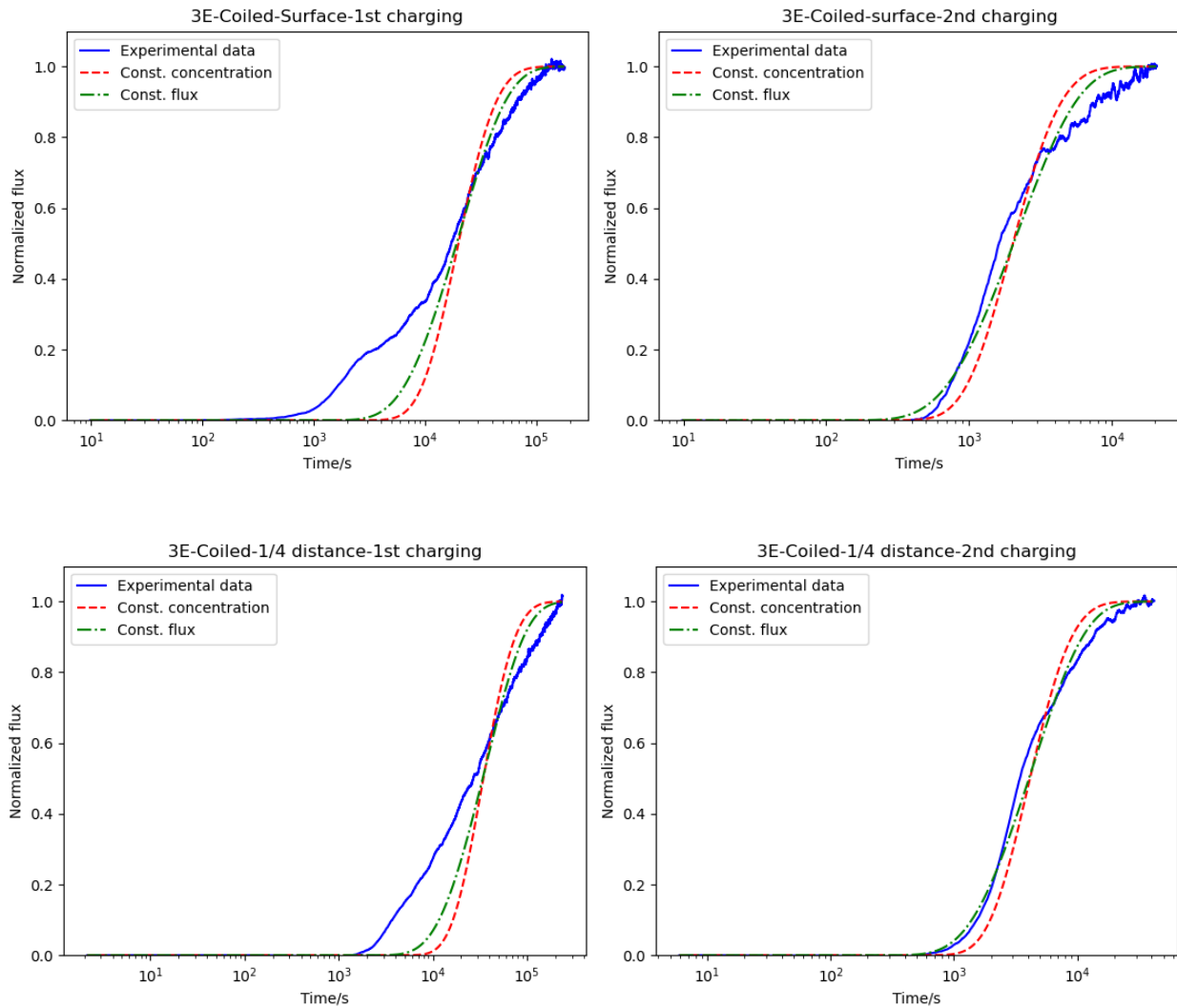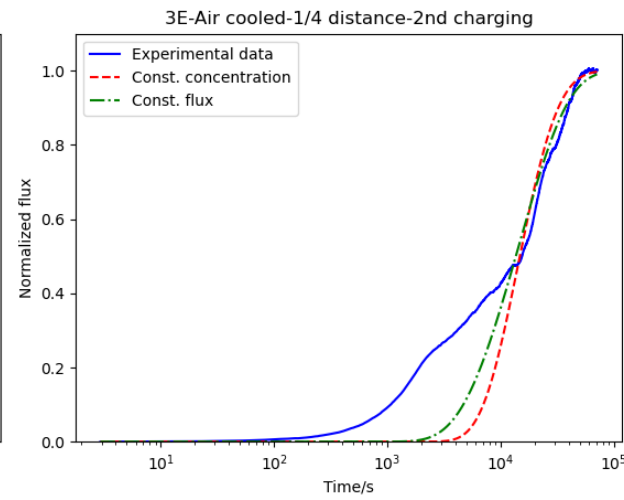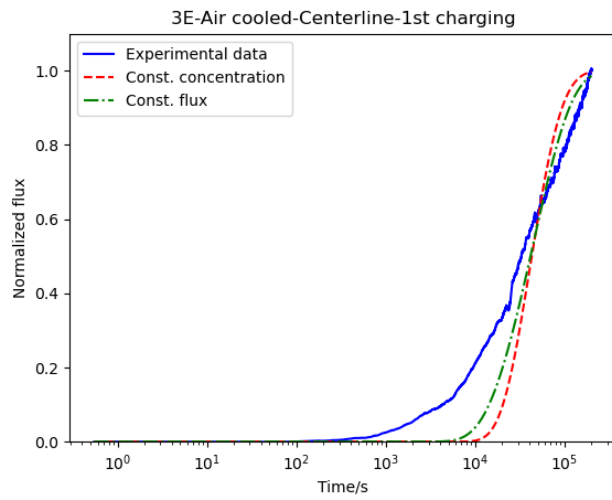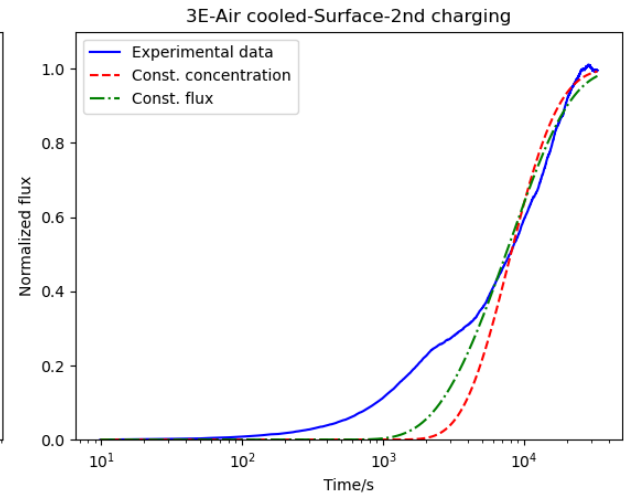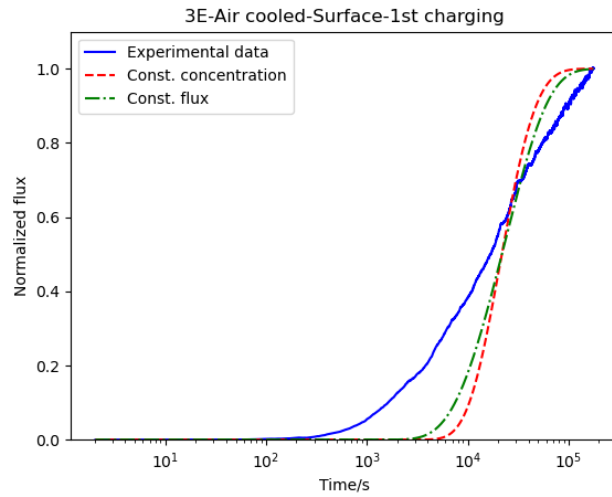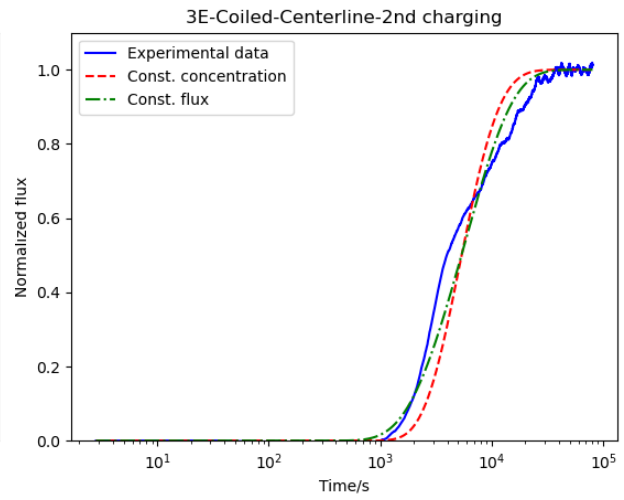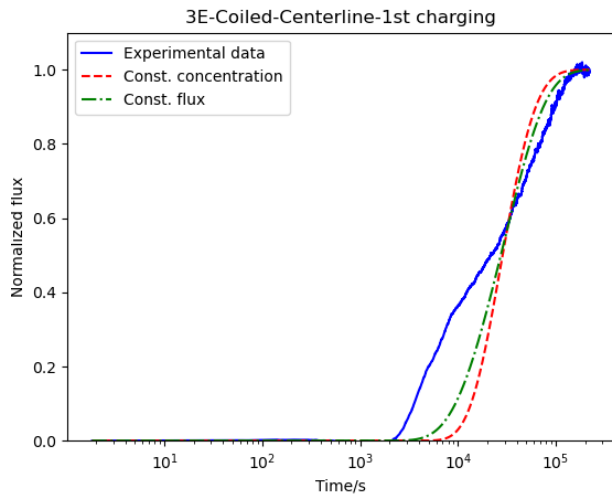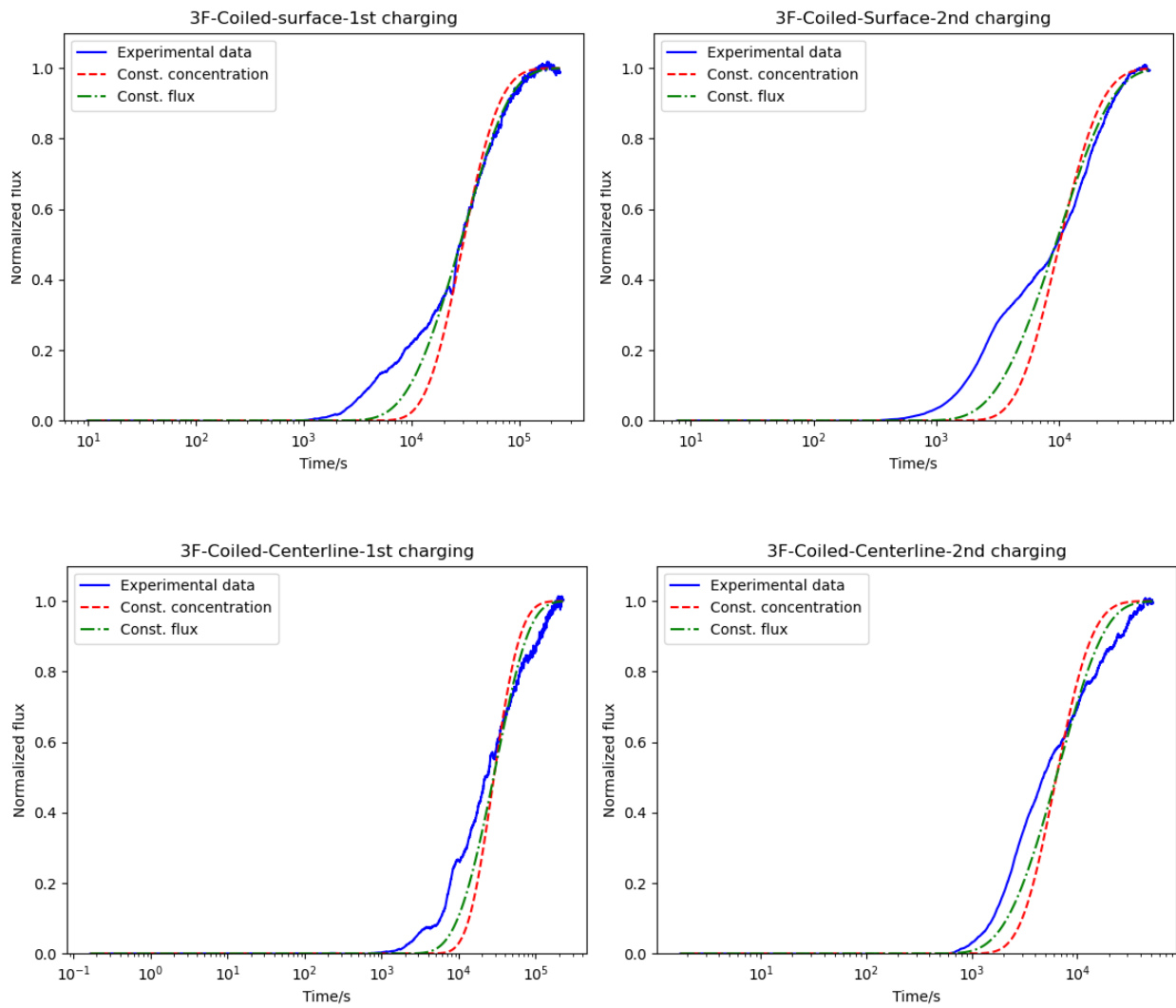
Fig. B. 6 Curve-fitting results of hydrogen permeation curves of Group I samples on logarithmic scale.

Appendix B-6 Hydrogen permeation test results of Group I samples

The oxidation current curves of hydrogen permeation tests on Group II samples are shown as follows in Fig. B. 7.
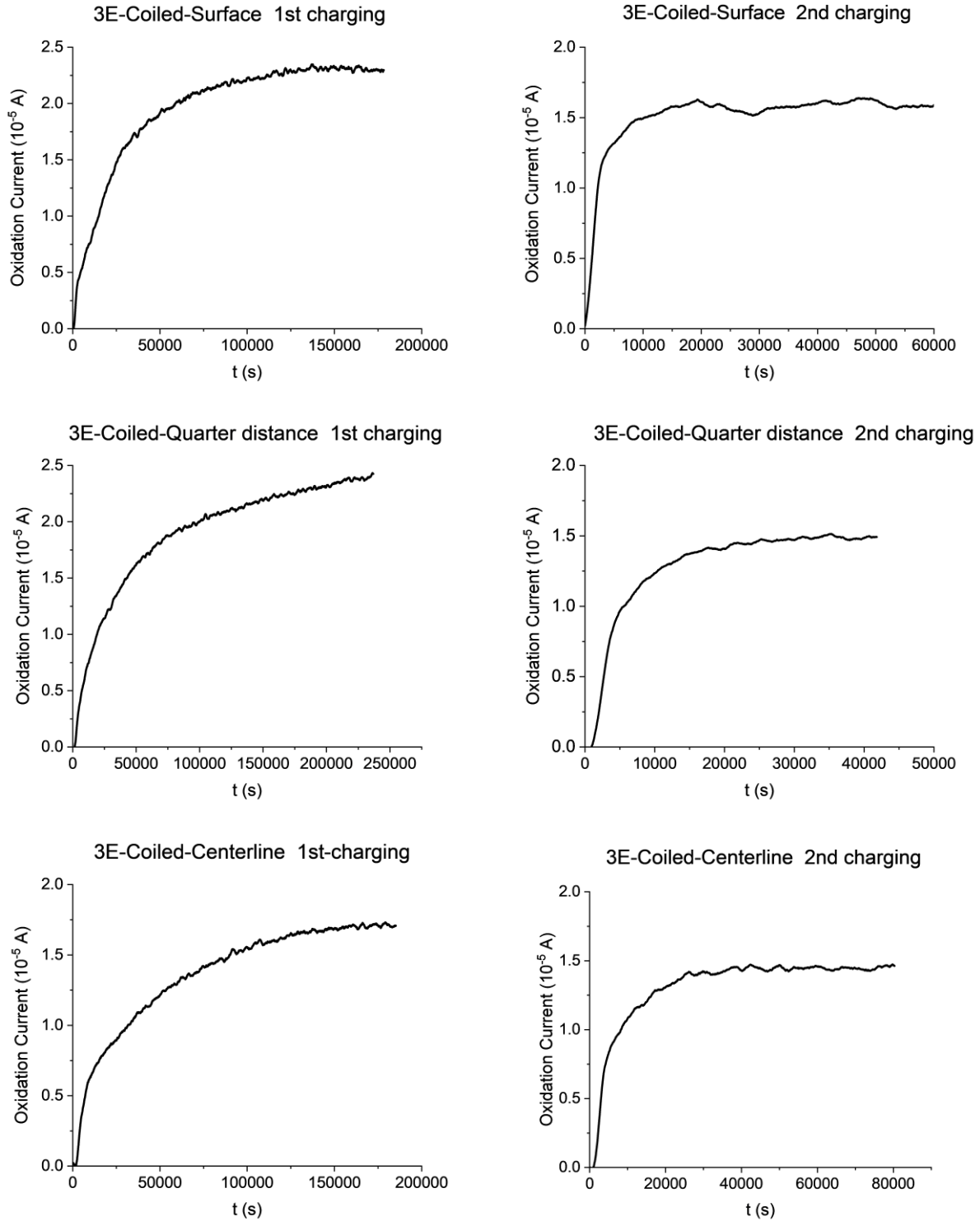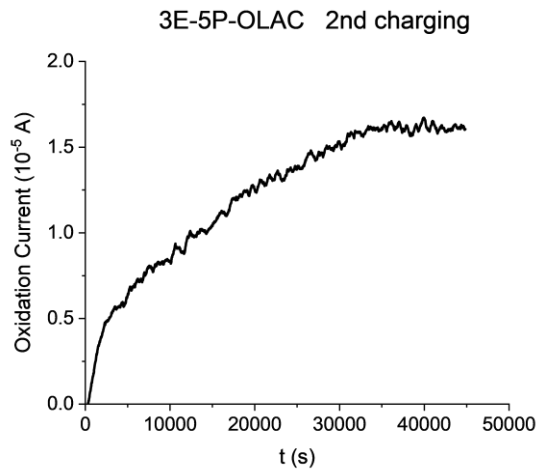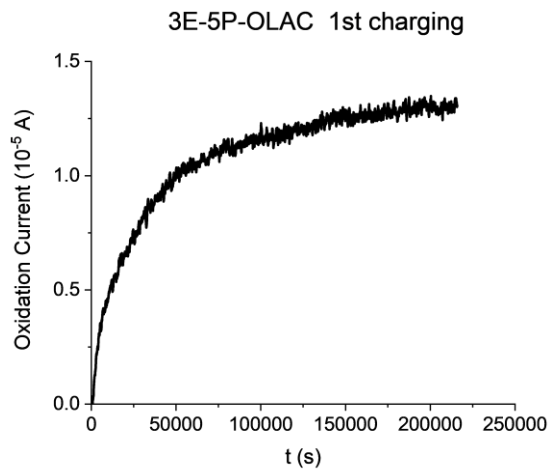
3F-Coiled-Surface 1st charging
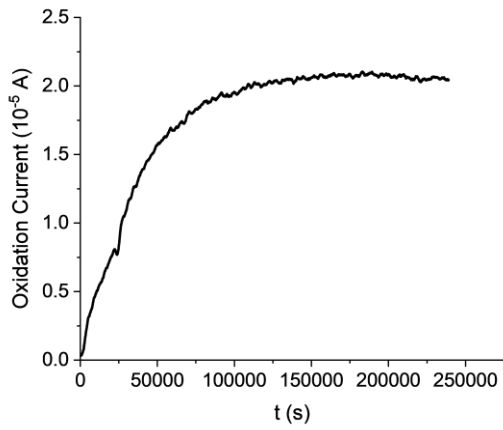
3F-Coiled-Surface 2nd charging
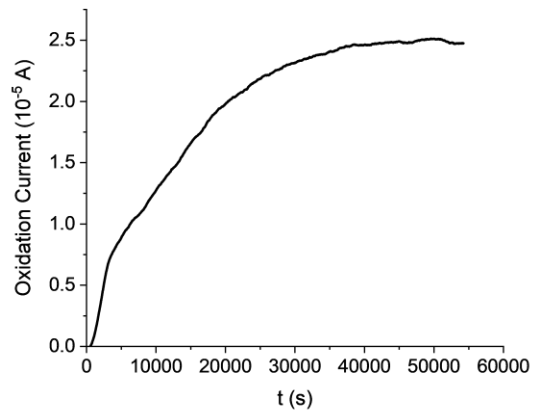
3F-Coiled-Centerline 1st charging
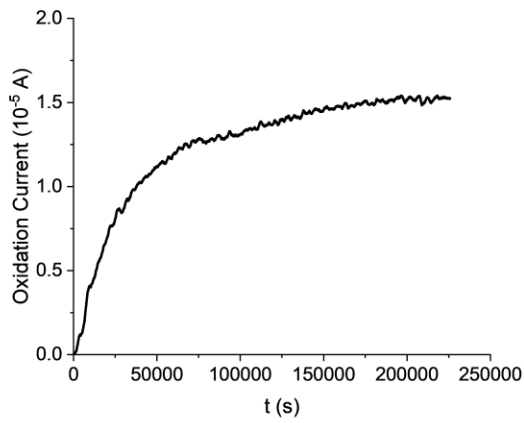
3F-Coiled-Centerline 2nd charging
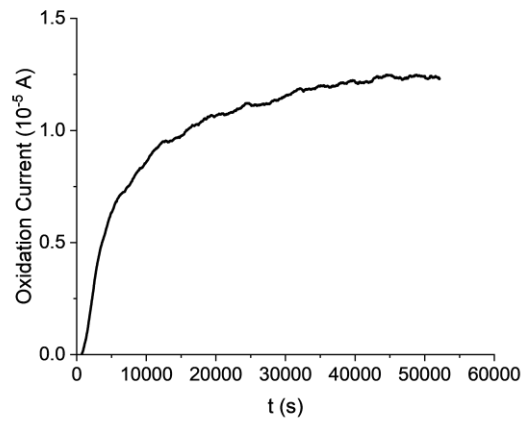
3E-Air cooled-Surface 1st charging
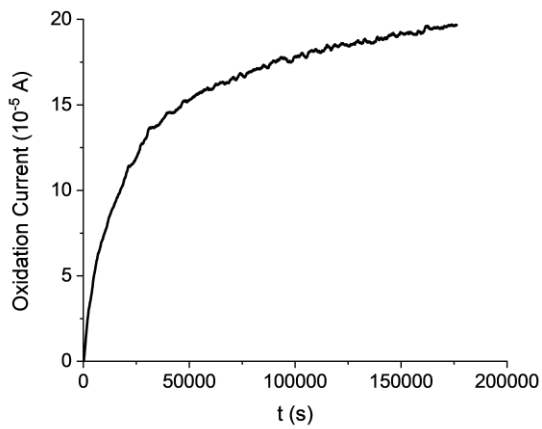
3E-Air cooled-Surface 2nd charging
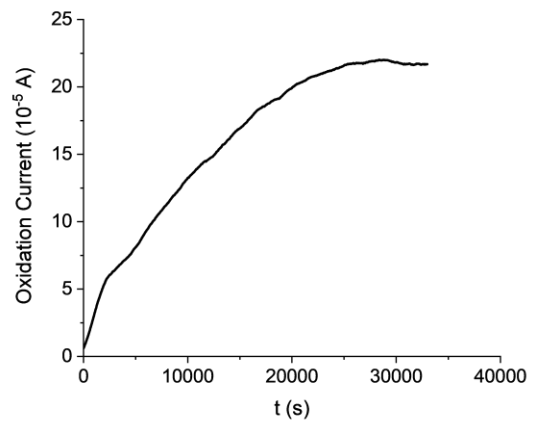
3E-Air cooled-Quarter distance 1st charging
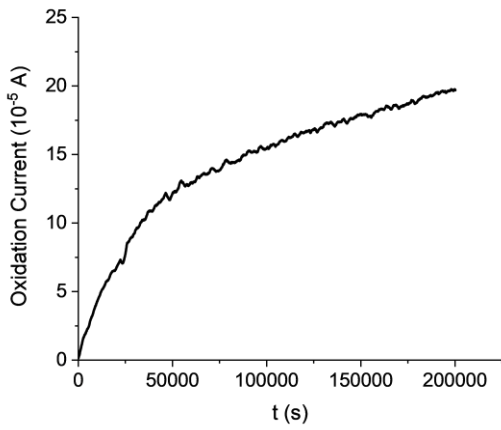
3E-Air cooled-Quarter distance 2nd charging
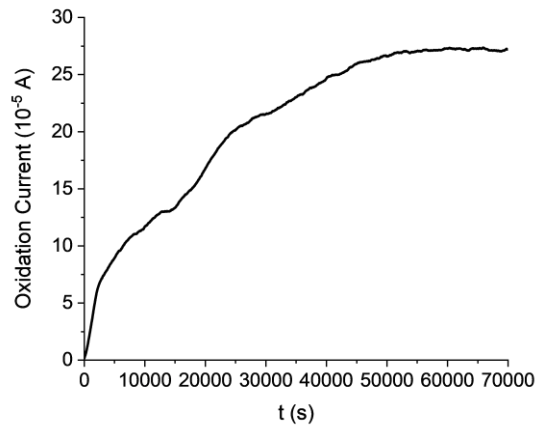
3E-Air cooled-Centerline 1st charging
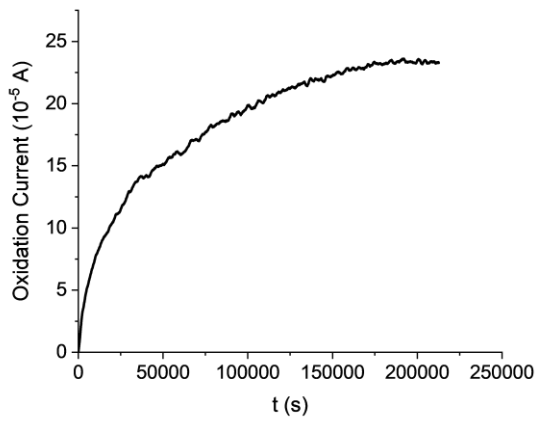
3E-Air cooled-Centerline 2nd charging
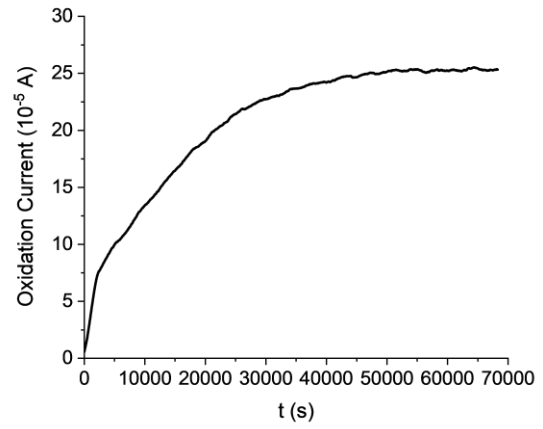
3F-Water quenched-Surface 1st charging
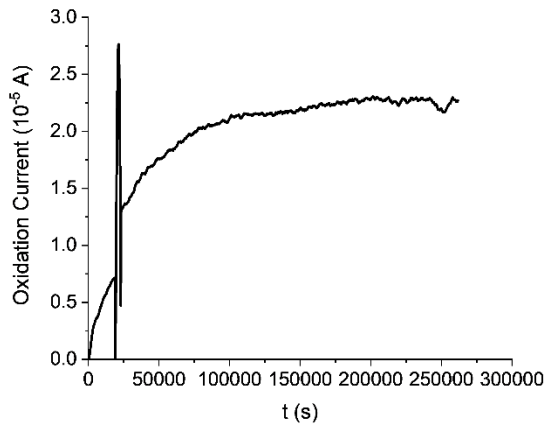
3F-Water quenched-Surface 2nd charging
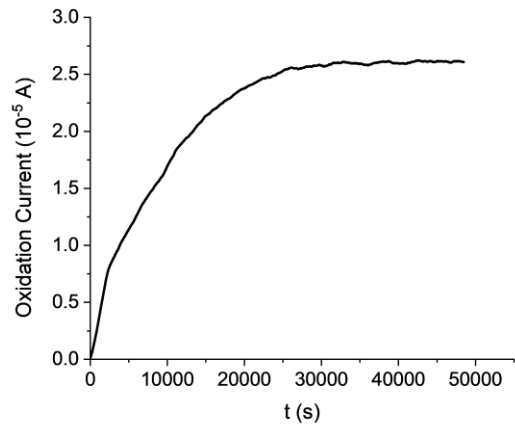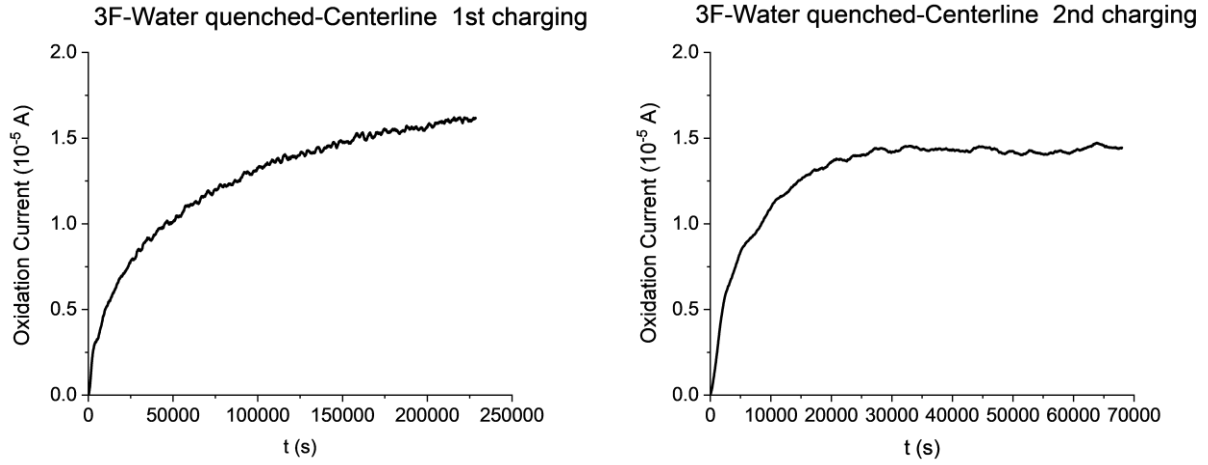
Fig. B. 7 Hydrogen permeation test results of Group I samples.

Appendix C-1 Rough rolling schedule for Group II plates

Three different rough rolling schedules were applied on Group II plates, as shown in Fig. C.1-Fig. C.3. It is worth mentioning that the original thickness (before rough rolling) and final thickness (after rough rolling) of all Group II plates are the same.
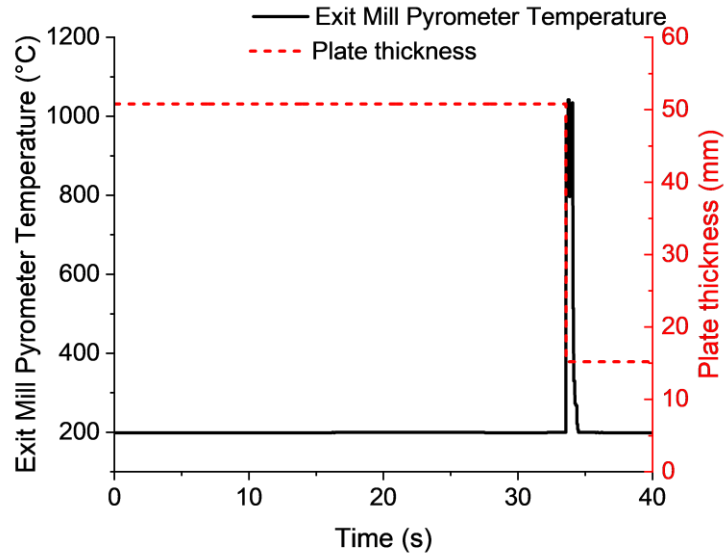
Fig. C. 1 Rough rolling schedule for 3B-1P.
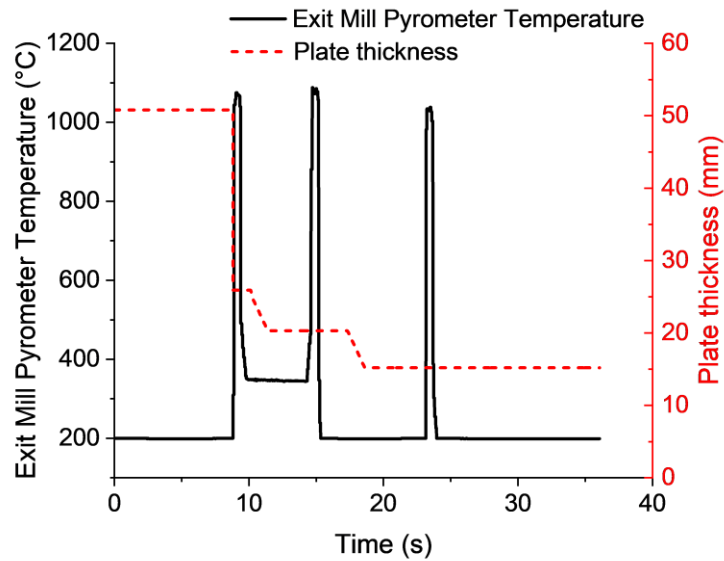
Fig. C. 2 Rough rolling schedule for 3E-3P.
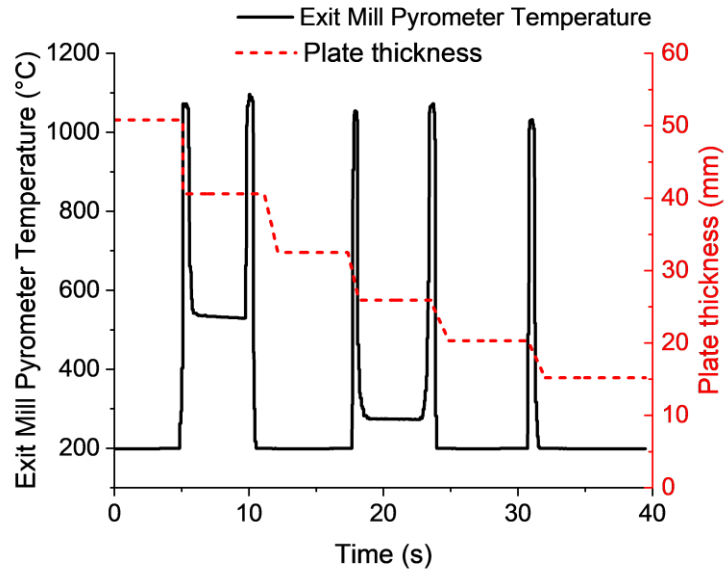
Fig. C. 3 Rough rolling schedule for 3B-5P/3E-5P-4MIN.

Appendix C-2 OM images of Group II plates showing PAGs

The PAG size of Group II plates are measured on OM images. Due to the variation in PAG size, difference magnification is used. Typical OM images for each sample are shown as follows in Fig. C.4. The PAG size measurement results are shown in Table 5-1.
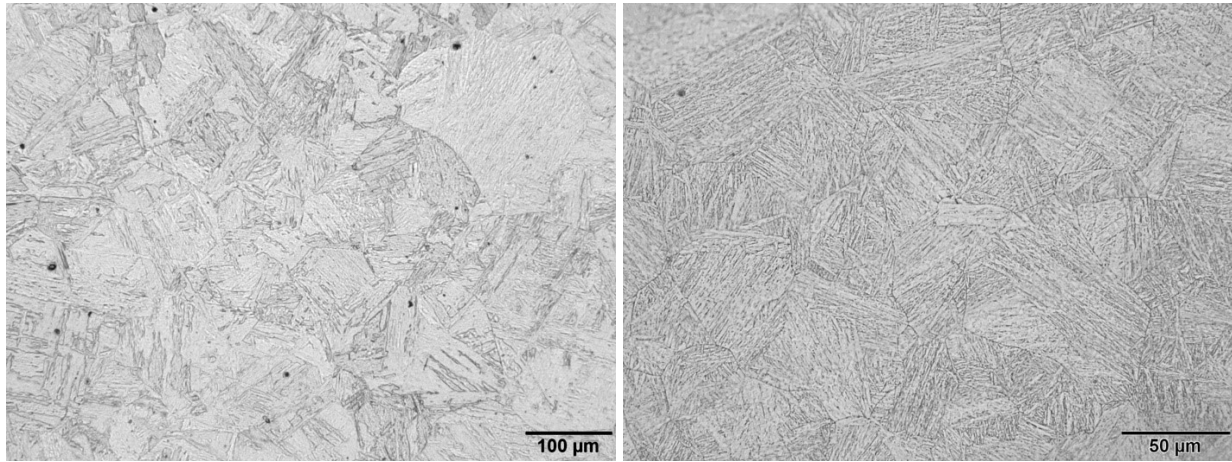
a)

b)
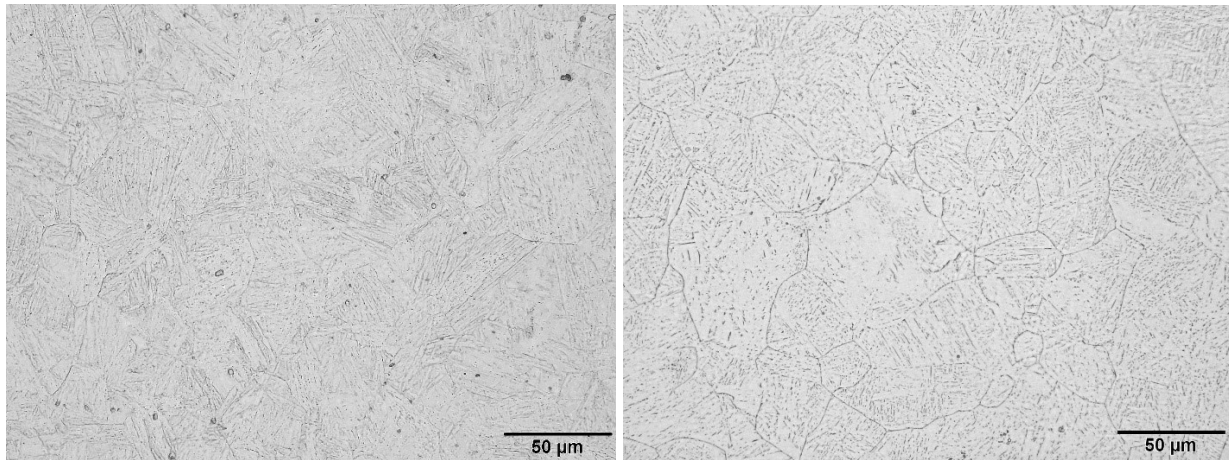
c)

d)
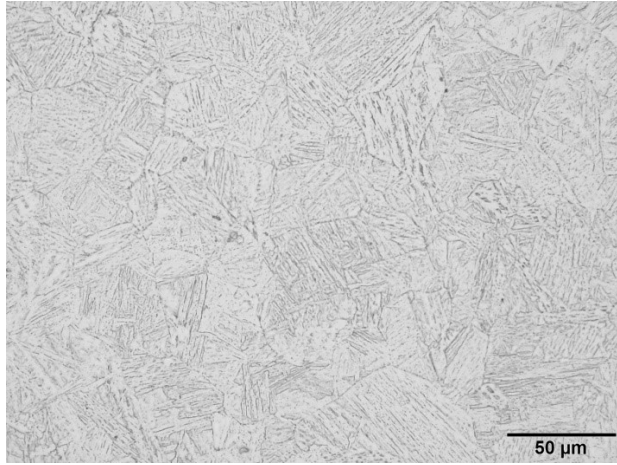
e)
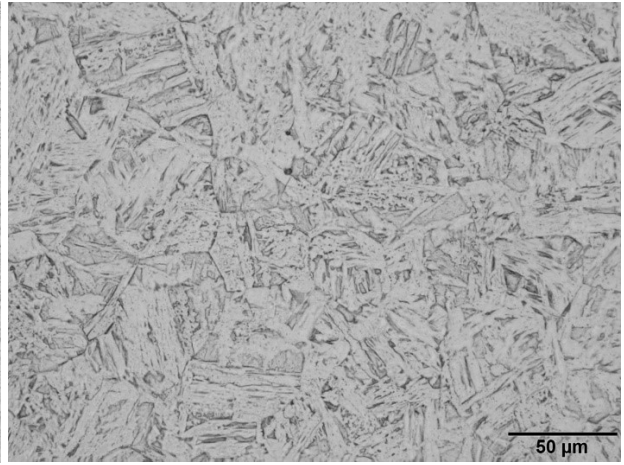
f)
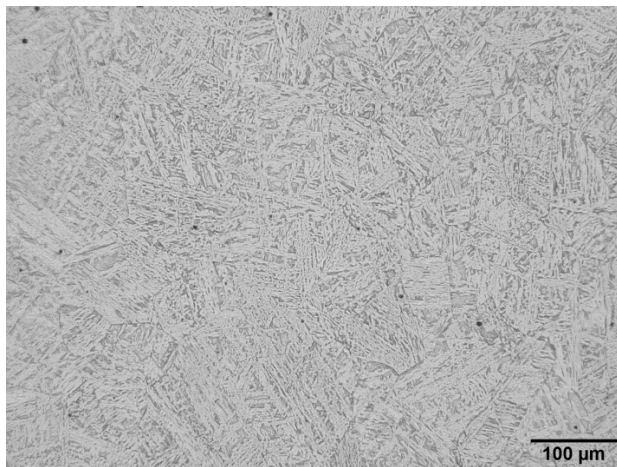
g)

Fig. C. 4 OM images showing microstructures and PAGs of Group II samples. 3F-0P (a); 3B-1P (b); 3B-1P (c); 3B-5P (d); 3E-5P-4MIN (e); 3E-5P-OLAC (f); 3E-4P-1P-OLAC (g).

Appendix C-3 SEM images of NbC/TiN precipitates in Group II plates

The count density of complex NbC/TiN precipitates in each Group II plate is manually measured on five (5) SEM images at a magnification of 30k × using in-lens detector. Some typical SEM images for these samples are shown as follows in Fig. C.5. The measurement results are shown in Fig. 5.19.

3F-0P

500 nm

a)

3B-1P

500 nm

b)

3E-3P

500 nm

c)

3B-5P

500 nm

d)

3E-5P-4MIN

500 nm

e)
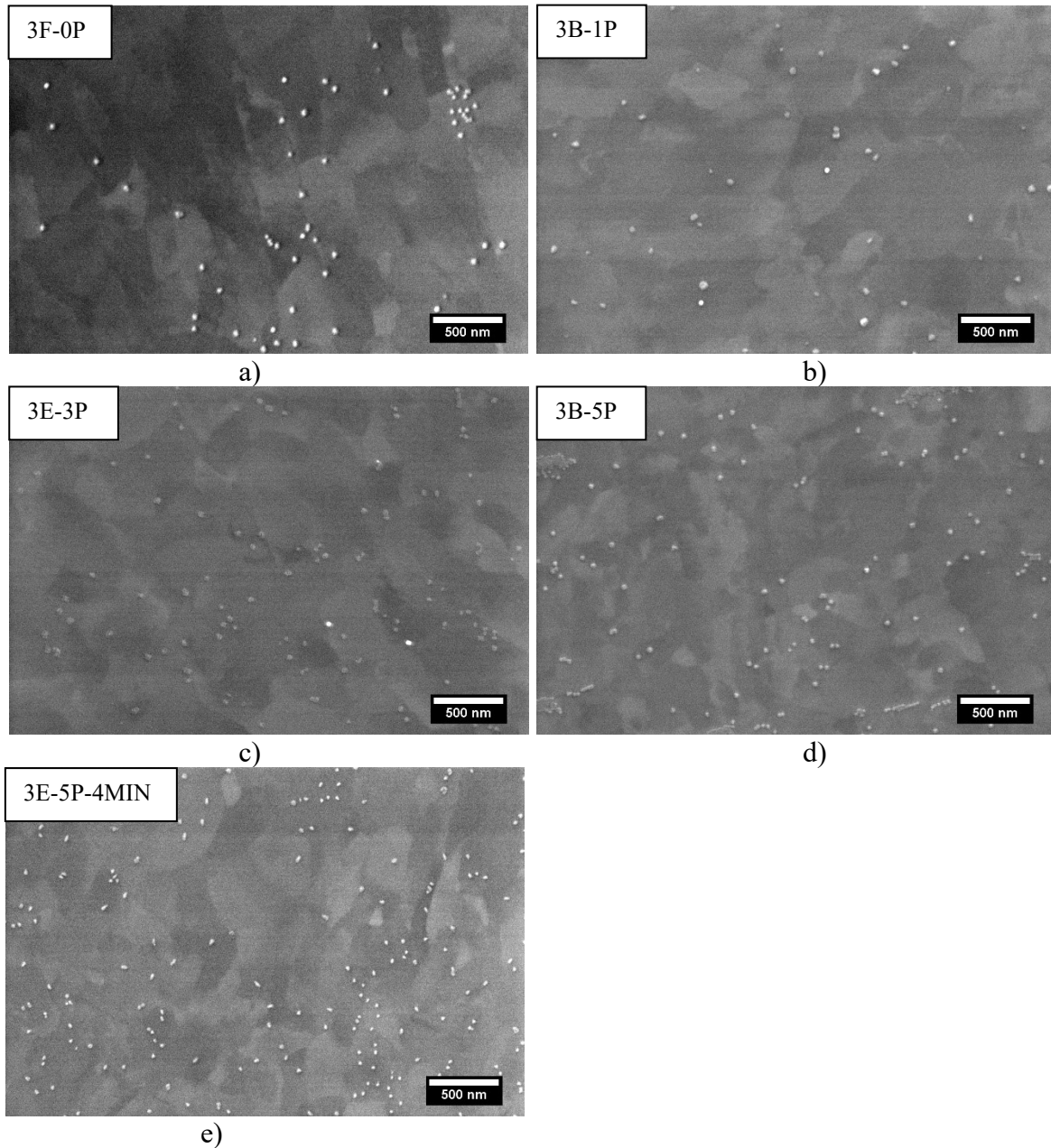
Fig. C. 5 SEM images of Group II samples showing complex NbC/TiN precipitates.

Appendix C-4 Normalized hydrogen permeation curves of Group II samples

The normalized hydrogen permeation curves of Group II samples are shown in Fig. C.6. The big gap between 1st and 2nd transient proves the existence of large number of irreversible traps in these samples.

a)

b)

c)

d)
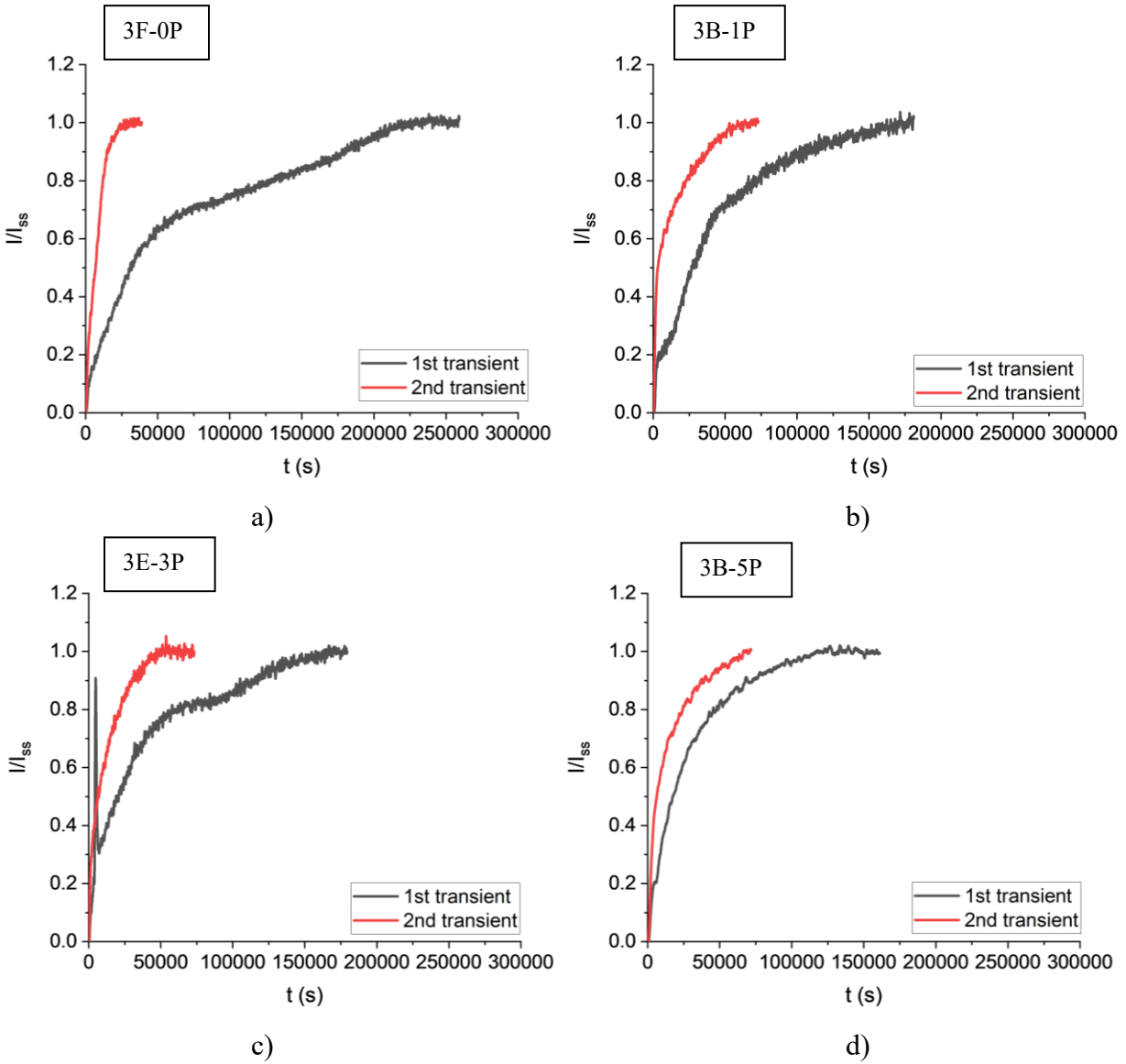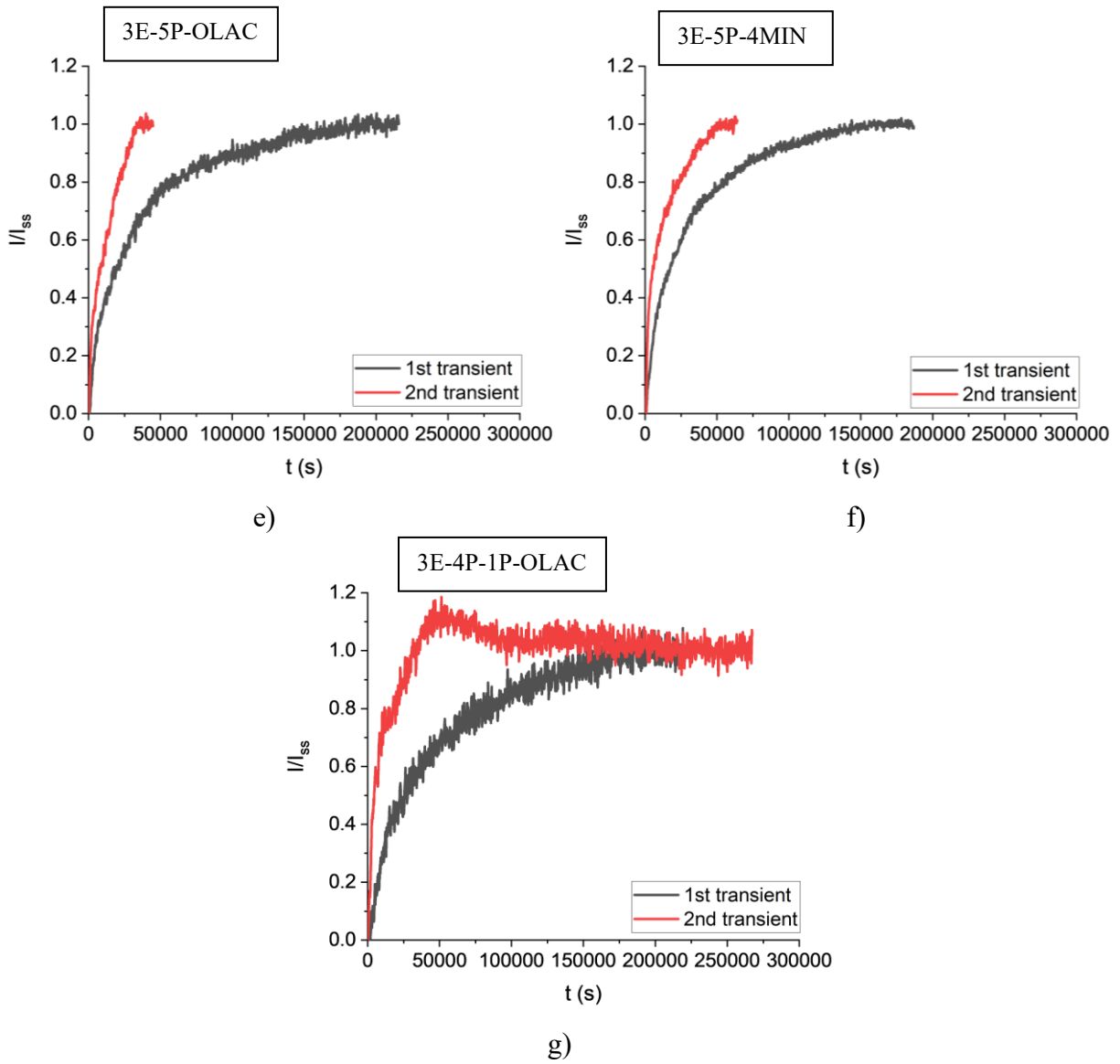
Fig. C. 6 Normalized hydrogen permeation curves of Group II samples.

Appendix C-5 Curve-fitting results of hydrogen permeation curves of Group II samples

The hydrogen permeation curves of Group II samples are fitted with equations (3-4) and (3-5) for constant concentration condition and constant flux condition, respectively. The results plotted on logarithmic scale and on linear scale are shown as follows in Fig. C.7. D_{eff} values of Group II samples obtained via curve-fitting method is shown in Table 5-4.

3E-3P-2nd charging

3B-5P-1st charging

3B-5P-2nd charging
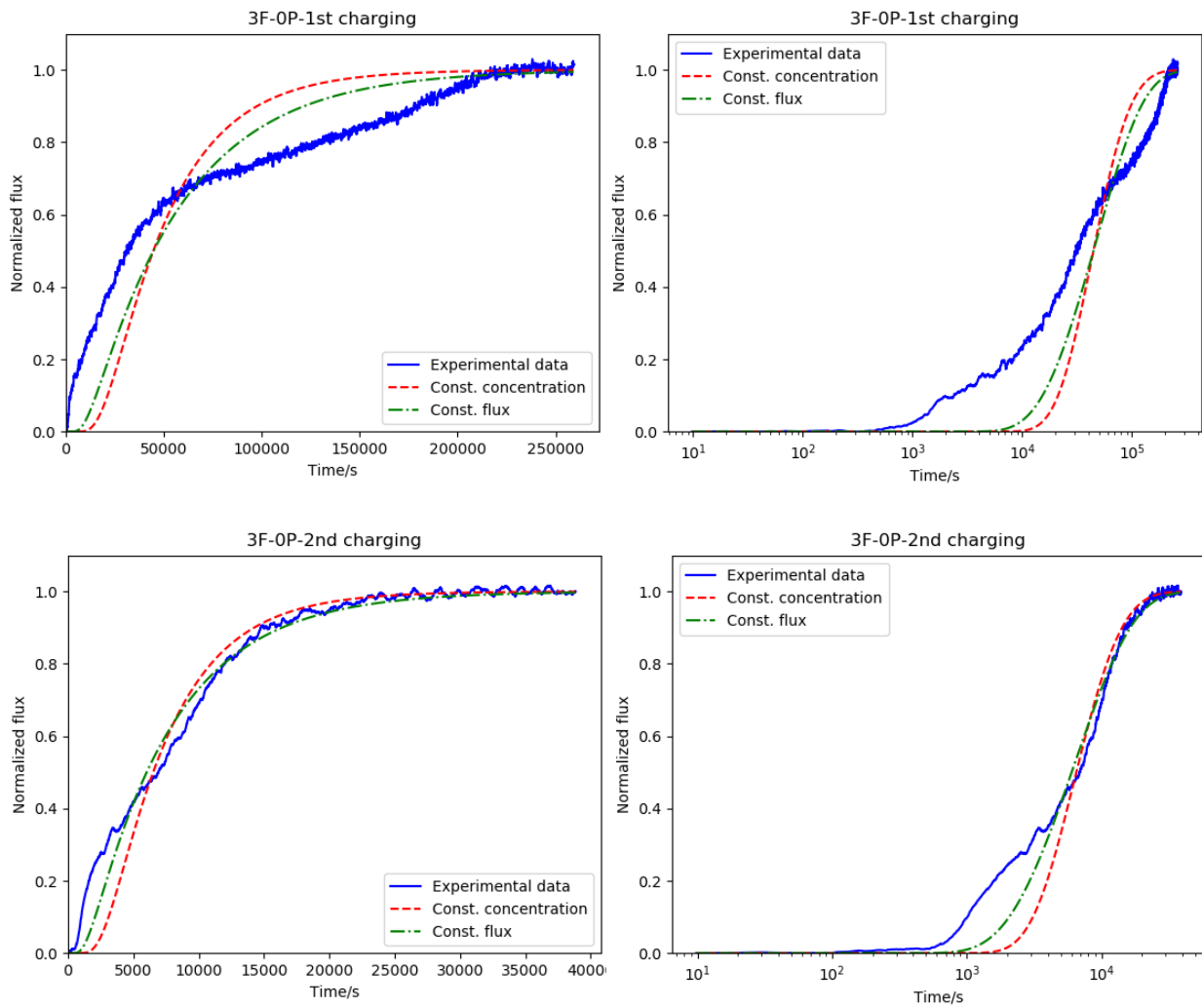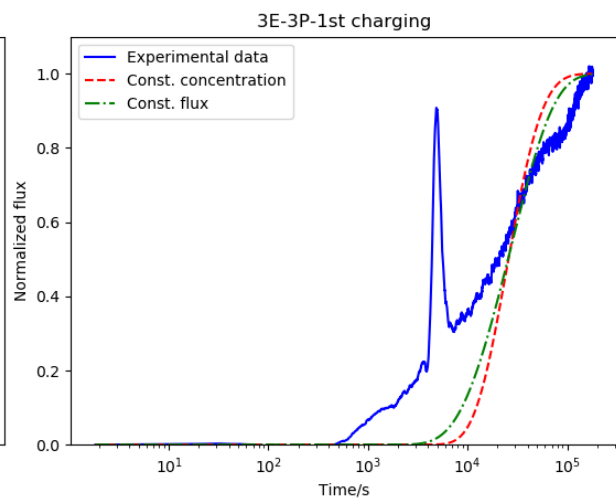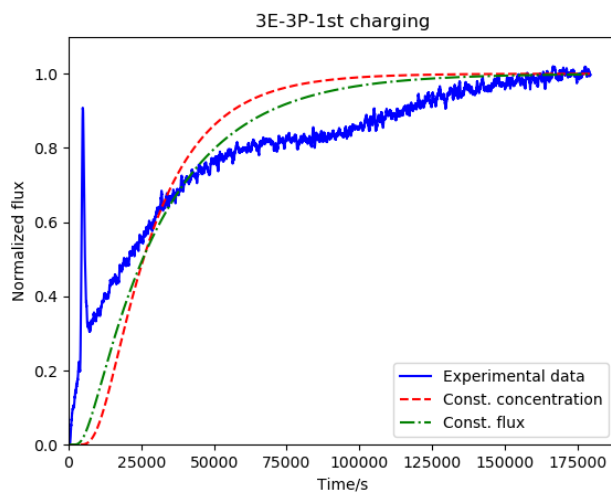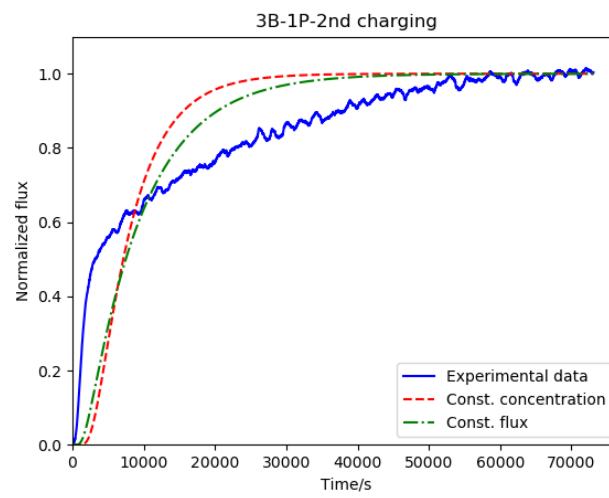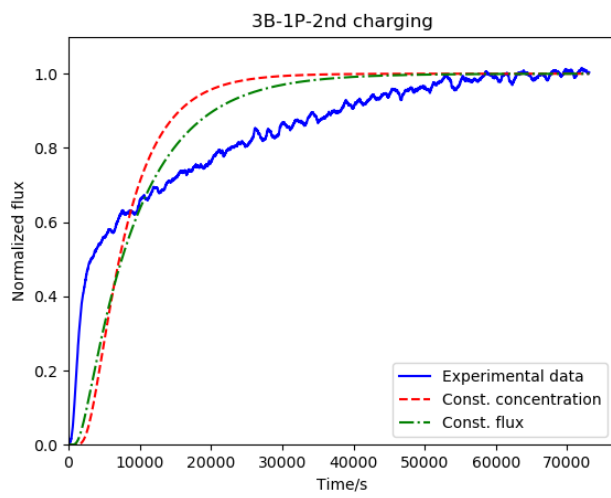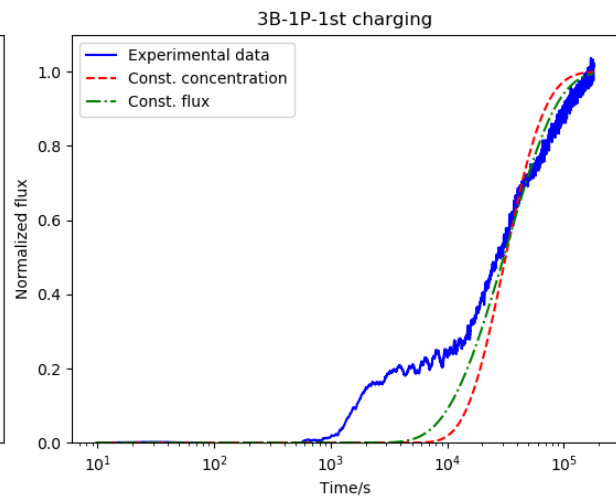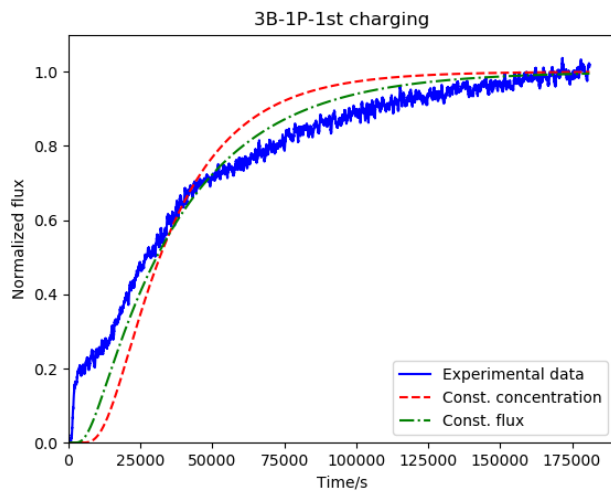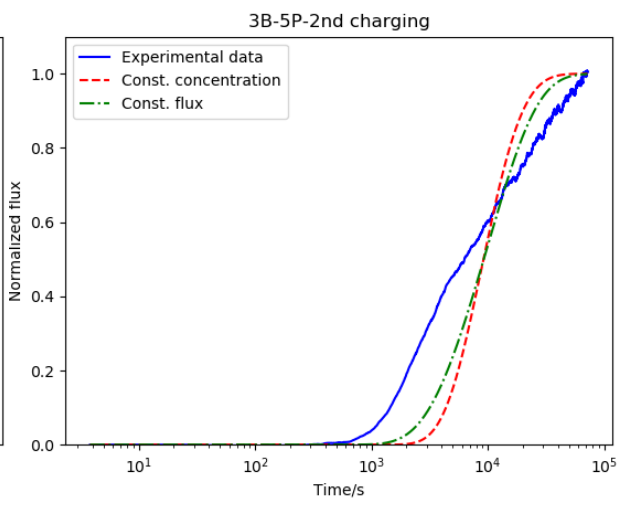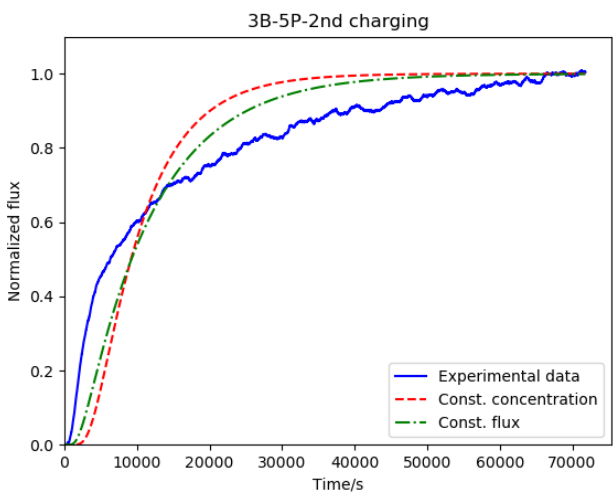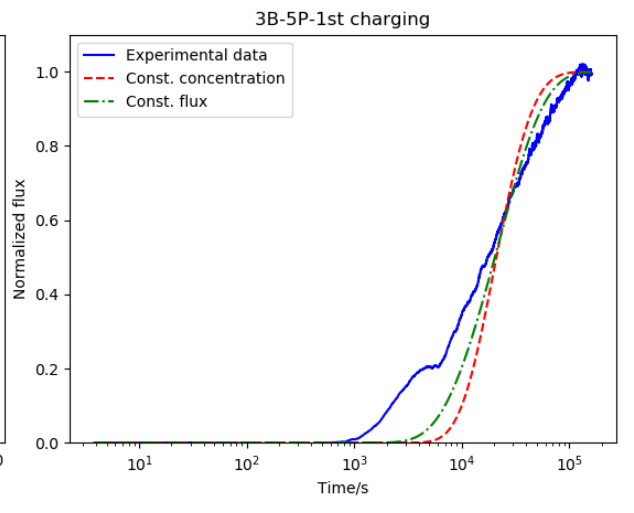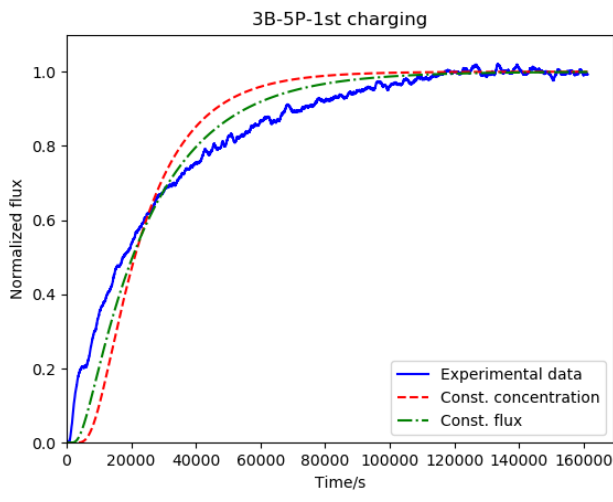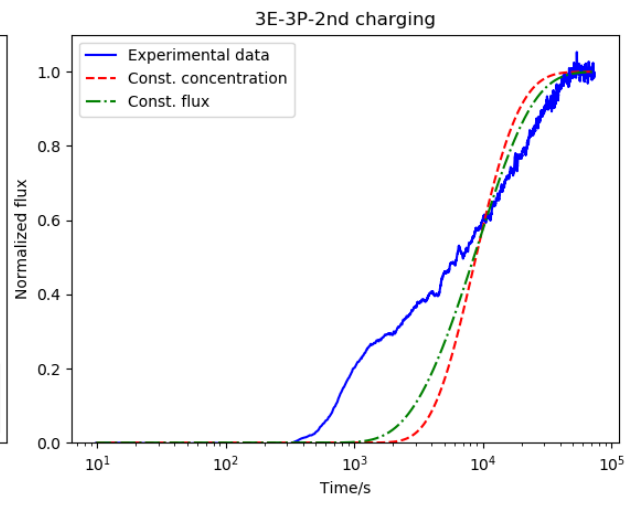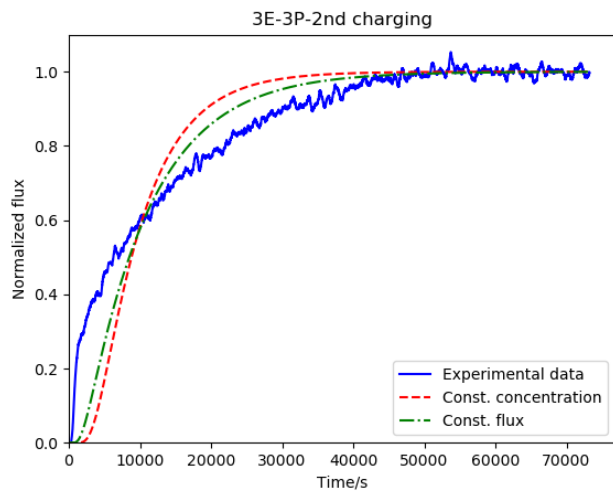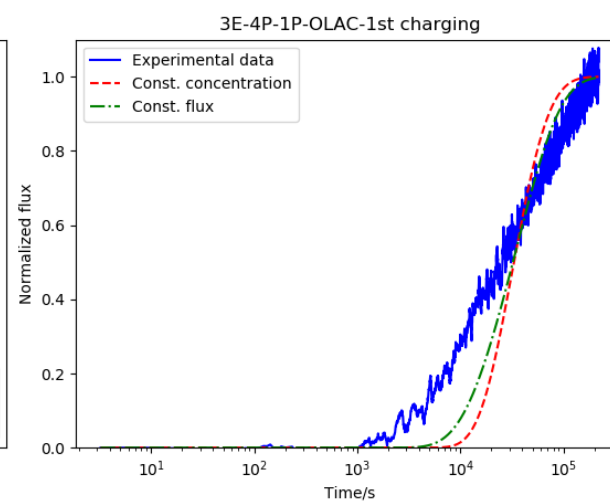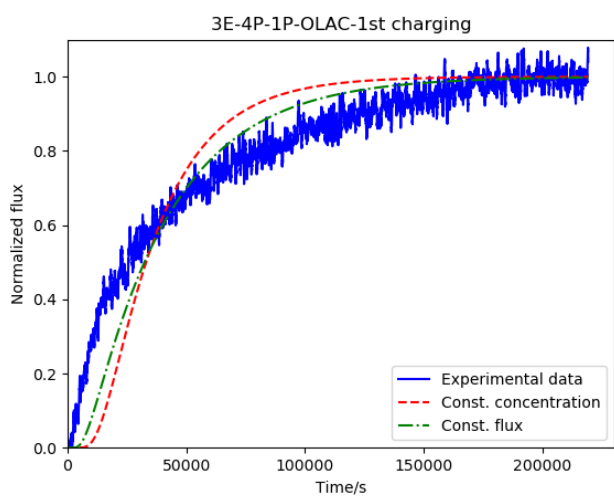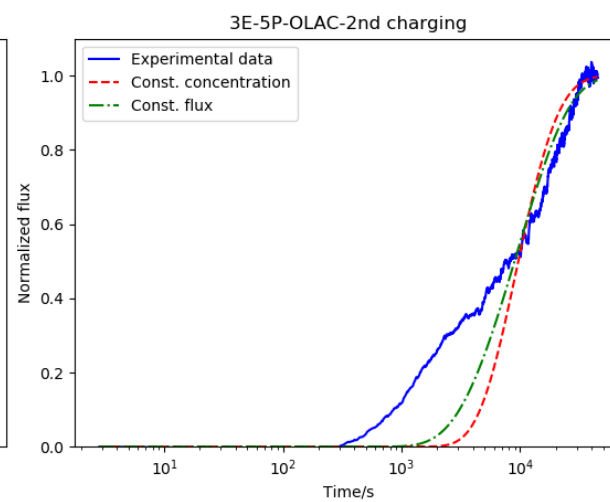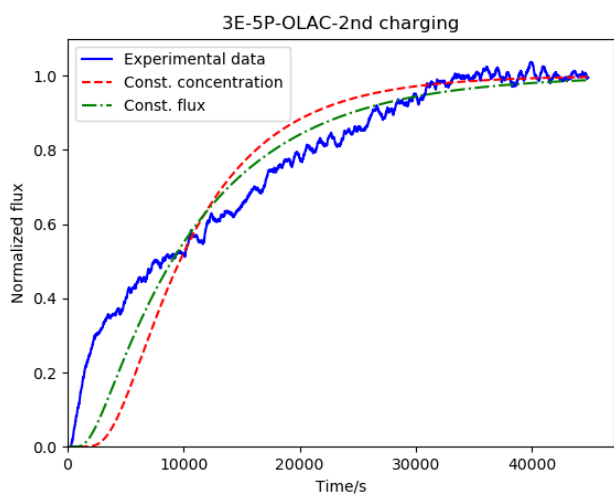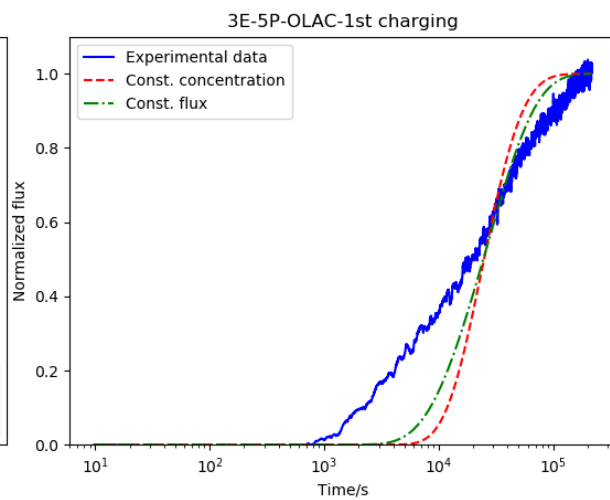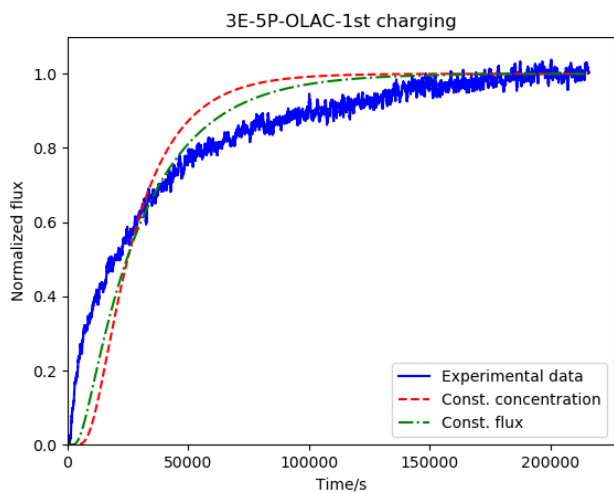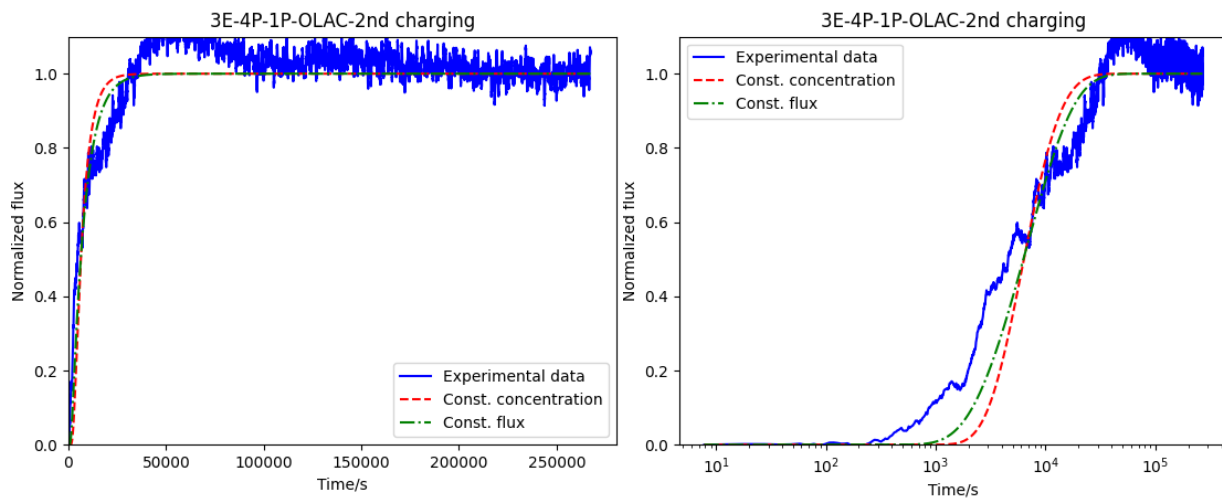
Fig. C. 7 Curve-fitting results of Group II samples on linear and logarithmic scale.

Appendix C-6 Hydrogen permeation test results of Group II samples

The oxidation current curves of hydrogen permeation tests on Group II samples are shown as follows in Fig. C. 8.

3B-5P 1st charging

3B-5P 2nd charging

3E-5P-4MIN 1st charging

3E-5P-4MIN 2nd charging

3E-4P-1P-OLAC 1st charging

3E-4P-1P-OLAC 2nd charging
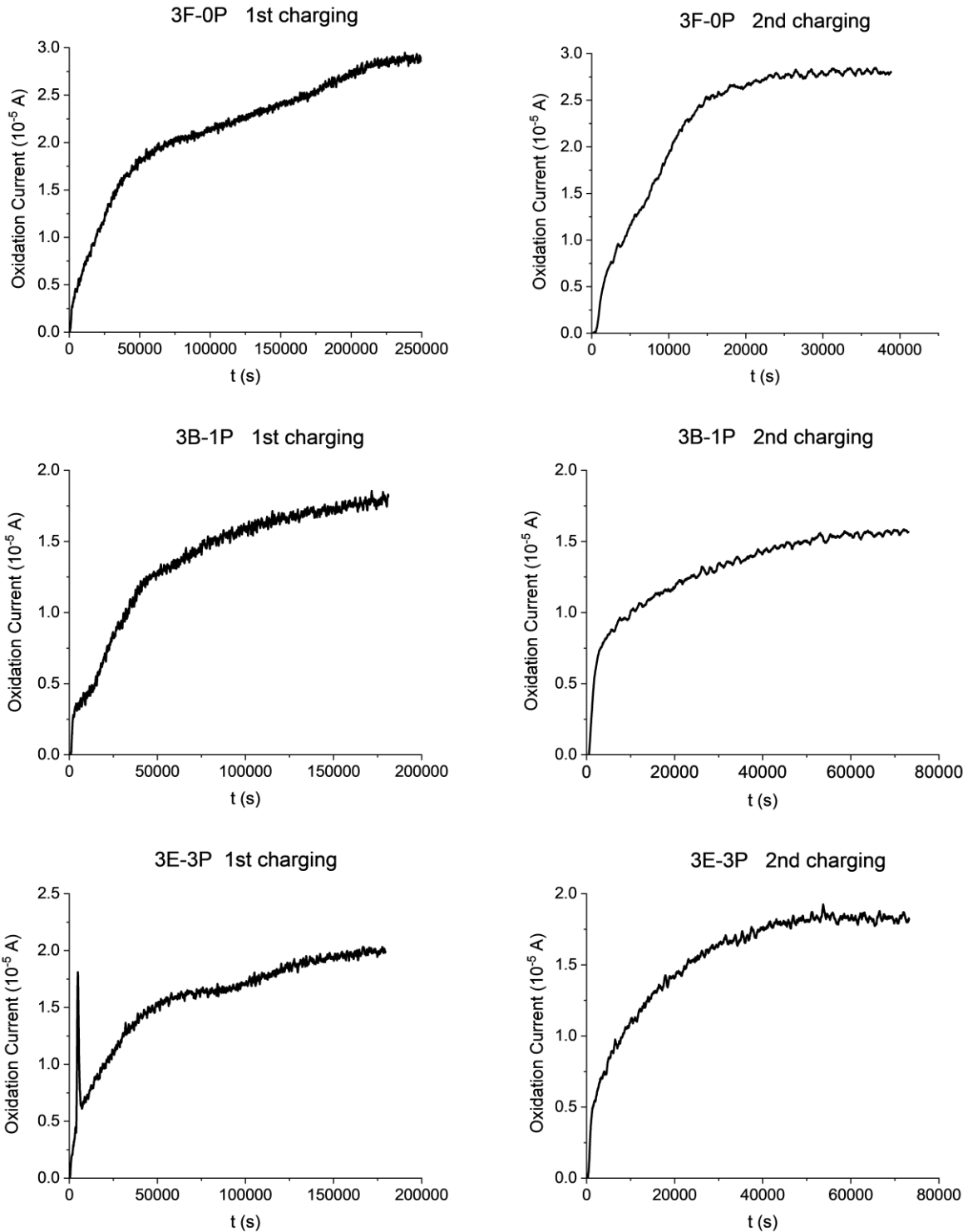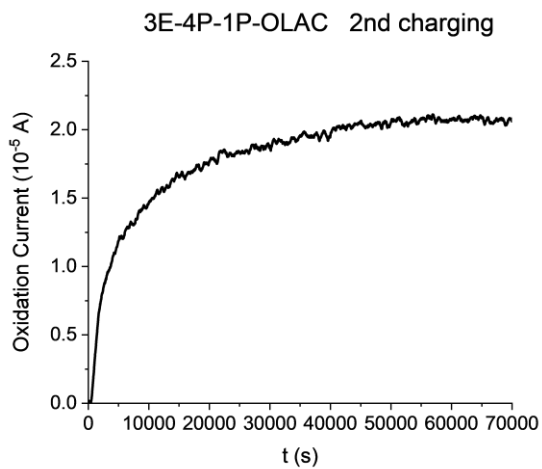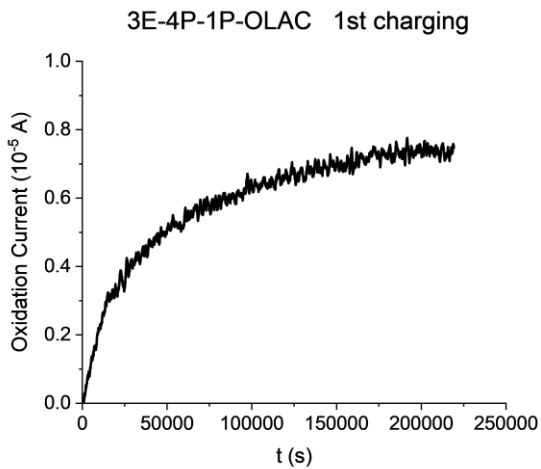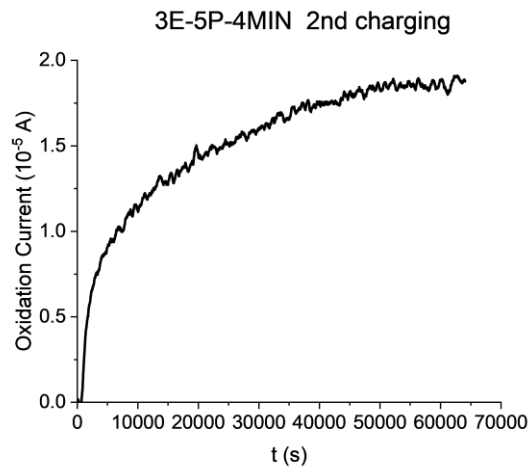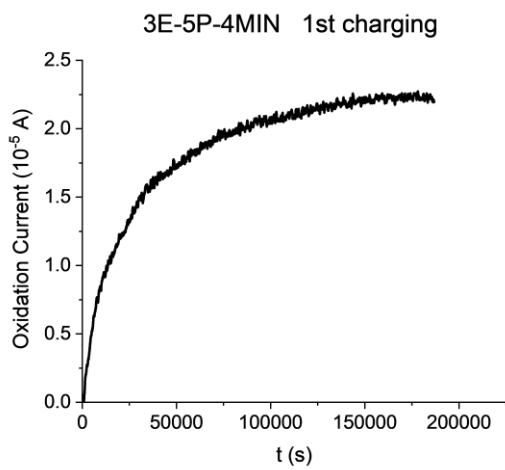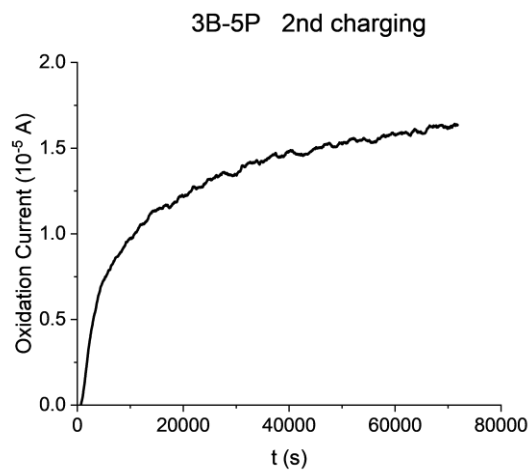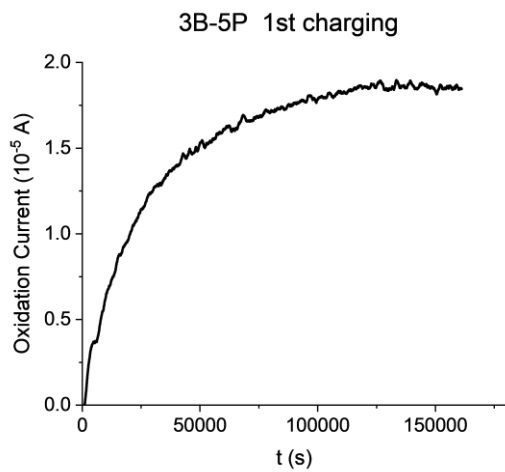
Fig. C. 8 Hydrogen permeation results of Group II samples.

Appendix D CCT diagram of X70 steel

In this section, a CCT diagram of the X70 steel studied in this work is established based on the dilatometer data of Gleeble testing system under various cooling rates, including 50°C/s, 30°C/s, 10°C/s, 3°C/s, 1°C/s and 0.3°C/s. Microstructure of the CCT samples were studied via OM and EBSD, which is used to validate the accuracy of the CCT diagram. Furthermore, a model is developed on the basis of Avrami equation to predict the phase composition of samples under each cooling rate using Bayesian Optimization method. With this model, more detailed information about phase transformation is revealed and added to the CCT diagram.

D.1 CCT diagram

Six (6) CCT samples without deformation process were heated up to 1200°C before cooled down to room temperature under 50°C/s, 30°C/s, 10°C/s, 3°C/s, 1°C/s and 0.3°C/s cooling rates, respectively. The dilatometer data of these cooling rates were plot with temperature and shown in Fig. D.1. Then tangent lines for high temperature phase (ferrite) and low temperature phase (bainite) are found using linear regression method (Fig. D.2), indicating thermal expansion coefficient of the phases. According to lever rule, the fraction of transformed phase (f) at corresponding temperature (T) is calculated as shown in Fig. D.3, and the transformation curves (f-T curve) are obtained (Fig. D.4) along with the starting temperature (T_s) of the high temperature transformation (ɣ-Fe → α-Fe) and the end temperature (T_e) of the low temperature transformation (ɣ-Fe → bainite) also determined (Table D-1).
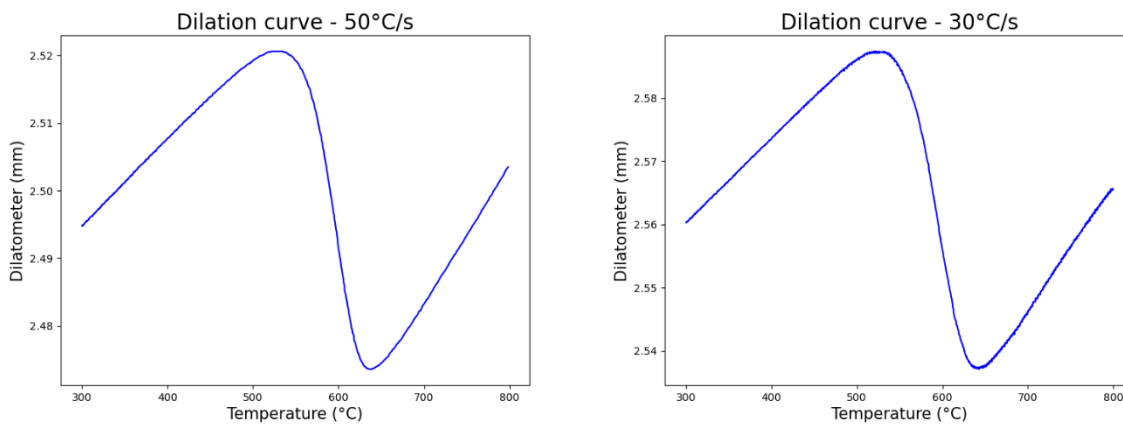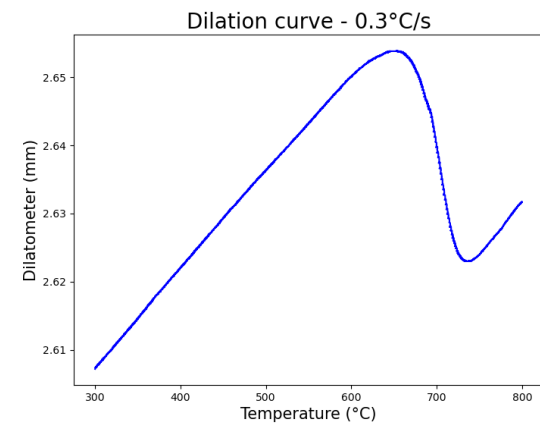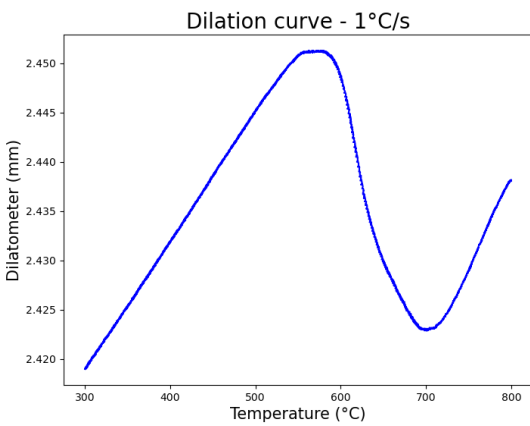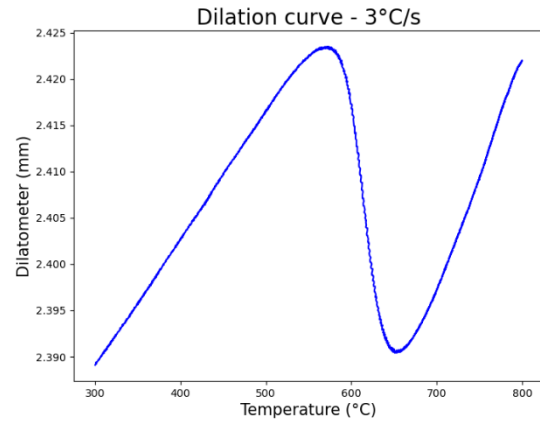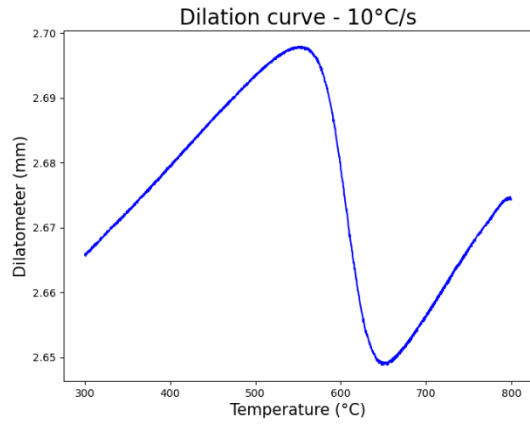
Fig. D. 1 Original Gleeble test data under various cooling rates.
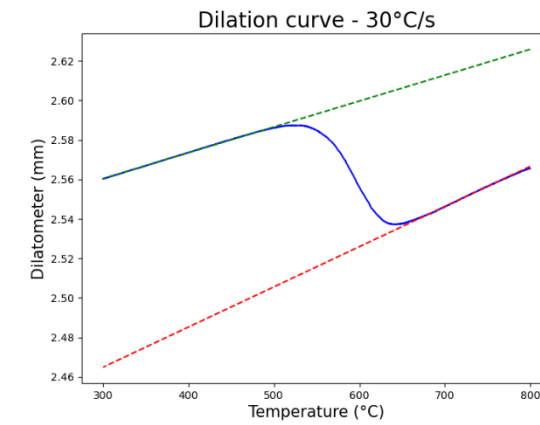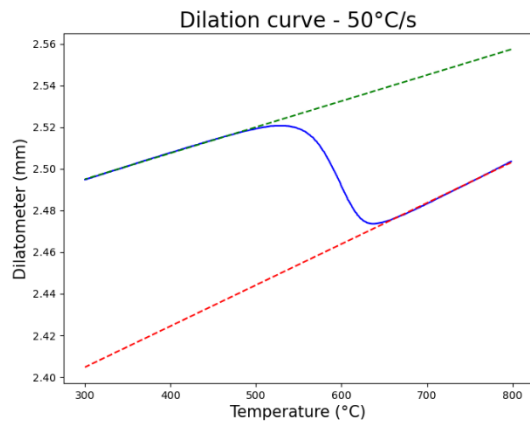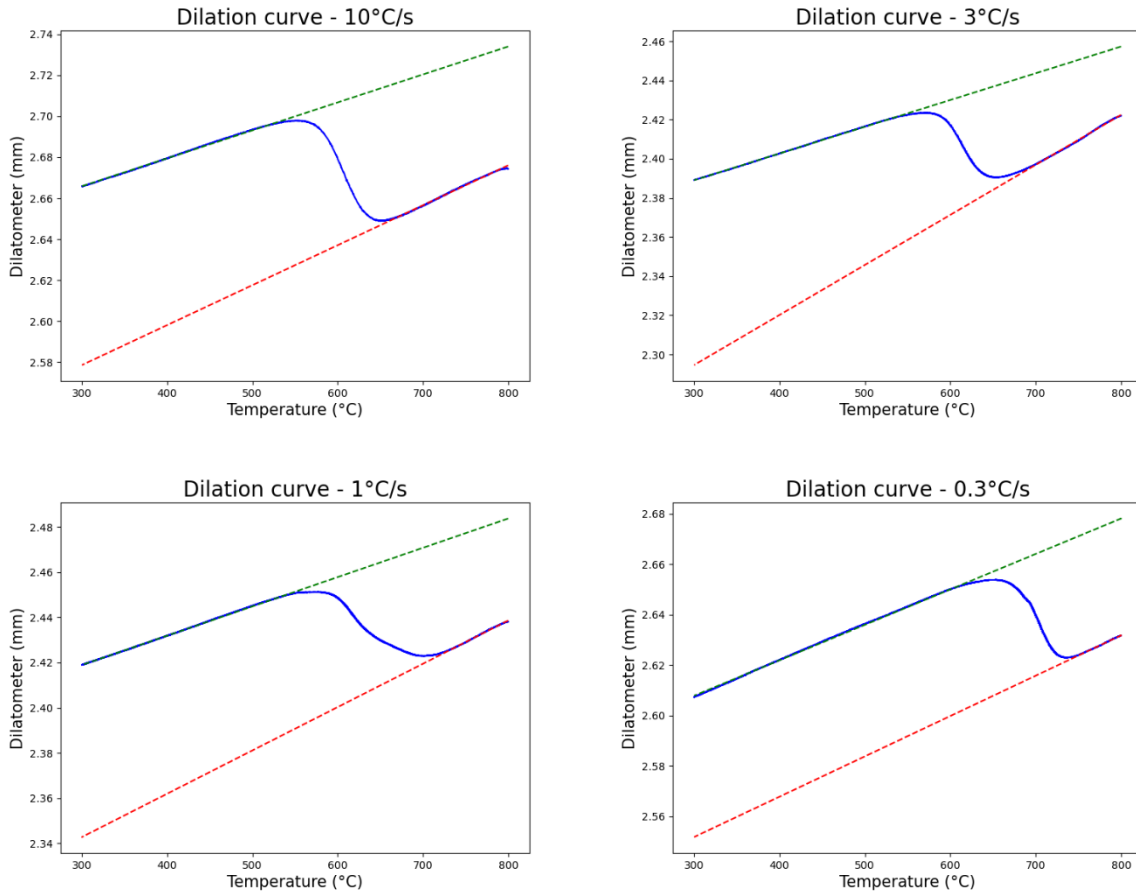
Fig. D. 2 Tangent lines for dilation curves.

$$f = \frac{BC}{AC}$$
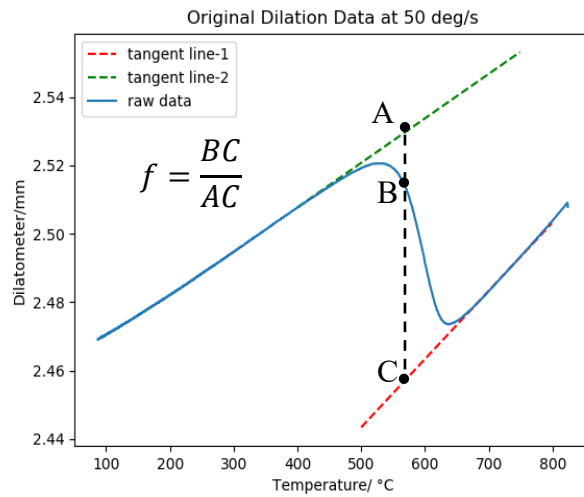
Fig. D. 3 Lever rule applied on dilation curve.
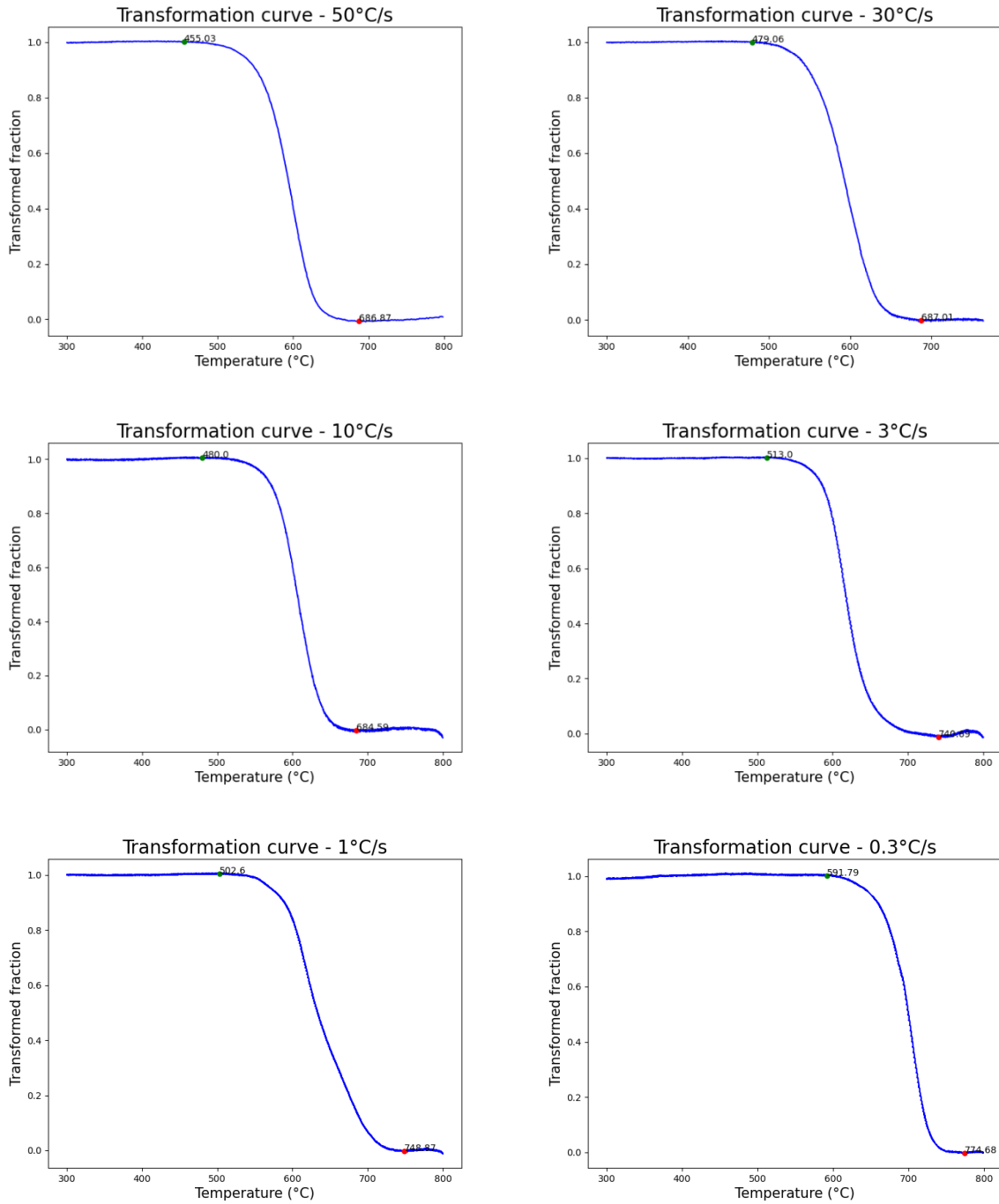
Fig. D. 4 Transformation curves (f-T curves) with starting and ending temperatures of the transformation.

Table D- 1 Starting and ending temperatures of transformation.

#	Cooling rate °C/s	T_s °C	T_e °C
1	50	686.87	455.03
2	30	687.01	479.06
3	10	684.59	480
4	3	740.69	513
5	1	748.87	502.6
6	0.3	774.68	591.79

In addition, deflection points on dilation curves and transformation curves (f-T curves) of 1°C/s and 0.3°C/s were observed, indicating the starting or ending of transformation ɣ-Fe → pearlite under low cooling rates. The positions (temperatures) of the points were determined by the cross points of tangent lines of adjacent points, as shown in Fig.D.5.
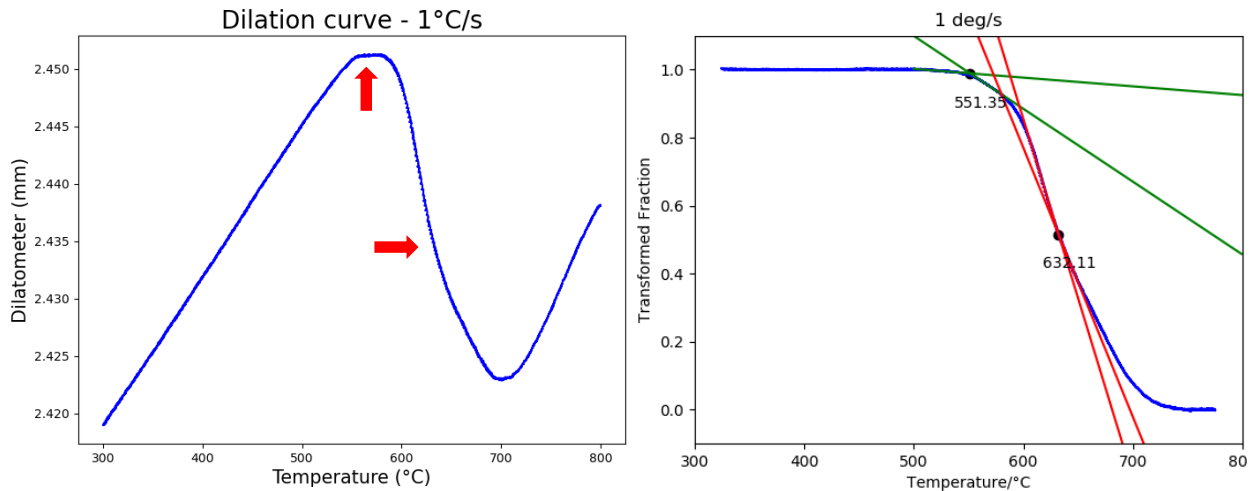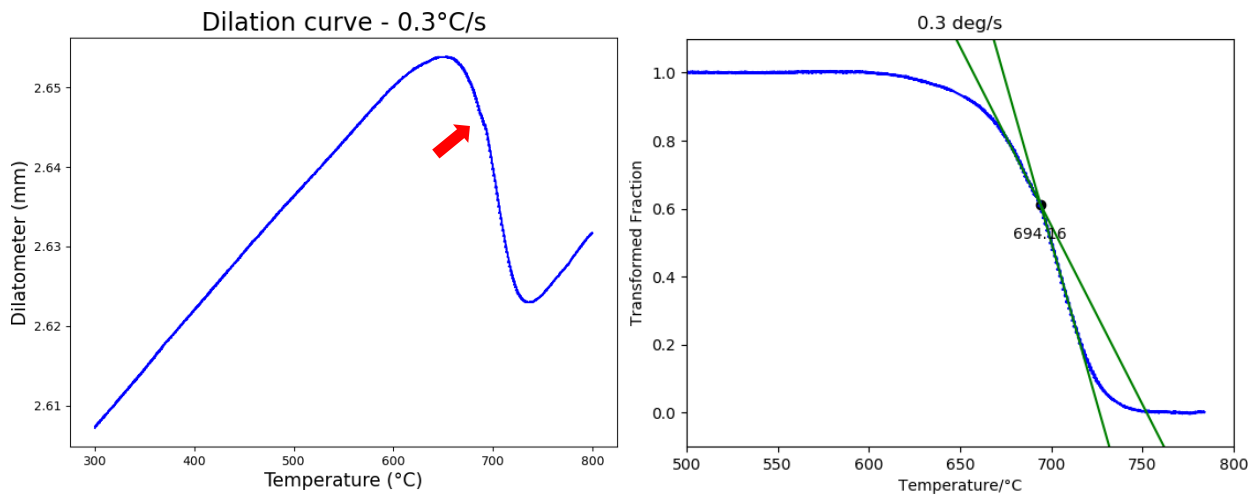
Fig. D. 5 Deflection points on dilation curves of 1°C/s and 0.3°C/s.

A heating dilatometry curve was also obtained, based on which Ac1[6], Ac3[7] and Ac1f [8]are determined by means of tangent lines (Fig. D.6). The results are Ac1= 761°C, Ac3= 934°C and Ac1f = 685°C. The values of Ac1 and Ac3 are very close to those published in reference [222], which are 760°C and 920°C, respectively.

---
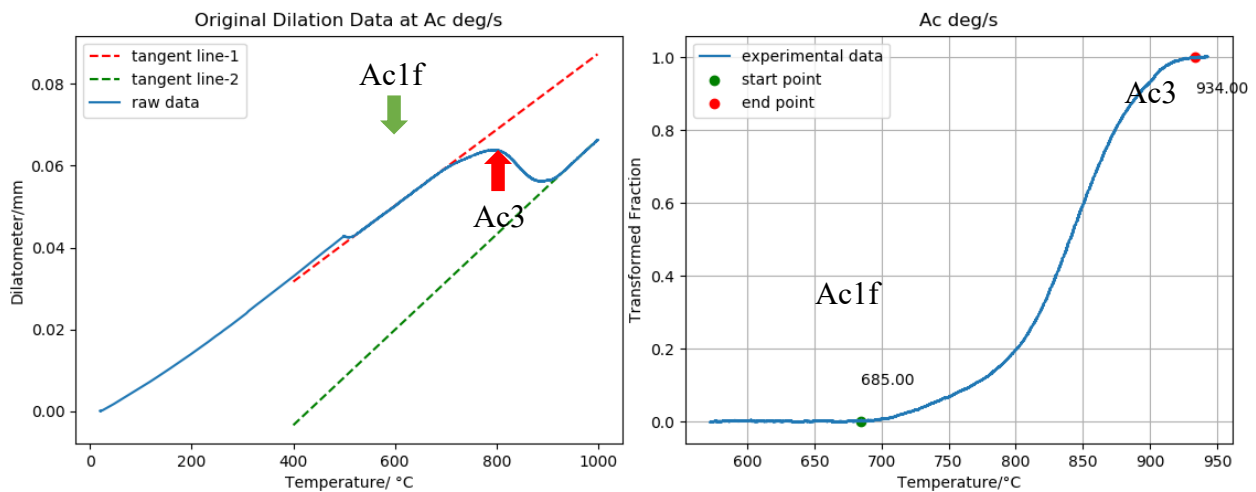
[6] Ac1: Lower critical temperature, at which austenite starts to transform from ferrite.
[7] Ac3: Upper critical temperature, at which austenite is completely transformed from ferrite.
[8] Ac1f: pearlite dissolution finish temperature, at which pearlite begin to transform into austenite.

231
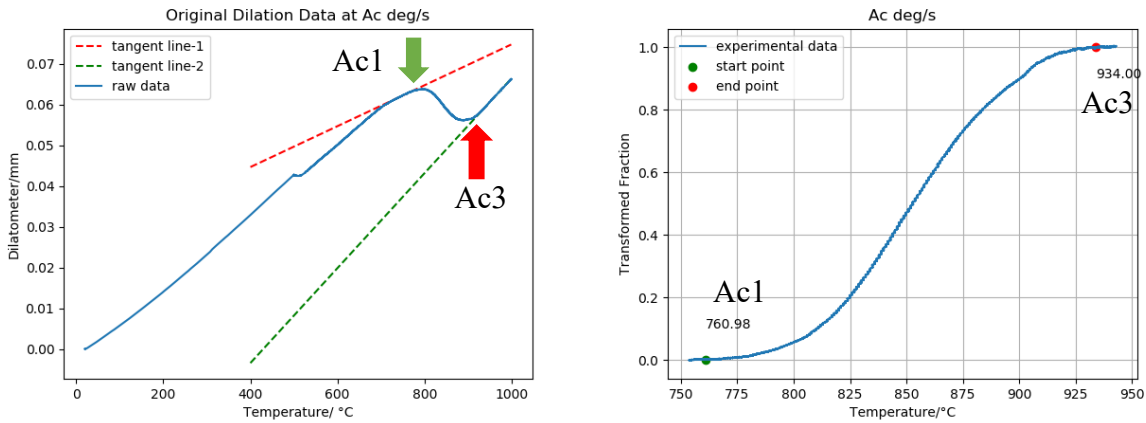
Fig. D. 6 Determination of Ac1, Ac3 and Ac1f on heating dilatometry curve.

With the above information, a CCT diagram is built up and shown in Fig. D.7.
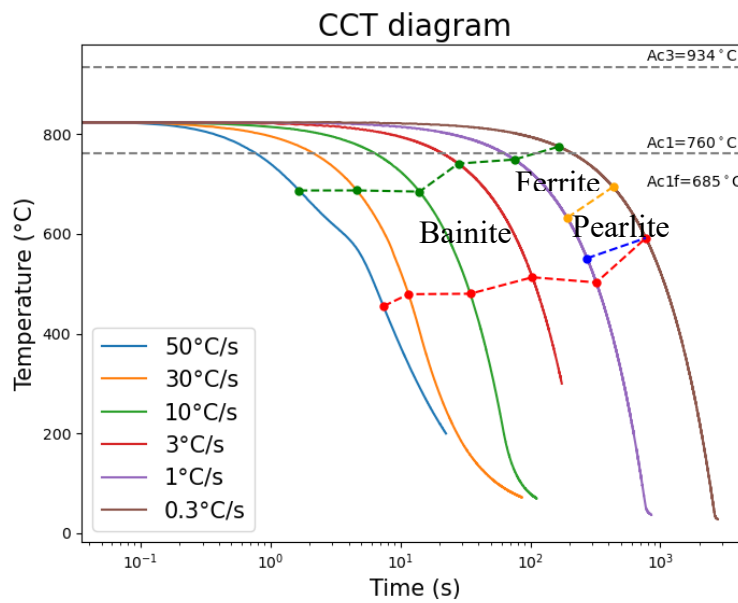
Fig. D. 7 CCT diagram of X70 steel.

D.2 Microstructure of CCT samples

The CCT samples were sectioned and mounted for microstructure characterization via OM and EBSD. In Fig. D.8, the microstructures of samples under different cooling rate are clearly revealed by OM images after etched in 2% Nital. Fig.D.8 a-b) shows that in the sample of 50°C/s cooling rate, ferrite and bainite are observed. However, in EBSD images (Fig.D.9 a-b), M/A constituents are also clearly shown. In Kernel Average Misorientation (KAM) map, bainite is

greenish and ferrite is blueish due to the higher dislocation density in the former than the latter; and in Band Contrast (BC) map, M/A is black, because this area was not well indexed during scanning as a result of the different lattice structure of martensite (bct) from ferrite/bainite (bcc).

Samples of 30°C/s, 10°C/s and 3°C/s consist of ferrite, bainite and M/A constituents. In sample of 1°C/s, pearlite is observed as well as polygonal ferrite (PF) and bainite, and the sample of 0.3°C/s only contains polygonal ferrite (PF) and degraded pearlite (DP). Therefore, the microstructure characterization results are consistent with the phase composition indicated by the CCT diagram.

Also, EBSD BC maps show that the average size of M/A constituents increases as the cooling rate decreases (as shown in Fig.D.10), which is probably because the carbon rejected during austenite decomposition has more sufficient time for redistribution under lower cooling rate.
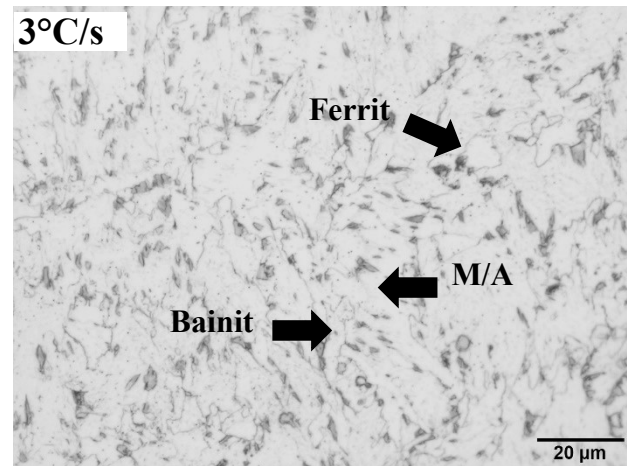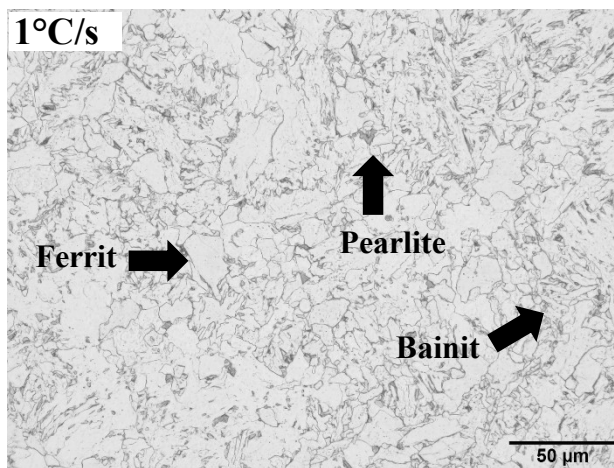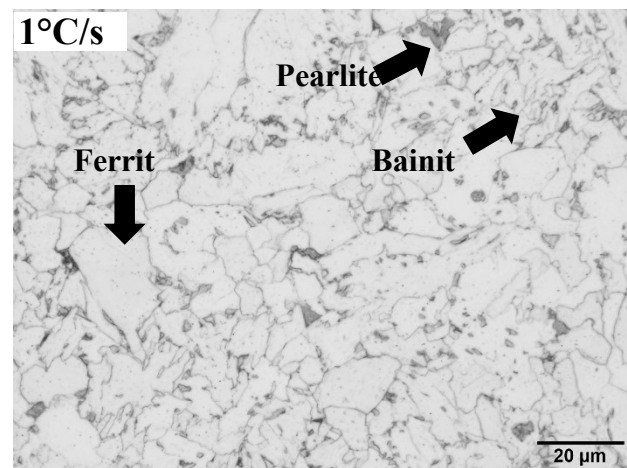

a)

b)

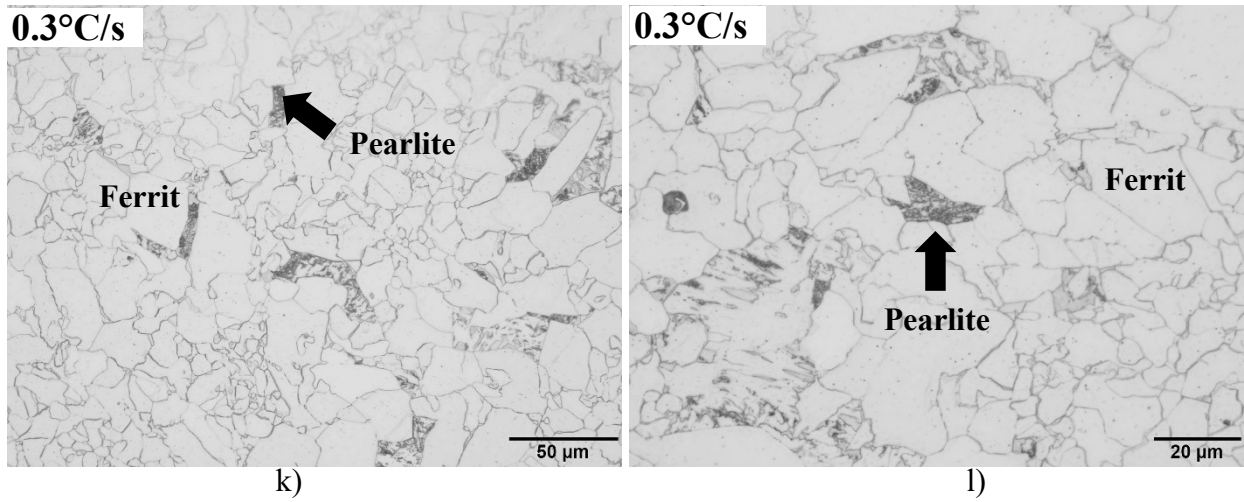
c)

d)
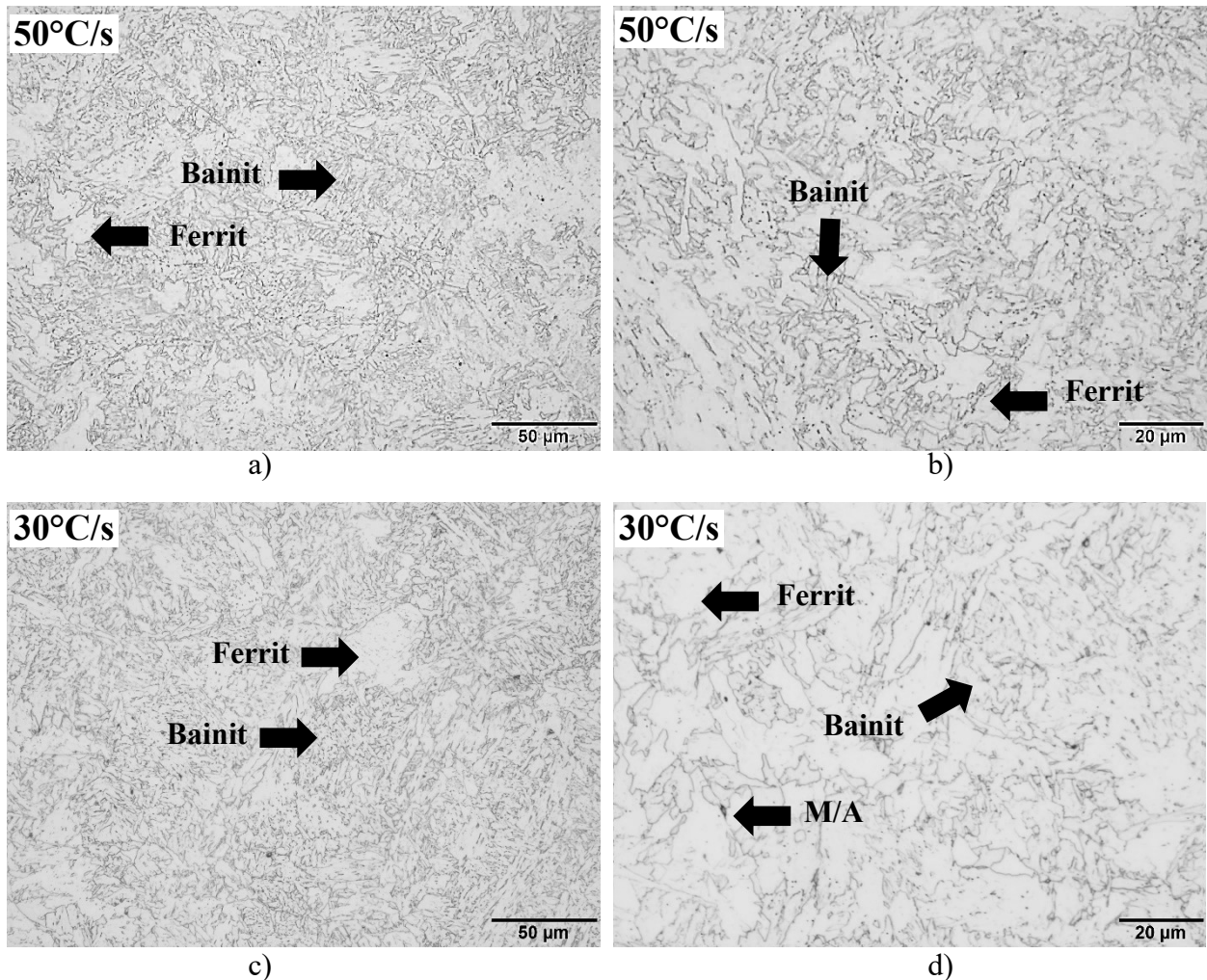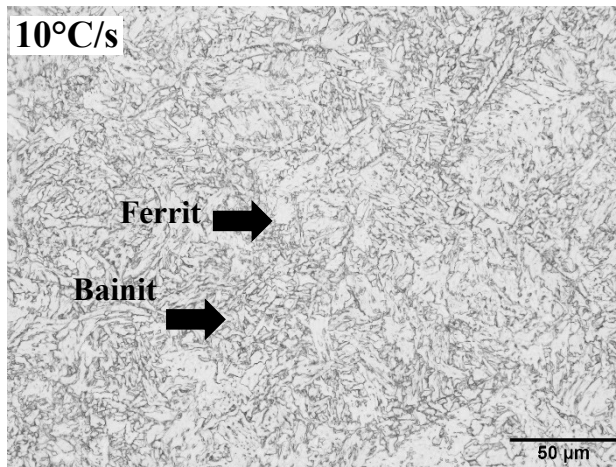
e)
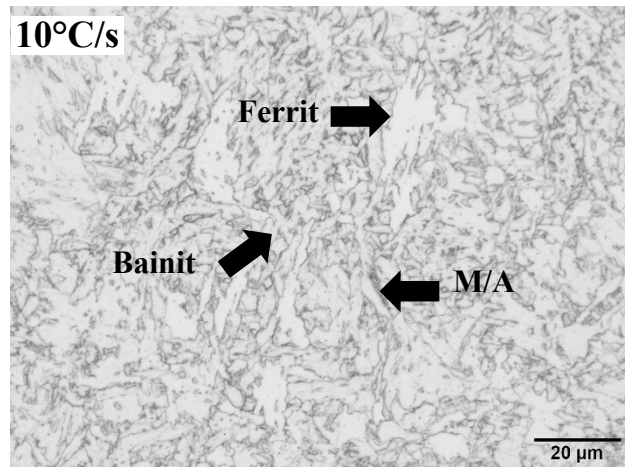
f)
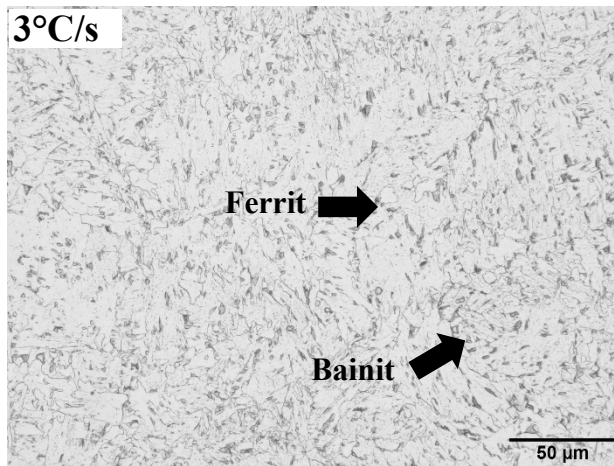
g)

h)

i)

j)

Fig. D. 8 OM images showing microstructure of X70 steel under various cooling rate.
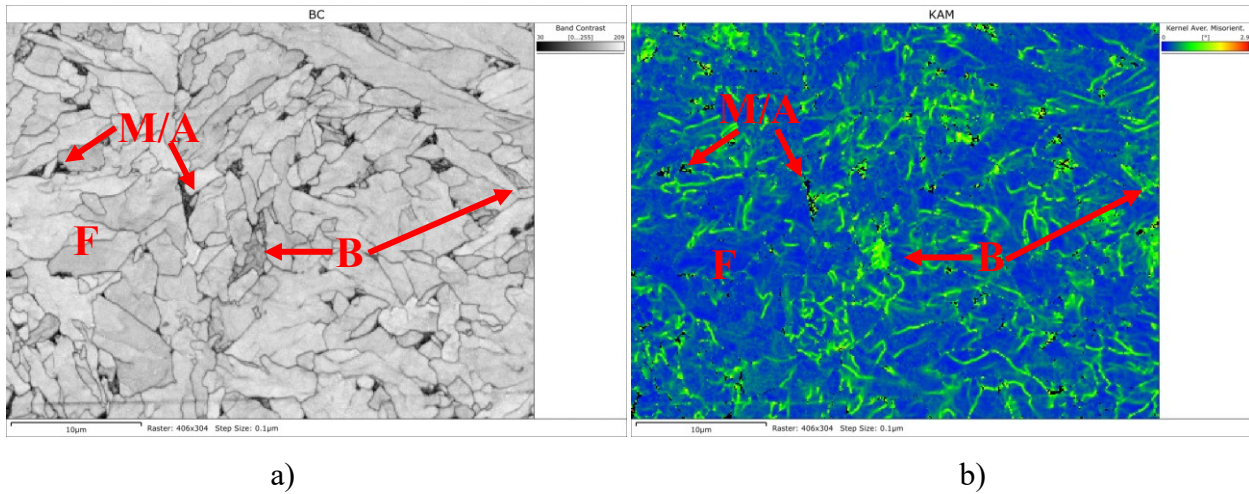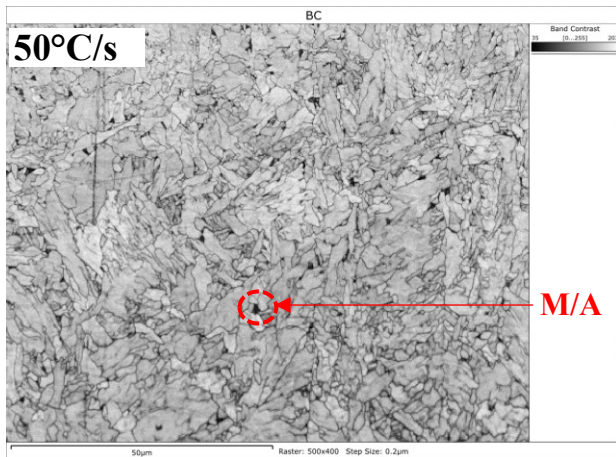
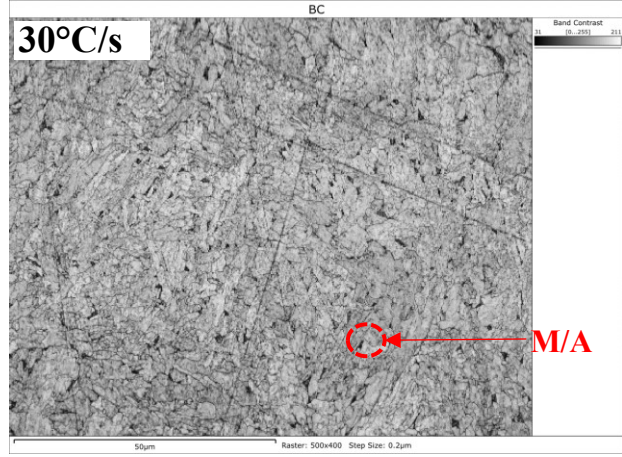

Fig. D. 9 EBSD Band Contrast map a) and Kernel Average Misorientation map b) of CCT sample with a cooling rate of 50 °C/s.

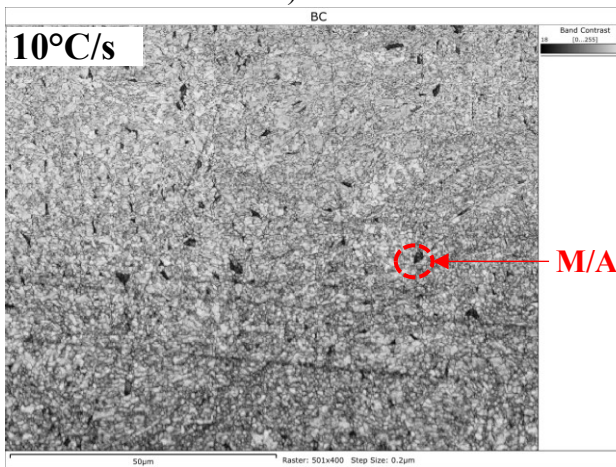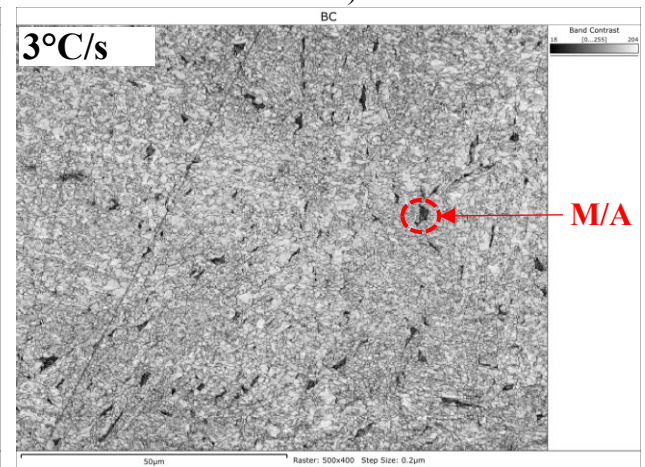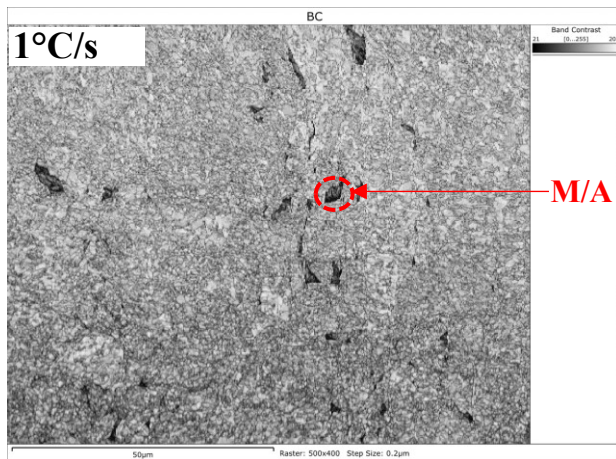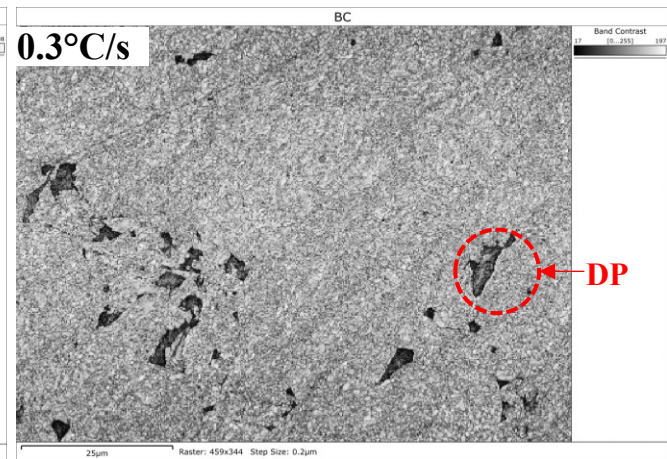Fig. D. 10 EBSD Band Contrast map of Gleeble test samples.

D.3 Phase transformation model

Avrami equation is commonly used to describe the transformation process of solids under isothermal condition. Venkatraman et al.[223] modified the equation as follows for application to continuous cooling transformation:

$$
\left.
\begin{aligned}
f &= 1 - exp\left(-\left(\frac{t}{\tau}\right)^n\right) \\
\tau &= \tau_0 exp\left(-\frac{Q}{RT}\right)
\end{aligned}
\right\} \qquad \text{(D-1)}
$$

Wherein f is the fraction transformed; Q is the activation energy; τ is the characteristic time; and n, Q, τ_0 are three parameters determined by the material, which are also called "Avrami parameters".

A model is proposed based on the modified Avrami equation above to make predictions about the phase fractions of X70 steel after different cooling rate in the Gleeble test using the transformation curves (f-T curves). The value of Q for each phase is taken as 200kJ/mol for ferrite ,110kJ/mol for pearlite, 80kJ/mol for bainite and 10kJ/mol for M/A[224-228]. For each sample, the transformation curves of all existing phases obtained by the modified Avrami equation are summed up and compared with the experimental data so that the Avrami parameters n and τ_0 as well as the transformed fraction of each phase can be determined by minimizing the loss function (i.e., mean square error/MSE). The simulated and experimental transformation curves are shown in Fig. D.11 and the curve-fitting results are listed in Table D-2.

It is predicted that as the cooling rate increases the fraction of ferrite increases except for under 0.3°C/s and the fractions of bainite and M/A gradually decrease, as seen in Fig. D.12. As compared with the characterization results in section D.2, the fraction of M/A seems overestimated. This is probably because M/A constituents consist of martensite and austenite and the ratio of the two components changes with the cooling rate, however only martensite is considered in the model.

The n values of high temperature phase fluctuated at a higher level than those of low temperature phase, and the τ_0 values of all phases increase exponentially with decreased cooling rate, except the n and τ_0 of the 0.3°C/s sample, as shown in Fig. D.13 and Fig. D.14. The deviant curve-fitting results of the 0.3°C/s sample are also shown in the much higher MSE as compared with other samples in Table D-2. This might be due to the degradation of pearlite as a result of

prolonged exposure to high temperature under such a slow cooling rate, which is not considered in the model.
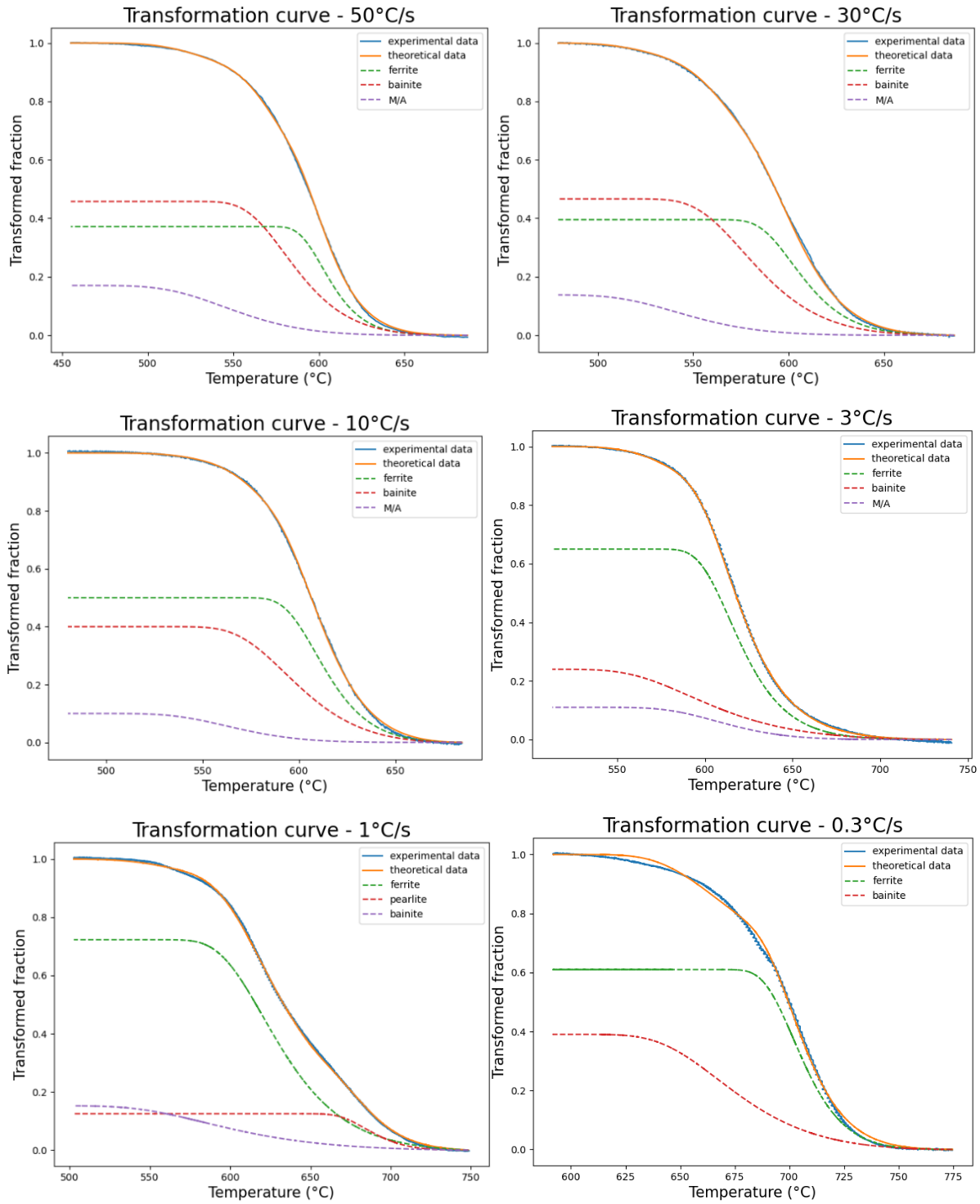

Fig. D. 11 Transformed fraction of each phase obtained by curving fitting with experimental data using modified Avrami equation.

Table D- 2 Avrami parameters and volume fraction of each phase obtained by curve fitting with experimental data.

|		Cooling rate (°C/s)					
	Parameters	50	30	10	3	1	0.3
Ferrite	Q (kJ/mol)	200	200	200	200	200	200
	n	1.72	1.40	1.44	1.47	0.96	1.96
	τ_0 ($\times 10^{12}$)	1.48	2.51	5.50	25.12	62.49	12.88
	Fraction (%)	37	40	50	65	72	61
Pearlite	Q(kJ/mol)	-	-	-	-	110	110
	n	-	-	-	-	2.25	1.62
	τ_0 ($\times 10^7$)	-	-	-	-	6.78	47.86
	Fraction (%)	-	-	-	-	13	39
Bainite	Q(kJ/mol)	80	80	80	80	80	-
	n	2.07	1.90	1.84	1.52	1.25	-
	τ_0 ($\times 10^5$)	1.74	3.16	6.46	34.67	125.89	-
	Fraction (%)	46	47	40	24	15	-
M/A	Q(kJ/mol)	10	10	10	10	-	-
	n	3.90	4.32	4.29	4.55	-	-
	τ_0 ($\times 10^1$)	1.29	2.19	5.37	18.20	-	-
	Fraction (%)	17	13	10	11	-	-
MSE ($\times 10^{-5}$)		2.36	2.27	2.93	2.11	2.97	14.47
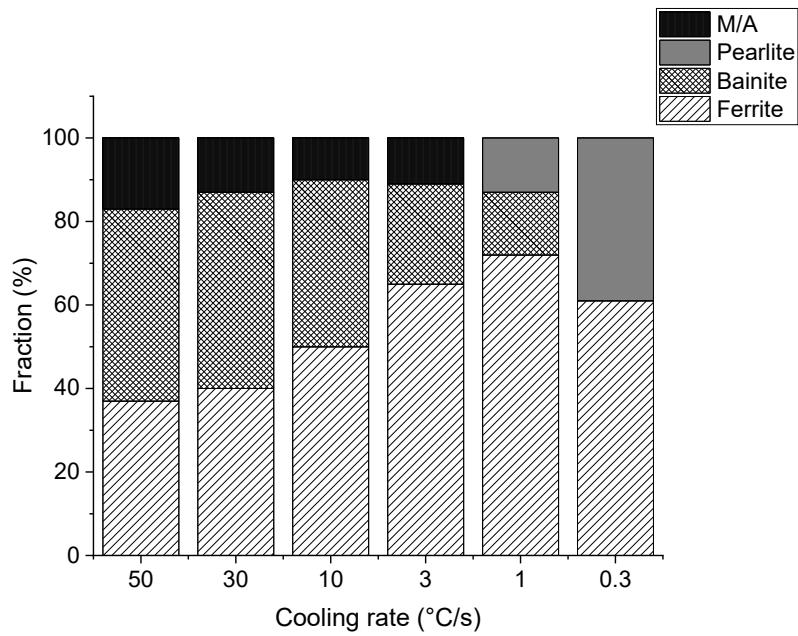
Fig. D. 12 Phase fraction of Gleeble test samples.
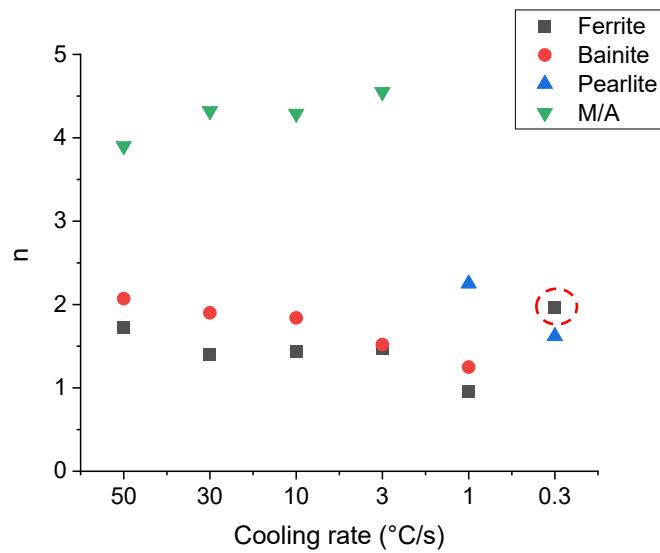

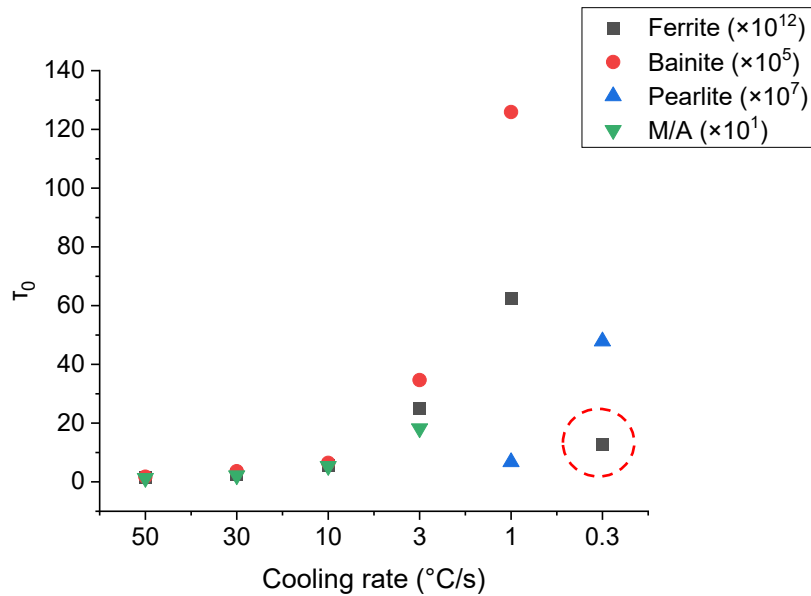Fig. D. 13 Values of Avrami parameter n of phases in Gleeble test samples.

Fig. D. 14 Values of Avrami parameter τ_0 of phases in Gleeble test samples.

D.4 Summary

The conclusions of this section are summarized as follows:

1) A CCT diagram of X70 steel (without deformation) is established based the dilatometry test results under six (6) cooling rate and confirmed by the microstructure characterization results of the tested samples.

2) A transformation model is developed to predict phase composition of transformation under these cooling rates based on the dilatometry curves, which fits well with experimental f-T curve and gives reasonable prediction results and Avrami parameters (n, τ_0).

3) To improve the accuracy of the transformation model, the decomposition of pearlite under low cooling rate and the austenite component in M/A constituents might need to be considered.